DYNAMIC LOADS ANALYSIS OF SPACE VEHICLE SYSTEMS

LAUNCH AND EXIT PHASE

by

Raymond H. Schuett
Bruce A. Appleby
Jack D. Martin

Report No. GDC-DDE66-012

June 1966

This work was performed for the Jet Propulsion Laboratory, California Institute of Technology, sponsored by the National Aeronautics and Space Administration under Contract NAS7-100.

GENERAL DYNAMICS
Convair Division

FOREWORD

This report was prepared for the Jet Propulsion Laboratory, Pasadena, California, by the Convair division of General Dynamics, San Diego, California. The task was accomplished under Contract NASA 7-100, Subcontract JPL 950994, entitled "Engineering Manual on Dynamic Loads Analysis for Space Launch Vehicles" during the period from July 1965 to June 1966. The work was initiated by Mr. William Gayman who provided technical coordination and administration of the task for the Jet Propulsion Laboratory. The Project Leader for the Convair division was Mr. C. Desmond Pengelley.

TABLE OF CONTENTS

TABLE OF CONTENTS, Contd

TABLE OF CONTENTS, Contd

TABLE OF CONTENTS, Contd

TABLE OF CONTENTS, Contd

LIST OF ILLUSTRATIONS

LIST OF ILLUSTRATIONS, Contd

LIST OF ILLUSTRATIONS, Contd

LIST OF ILLUSTRATIONS, Contd

LIST OF TABLES

1/INTRODUCTION

1/INTRODUCTION

This document constitutes one volume of a two-volume work dealing with the structural dynamics of space vehicle systems. The overall purpose is twofold, namely to educate and to coordinate.

This volume considers dynamic loads encountered during the launch and exit phases. The companion volume, Ref. 1.1, treats the problem of overall system integration, including interface communication between contractors and integrating agency, methods of defining contractual specifications, and logical treatment of dynamic interaction between major components (such as payload and booster) that are built by separate organizations.

The work is addressed to graduate students in engineering and mechanics, as well as practicing engineers and members of technical management. A sound education in these fields is assumed although references are listed for background study. Specific knowledge of missile technology is not required. The goal is to provide an overall practical picture of the current state of the art rather than solutions, and to describe current methods rather than proofs. A comprehensive bibliography is given from which formal proofs can be obtained. Numeric examples are used to illustrate procedures and typical results, the Atlas/Centaur/Surveyor vehicle being used as a model. Many unsolved problems still exist and empirical - often intuitive - approaches are used. Comments and suggestions, based on practical judgement and experience, are presented where possible.

This volume is divided into sections that have their own lists of symbols and bibliographies. One section covers basic analytical tools common to all phases of structural dynamic technology. While it offers nothing that does not already exist in classical texts, it collects and summarizes those techniques applicable to the problem at hand and presents them in a consistent, convenient form. Subsequent sections concentrate on individual problem areas such as ground wind loads, thrust buildup and launcher induced loads, flight loads, etc. The central theme is on low-frequency phenomena that include the first five or ten modes of the vehicle, but a brief outline is included of methods of dealing with random loads, such as buffet, that become significant at much higher frequencies in the spectrum.

An analytical obstacle in the past has been the numeric problems involved in handling and solving the large number of equations required for adequate description of the vehicle; however, the advent of electronic computers has made possible the execution of routines involving vast amounts of data. Computer solutions have been used in preparing the illustrative examples.

Applied forces in many cases are still not described by firm criteria since data from which such criteria could be obtained are still in the formative stage. Examples include the vortex shedding and gust spectra of ground winds, the thrust buildup and decay characteristics of individual rocket engines, and the wind profiles and gusts of winds aloft. The first two require test data on the particular vehicle and engine, while the criteria for winds aloft are obtained from freely rising balloons, which yield velocity profiles lacking in detail and must be supplemented by gust data obtained from aircraft experience.

The application of dynamic analysis to the design and testing of space vehicle systems, especially the payload or spacecraft, is often grossly simplified, in the conservative direction, causing unnecessary design penalties and test problems. A typical example is the vibration test requirements for a payload or spacecraft which, in the lower frequencies, quite often require input excitation equivalent to the maximum response the article will see. This problem is caused by inadequate dynamic modeling of the interfaces between stages built by different contractors, and also the uncertainty as to exactly how the design or test data will be applied. The inaccuracies so introduced are illustrated in Ref. 1.2 where the vibration testing of a simple model is conducted using oversimplified criteria, as sometimes applied to spacecraft, and is then duplicated by a more sophisticated simulation of what actually is expected to occur. The many differences in results are often expressed in orders of magnitude rather than in percentages.

The work presented herein strives for a better understanding and use of dynamic analysis data by describing the forces to which a space vehicle system is exposed, techniques to obtain responses, and application of results.

REFERENCES

1.1 W. H. Gayman and J. A. Garba, Dynamic Load Analyses of Space Vehicle Systems-Launch and Exit Phase, JPL Technical Memorandum 33-286 (To be published).

1.2 W. H. Gayman, A Note on Boundary Condition Simulation in the Dynamic Testing of Spacecraft Structures, JPL Technical Report No. 32-938, 15 April 1966.

2/ ANALYTICAL TECHNIQUES

NOMENCLATURE

A	Area	ft^2
C	Flexibility matrix	ft/lb or rad/ft-lb
$C_{N/\alpha}$	Normal force coefficient per angle of attack	1/rad
C_B	Coulomb friction coefficient	ft-lb
$\overline{C}_F$	Equivalent admittance for gimbal friction	ft-lb-sec/rad
$\overline{C}_L$	Discharge coefficient of leakage bypass orifice	$ft^3/sec/\sqrt{lb/ft^2}$
C_V	Viscous friction coefficient	ft-lb-sec/rad
D	Dynamic matrix	sec^2
E	Young's modulus	lb/ft^2
F	Force; load vector function (e.g., F(x))	lb; adjustable
G	Shear modulus	lb/ft^2
$H(\omega)$	Complex frequency response	adjustable
I	Area moment of inertia; mass moment of inertia; unity matrix	ft^4; $lb\text{-}sec^2\text{-}ft$; N.D.
J	Polar moment of inertia	ft^4
K	Stiffness; autopilot gain; shear effectiveness factor	lb/ft or $\frac{ft\text{-}lb}{rad}$; adjustable; N.D.
KE	Kinetic energy	ft-lb
L	Length; Laplace function	ft; N.D.
M	Mass matrix; moment	$\frac{lb\text{-}sec^2}{ft}$; ft-lb
N	Number of samples or experiments	N.D.
N_x	Axial force/unit circumferential length	lb/ft
P	Pressure; probability	lb/ft^2; N.D.
PE	Potential energy	ft-lb
Q	Generalized force	lb

NOMENCLATURE, Contd

R	Gas constant; radius	ft/° F; ft
S	Shear	lb
S_o	Static moment about fixed point	ft-lb
S_R	Reference area	ft^2
T	Thrust; time; temperature	lb; sec; ° F
U	Assumed mode shape	ft/ft
V	Volume; velocity	ft^3; ft/sec
W	Weight; work	lb; ft-lb
$Z(\omega)$	Complex impedance	lb/ft
a	Radius of tank	ft
b	Minor semi-axis of elliptical tank bottom	ft
d	Longitudinal flexibility matrix; element of dynamic matrix	ft/lb or $\frac{rad}{in.-lb}$; sec^2
f	Function, e.g., f(x)	adjustable
h	Thickness	ft
i	Station index; complex number $\sqrt{-1}$	N.D.
j	Station index	N.D.
k	Statistical index	N.D.
m	Mode index; mass	N.D.; $\frac{lb\text{-}sec^2}{ft}$
n	Mode index; time index	N.D.
p	Pressure	lb/ft^2
q	Dynamic pressure	lb/ft^2
r	Radial coordinate for cylindrical tank	ft
s	Laplace operator	N.D.
t	Time	sec
u	Displacement; function describing a random process	adjustable

NOMENCLATURE, Contd

u_x	Longitudinal displacement of a shell element	ft
v	Volume	ft^3
w	Weight; mode participation factor	lb; ft/ft
w_r	Radial displacement of a shell element	ft
x	Coordinate along neutral axis	ft
y	Coordinate normal to neutral axis	ft
z	Coordinate normal to neutral axis (slosh mass)	ft
Δ	Increment	N.D.
$\sum$	Summation	N.D.
Φ	Velocity potential; complete mode shapes	ft/sec;ft/ft
Λ	Deflation matrix	N.D.
$\Phi(\omega)$	Power density spectra; power spectra	adjustable
α	Angle of attack	rad
γ	Adiabatic constant; mode participation factor; shear slope of a mode	N.D.; ft; rad/ft
δ	Engine gimbal angle; control system coordinate	rad; adjustable
ϵ	Strain; iteration convergence criterion	in./in.; N.D.
ζ	Damping coefficient	N.D.
θ	Rotation displacement in xy plane	rad
λ	Eigenvalue	sec^2
μ	Vector to release translation of fixed point; mean	N.D. adjustable
ν	Poisson's ratio	N.D.
ξ	Normal mode coordinate	ft/ft
π	3.1416	N.D.
ρ	Density	$lb\text{-}sec^2\text{-}ft^2$

NOMENCLATURE, Contd

σ	Stress; standard deviation; modal slopes	lb/in.^{2}; adjustable; rad/ft
τ	Vector to release rotation of fixed point; autopilot filter value; time lag; period	ft or N.D.; sec; sec; sec
ϕ	Modal displacements	ft/ft
ψ	Rotation about x-axis	rad
$\psi(\tau)$	Autocorrelation function	adjustable
ω	Frequency	rad/sec
m	Generalized mass	$\frac{\text{lb-sec}^2}{\text{ft}}$
$\lfloor\ \rfloor$	Row matrix	
$[\ ]$	Square matrix	
$\{\ \}$	Column matrix	
$\lceil\ \rceil$	Diagonal matrix	
$\cdot\cdot$	Second derivative with respect to time	
$\cdot$	First derivative with respect to time	
$'$	d/ds; transpose	
$''$	d^2/ds^2	
$\propto$	Proportional to	
$\bar{x}$	Conjugate of x	
x^*	Conjugate transpose of x	

Also,

A, T, R are transformation matrices

and

A, B, D, E, F, V, W, a, b, c, d, e, f, g, v, w, x, α, β, γ are used as substitutions for expressions and are defined in the text when so used.

2/ ANALYTICAL TECHNIQUES

This section provides the basic analysis methods used in the solution of structural dynamics problems. It is the intention of this section to present these methods without mathematical proofs and indicate, in only a general manner, their application to problems. The proofs required are well covered in classical literature (Refs 2.1 to 2.4). Specific applications appear in later sections.

2.1 BASIC EQUATIONS OF MOTION

The solution of dynamics problems is approached by developing a set of governing equations through consideration of the condition of dynamic equilibrium or of energy relationships of the system under applied external forces. For an undamped system the general form of these equations, in matrix notation, is

$$[M]\{\ddot{u}\} + [K]\{u\} = \{F\} \tag{2.1}$$

where [M] is a matrix of masses, [K] is a stiffness matrix, {u} and {ü} are the displacement and acceleration vectors, respectively, and {F} is a vector of external forces.

A very useful characteristic of elastic systems is that they will respond or vibrate in natural orthogonal modes. The total displacement of a system can then be expressed as a summation of individual natural mode displacements. This is given by

$$\{u\} = [\Phi]\{\xi\} \tag{2.2}$$

where $[\Phi]$ is a matrix of mode shapes and ξ_n is the time-dependent amplitude of mode n. Substituting Eq. 2.2 into Eq. 2.1 yields

$$[M][\Phi]\{\ddot{\xi}\} + [K][\Phi]\{\xi\} = \{F\} \tag{2.3}$$

Premultiplying both sides of Eq. 2.3 by $[\Phi]'$ gives

$$[\Phi]'[M][\Phi]\{\ddot{\xi}\} + [\Phi]'[K][\Phi]\{\xi\} = [\Phi]'\{F\} \tag{2.4}$$

The requirements of orthogonality and harmonic motion of the natural modes provide the relationships

$$[\Phi]'[M][\Phi] = [m] \tag{2.5}$$

and

$$[\Phi]'[K][\Phi] = [\omega^2][m] \tag{2.6}$$

Substituting Eqs 2.5 and 2.6 into Eq. 2.4, we obtain

$$\{\ddot{\xi}\} + [\omega^2]\{\xi\} = [m]^{-1}[\Phi]'\{F\} = [m]^{-1}\{Q\} \tag{2.7}$$

Eq. 2.7 is a set of n uncoupled equations in terms of ξ_n, ω_n, the generalized mass m_n, and the generalized force Q_n. The solutions of these equations identify the time-dependent values of ξ_n which are then used in Eq. 2.2 to give complete system response. Detailed discussions, derivations, and proofs of the equations of motion, orthogonality of natural modes, and normal mode theory are given in Refs 2.1 to 2.4.

The use of normal mode theory requires determination of these natural modes of vibration. If harmonic motion is assumed and the applied forces are equal to zero, then Eq. 2.1 can be written as

$$-\omega^2[M]\{u\} + [K]\{u\} = 0 \tag{2.8}$$

or

$$\{u\} = \omega^2[K]^{-1}[M]\{u\}$$

Each of these equations is in a form suitable for solutions to obtain the orthogonal modes and their natural frequencies. Many numeric techniques have been developed to obtain these characteristics and several are discussed in Section 2.3.

The above discussion presents the fundamental approach to structural dynamic response analyses. The fact that the response of a linear structural system is adequately described by superposition of its normal modes indicates the importance of normal modes. The mathematical model used to represent the physical system, methods employed to obtain vehicle modes, and techniques achieving response solutions will now be covered in detail.

2.2 MATHEMATICAL MODELS

The stages of a launch vehicle typically consist of cylindrical tanks (containing propellants), with engines and other equipment attached at the aft end by means of some support structure and with either another stage or a payload attached at the forward end. The payload commonly (though not always) is supported by a truss or adapter and covered by a fairing. In this case the payload and fairing are each cantilevered from an attaching ring on the launch vehicle and are not physically connected. The formation of a mathematical model of such a launch vehicle requires care and a knowledge of the structure because the accuracy of the analysis of the response of a vehicle to a force depends largely on the correctness of the mathematical model. This section discusses in detail the various aspects of modeling.

2.2.1 LATERAL MODEL OF A CYLINDRICAL LIQUID PROPELLANT VEHICLE.

In most instances, the lateral dynamic characteristics of a liquid rocket space vehicle

system can be considered to be adequately represented by simple one-dimensional beam theory. It is common practice, and certainly more convenient, to replace the continuous structure by a lumped parameter idealization. In such an idealization, the analyst concentrates on those aspects of the system which are felt to be dominant (major masses, major structural elements, propellants). The discrete model is formed by concentrating the distributed mass at selected points along the beam. These points are ideally the centers of gravity of the distributed masses concentrated at the points.

Elastic properties are expressed in lumped fashion as a set of flexibility coefficients, C_{ij}, or stiffness influence coefficients, K_{ij}. These coefficients have physical significance in that C_{ij} can be considered as the deflection of point i due to a unit load at j, and K_{ij} as equated to the force produced at point i due to a unit deflection at point j, if all coordinates other than j are temporarily restrained. (Flexibility and stiffness influence coefficients are covered in more detail in Section 2.2.2.)

The mathematical description of this discrete model is a set of simultaneous and linear ordinary differential equations. Such equations lend themselves readily to matrix techniques and digital computer computation.

The one-dimensional beam representation is the simplest lateral model and may not fulfill all necessary requirements for a specific problem. This can necessitate recognition of nonstructural modes (sloshing), local response characteristics (engines), or multiple load paths not accounted for in the simple beam analogy. A further refinement of the model is then necessary.

2.2.1.1 Mass and Moment of Inertia. The distributed mass and moment of inertia data must be lumped into discrete, point masses, the number of which determine the degrees of freedom given to the model. The number of mass stations is influenced by the number of bending modes to be calculated.

It has been found that for one-dimensional beam bending models the required number of mass stations should be approximately ten times the number corresponding to the highest elastic bending mode to be calculated. For example, if three elastic bending modes are to be calculated, then approximately 30 mass stations are required to represent adequately the bending dynamics of the third mode. This criterion has been established empirically by calculating mode shape, frequency, and generalized mass corresponding to the first three elastic bending modes for typical vehicle configurations in which the number of mass stations used was successively increased from 18 to 40. As expected, the accuracy increased as additional stations were utilized. However, it was observed that no further significant increase in accuracy was achieved by using more than 30 mass stations. Additional information regarding the number of mass stations to use is given in Ref. 2.39.

For a more complex model (such as one with branched beams) the above general rule may not be strictly applicable. For a branched system, the general rule may be applied to the primary beam of the system, and masses lumped on the secondary branches in about the same distribution. It must be emphasized that as the model

diverges from the single beam concept, mass lumping rules become less applicable and more reliance must be placed upon the experience of the analyst.

Note that only rigid masses are to be included in this distribution; that is, only those masses which can be considered to act as an integral part of the unrestrained beam during its vibrations. It cannot be over-emphasized that items such as pumps, equipment pods, etc., which are actually, or simulated to be, mounted elastically to the main structure, may significantly alter the bending characteristics of the higher frequency modes.

Whether or not such masses are to be treated as integral to the beam or as separate elastically attached masses depends upon: 1) whether or not the frequencies of the body modes to be computed are less than or greater than the mount frequencies of the discrete masses, and 2) whether or not these masses are great enough to materially affect the result.

Accurate representation of the distributed mass at discrete points would require inclusion of the mass moment of inertia of the distributed mass at that point. With liquid propellant, the effective moment of inertia is not easily determined. Fortunately, these moments of inertia have only a small influence on the modal quantities of the first two bending modes and can be neglected, as shown in the work of Ref. 2.5. A better representation could be obtained by using more mass stations rather than including moments of inertia.

Because of the small effect in the lower bending modes and the uncertainty of the effective moment of inertia, it has been common practice to neglect this term. Also, this allows for much more efficient computation since this eliminates half the coordinates in the solution of characteristic equations.

2.2.1.2 Sloshing Propellants. Space vehicle system propellants constitute a large percentage of the total system weight. Part of this propellant can be considered as rigid or distributed mass on the idealized beam while a smaller portion must be allowed to slosh in the lateral model. This sloshing mass becomes more important in later flight times when it becomes a sizeable proportion of total vehicle weight. If the frequencies of the sloshing modes and the frequency of the first structural mode are widely separated (ratio of 1:3 or greater) the effect of sloshing upon loads is small and in preliminary work can safely be ignored. However, as the separation between the sloshing frequencies and the structural frequency becomes small the effect of sloshing upon loads may be significant.

Several methods have been developed to describe propellant sloshing modes and frequencies. The general approach, as related to lateral models, is to derive the hydrodynamic equations in a form suitable for a mechanical analogy. It can be shown for a cylindrical tank that if: 1) the tank walls are rigid, 2) the fluid is incompressible and irrotational, and 3) only small disturbances are admitted, then pendulum or spring mass analogies can be devised which will reproduce the characteristics of the fundamental

mode of sloshing oscillation. Attaching the equivalent spring mass to the lateral model is easily accomplished and is therefore preferred over the pendulum. The second and higher sloshing modes are not generally considered because the magnitude of lateral force contribution from these modes decreases rapidly with increasing order; furthermore, test experience indicates that a great deal of turbulent mixing occurs and that damping effects are greater in higher modes.

Techniques for deriving the mechanical analogies for slosh and their limitations are discussed in the literature (Refs 2.6 and 2.7).

2.2.1.3 Engine Representation. Thrust-vector control of liquid-propellant vehicles is generally maintained by gimballing the rocket engines. Since the entire engine is gimballed rather than just the thrust vector, this gimballing action will cause inertial forces as well as thrust forces to act on the missile body. These inertial forces are appreciable, and their lateral components will exceed those of the thrust forces when the engine is gimballed sinusoidally at a sufficiently high frequency. The thrust vector displacement consists of two components: 1) the displacement contained within the elastic mode (including the flexibility of the engine mounting and actuator structure) while the servo positioning system is locked, and 2) the additional degree of rotational freedom added to represent the motion accompanying the action of the positioning servo.

The engine is incorporated into the lateral model by attaching a mass and moment of inertia at the appropriate location on the one-dimensional beam. Since the engine itself is quite rigid, the only elasticity normally considered is the mounting structure and actuator system. This structure is generally complex and test data are often required for proper simulation. One such test would be a vibration test to determine the resonant frequency of the engine on its mounts and use the results to obtain the equivalent rotational spring connecting the engine to the vehicle. This primary frequency is often low enough to fall within the range of the lower vehicle bending frequencies and as a result could have a significant effect on bending stability.

Other means of obtaining thrust vector control are used and may require engine representation in the lateral model. Control concepts such as movable nozzles or stream deflection involve little or no additional mass motion and, therefore, only the fixed engine representation would have a significant effect on the lateral modes.

2.2.1.4 Branch Beams. Frequently, vehicle construction will be such that major portions are cantilevered within another structure or are connected through different load paths. Examples are: payloads enveloped by fairings, engine compartments of upper stages suspended in the interstage adapter wells, or multi-engine vehicles having independent load paths for each engine - such as a center engine supported on the tank cone and peripheral engines mounted to the cylindrical structure of the vehicle.

Such conditions are illustrated in Fig. 2.1. Realistic representations of these arrangements are required not only for true definition of gross vehicle response but

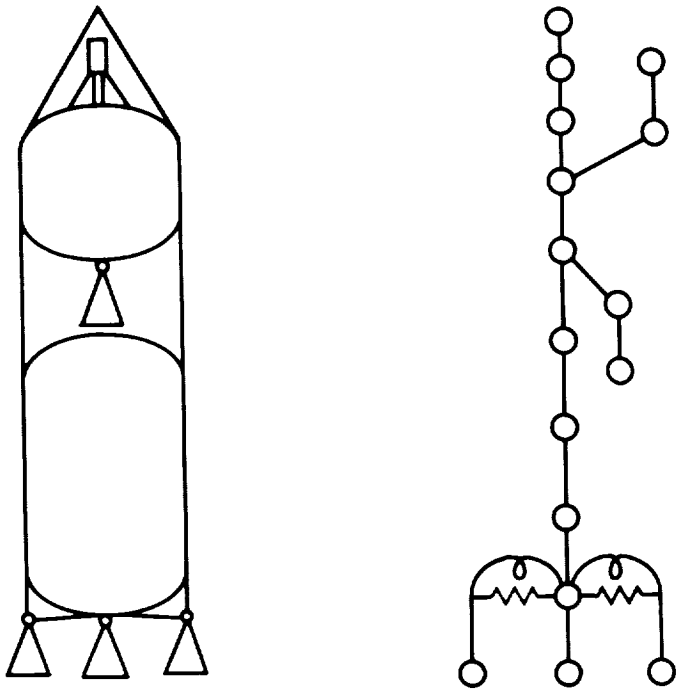

Fig. 2.1. Example of Branched System

also to investigate possible interference between parts. These multiple paths can be accounted for by appropriate branch beams from the major planar beam. So long as the analysis is restrained to one dimensional motion, there is no significant added complexity introduced by the branch beams since the compatibility relationships at the junction points can be easily satisfied. Note the model in Fig. 2.1. Branch beams can be attached in two ways: 1) by secondary beam elements, as is done for the payload fairing and the upper stage engine structure, or 2) by concentrating elasticity in lateral linear and angular springs, as is done for the external engines of the booster. The only mathematical consideration in choosing which analogy is more appropriate is that the beam element will influence more elements of the flexibility (or stiffness) matrix than will springs, due to the off-diagonal cross-coupling terms.

Generally, these branch beam conditions are encountered with relatively small masses and do not alter the gross vehicle modes significantly except that an additional mode is accounted for where the two branches are out of phase but at nearly the same frequency as the in-phase mode. When these branch beams involve engine displacements, they can be significant for control and stability analyses. For other portions of the vehicle they should be included to obtain proper load distribution and clearance envelopes.

2.2.1.5 Local Structure Effects. One of the major difficulties encountered in describing a vehicle is the effect of local structures such as joints between the interstage adapters and vehicle stages, trusses on which payload or engines are mounted, or play in joints such as engine gimbal blocks when the engine is not under thrust. In the case of an adapter joint, its stiffness may vary under compression or tension. Although

these joints are usually in compression, it is possible during the period of maximum aerodynamic loading for the combination of axial and bending loads to cause one side of the cylinder to be in tension. Depending on the characteristics of the joint, this could lead to a significant error in frequency and mode shape. The variation in stiffness of the joint under these conditions is difficult to determine accurately by analysis and usually test verification is necessary to determine the significance of this effect. Once these values are obtained, they can be substituted in the model and used for the modal calculations.

Similar problems can exist for the local structure supporting engines or payloads since these structures are often redundant, carrying loads to a flexible shell. It is possible to obtain these influence coefficients analytically, but a final check with test results is advisable. The free play occasionally found in connections such as an upper stage engine gimbal (when not under thrust) during first stage flight is random and difficult to represent. These can produce some low-frequency pendulum or inverted pendulum modes of significance if the mass involved is appreciable. To determine such effects some crude pendulum-spring mass analogies can be used to establish whether or not further consideration is necessary.

The above are a few local effects to be examined in construction of the lateral model. In general, joints that carry significant loads or components of sizeable mass should be examined in some detail to establish the degree of representation required in the lateral model.

2.2.1.6 Local Nonlinearities. If major nonlinearities exist, the system and its response cannot be described correctly with conventional normal mode analysis techniques. The effect of a separation joint possessing nonlinear bending stiffness was investigated through the use of quasi-normal modes and a Rayleigh - Ritz analysis in the work of Ref. 2.5. In the analysis, the assumed mode shapes are those of the vehicle having an infinitely stiff separation joint plus one additional mode having a single concentrated nonlinear rotational spring located at the separation point with the remainder of the vehicle considered as rigid. The Lagrange equations produced simultaneous equations in the normal mode coordinates with inertial coupling between the orthogonal elastic modes and the nonlinear spring mode.

To the equations of motion developed with the above techniques were added the control sensors, engine representation, and control system representation for a bending stability analysis. Because of the nonlinearities in both the vehicle structure and the engine actuators the solution was obtained with an analog computer. The study presents an approach for solving problems in structures with nonlinearities using models modified to account for local peculiarities.

2.2.1.7 Temperature. The primary structure of space vehicle systems is subject to temperature changes of hundreds of degrees varying from cryogenic levels to the extremes resulting from aerodynamic heating. This increase in temperature causes a

reduction in the material moduli which in turn leads to a small reduction in frequencies and altered mode shapes. For typical systems, temperature considerations are unimportant until after the period of maximum aerodynamic pressure and then only for certain portions of the vehicle. Since the period of maximum heating usually occurs after the period of maximum disturbance and only affects parts of the structure, its significance is greatly reduced. The heating of various portions of the vehicle can be predicted within tolerances necessary for modal analyses to establish the resultant variation in modal parameters.

2.2.1.8 Axial Load. Axial loads caused by longitudinal acceleration of several g's during flight will cause a slight decrease in bending mode frequency through two mechanisms: 1) the effect of axial load on beam vibration, and 2) the reduction in equivalent skin on stringer-skin structure. The first effect can be represented analytically. The second can be included after calculating or obtaining the equivalent skin from empirical data. The total effect of axial loads is generally very small and in nearly all cases can be ignored.

2.2.1.9 Solid Boosters. The solid propellant grain behaves as a visco-elastic solid. This visco-elastic mass must be represented in some manner when the elastic properties of the booster are calculated. The simplest and most straightforward method of accomplishing this is to consider the grain as an inert mass, rigidly attached to the case. This method, while it has several shortcomings, is in wide use and has been found to yield satisfactory results.

The visco-elastic properties of the grain could be used to provide a more comprehensive analysis of the elastic motion. There are several analytical models which adequately describe the dynamic behavior of the visco-elastic solid (Refs 2.8 and 2.9). However, it is generally felt that this area of analysis does not need to be considered for loads analysis.

There are several reasons why the visco-elastic properties of the solid propellant grain are not used in calculations of booster elastic properties. First, they are found to be relatively unimportant for booster vehicles having a reasonable slenderness ratio. The grain structure, in response to stress, exhibits a complicated behavior which can be represented as instantaneous elasticity, delayed elasticity, and viscous flow. For small stresses occurring for short times, the properties could be approximated by considering only the range from 500 to 2000 psi at an ambient temperature of 70-80° F. Thus, the contribution to the bending stiffness is quite small compared with that of the vehicle shell, which is commonly referred to as the solid propellant rocket motor case.

A second consideration is the variable nature of the grain properties themselves. The nature of the approximations which can be used for the model to represent the grain would vary depending on the stress level within the grain, frequency of the application of stress, and temperature. The modulus of elasticity is quite temperature-dependent, exhibiting a change of roughly a factor of 10 for every 40° F of change in grain

temperature. This property alone makes it cumbersome to describe adequately the solid propellant grain motion. This difficulty in analysis, along with the relative unimportance of the visco-elastic effects on lower modes, has prompted most analysts to omit these effects from the model used to describe the lateral elastic motion of the booster. Bending mode tests run by various motor manufacturers have indicated that these omissions do not affect the adequacy of the calculations for lower modes. The above should not be taken to imply that the visco-elastic behavior of the solid propellant grain is not important in all problems. It does become quite important under certain conditions, particularly in the analysis of the longitudinal modes.

From this it follows that aspects important for the liquid cylindrical vehicle lateral model are also to be considered for solid boosters. Propellant sloshing, of course, does not exist. Because of the thicker tank walls of solid boosters, the effects of adapter stiffness and joints are more predominant in the lower frequency modes and should be carefully examined.

2.2.1.10 Weight and Stiffness Lumping. The weight and stiffness data are usually generated in the form shown in Figs 2.2 and 2.3. From these continuous distributions the analyst derives a lumped parameter idealization. While many idealizations are possible the analyst can enhance the accuracy of the model and simplify later work which uses the modes by his judicious selection of lumping points.

The first step in the idealization is to select the points at which to "lump." These will be referred to as panel points and the beam between any two panel points as a segment. The number of panel points to use has been discussed in previous sections. The consideration now is where to locate the panel points. The analyst bases his choice of

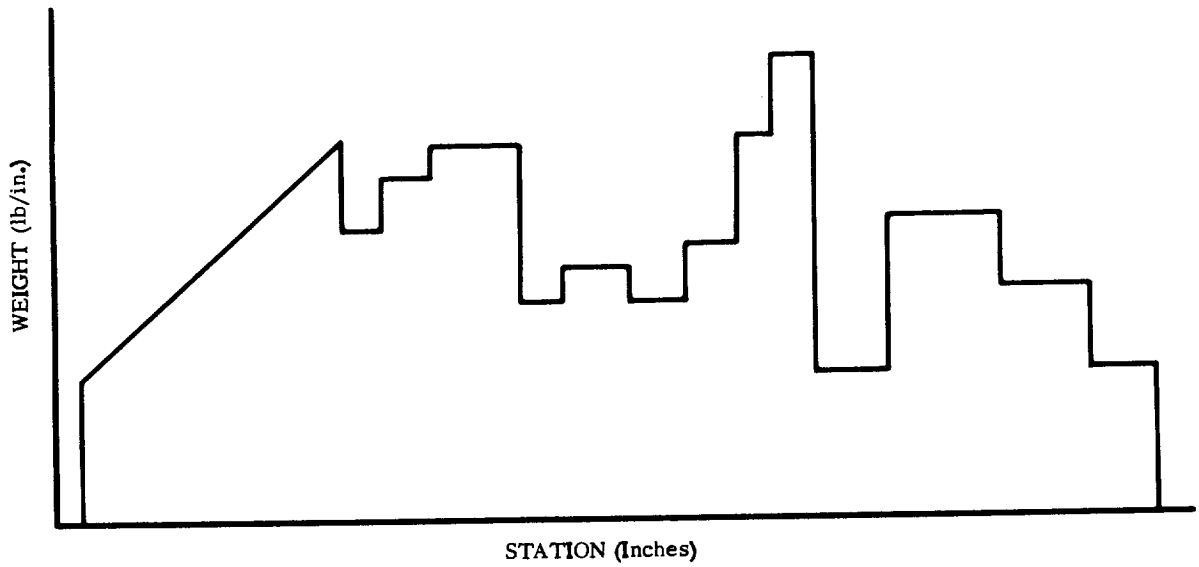

Fig. 2.2. Typical Weight Distribution

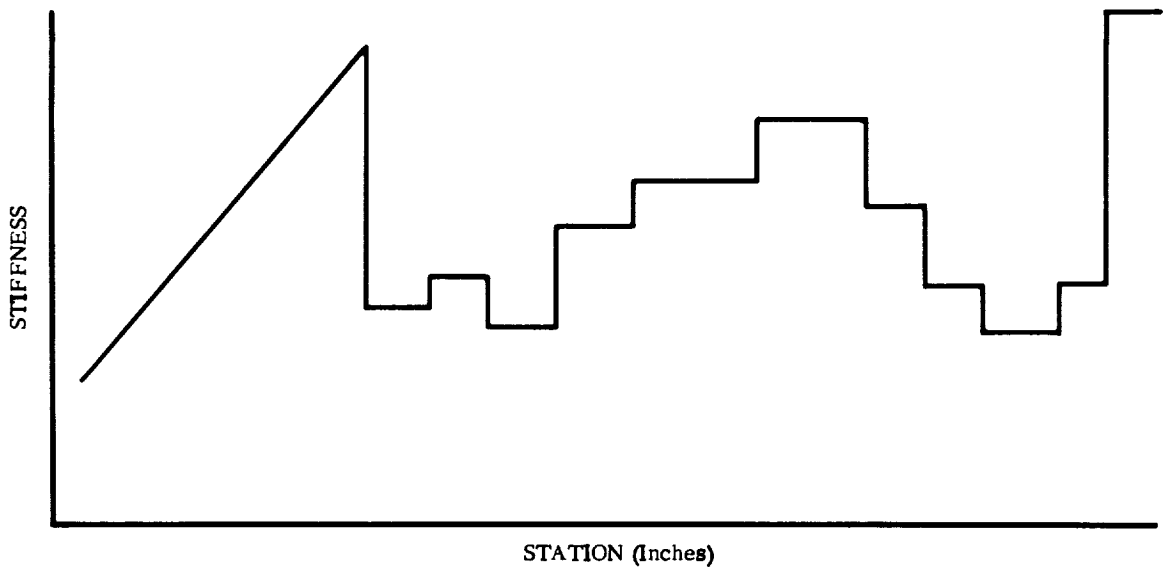

Fig. 2.3. Typical Stiffness Distribution

panel points on the following considerations (there may be additional considerations in some instances):

a. Distances between panel points should have some degree of uniformity.

b. Important model points such as the intersection of branch beams and the engine gimbal points are needed.

c. Points which may be required in later analyses (e.g., centers of pressure of local "concentrated" aerodynamic loads, gyro locations, gimbal points, etc.).

d. Large concentrated masses should be represented at their center of gravity.

e. Better approximations of the stiffness data can be made by the appropriate choice of panel points.

The first consideration applies to parts of the model represented as beams. The total length of the beam can be divided by the number (or approximate number) of panel points selected for the beam and the resulting length used as a guide for segment length. It is emphasized that this length is a guide only and not an inflexible quantity. It is best to avoid any unusually long or short segments compared with the majority of segments. The reason for this recommendation is that the normal modes are, in a sense, an approximation of a curve by a series of straight lines. An unusually long segment may not give a good "approximation," especially if a large amount of bending occurs within the segment. Also, the combination of long and short segments could cause elements of the stiffness matrix to differ by three magnitudes, or more. This causes numeric problems in matrix inversion.

The second consideration arises from launch vehicle construction and geometry. Examples of panel point location dictated by vehicle geometry are connections of beams

with branch beams, engines and sloshing propellants. There may be other items in this category; inspection of the vehicle geometry will reveal them. The third consideration is one that is easily overlooked but yet merits a great deal of attention from the analyst. The modal deflections and slopes (and frequently the modal shears and moments) are used in subsequent loads and stability analyses. In these analyses, data at certain points are required as input and/or output. An example of required input data is modal deflection and slope at gyro locations for use in stability analyses. An example of required output data is moment and shear at critical stations from load analyses. The analyst should ask himself, "To what use will the model and the modes be put and how can this use be facilitated by the choice of panel points?"

The weight of each segment or attached component should be distributed to maintain the center of gravity of that segment or component as well as overall center of gravity. Deviation from this representation will decrease the accuracy of the model.

Stiffness data are generally input at the panel points describing the weight distribution. Additional points are used for accurate representation to indicate changes in stiffness. These massless points are eliminated in generation of the stiffness matrix as described in Section 2.2.2.

2.2.1.11 Stiffness and Flexibility Matrices. The primary purpose of the mathematical model is to obtain a representation of the real system which can then be represented in mathematical terms. The general approach to dynamic problems, as given by Eqs 2.1 to 2.8, requires the formation of the mass, stiffness, and dynamic matrices. Formation of Eq. 2.8 requires the mass matrix and the inverse of the stiffness matrix. Since the inverse of the stiffness matrix is the flexibility matrix, one may question a method of analysis beginning with the stiffness matrix when a flexibility matrix can be derived directly. The main advantage of the stiffness approach is the straightforward manner of deriving a coupled matrix which lends itself toward formulation of computer logic capable of assembling a coupled stiffness matrix for very complicated systems. Also, with high-speed, accurate computers available, the matrix inversion can usually be accomplished efficiently and accurately. For certain specific problems it may be desirable to develop the flexibility matrix.

In this section the approach (as presented in Ref. 2.10) for developing the stiffness matrix for a lateral model will be given. The flexibility approach and a mass coupling technique are also presented.

2.2.1.11.1 Free Element Stiffness Matrix. Bending and shear stiffnesses are identified at points along the structure, including all mass stations. The nature of the stiffness distributions may justify stiffness definition at an intermediate point between mass concentrations. Thus the model is formed from a series of connected massless beams, with mass and inertia concentrations located at some or all the junctions of the beams. While the stiffness of the vehicle may be distributed in a complex fashion, it may be

represented with acceptable accuracy by a series of straight line segments. This results in giving each beam segment a trapezoidal stiffness distribution.

In the approach to be outlined, the 4 × 4 stiffness matrix of each element of the beam is first obtained by inverting the 4 × 4 flexibility matrix of this element. (The element stiffness matrices are developed by this technique because it is easier mathematically and more accurate.) The matrix is then coupled by constructing a matrix composed of the individual 4 × 4 matrices. In this coupled matrix, the terms for common points of adjacent elements are the sum of the terms for the individual matrices. With this matrix form, restraints or boundary conditions are imposed which will represent the system to be analyzed. The derivation of the stiffness matrix is now given (see Fig. 2.4).

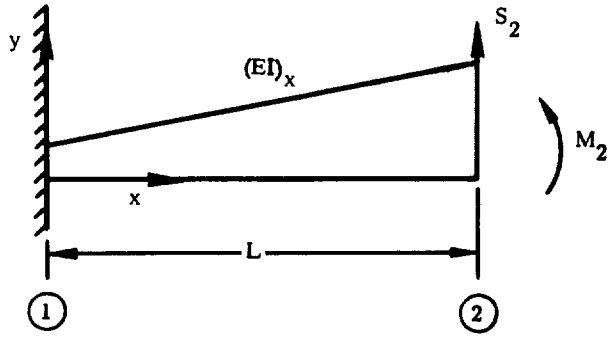

Fig. 2.4. Cantilever Beam in Bending

The bending rigidity, for a value of x, is

$$(E\,I)_x = (E\,I)_2 \left[1 + \frac{(L-x)}{L}\left\{\frac{(E\,I)_1}{(E\,I)_2} - 1\right\}\right] \tag{2.9}$$

The general equation of the elastic curve of a deflected beam is

$$\frac{d^2y}{dx^2} = \frac{M}{E\,I} = \frac{M_2 + S_2\,(L-x)}{(EI)_x} \tag{2.10}$$

Integrating Eq. 2.10 and substituting the boundary conditions $\frac{dy}{dx} = y = 0$ at $x = 0$, then y_2 and θ_2, the deflection and slope at $x = L$, are:

$$\left.\begin{aligned} y_2 &= \frac{-M_2 L^2}{e\beta^2}\left[\ln(1+\beta) - \beta\right] - \frac{S_2 L^3}{e\beta^3}\left[\beta - \frac{\beta^2}{2} - \ln(1+\beta)\right] \\ \theta_2 &= \frac{M_2 L}{e\beta}\ln(1+\beta) + \frac{S_2 L^2}{e\beta^2}\left[\beta - \ln(1+\beta)\right] \end{aligned}\right\} \tag{2.11}$$

where

$$e = (EI)_2$$

$$\beta = \frac{EI_1}{EI_2} - 1$$

Substituting the series expansion of $\ln(1+\beta)$ into Eq. 2.11 (valid for $-1 < \beta \leq 1$),

$$\left.\begin{aligned} y_2 &= \frac{M_2 L^2}{e}\left[\frac{1}{2} - \frac{\beta}{3} + \frac{\beta^2}{4} - \cdots\right] + \frac{S_2 L^3}{e}\left[\frac{1}{3} - \frac{\beta}{4} + \frac{\beta^2}{5} - \cdots\right] \\ \theta_2 &= \frac{M_2 L}{e}\left[1 - \frac{\beta}{2} + \frac{\beta^2}{3} - \cdots\right] + \frac{S_2 L^2}{e}\left[\frac{1}{2} - \frac{\beta}{3} + \frac{\beta^2}{4} - \cdots\right] \end{aligned}\right\} \quad (2.12)$$

By a similar procedure, the deflection due to shear at $x = L$ is

$$\left.\begin{aligned} y_2 &= \frac{S_2 L}{g}\left[1 - \frac{\gamma}{2} + \frac{\gamma^2}{3} - \cdots\right] \\ \theta_2 &= 0 \end{aligned}\right\} \quad (2.13)$$

where

$$g = (KAG)_2$$

$$\gamma = \frac{(KAG)_1}{(KAG)_2} - 1$$

K is the shear effectiveness factor for the structure, i.e., that fraction of the cross-sectional area which is carrying shear load. This can vary widely and depends on the type of structure. Putting Eqs 2.12 and 2.13 into matrix form,

$$\begin{Bmatrix} y_2 \\ \theta_2 \end{Bmatrix} = \begin{bmatrix} C_{11} & C_{12} \\ C_{21} & C_{22} \end{bmatrix} \begin{Bmatrix} S_2 \\ M_2 \end{Bmatrix} \quad (2.14)$$

where C_{11}, C_{12}, C_{21}, and C_{22}, the elements of the flexibility matrix, are the coefficients of Eqs 2.12 and 2.13.

$$C_{11} = \frac{L^3}{e}\left[\frac{1}{3} - \frac{\beta}{4} + \frac{\beta^2}{5} - \ldots\right] + \frac{L}{g}\left[1 - \frac{\gamma}{2} + \frac{\gamma^2}{3} - \ldots\right]$$

$$C_{12} = C_{21} = \frac{L^2}{e}\left[\frac{1}{2} - \frac{\beta}{3} + \frac{\beta^2}{4} - \ldots\right]$$

$$C_{22} = \frac{L}{e}\left[1 - \frac{\beta}{2} + \frac{\beta^2}{3} - \ldots\right]$$

By inversion of Eq. 2.14,

$$\begin{Bmatrix} S_2 \\ M_2 \end{Bmatrix} = \frac{1}{B}\begin{bmatrix} C_{22} & -C_{12} \\ -C_{21} & C_{11} \end{bmatrix}\begin{Bmatrix} y_2 \\ \theta_2 \end{Bmatrix} = [K]\begin{Bmatrix} y_2 \\ \theta_2 \end{Bmatrix} \tag{2.15}$$

where

$$B = C_{11}C_{22} - C_{12}^2$$

and [K] is the stiffness matrix.

Considering a free element, with the same stiffness as the cantilever beam (as shown in Fig. 2.5), the equilibrium equations are:

$$S_1 + S_2 = 0$$

$$M_1 + S_1 L + M_2 = 0$$

Also from Fig. 2.5,

$$y^* = y_2 - y_1 - \theta_1 L$$

$$\theta^* = \theta_2 - \theta_1$$

Eq. 2.15 now becomes:

$$\begin{Bmatrix} S_2 \\ M_2 \end{Bmatrix} = \frac{1}{B}\begin{bmatrix} C_{22} & -C_{22} & -C_{12}\left(C_{12} - LC_{22}\right) \\ -C_{12} & C_{12} & C_{11}\left(LC_{12} - C_{11}\right) \end{bmatrix}\begin{Bmatrix} y_2 \\ y_1 \\ \theta_2 \\ \theta_1 \end{Bmatrix} \tag{2.16}$$

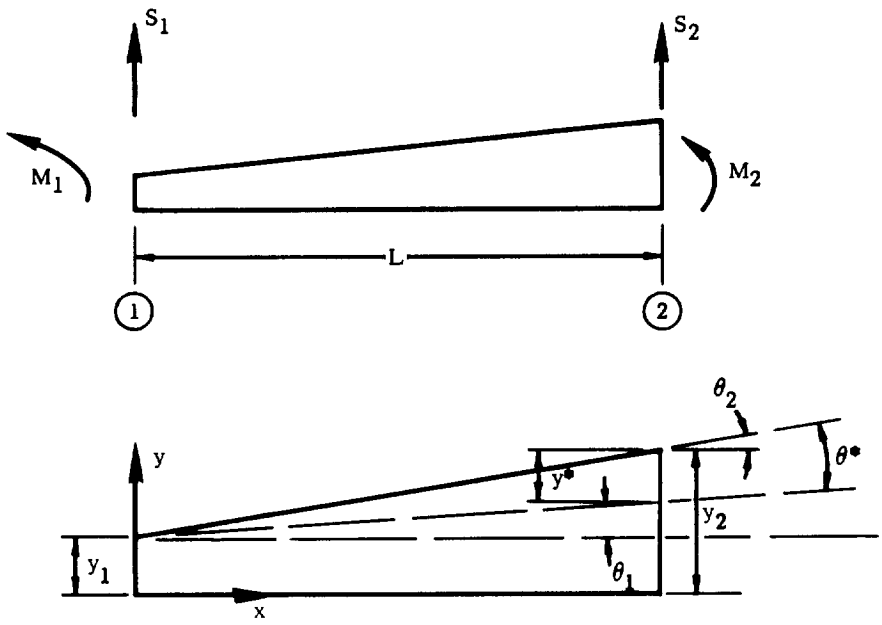

Fig. 2.5. Free Beam in Bending and Shear

Expanding this to include point 2 (by use of the equilibrium equations):

$$\begin{Bmatrix} S_2 \\ S_1 \\ M_2 \\ M_1 \end{Bmatrix} = \frac{1}{B} \begin{bmatrix} C_{22} & -C_{22} & -C_{12} & (C_{12} - LC_{22}) \\ -C_{22} & C_{22} & C_{12} & (LC_{22} - C_{12}) \\ -C_{12} & C_{12} & C_{11} & (LC_{12} - C_{11}) \\ (C_{12} - LC_{22}) & (LC_{22} - C_{12}) & (LC_{12} - C_{11}) & (C_{11} - 2LC_{12} + L^2 C_{22}) \end{bmatrix} \begin{Bmatrix} y_2 \\ y_1 \\ \theta_2 \\ \theta_1 \end{Bmatrix} \quad (2.17)$$

where C_{11}, C_{12}, and C_{22} remain as identified previously.

Locally significant components can generally be included in the model by attaching a mass and/or moment of inertia at the appropriate location by means of springs representing the elasticity of the mounting structure. The stiffness matrices of elements representing translational and rotational springs of Fig. 2.6 can be written directly as:

$$\begin{Bmatrix} S_1 \\ S_2 \end{Bmatrix} = \begin{bmatrix} K_T & -K_T \\ -K_T & K_T \end{bmatrix} \begin{Bmatrix} y_1 \\ y_2 \end{Bmatrix} \quad (2.18)$$

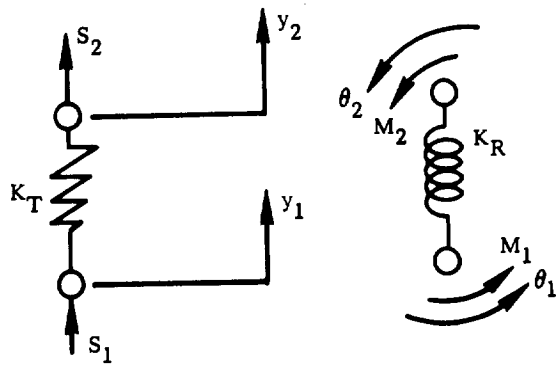

Fig. 2.6. Translational and Rotational Springs

$$\begin{Bmatrix} M_1 \\ M_2 \end{Bmatrix} = \begin{bmatrix} K_R & -K_R \\ -K_R & K_R \end{bmatrix} \begin{Bmatrix} \theta_1 \\ \theta_2 \end{Bmatrix} \tag{2.19}$$

2.2.1.11.2 Coupled Unrestrained Stiffness Matrix. The unrestrained stiffness matrix is generated from each beam element, and a 2 x 2 stiffness matrix is generated from each spring element. Consider a beam element. If an element is attached to a beam, this element must either be another beam or a spring (Fig. 2.7). When two beam elements are connected to the same node, coupling with respect to both translation and rotation occurs.

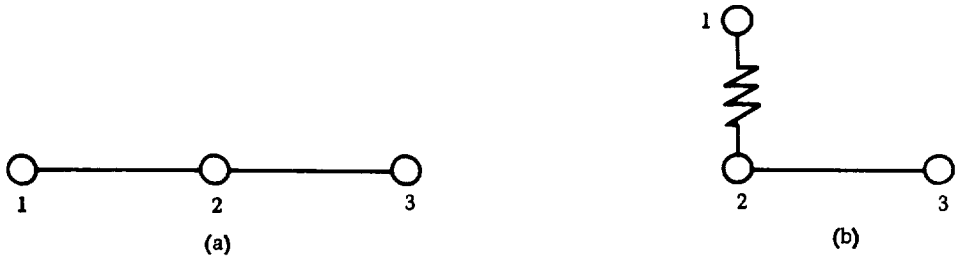

Fig. 2.7. Example of Attachments to a Beam Element

The stiffness matrix layout corresponding to Fig. 2.7a is given in Fig. 2.8. An element in the matrix of Fig. 2.8 gives the magnitude of the shear S_i or moment M_i at node i due to a unit deflection y_j or slope θ_j at node j. Notice that the two beam stiffness matrices overlap at node 2, indicating node 2 feels the effect of both beams. An element in this portion of the matrix is obtained by adding the corresponding element of the two individual stiffness matrices.

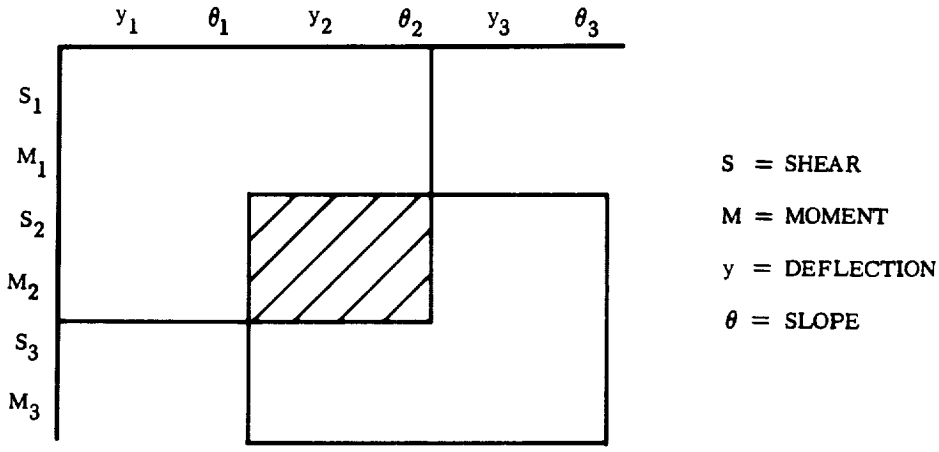

Fig. 2.8. Stiffness Matrix Layout for Attachment of Two Beams

The stiffness matrix layout corresponding to Fig. 2.7b is given in Fig. 2.9. The two stiffness matrices again overlap at node 2, but this time at one element. Coupling a beam with a spring only affects one degree of freedom, for a spring can have but one degree of freedom. (If instead of a translational spring connected at node 2, a rotational spring were connected, then coupling would be at element M_2, θ_2.)

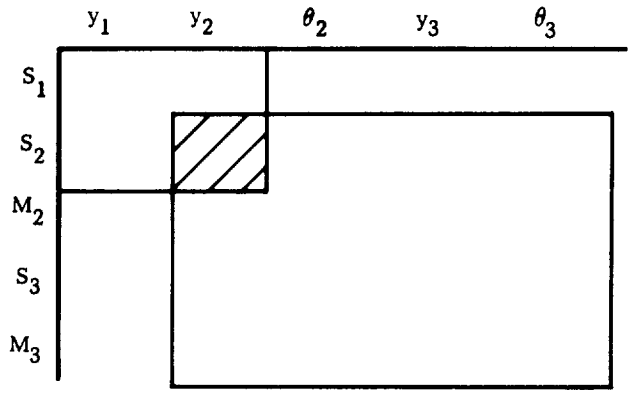

Fig. 2.9. Stiffness Matrix Layout for Attachment of Beam with a Spring

2.2.1.11.3 Reducing the Stiffness Matrix. The stiffness matrix as developed in the preceding paragraphs may contain coordinates which can be eliminated by consideration of the restraints put on a system and the application of boundary conditions to the system. Together, the restraints and boundary conditions can be considered to be in two classes. These are:

a. Nodes that have zero generalized displacements but may have nonzero generalized forces.

b. Nodes that have zero generalized forces (no mass or moment of inertia) but may have nonzero generalized displacements.

The equation $\{F\} = [K]\{u\}$ may be rearranged and partitioned as follows:

$$\begin{Bmatrix} S_s \\ M_s \\ \hdashline S_r \\ M_r \end{Bmatrix} = \left[\begin{array}{cc:cc} a & & b & \\ & & & \\ \hdashline & & & \\ b' & & c & \end{array}\right] \begin{Bmatrix} y_s \\ \theta_s \\ \hdashline y_r \\ \theta_r \end{Bmatrix} \qquad (2.20)$$

where the S_s and M_s are shears and moments, respectively, that have the nonzero displacements and slopes y_s and θ_s. The S_r and M_r are shears and moments, respectively, that have the zero displacements and slopes y_r and θ_r. If

$$\{F_s\} \equiv \begin{Bmatrix} S_s \\ M_s \end{Bmatrix} \qquad \{F_r\} \equiv \begin{Bmatrix} S_r \\ M_r \end{Bmatrix}$$

and

$$\left|\Phi_s\right| \equiv \begin{Bmatrix} y_s \\ \theta_s \end{Bmatrix} \qquad \left|\Phi_r\right| \equiv \begin{Bmatrix} y_r \\ \theta_r \end{Bmatrix} \equiv \{0\}$$

then Eq. 2.20 becomes

$$\begin{Bmatrix} F_s \\ \hline F_r \end{Bmatrix} = \left[\begin{array}{c|c} a & b \\ \hline b' & c \end{array}\right] \begin{Bmatrix} \Phi_s \\ \hline 0 \end{Bmatrix} \tag{2.21}$$

Eq. 2.21 is equivalent to the following two matrix equations.

$$\left|F_s\right| = [a]\left|\Phi_s\right| \tag{2.22}$$

and

$$\left|F_r\right| = [b']\left|\Phi_s\right| \tag{2.23}$$

If there are no boundary conditions associated with the load vector $\{F_s\}$, the matrix $[a]$ is the final stiffness matrix $[K]$ and $\{\Phi_s\}$ is the mode shapes $\{\Phi\}$. If there are also boundary conditions calling for zero generalized forces then matrix Eq. 2.22 is rearranged to become

$$\left|F_s\right| = \begin{Bmatrix} F_u \\ \hline F_t \end{Bmatrix} = \left[\begin{array}{c|c} d & e \\ \hline e' & g \end{array}\right] \begin{Bmatrix} \Phi_u \\ \Phi_t \end{Bmatrix} \tag{2.24}$$

where the F_u are the nonzero generalized forces that have the generalized displacements Φ_u, and the F_t are the zero generalized forces that have the generalized displacements Φ_t.

Eq. 2.24 is equivalent to the two matrix equations,

$$[d]\left|\Phi_u\right| + [e]\left|\Phi_t\right| = \left|F_u\right|$$

and

$$[e']\left|\Phi_u\right| + [g]\left|\Phi_t\right| = \left|F_t\right| \equiv \{0\}$$

Therefore,

$$\left|\Phi_t\right| = -[g]^{-1}[e']\left|\Phi_u\right| \tag{2.25}$$

and

$$\left|F_u\right| = \left[[d] - [e][g]^{-1}[e']\right]\left|\Phi_u\right| \equiv [K]\left|\Phi_u\right| \tag{2.26}$$

In this case (the case of zero generalized forces) the matrix $\left([d] - [e][g]^{-1}[e']\right)$ is the final stiffness matrix $[K]$ and $\{\Phi_u\}$ is a mode shape $\{\Phi\}$.

2.2.1.11.4 Calculation of Free-Free Modes. The foregoing analysis was made for a restrained system, one that is fixed at least in one place with respect to both rotation and translation. In the analysis of a free-free system the structure must be restrained temporarily at one point. Otherwise, an external force or moment would cause the whole system to move as a rigid body. The solution to the problem would then be impossible. It can be shown that the eigenvalue problem reduces to the form:

$$[C][M][\Phi] = \lambda\left[\{\Phi\} - \{\mu\}y_o - \{\tau\}\theta_o\right] \tag{2.27}$$

In Eq. 2.27 the term $-\{\mu\}y_o$ releases the fixed point with respect to translation, while the term $-\{\tau\}\theta_o$ releases the fixed point with respect to rotation. By applying the principles of linear and angular momentum to the system, Eq. 2.27 can be expressed as a standard eigenvalue problem

$$\left[[C][M] + [T] + [R]\right]\{\Phi\} = \lambda\{\Phi\} \tag{2.28}$$

where, as explained in the foregoing,

$$[T]\{\Phi\} \equiv \lambda\{\mu\}y_o$$

$$[R]\{\Phi\} \equiv \lambda\{\tau\}\theta_o$$

and $\left[[C][M] + [T] + [R]\right]$ is the final dynamic matrix. The derivation of $[T]$ and $[R]$ is now given.

Referring to Eq. 2.27,

μ_i = 1.0 if point i has a translation degree of freedom

μ_i = 0 if point i has a pitching degree of freedom

τ_i = the perpendicular distance from the pitch axis through point zero (origin) to point i if point i has a translational degree of freedom (positive if measured forward of point zero)

τ_i = 1.0 if point i has a pitch degree of freedom

Applying the conservation of linear momentum yields

$$m_o y_o + \{\mu\}' [M] \{\Phi\} = 0 \tag{2.29}$$

where m_o is the mass at the restrained point. The conservation of angular momentum yields

$$I_o \theta_o + \{\tau\}' [M] \{\Phi\} = 0 \tag{2.30}$$

where I_o is the moment of inertia at the restrained point.

Multiplying Eq. 2.27 by $\{\mu\}'[M]$ yields

$$\{\mu\}'[M]\{\Phi\} - y_o \{\mu\}'[M]\{\mu\} - \theta_o \{\mu\}'[M]\{\tau\} = \omega^2 \{\mu\}'[M][C][M]\{\Phi\}$$

Defining

$$\lfloor A \rfloor = \{\mu\}' [M] [C] [M]$$

and substituting from Eq. 2.29,

$$-m_o y_o - y_o \{\mu\}' [M] [\mu] - \theta_o \{\mu\}' [M] \{\tau\} = \omega^2 \lfloor A \rfloor \{\Phi\}$$

The total mass is

$$M_T = m_o + \{\mu\}' [M] \{\mu\}$$

and the static mass moment about a pitch axis through point zero is

$$S_o = \{\mu\}' [M] \{\tau\}$$

Therefore

$$M_T y_o + S_o \theta_o = -\omega^2 \lfloor A \rfloor \{\Phi\} \tag{2.31}$$

Multiplying Eq. 2.27 by $\{\tau\}'[M]$ yields

$$\{\tau\}'[M]\{\Phi\} - y_o \{\tau\}'[M]\{\mu\} - \theta_o \{\tau\}'[M]\{\tau\} = \omega^2 \{\tau\}'[M][C][M]\{\Phi\}$$

Defining

$$\lfloor B \rfloor = \{\tau\}' [M] [C] [M]$$

and substituting from Eq. 2.30,

$$-I_o\theta_o - y_o\{\tau\}'[M]\{\mu\} - \theta_o\{\tau\}'[M]\{\tau\} = \omega^2\lfloor B\rfloor\{\Phi\}$$

The mass moment of inertia of total structure about a pitch axis through point zero is

$$I_T = I_o + \{\tau\}'[M]\{\tau\}$$

Therefore

$$I_T\theta_o + S_o y_o = -\omega^2\lfloor B\rfloor\{\Phi\} \tag{2.32}$$

Solving Eq. 2.32 for θ_o gives

$$\theta_o = -\frac{S_o y_o + \omega^2\lfloor B\rfloor\{\Phi\}}{I_T} \tag{2.33}$$

Substituting this in Eq. 2.31 and defining

$$W = I_T M_T - S_o^2$$

gives

$$y_o = \omega^2\left[\frac{S_o}{W}\lfloor B\rfloor - \frac{I_T}{W}\lfloor A\rfloor\right]\{\Phi\} \tag{2.34}$$

Substituting this in Eq. 2.33 gives

$$\theta_o = \omega^2\left[\frac{S_o}{W}\lfloor A\rfloor - \frac{M_T}{W}\lfloor B\rfloor\right]\{\Phi\} \tag{2.35}$$

By satisfying

$$[T]\{\Phi\} \equiv \lambda\{\mu\}y_o$$

$$[R]\{\Phi\} \equiv \lambda\{\tau\}\theta_o$$

it is seen that the T and R matrices are

$$[T] = \{\mu\}\left[\frac{S_o}{W}[B] - \frac{I_T}{W}[A]\right]$$
$$[R] = \{\tau\}\left[\frac{S_o}{W}[A] - \frac{M_T}{W}[B]\right] \tag{2.36}$$

2.2.1.11.5 Flexibility Matrix. The inverted stiffness matrix is in reality the flexibility matrix of the system; i.e., it expresses displacements in terms of forces:

$$\{y\} = [C]\{F\}$$

If the model is statically determinate, the development of the flexibility matrix directly is much simpler than inverting the stiffness matrix. However, if the structure is indeterminate, the calculation of the elements of the flexibility matrix becomes more complex, rapidly becoming involved and tedious with increasing numbers of redundancies. The element C_{ij} of the flexibility matrix may be thought of as the deflection at point i resulting from a unit load at point j. The principle of reciprocal relations will force symmetry of the matrix, reducing the quantity of coefficients to be evaluated.

The flexibility matrix is formed by developing individual flexibility matrices for each element in the system. They are considered as cantilevers.

$$\begin{Bmatrix} \bar{y}_i \\ \bar{\theta}_i \end{Bmatrix} = \begin{bmatrix} C_{11} & C_{12} \\ C_{21} & C_{22} \end{bmatrix} \begin{Bmatrix} \bar{S}_i \\ \bar{M}_i \end{Bmatrix} \tag{2.37}$$

Note that $\bar{y}_i$ and $\bar{\theta}_i$ are relative to the end considered fixed and $\bar{S}_i$ and $\bar{M}_i$ are the total loads applied to the end considered free. Consequently, the total deflection value is found by transforming $\bar{y}_i$ and $\bar{\theta}_i$ from relative coordinates to absolute coordinates:

$$\begin{Bmatrix} y_i \\ \theta_i \end{Bmatrix} = [T] \begin{Bmatrix} \bar{y}_i \\ \bar{\theta}_i \end{Bmatrix} \tag{2.38}$$

The total applied loads, S_i and M_i, can be considered to be functions of the external loads applied to each mass of the structure, expressed by the transformation

$$\begin{Bmatrix} \bar{S}_i \\ \bar{M}_i \end{Bmatrix} = [R] \begin{Bmatrix} S_i \\ M_i \end{Bmatrix} \tag{2.39}$$

Thus the relationship between total deflection (y_i and θ_i) and the external loads applied to each mass (S_i and M_i) is developed by substituting the transformed values,

$$\begin{Bmatrix} \bar{y}_i \\ \bar{\theta}_i \end{Bmatrix} = [C] \begin{Bmatrix} \bar{S}_i \\ \bar{M}_i \end{Bmatrix}$$

$$[T] \begin{Bmatrix} \bar{y}_i \\ \bar{\theta}_i \end{Bmatrix} = [T][C][R] \begin{Bmatrix} S_i \\ M_i \end{Bmatrix}$$

$$\begin{Bmatrix} y_i \\ \theta_i \end{Bmatrix} = [T][C][R] \begin{Bmatrix} S_i \\ M_i \end{Bmatrix}$$

$$[T][C][R] = [\overline{C}] = \text{coupled flexibility matrix} \qquad (2.40)$$

For a redundant structure, the influence coefficients are not so readily attained and use must be made of an appropriate static analysis such as virtual work or Castigliano's theorem (Ref. 2.11).

2.2.1.11.6 Transformed Mass Matrix. Another alternative technique for forming the dynamic matrix is to transform the coordinate system from the absolute to the relative sense. The equations of motion formed previously consider the displacements of the respective coordinates to be referenced to a fixed point, or neutral position. The displacements may also be expressed relatively, or referenced to an adjacent coordinate. Furthermore, the inherent relationship between the displacements in absolute terms, y, and the displacements in relative terms, $\bar{y}$, is readily expressed by a simple transformation matrix:

$$\{y\} = [T]\{\bar{y}\}$$

The kinetic and potential energies of the system can then be written (in matrix notation) in terms of relative coordinates as

$$2KE = \{\dot{\bar{y}}\}'[T]'[M]\{\dot{\bar{y}}\}$$

$$2PE = \{\bar{y}\}'[C]^{-1}\{\bar{y}\}$$

where C is the uncoupled flexibility matrix consisting of 2 × 2 matrices for cantilevered elements. Using Lagrange's equation,

$$\frac{d}{dt}\left(\frac{\partial KE}{\partial \dot{y}_i}\right) + \frac{\partial PE}{\partial y_i} + \frac{\partial W}{\partial y_i} = 0 \tag{2.41}$$

the equations of motion become

$$[T]'[M][T]\{\ddot{\bar{y}}\} + [C]^{-1}\{\bar{y}\} = 0 \tag{2.42}$$

and the dynamic matrix is

$$[C][T]'[M][T] \quad \{\Phi\} = \lambda\{\Phi\} \tag{2.43}$$

This approach is very similar to the method in the previous section with the transformation of coordinates coupling the mass matrix instead of the flexibility matrix. Note that the modes $\{\Phi\}$ are in terms of relative coordinates and must be premultiplied by the transform matrix $[T]$ to obtain absolute vectors.

2.2.2 TORSIONAL MODEL OF A CYLINDRICAL LIQUID PROPELLANT VEHICLE. The construction of torsional models follows the same principal ground rules established for the lateral model. One difference is in the treatment of propellant for liquid boosters. In the case of the liquid propellant vehicle vibrating in pure torsion, the propellant is virtually unexcited. Since the only stress condition is that of shear, the liquid can participate only to the extent allowed by its viscosity. It is most probable that the fluids in the vehicle tanks can be considered nonviscous, and therefore contribute nothing to the moment of inertia. It is evident that under these conditions, the quantity of propellant has no effect on the torsional vibration characteristics of the vehicle. Hence these characteristics do not vary with time in flight.

The development of the stiffness and flexibility matrices are the same as given for the lateral beam with the terms representing bending stiffness (EI) set equal to zero. For terms representing shear stiffness, GJ replaces KAG.

2.2.3 LONGITUDINAL MODEL OF A CYLINDRICAL LIQUID PROPELLANT VEHICLE. A longitudinal model is a close-coupled system and is similar to the torsional model. In pure longitudinal cases, it is possible to represent the real system by a model of masses connected by linear translational springs. The longitudinal case therefore reduces to the lateral case with only translational springs. Looking at the model from another viewpoint, it is the same as the torsional model except that moment of inertia is replaced by mass and rotational springs are replaced by translational springs.

The tacit assumption of available spring rates has been made in the above discussion. The development of spring rates is not as easy and straightforward in the

longitudinal case. Further, two types of structure are considered, i.e., structures not containing propellants and the propellant tanks. For the case of structures not containing propellants the spring rate development is analogous to the torsional case with the substitution of A = J and E = G in the stiffness terms. The development of spring rates (and the model) for propellant tanks is covered in detail in Ref. 2.12. The major portion of this development is given in the following discussion.

2.2.3.1 Fluid Equations for Elastic Tank. The analysis of a coupled elastic tank and propellant mass, even for a highly simplified case, becomes a very complicated eigenvalue problem. Specifically, a solution must be obtained that satisfies the differential equations for the liquid and the elastic shell, as well as appropriate boundary conditions at the tank walls, the tank bottom, and the liquid free surface. A rigorous analysis of this type is reported in Ref. 2.13. The results yield the natural frequencies for the tank and propellant.

A second analysis of this type, using highly simplified shell equations, is reported in Ref. 2.14. In this case, the natural frequencies and a forced vibration solution are obtained for a cylindrical tank.

A number of other analyses have also been attempted for the coupled liquid and elastic container. Most of these generate a great deal of mathematical analysis that is of very little use in defining an analytical model for the tank. It is apparent, then, that other more simplified techniques must be used. The continuous analysis can then be used as a check on the dynamic characteristics of the simplified representation.

A major building block in the development of a longitudinal structural model is a lumped parameter model for each propellant tank. In general, such tank models have been restricted to a single (predominant) mode of the coupled elastic shell and propellant mass. However, there is reason to believe that a single-mode model is not adequate in all cases. Furthermore, the development of a multimode model for the propellant tank is feasible.

As a basis for developing a tank model, first it is necessary to establish a set of approximate equations for the shell and the liquid. For example, consider the tank shown in Fig. 2.10, filled to a height L with a nonviscous, incompressible liquid, where the axial acceleration of the base is $\ddot{x}$. If it is assumed that the tank shell is thin, that any effects of preloading can be neglected, and that the loading is axially symmetric, the following equations can be developed (Ref. 2.14).

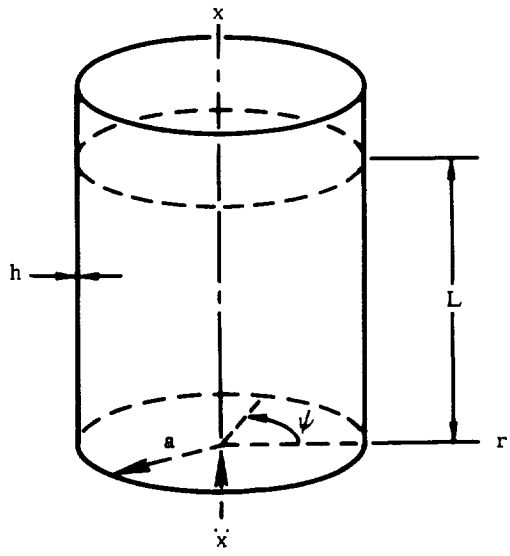

Fig. 2.10. Cylindrical Tank and Liquid

$$\frac{Eh^3}{12(1-\nu^2)}\frac{d^4 w_r}{dx^4} + \frac{Eh}{a^2} W_r + \frac{\nu}{a} N_x = p \Bigg]_{r=a} \tag{2.44}$$

$$\frac{du_x}{dx} = \frac{1-\nu^2}{Eh} N_x - \frac{\nu}{a} w_r \tag{2.45}$$

where

w_r = the radial displacement of a shell element

u_x = the longitudinal displacement of a shell element

N_x = the axial force/unit circumferential length

p = the liquid pressure

E = Young's modulus

ν = Poisson's ratio

a = the shell radius

h = the shell thickness

Eqs 2.44 and 2.45 are essentially the same as those defined for a cylindrical shell (Ref. 2.15) and a static loading condition. If, in addition, the shell is very thin, the $\frac{d^4 w_r}{dx^4}$ term contributes very little to the gross deformation of the shell. Neglecting this term, Eq. 2.44 becomes

$$w_r = \frac{a^2}{Eh} p \Bigg]_{r=a} - \frac{a\nu}{Eh} N_x \tag{2.46}$$

For a nonviscous, incompressible liquid, the fluid velocities are defined in terms of a velocity potential Φ by Laplace's equation, i.e.,

$$\frac{\partial^2 \Phi}{\partial r^2} + \frac{1}{r}\frac{\partial \Phi}{\partial r} + \frac{1}{r^2}\frac{\partial^2 \Phi}{\partial \psi^2} + \frac{\partial^2 \Phi}{\partial x^2} = 0 \tag{2.47}$$

where

$$-\frac{\partial \Phi}{\partial r} = \frac{dr}{dt}$$

$$-\frac{1}{r}\frac{\partial \Phi}{\partial \psi} = r\frac{d\psi}{dt}$$

$$-\frac{\partial \Phi}{\partial x} = \frac{dx}{dt}$$

When all forces applied to the fluid are axially symmetric, Φ is not a function of the coordinate ψ and Eq. 2.47 reduces to

$$\frac{\partial^2 \Phi}{\partial r^2} + \frac{1}{r}\frac{\partial \Phi}{\partial r} + \frac{\partial^2 \Phi}{\partial x^2} = 0 \tag{2.48}$$

For small fluid velocities, the total fluid pressure is given by

$$p = \rho\left[\frac{\partial \Phi}{\partial t} + \ddot{x}(x - L)\right] \tag{2.49}$$

Eqs 2.45, 2.46, 2.48, and 2.49 are used along with the appropriate boundary conditions of the liquid surface, tank wall, and tank bottom to form the basis for the analysis given in Ref. 2.14. In this analysis, the effects of shell inertia for a thin shell are neglected in comparison to the liquid inertia, such that Eqs 2.45 and 2.46 also apply to the dynamic condition.

In order to further simplify the development of a lumped parameter model, the velocity potential term in Eq. 2.49 is usually neglected; i.e., the following approximation is made:

$$p \cong \rho \ddot{x}(L - x) \tag{2.50}$$

Eqs 2.45, 2.46, and 2.50 are then used to develop the tank model. This neglects all contributions due to the liquid velocities, as defined by the velocity potential Φ, and the liquid-free surface waves.

Eqs 2.45, 2.46, and 2.50 can also be used as a basis for developing a multimode tank model by dividing the tank into two or more sections. This approach can account for the higher tank modes as well as variations in tank geometry and skin thickness.

2.2.3.2 Model for Cylindrical Tanks with Large Ullage Volume. The propellant tank most commonly encountered is usually an internally pressurized circular cylinder with a rounded bottom. In many cases, the bottom is approximately elliptical in shape and can be either concave upward or downward.

In this section, a basic single-mode tank model is developed for the case of a large tank ullage volume where the pressure essentially remains constant. This model is then modified to account for the individual effects of stringer reinforcement and a buckled skin with stringer reinforcement.

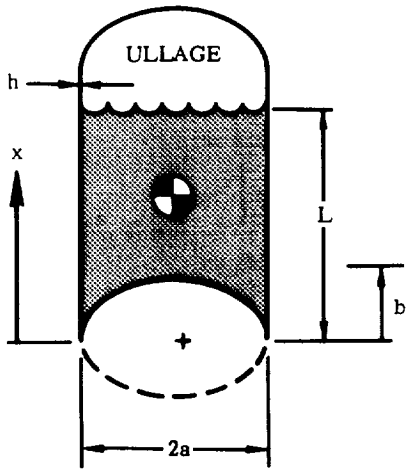

Fig. 2.11. Partially Filled Tank

2.2.3.2.1 Basic Single Mass Model. The tank shown in Fig. 2.11 is partially filled with an incompressible liquid to a depth L and the tank ullage is pressurized with a gas to some constant pressure. The tank is an elastic circular cylinder with a radius a and a constant thickness h. The tank bottom, also elastic, has an elliptical shape, where the major semi-axis is a and the minor semi-axis is b. The bottom can be either concave upward or downward. In addition, it is assumed that all loading on the tank and liquid is axisymmetric.

For an axial acceleration of $\ddot{x}$, the liquid pressure acting upon the wetted portion of the tank is given by Eq. 2.50. Hoop stresses are produced in the tank skin due to this pressure. These stresses result in radial and longitudinal displacements for each element of the tank with respect to the bottom. The radial displacement, which is proportional to the pressure, is shown in Fig. 2.12a.

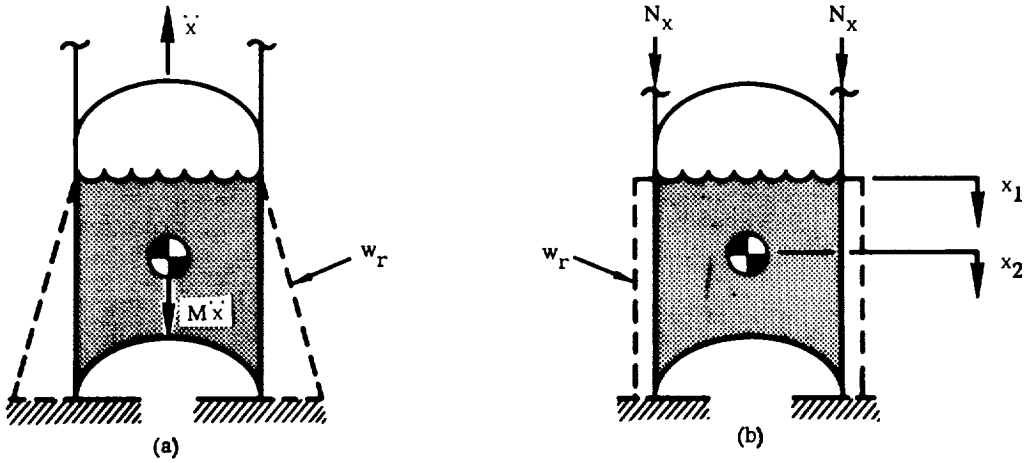

Fig. 2.12. Tank Strains

When the tank is assembled with a vehicle, an acceleration of the masses above the tank results in a longitudinal force acting on the top of the tank. This force produces an additional axial stress in the tank skin and displaces the tank and the liquid center of gravity.

A flexibility matrix can be developed relating displacements at the top and center of gravity of the tank to a force at the top and an effective "liquid inertia force" acting at the center of gravity of the liquid when the bottom of the tank is fixed as shown in Fig. 2.12. A stiffness matrix and a corresponding model for the tank can then be developed. This approach yields the same single-mass tank model as that obtained in Refs 2.14 and 2.16.

The equivalent single-mass model is indicated in Fig. 2.13. Nodes 1 and 2 of the lumped parameter model are used to signify, respectively, the tank top and the liquid center of gravity. The displacements of these points relative to the tank bottom (i.e., relative to x = 0 in Fig. 2.11) are denoted by x_1 and x_2. The force acting at the top of the tank is F_1 and the effective force acting at the center of gravity is F_2. The force F_2 represents the total inertia force of the fluid due to the acceleration $\ddot{x}$, i.e.,

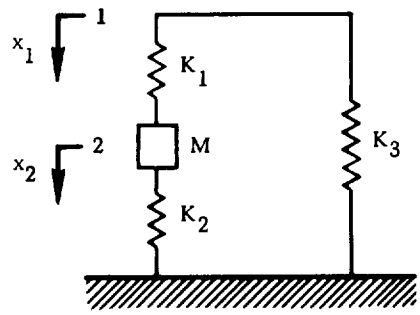

Fig. 2.13. Equivalent Tank Model

$$F_2 = V\rho\ddot{x} = M\ddot{x} \tag{2.51}$$

where V, ρ, $\ddot{x}$, and M are the tank volume, fluid mass density, fluid acceleration, and the fluid mass, respectively. The liquid volume V for the cylindrical tank with an elliptical bottom is given by

$$V = \pi a^2 L D \tag{2.52}$$

where

$$D = 1 - \frac{2}{3}\frac{b}{L} \tag{2.53}$$

Therefore

$$F_2 = \pi a^2 L D \rho \ddot{x} \tag{2.54}$$

$$\rho\ddot{x} = \frac{F_2}{\pi a^2 L D} \tag{2.55}$$

It should be noted that when the bulkhead in Fig. 2.11 is inverted (the dashed line), b takes on a negative value but the above expressions remain valid.

The relationship between displacements and the liquid inertia force are developed first. The longitudinal and circumferential stresses and strains in the thin tank skin due to the fluid pressure, p, are (to a close approximation) given by

$$\left.\begin{aligned} \sigma_x &= 0 \\ \sigma_y &= \frac{pa}{h} \\ \epsilon_x &= \frac{\nu pa}{Eh} \\ \epsilon_y &= \frac{pa}{Eh} \end{aligned}\right\} \qquad (2.56)$$

where σ_x and σ_y are the tank longitudinal and hoop stresses, ϵ_x and ϵ_y are the longitudinal and hoop strains, ν is Poisson's ratio, and E is Young's modulus. Positive stresses are defined to be compressive in the longitudinal direction and tensile in the hoop direction; positive displacements of the tank top and liquid center of gravity are downward.

The longitudinal displacement of the tank at the liquid surface due to the fluid pressure, p, is

$$x_{12} = \int_0^L \epsilon_x \, dx \qquad (2.57)$$

where ϵ_x is given by Eq. 2.56. Thus, substituting Eq. 2.50 into 2.56,

$$x_{12} = \int_0^L \frac{\nu a \rho \ddot{x} (L - x) \, dx}{Eh} = \frac{\nu a L^2 \rho \ddot{x}}{2Eh} \qquad (2.58)$$

Substituting in the expression for $\rho\ddot{x}$ from Eq. 2.55 yields

$$x_{12} = \frac{\nu L F_2}{2\pi DEha} \qquad (2.59)$$

The tank wall radial displacement w_r due to p (Eq. 2.50) is given by

$$w_r = a\epsilon_y = \frac{pa^2}{Eh} = \frac{\rho a^2 (L - x) \ddot{x}}{Eh} \qquad (2.60)$$

The displacement of the center of gravity due to w_r and the tank bottom stiffness is then approximated by

$$x_{22} = \frac{1}{\pi a^2 D} \int_o^{L/2} 2\pi a w_r \, dx + \frac{F_2}{K_B} = \frac{3}{4} \frac{\rho \ddot{x} a L^2}{DEh} + \frac{F_2}{K_B} \tag{2.61}$$

where K_B is the tank lower bulkhead stiffness (the appropriate values for K_B are defined parametrically later). Substituting Eq. 2.55 for $\rho\ddot{x}$ into Eq. 2.51 yields

$$x_{22} = \frac{3 L F_2}{4\pi a D^2 E h} + \frac{F_2}{K_B} \tag{2.62}$$

Considering an axial load acting on the tank, as shown in Fig. 2.12 b, F_1 is an axial load in the tank skin resulting in a load per unit circumferential length of the tank skin given by

$$N_x = \frac{F_1}{2\pi a} \tag{2.63}$$

The stresses and strains in the tank due to F_1 are

$$\left.\begin{aligned} \sigma_x &= \frac{F_1}{2\pi a h} \\ \sigma_y &= 0 \\ \epsilon_x &= \frac{F_1}{2\pi a E h} \\ \epsilon_y &= \frac{\nu F_1}{2\pi a E h} \end{aligned}\right\} \tag{2.64}$$

while the displacements of the tank top and center of gravity due to F_1 are

$$x_{11} = \int_o^L \epsilon_x \, dx = \frac{L F_1}{2\pi a E h} \tag{2.65}$$

$$x_{21} = \frac{L}{2} \int_o^L 2\pi a^2 \epsilon_y \, dx \cdot \frac{1}{V} = \frac{\nu L F_1}{2\pi a D E h} \tag{2.66}$$

The axial stiffness of the tank skin is

$$K = \frac{2\pi a E h}{L} \tag{2.67}$$

Then the relationships between forces and displacements from Eqs 2.59, 2.62, 2.65, and 2.66 are

$$\left.\begin{aligned} d_{11} &= \frac{x_{11}}{F_1} = \frac{1}{K} \\ d_{12} &= \frac{x_{12}}{F_2} = \frac{\nu}{DK} \\ d_{21} &= \frac{x_{21}}{F_1} = \frac{\nu}{DK} \\ d_{22} &= \frac{x_{22}}{F_2} = \frac{3}{2D^2K} + \frac{1}{K_B} \end{aligned}\right\} \tag{2.68}$$

or, in matrix notation,

$$\begin{Bmatrix} x_1 \\ x_2 \end{Bmatrix} = \begin{bmatrix} d_{11} & d_{12} \\ d_{21} & d_{22} \end{bmatrix} \begin{Bmatrix} F_1 \\ F_2 \end{Bmatrix} = [d]\,|F| \tag{2.69}$$

The [d] matrix in Eq. 2.68 can be inverted to obtain a stiffness matrix for the tank. The springs of the equivalent model for the tank can be obtained from this matrix. From Eq. 2.68, F_1 and F_2 are

$$F_1 = \frac{3K + \dfrac{2D^2K^2}{K_B}}{3 - 2\nu^2 + \dfrac{2D^2K}{K_B}} x_1 - \frac{2\nu DK}{3 - 2\nu^2 + \dfrac{2D^2K}{K_B}} x_2 \tag{2.70}$$

$$F_2 = \frac{-2\nu\ DK}{3 - 2\nu^2 + 2D^2\dfrac{K}{K_B}} x_1 + \frac{2D^2K}{3 - 2\nu^2 + 2D^2\dfrac{K}{K_B}} x_2 \tag{2.71}$$

or, in matrix notation,

$$\begin{Bmatrix} F_1 \\ F_2 \end{Bmatrix} = \begin{bmatrix} K_{11} & K_{12} \\ K_{21} & K_{22} \end{bmatrix} \begin{Bmatrix} x_1 \\ x_2 \end{Bmatrix} \tag{2.72}$$

Therefore,

$$\left.\begin{aligned} K_{11} &= \frac{3K + 2D^2 \frac{K^2}{K_B}}{3 - 2\nu^2 + 2D^2 \frac{K}{K_B}} \\ K_{12} &= K_{21} = \frac{-2\nu DK}{3 - 2\nu^2 + 2D^2 \frac{K}{K_B}} \\ K_{22} &= \frac{2D^2 K}{3 - 2\nu^2 + 2D^2 \frac{K}{K_B}} \end{aligned}\right\} \tag{2.73}$$

The springs of the equivalent tank model shown in Fig. 2.13, determined from the coefficients of the stiffness matrix (as indicated in Ref. 2.17), are

$$\left.\begin{aligned} K_1 &= -K_{12} \\ K_2 &= K_{22} + K_{12} \\ K_3 &= K_{11} + K_{12} \end{aligned}\right\} \tag{2.74}$$

Thus,

$$\left.\begin{aligned} K_1 &= \frac{2\nu DK}{3 - 2\nu^2 + 2D^2 \frac{K}{K_B}} \\ K_2 &= \frac{2D(D - \nu)K}{3 - 2\nu^2 + 2D^2 \frac{K}{K_B}} \end{aligned}\right\} \tag{2.75}$$

$$K_3 = \frac{\left(3 - 2\nu D + 2D^2 \frac{K}{K_B}\right) K}{3 - 2\nu^2 + 2D^2 \frac{K}{K_B}} \Bigg| \qquad (2.75)$$

(Contd)

2.2.3.2.2 Spring Rate for Elliptical Tank Bottom. In Ref. 2.18, spring constants are presented for ellipsoidal tank bottoms, as determined from an analysis using linear membrane theory. Graphs from which the spring constants can be obtained are reproduced here.

Consider, once again, the tank shown in Fig. 2.11. From Ref. 2.18 the tank bottom spring rate is given by:

$$K_B = E h_B \frac{2\pi (3e - 2f)^2}{9\left[H(f, \nu) - 2eG(f, \nu) + e^2 F(f, \nu)\right]} \qquad (2.76)$$

where

E = Young's modulus

h_B = bulkhead thickness

a = radius of cylinder

b = bulkhead semiminor axis

L = height of liquid in cylindrical portion of tank

e = L/a

f = b/a

ν = Poisson's ratio

The functions $H(f, \nu)$, $G(f, \nu)$, and $F(f, \nu)$ are given in Figs 2.14, 2.15, and 2.16. These functions are derived in Ref. 2.18.

When the tank bottom is inverted as indicated by the dashed lines in Fig. 2.11 the expression for the spring rate becomes

$$K_B' = E h_B \frac{2\pi (3e + 2f)^2}{9\left[H(f, \nu) + 2eG(f, \nu) + e^2 F(f, \nu)\right]} \qquad (2.77)$$

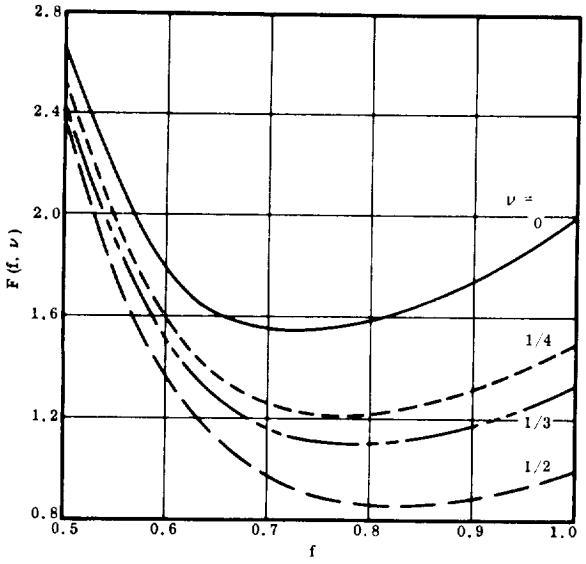

Fig. 2.14. Variation of F (f, ν) with Depth-to-Radius Ratio for Various Values of Poisson's Ratio

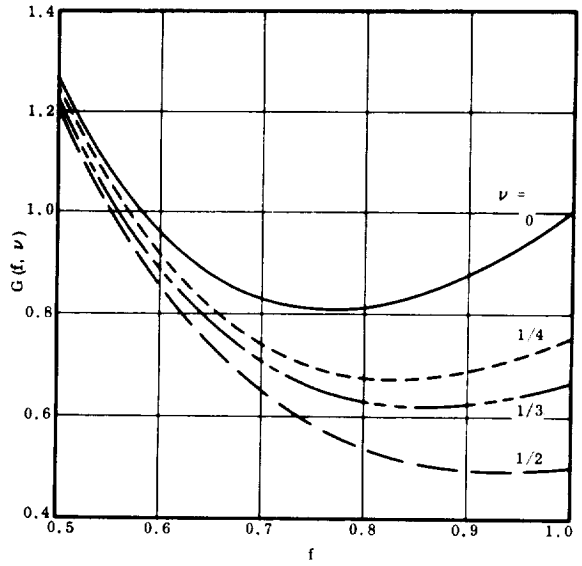

Fig. 2.15. Variation of G (f, ν) with Depth-to-Radius Ratio for Various Values of Poisson's Ratio

2.2.3.2.3 Tank with Stringers and Buckled Skin. A model cylinder with skin and stringer construction is shown in Fig. 2.17. If the stringers have negligible radial stiffness and the skin is unbuckled and can displace longitudinally and radially, the tank models described in the preceding sub-sections can be combined in parallel with a spring K_s, where

$$K_s = \frac{(AE)}{L} \text{ stringers} \qquad (2.78)$$

is the total axial stiffness of the stringers in the cross-section.

When the skin is partially buckled in the axial direction, the axial stiffness of the tank skin is

$$K_{Bu} = \left[\frac{(AE) \text{ skin}}{L}\right] \text{ effective} \qquad (2.79)$$

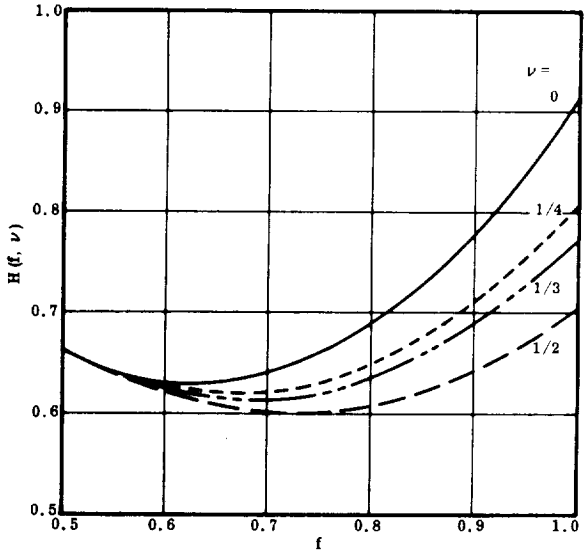

Fig. 2.16. Variation of H (f, ν) with Depth-to-Radius Ratio for Various Values of Poisson's Ratio

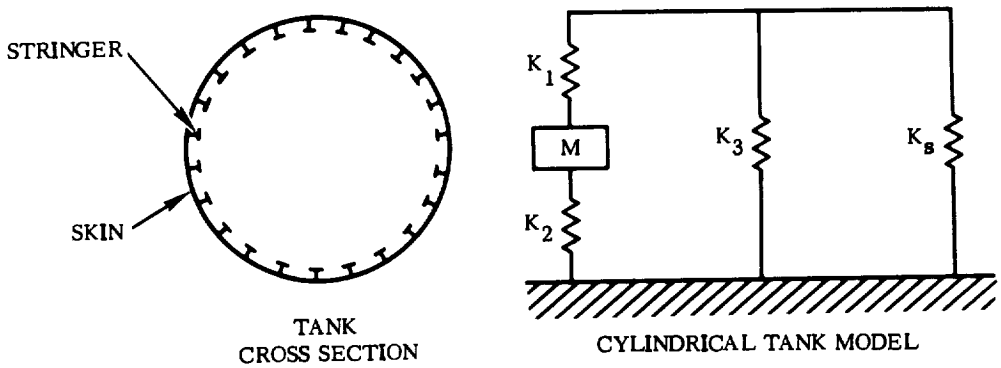

Fig. 2.17. Skin-Stringer Cylinder Tank Model

and the flexibility coefficient d_{11} in Eq. 2.68 becomes

$$d_{11} = \frac{1}{K_{Bu} + K_s} \tag{2.80}$$

The center-of-gravity displacement due to the axial load F_{Bu} carried by the buckled skin is then (neglecting the bulkhead and liquid compressibility effects)

$$x_{21} = \frac{\nu F_{Bu}}{K} \tag{2.81}$$

where K is the axial spring constant for the skin when unbuckled, Eq. 2.67. That portion of the load carried by the buckled skin is given by

$$F_{Bu} = \frac{K_{Bu} F_1}{K_{Bu} + K_s} \tag{2.82}$$

where F_1 is the total axial load carried by the skin and stringers. Then

$$x_{21} = \frac{\nu K_{Bu} F_1}{K(K_{Bu} + K_s)} \tag{2.83}$$

and

$$d_{21} = \frac{x_{21}}{F_1} = \frac{\nu K_{Bu}}{K(K_{Bu} + K_s)} \tag{2.84}$$

The center-of-gravity displacement due to acceleration of the liquid in the tank is still (neglecting bulkhead and compressibility effects)

$$d_{22} = \frac{3}{2K} \tag{2.85}$$

Consequently, the flexibility matrix becomes

$$[d] = \begin{bmatrix} \dfrac{1}{K_{Bu} + K_s} & \dfrac{\nu K_{Bu}}{K(K_{Bu} + K_s)} \\ \dfrac{\nu K_{Bu}}{K(K_{Bu} + K_s)} & \dfrac{3}{2K} \end{bmatrix} \tag{2.86}$$

After inverting the [d] matrix and solving for the spring rates, the values for the model in Fig. 2.18 are

$$\left.\begin{aligned} K_1^{**} &= \frac{2\nu K_{Bu}}{3 - \dfrac{2\nu^2 K_{Bu}^2}{K(K_{Bu} + K_s)}} \\ K_2^{**} &= \frac{2K - 2\nu K_{Bu}}{3 - \dfrac{2\nu^2 K_{Bu}^2}{K(K_{Bu} + K_s)}} \\ K_3^{**} &= \frac{(3 - 2\nu) K_{Bu} + 3K_s}{3 - \dfrac{2\nu^2 K_{Bu}^2}{K(K_{Bu} + K_s)}} \end{aligned}\right\} \tag{2.87}$$

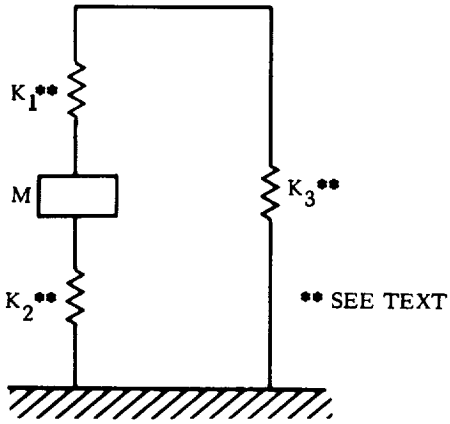

Fig. 2.18. Skin-Stringer Model with Buckled Skin

2.2.3.3 Model for Cylindrical Tank with Small Ullage Volume. When the tank ullage volume is small, any longitudinal oscillation of the structure can produce a corresponding oscillation of significant magnitude in the ullage pressure. This can be the result of a longitudinal force transient such as thrust buildup or launcher release.

The change in ullage pressure is due to a change in ullage volume and ullage gas weight (if a pressure regulator is involved). In this section, a single-mode tank model is developed for such a case. The effect of gas compressibility is included in the model spring rates while the pressure change associated with a change in gas weight is used as the forcing function for the tank.

In order to formulate an analytical representation for the perturbation changes in the tank ullage, the following assumptions are made.

a. The gas, or mixture of gases, in the tank ullage behaves in a quasi-static manner.

b. The gas process is adiabatic.

c. The perturbation variables are small.

The equation of state for a gas (or a mixture of gases) at low pressure is given to a close approximation by the equation below:

$$PV = WR_m T \tag{2.88}$$

where P is pressure, V is volume, W is weight, T is temperature, and R_m is the gas constant for the mixture. In a strict sense, Eq. 2.88 applies to a condition of thermodynamic equilibrium. It also applies (approximately) for a perturbation condition when the changes in these variables are slow enough, and small enough, such that the gas is at all times close to thermodynamic equilibrium. The gas is then said to behave in a quasi-static manner.

For an additional relationship between the variables in the tank ullage, it is convenient to assume that the process is adiabatic. In such case,

$$T \propto P^{\left(\frac{\gamma_m - 1}{\gamma_m}\right)} \tag{2.89}$$

where γ_m is the adiabatic exponent for the gas. In general, a polytropic exponent would be used for Eq. 2.89. However, in the frequency range of interest it can be assumed that there is little chance for heat transfer to the gas so that the polytropic exponent is close to the adiabatic value.

Eqs 2.88 and 2.89 can now be combined to form the following equation:

$$P = \text{const.}\left(\frac{WR_m}{V}\right)^{\gamma_m} \tag{2.90}$$

A given tank may contain a mixture of gases. The total weight is then given by

$$W = W_1 + W_2 + \ldots. \tag{2.91}$$

and the effective gas constant, R_m, is defined by

$$R_m = \frac{W_1 R_1 + W_2 R_2 + \ldots}{W} \tag{2.92}$$

where R_1, R_2, etc., are the gas constants for the individual gases.

For small perturbations during flight, the change in tank pressure is defined by the first terms of a Taylor's series, where the partial derivatives are evaluated at the steady-state (or equilibrium) condition, i.e.,

$$\Delta P = \left.\frac{\partial P}{\partial W}\right]_{s.s.} \Delta W + \left.\frac{\partial P}{\partial V}\right]_{s.s.} \Delta V \tag{2.93}$$

where ΔW is the change in ullage gas weight and ΔV the change in ullage volume.

For the steady-state condition,

$$\bar{P} = \text{const.}\left(\frac{\bar{W} R_m}{\bar{V}}\right)^{\gamma_m} \tag{2.94}$$

The partial derivatives in Eq. 2.93 can be evaluated by using Eq. 2.94 to define the proportionality constant, so that

$$\Delta P = p_a = K_w \frac{\dot{w}}{s} - K_v v \tag{2.95}$$

where s is the Laplace operator, and

$$\left.\begin{aligned} K_w &= \frac{\gamma_m \bar{P} R_g}{\bar{W} R_m} \\ K_v &= \frac{\gamma_m \bar{P}}{\bar{V}} \end{aligned}\right\} \tag{2.96}$$

where R_g is the gas constant for the pressurizing gas and where $\dot{w} = \Delta\dot{W}$, $v = \Delta V$, and the bars denote steady-state quantities.

Fig. 2.19 shows a thin skin, cylindrical tank shell with an elliptical bulkhead for the bottom. The top of the tank is assumed to be rigid and the tank is nearly filled with liquid. Forces F_1 acting on the top of the tank, an effective inertia force F_2 acting at the liquid center of gravity, and an ullage pressure change p_a' acting in the ullage space are also shown. The pressure change p_a' represents only that portion of the total pressure change in the ullage that can be attributed to a change in gas weight. The compressibility effect, due to a change in ullage volume, is included in the model spring rates. Therefore, from Eq. 2.95, p_a' is defined by

$$s p_a' = K_w \dot{w} \tag{2.97}$$

or

$$p_a' = p_a + K_v v \tag{2.98}$$

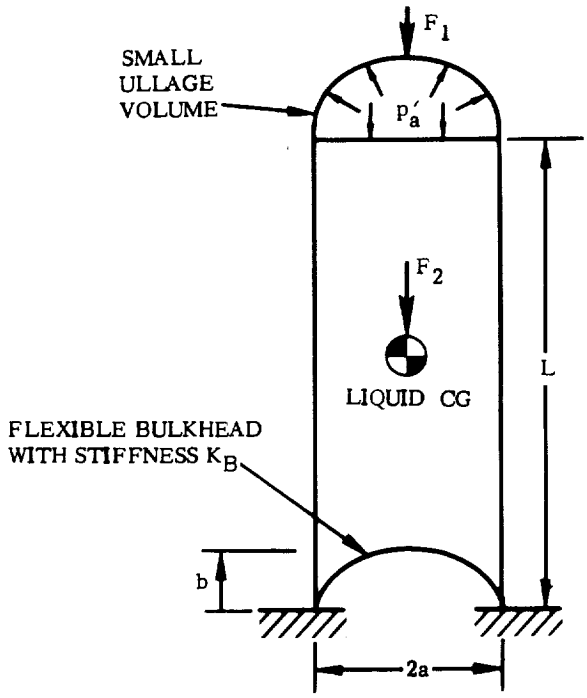

Fig. 2.19. Tank with Small Ullage Volume

If the displacements of the tank top and liquid center of gravity are x_1 and x_2, and the change in ullage volume is v_a, then the relationship between forces, pressure, displacement, and change in ullage volume is given by the matrix equations

$$\begin{vmatrix} x_1 \\ x_2 \\ v_a \end{vmatrix} = \begin{bmatrix} \bar{d}_{11} & \bar{d}_{12} & \bar{d}_{1v} \\ \bar{d}_{21} & \bar{d}_{22} & \bar{d}_{2v} \\ \bar{d}_{v1} & \bar{d}_{v2} & \bar{d}_{vv} \end{bmatrix} \begin{vmatrix} F_1 \\ F_2 \\ p'_a \end{vmatrix} = [\bar{d}] \, |F| \tag{2.99}$$

or

$$\left|\begin{array}{c} x_1 \\ \hline x_2 \\ \hline v_a \end{array}\right| = \left[\begin{array}{c|c|c} d_{11} - \dfrac{d_{v1}^2}{C + d_{vv}} & d_{21} - \dfrac{d_{2v}\, d_{v1}}{C + d_{vv}} & \dfrac{C\, d_{v1}}{C + d_{vv}} \\ \hline d_{12} - \dfrac{d_{1v}\, d_{v2}}{C + d_{vv}} & d_{22} - \dfrac{d_{2v}^2}{C + d_{vv}} & \dfrac{C\, d_{v2}}{C + d_{vv}} \\ \hline \dfrac{C\, d_{1v}}{C + d_{vv}} & \dfrac{C\, d_{2v}}{C + d_{vv}} & \dfrac{C\, d_{vv}}{C + d_{vv}} \end{array}\right] \left|\begin{array}{c} F_1 \\ \hline F_2 \\ \hline p'_a \end{array}\right| \tag{2.100}$$

where $C = \dfrac{1}{K_v}$ is the compliance of the gas in the ullage volume, and

$$\begin{bmatrix} d_{11} & d_{12} & d_{1v} \\ d_{21} & d_{22} & d_{2v} \\ d_{v1} & d_{v2} & d_{vv} \end{bmatrix} = [d]$$

$$
= \left|\begin{array}{c|c|c}
\dfrac{1}{K} & \dfrac{\nu}{DK} & \dfrac{2\pi a^2\left(\nu-\frac{1}{2}\right)}{K} \\
\hline
 & & \dfrac{2\pi a^2\left(1-\frac{\nu}{2}\right)}{DK} \\
\dfrac{\nu}{DK} & \dfrac{3}{2D^2K}+\dfrac{1}{K_B} & +\dfrac{\pi a^2}{K_B} \\
\hline
 & \dfrac{2\pi a^2\left(1-\frac{\nu}{2}\right)}{DK} & \dfrac{2\pi^2 a^4\left(\frac{5}{2}-2\nu\right)}{K} \\
\dfrac{2\pi a^2\left(\nu-\frac{1}{2}\right)}{K} & & \\
 & +\dfrac{\pi a^2}{K_B} & +\dfrac{\pi^2 a^4}{K_B}
\end{array}\right| \qquad (2.101)
$$

The compliance C could be defined to include flexibility of the tank upper bulkhead. As the ullage volume increases, C becomes infinite and the model reduces to the basic tank model.

The $[\bar{d}]$ matrix can be inverted to obtain a stiffness matrix:

$$
[\bar{d}]^{-1} = [K] = \begin{bmatrix} K_{11} & K_{12} & K_{1v} \\ K_{21} & K_{22} & K_{2v} \\ K_{v1} & K_{v2} & K_{vv} \end{bmatrix} \qquad (2.102)
$$

A tank model where the ullage gas compressibility is included in the spring rates and where the applied forces are due to p_a' is shown in Fig. 2.20.

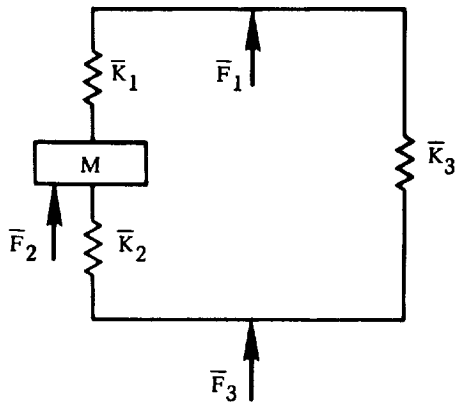

Fig. 2.20. Tank Model for Small Ullage Volume

The tank spring rates, defined in terms of the stiffness matrix, are

$$\left.\begin{aligned} \bar{K}_1 &= -K_{12} + \frac{K_{1v}\,K_{2v}}{K_{vv}} \\ \bar{K}_2 &= K_{22} + K_{21} - \frac{K_{2v}\,K_{v1} + K_{2v}^2}{K_{vv}} \\ \bar{K}_3 &= K_{11} + K_{12} - \frac{K_{1v}\,K_{2v} + K_{1v}^2}{K_{vv}} \end{aligned}\right\} \quad (2.103)$$

2.2.3.4 Multimode Models. In most analyses of current vehicles, the structural representations used have been based upon the tank model shown in Fig. 2.13. This model provides an approximation for the first (predominant) mode of the coupled propellant and elastic tank. However, it is known that higher modes exist in the tank and a limited number of these may have a significant energy content, compared to the first, and they do provide a resonant condition at discrete higher frequencies. This is shown in Ref. 2.14.

This implies one of two conditions. Either the higher tank modes are unimportant and their omission does not affect the overall structural modes, or certain structural modes are inaccurate because of this omission. The actual condition, of course, depends upon many factors such as the type of structure, the propellant level, etc.

There has been very little opportunity to determine the accuracy of predicted vehicle modes using current models. It is believed that, in most cases, the first mode predictions are adequate and that any errors are incurred in the higher modes. This should be particularly true when the propellant mass is large and represents a major part of the vehicle mass.

It is desirable to further explore the importance or contribution of the higher tank modes by developing a multimode tank model and using it in the structural representation for the vehicle. The initial results obtained by using this approach are discussed in this subsection.

A discrete model for higher tank modes can be developed in a manner similar to that used for the single-mass representation. Consider again the cylindrical tank with an elliptical bulkhead as shown in Fig. 2.21. Assume, for the present, that the bulkhead is inelastic (rigid) and that the liquid is incompressible.

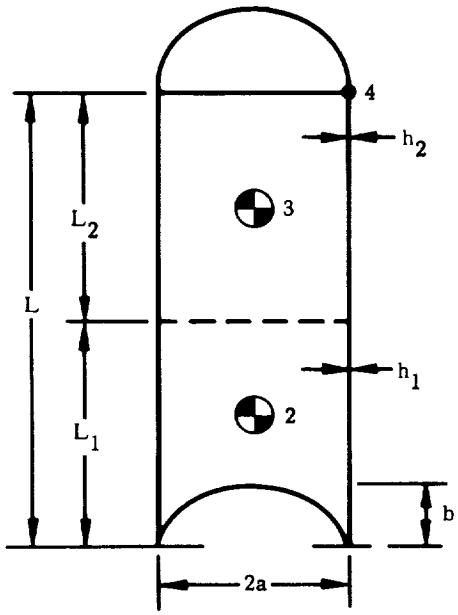

Fig. 2.21. Two-Element Tank

Let the tank and propellant be divided into two elements. A point on the tank at the liquid surface, the center of gravity of the upper element, and the center of gravity of the lower element are denoted by Stations 4, 3, and 2, respectively. The propellant heights are L_1 and L_2 while the tank wall thicknesses are h_1 and h_2.

The procedure used to develop a two-mass model is exactly the same as that used for the single-mass model. This procedure can be expanded to any number of elements.

The following quantity is similar to that from Eq. 2.53.

$$D_1 = 1 - \frac{2}{3}\frac{b}{L_1} \tag{2.104}$$

while the axial rates at the two tank elements are given by

$$\left.\begin{aligned} K_1 &= \frac{2\pi a E h_1}{L_1} \\ K_2 &= \frac{2\pi a E h_2}{L_2} \end{aligned}\right\} \tag{2.105}$$

Next, consider the individual effects of an axial acceleration $\ddot{x}$ on the two fluid elements. The resulting radial deflections of the tank are shown in Fig. 2.22a and b along with the corresponding inertial forces F_2 and F_3 acting at the two fluid center-of-gravity locations. Finally, an external force F_4 is considered at the top of the tank. This produces the radial tank deflection shown in Fig. 2.22c. The individual axial and radial deflections of the shell can be evaluated using the shell equations. This leads to the following influence coefficients.

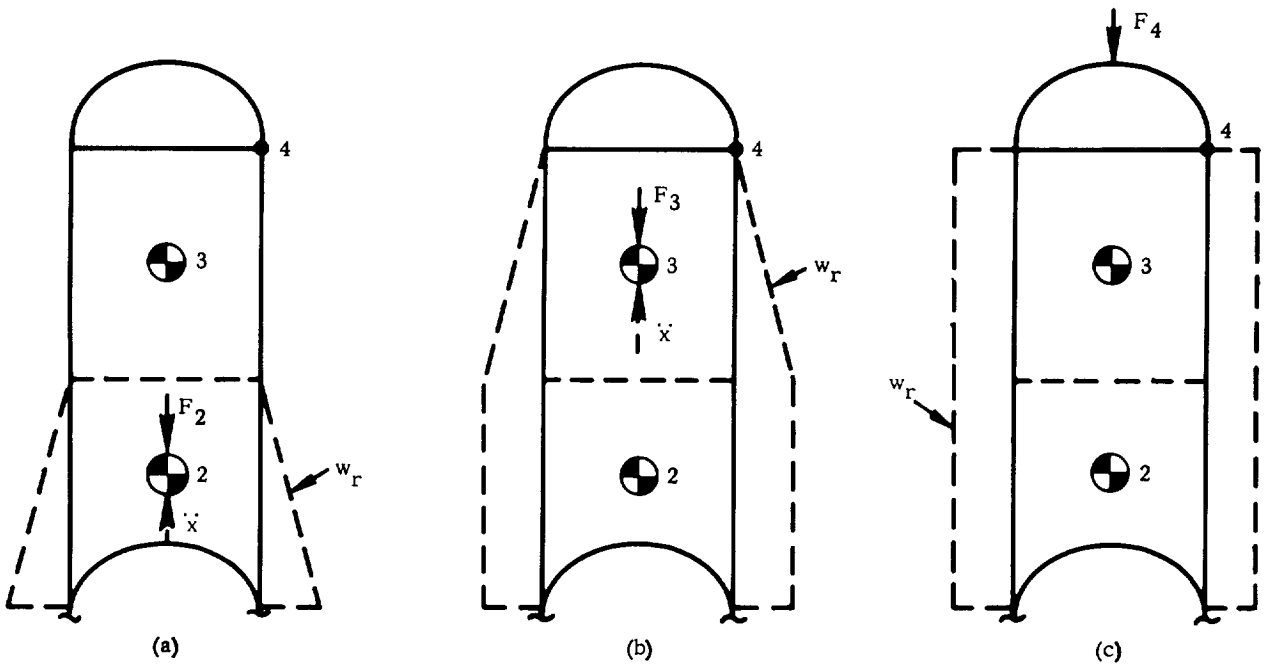

Fig. 2.22. Assumed Forces on Two-Element Tank

$$
\left.
\begin{aligned}
d_{32} &= \frac{x_{32}}{F_2} = \frac{2}{D_1 K_1} \\
d_{22} &= \frac{x_{22}}{F_2} = \frac{3}{2 D_1^2 K_1} \\
d_{42} &= \frac{x_{42}}{F_2} = \frac{\nu}{D_1 K_1} \\
d_{23} &= \frac{x_{23}}{F_3} = \frac{2}{D_1 K_1} \\
d_{33} &= \frac{x_{33}}{F_3} = \frac{4}{K_1} + \frac{3}{2 K_2} \\
d_{43} &= \frac{x_{43}}{F_3} = \frac{2\nu}{K_1} + \frac{\nu}{K_2} \\
d_{24} &= \frac{x_{24}}{F_4} = \frac{\nu}{D_1 K_1}
\end{aligned}
\right\} \qquad (2.106)
$$

$$\left.\begin{aligned} d_{34} &= \frac{x_{34}}{F_4} = \frac{2\nu}{K_1} + \frac{\nu}{K_2} \\ d_{44} &= \frac{x_{44}}{F_4} = \frac{K_1 + K_2}{K_1 K_2} \end{aligned}\right\} \qquad \text{(2.106 Contd)}$$

The influence matrix is then given by

$$[d] = \begin{bmatrix} d_{22} & d_{23} & d_{24} \\ d_{32} & d_{33} & d_{34} \\ d_{42} & d_{43} & d_{44} \end{bmatrix}$$

$$= \left[\begin{array}{c|c|c} \dfrac{3}{4 D_1^2 K_1} & \dfrac{2}{D_1 K_1} & \dfrac{\nu}{D_1 K_1} \\ \hline \dfrac{2}{D_1 K_1} & \dfrac{4}{K_1} + \dfrac{3}{2 K_2} & \dfrac{2\nu}{K_1} + \dfrac{\nu}{K_2} \\ \hline \dfrac{\nu}{D_1 K_1} & \dfrac{2\nu}{K_1} + \dfrac{\nu}{K_2} & \dfrac{K_1 + K_2}{K_1 K_2} \end{array}\right] \qquad (2.107)$$

where for $L_1 = L_2 = \dfrac{L}{2}$, Eqs 2.104 and 2.105 become

$$\left.\begin{aligned} K_1 &= \frac{4\pi a E h_1}{L} \\ K_2 &= \frac{4\pi a E h_2}{L} \\ D_1 &= 1 - \frac{4b}{3L} \end{aligned}\right\} \qquad (2.108)$$

For a particular tank, the coefficients of the [d] matrix can be evaluated. The [d] matrix can then be inverted to obtain a stiffness matrix. Fig. 2.23 shows a model which would correspond to the stiffness matrix given by

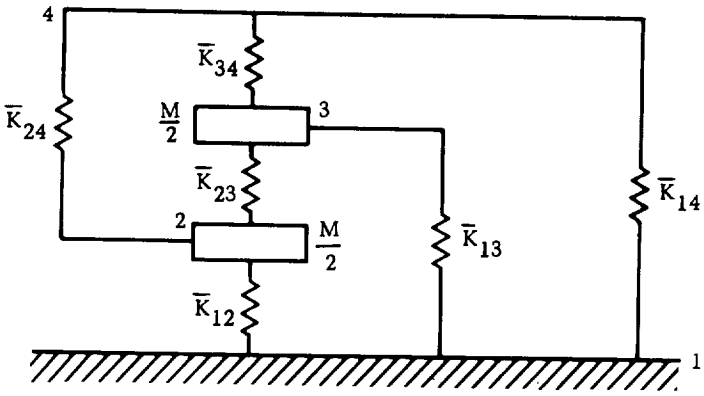

Fig. 2.23. Two-Mass Tank Model

$$[d]^{-1} = \begin{bmatrix} K_{22} & K_{23} & K_{24} \\ K_{32} & K_{33} & K_{34} \\ K_{42} & K_{43} & K_{44} \end{bmatrix} \tag{2.109}$$

where the model spring stiffnesses are related to the stiffness matrix by

$$\left.\begin{aligned} \bar{K}_{23} &= -K_{23} \\ \bar{K}_{24} &= -K_{24} \\ \bar{K}_{34} &= -K_{34} \\ \bar{K}_{12} &= K_{22} + K_{23} + K_{24} \\ \bar{K}_{13} &= K_{32} + K_{33} + K_{34} \\ \bar{K}_{14} &= K_{42} + K_{43} + K_{44} \end{aligned}\right\} \tag{2.110}$$

This model can be generalized for many degrees of freedom by writing general expressions for the influence coefficients of a multimass model. Also, the effects of a flexible tank bottom and liquid compressibility can be included in the process.

2.2.4 ADDING COMPONENTS USING MODE SYNTHESIS. Frequently it is desirable to make a parameter study to determine the effect on vehicle response resulting from changes in the characteristics of a specific area or component, e.g., a sloshing mass or engine system. Rather than make several analyses of the system, changing but a fraction of the parameters each time, the vibration characteristics of the system excluding the specific varying parameter may be calculated, and then modified by coupling the parameter back in through the mode synthesis technique (discussed in Refs 2.19 and 2.20).

The mode synthesis approach may result in a loss of accuracy. The analysis that considers the most information about the system will be the most accurate. The use of many modes in the mode synthesis technique will give theoretically more accurate results than using a minimum number of modes. This aspect is one which must be handled by discretion born of experience. As an example, in calculating the bending modes with sloshing propellants, three alternatives are available (all motions are relative to the undeformed axis of the beam):

a. Include the sloshing mass as an attached spring-mass to the beam in the modes calculation.

b. Assume the sloshing mass is included in the "rigid" propellants for modes calculation. The sloshing is then included through mode synthesis by adding the single spring-mass mode and subtracting the sloshing mass effects from the bending modes. This requires both inertial and elastic coupling in the synthesis.

c. Assume the sloshing mass can be eliminated in the "rigid" propellants for modes calculations. The sloshing is then included through mode synthesis by adding the simple spring mass mode. This requires only elastic coupling in the synthesis.

These alternatives are listed in order of accuracy of end results following the general rule stated previously. There are many examples where there would be little if any degradation of accuracy. As an example, consider a vehicle with first bending frequency of 5 cps and first slosh frequency of 1 cps. The sloshing is then essentially uncoupled from the elastic modes. If the slosh frequency were 4 cps, then considerable coupling is possible.

Although sloshing was used as an example, the same is true for any representation of this type, i.e., engines, payloads, sloshing propellants, any large component, or a specific parameter under investigation.

2.2.5 LATERAL-TORSIONAL-LONGITUDINAL COUPLING. The typical axisymmetric-cylindrical space vehicle is analyzed as if lateral, torsional, and longitudinal motion are not coupled. Actually, these vehicles are not completely symmetric and a possible coupling mechanism, however slight, can always be found. The importance of this coupling can vary greatly from vehicle to vehicle and even if it is known to exist from flight or experimental data, the coupling mechanism is difficult to identify. These

coupling problems often occur when the modal frequencies of two modes, say, one lateral and one torsional, are very close together. Then a very small coupling mechanism, such as center-of-gravity offset from the supposed line of symmetry, can result in coupled motion.

A comparison of the frequencies of the modes in the three directions should be made to determine the existence of modes of nearly equal frequency. If such a condition exists, it is necessary to examine the condition under which this may cause a significant problem. As an example, if excitation of a bending mode by an atmospheric disturbance occurred, could this cause excitation of a critical torsional mode at this same frequency? In most instances of coupling of this type, a periodic forcing function is necessary to transmit the energy from one direction to another.

Cylindrical vehicles with unsymmetric upper stages or payloads of large mass can cause coupling in the various directions in the low-frequency modes. The model and analysis then become complicated and approach that of the clustered boosters. Representation of this configuration requires detailed description in the unsymmetric stages and an analysis as described later for clustered boosters. Preliminary work would indicate the degree of sophistication to be used for adequate representation for loads analysis.

2.2.6 CLUSTERED BOOSTERS. One method for obtaining the higher thrust required for large payloads is to attach rocket engines or motors to a central core; for liquid boosters a peripheral ring of propellant tanks is attached to a center tank and the engines are supported on truss members connecting the tanks; for solid boosters, the motors are attached to a central solid or liquid booster. These clustered tank designs destroy axial symmetry and quite often planes of symmetry. Such configurations result in a more complicated lateral model where a number of cylindrical tanks are coupled by their elastic connections and must be allowed freedom in several directions for adequate description of vehicle modes (see Fig. 2.24).

For preliminary design it is sufficient to choose approximate planes of symmetry and analyze the vehicle for bending modes in pitch and yaw planes using branch beams connected to the central core by translational and rotational springs. Simplified torsional and longitudinal models will also suffice at this stage. These simple models can be used to identify possible problem areas (such as relative modal frequencies) and provide design criteria for the connections between tanks.

A complete analysis (or carefully conducted test) should be undertaken to describe all the primary modes of the clustered vehicle. This analysis would provide translation and rotation in two mutually perpendicular planes; torsion and longitudinal motion. The model of the tanks for translation and rotation in each of the two planes would be very similar to that discussed for the cylindrical booster. Provision must be made to account for the motion of the outer tanks in these two directions due to the torsional displacement of the center tank and the elastic connections. It is also possible that

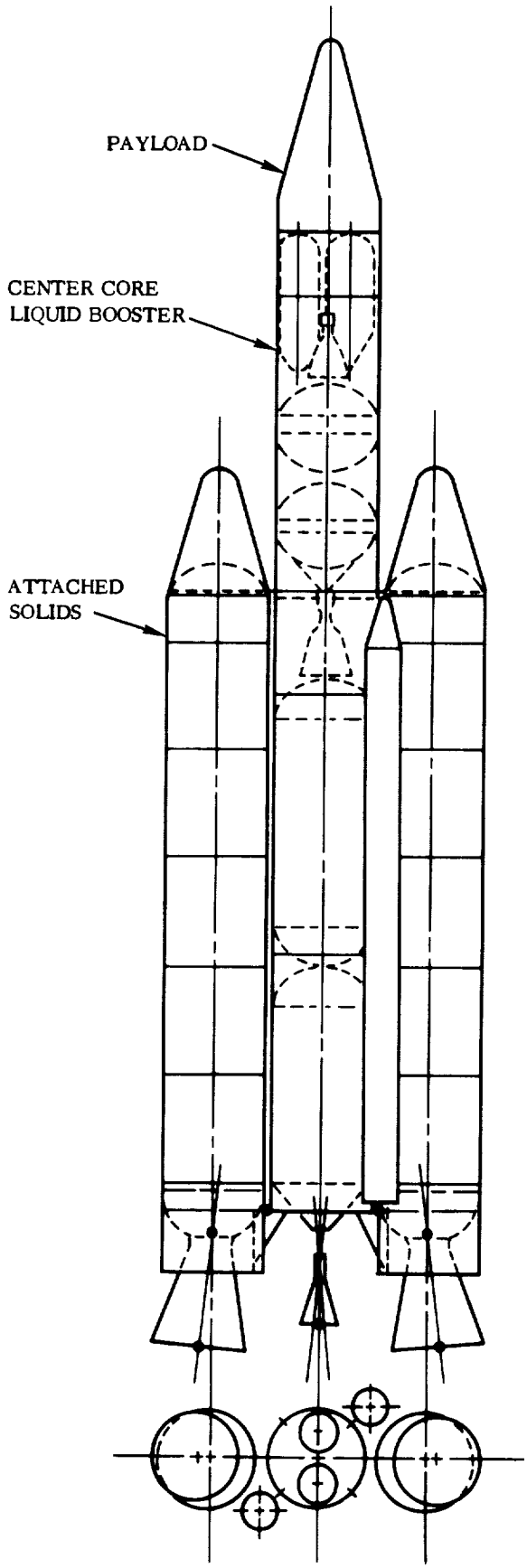

Fig. 2.24. Titan IIIC

longitudinal motion will couple with lateral and torsional displacement. As an example, consider a cluster arrangement where the connection at the bottom provides moment, shear, and axial restraints while the connection at the top provides only shear restraint. Then it is possible to find a mode where the external tanks are bending, causing moments and deflections at the connection to the center core which will result in longitudinal motion of the core. The significance of these types of modes can be ascertained only from the analysis (or test) and can vary greatly from vehicle to vehicle.

The torsional properties in the model can be represented by the torsional stiffness and roll inertia of each tank. The tanks must then be connected by the elastic properties of the truss. The complete model for the clustered booster then consists of the axial load, shear, bending moment, and torque. The top connection transmits only shear. Because of the nature of the connections, it can be seen that yaw bending and longitudinal coupling can occur. Pitch bending and torsion represent another possible coupling mechanism. Storey in Ref. 2.21 develops the coupled flexibility matrices for these two conditions. This method encountered difficulty in that the number of stations required for adequate representation of the system with the required transformations exceeded computer capacity.

The final Titan IIIC analysis presented in Ref. 2.22 utilizes the mode synthesis approach. The longitudinal, torsional, and pitch and yaw bending modes are determined for each tank and are then coupled by the elasticity of the connecting elements. The influence coefficients for these trusses were obtained experimentally. A comparison of analytical and 1/5-scale experimental results is given in Ref. 2.23.

The Saturn I vehicle consists of a center LO_2 tank with eight peripheral tanks for alternating LO_2 and RP-1. These tanks are connected at top and bottom by trusses providing axial, shear, and torsion restraint in both planes at the bottom plus moment restraint in the tangential planes. The top connection provides similar restraint except for the fuel tanks which do not transmit axial load. The trusses are not symmetric with respect to planes of symmetry of the tanks, but this effect is small so that planes of symmetry as defined by the tanks do not introduce large errors.

Milner (Ref. 2.24) establishes theoretically the uncoupling of pitch, yaw, and torsion modes for a symmetrical clustered booster and investigates the effect of minor asymmetry. Results of this study indicate that the effect of such coupling on natural frequencies is minor; mode shapes are not presented.

Lianis (Ref. 2.25) develops a matrix solution of the dynamics problem of a four-tank booster without center core. The flexibility matrix of the whole unit, with appropriate beam end fixity, is derived. This flexibility matrix together with a suitable mass matrix is used to derive equations of free vibration in matrix form. The tanks are assumed to be similar, but the solution can be modified accordingly for the case of nonsimilar tanks and for other tank configurations. The formulation is general so as to furnish any complex mode of vibration. Simple modes, however, can be obtained as particular cases of the general problem.

2.2.7 CORRECTING MODEL BASED ON TEST RESULTS. The final evaluation of analytical techniques is a comparison with experimental data. Perfect comparisons are indeed exceptions, since both the analytical model and experimental model are approximations to some extent. The analytical approximations have been discussed. The major experimental approximations are centered around suspension system effects and vehicle modifications required to accommodate the suspension system. No general rule can be made to obtain better agreement between test and analysis. Careful examination of the data and the structure will probably indicate several areas where the representation is inadequate or does not define the test specimen. Possible causes of differences are:

a. Effects of suspension system on test environment.

b. Stiffness of joints or trusses.

c. Assumed planes of symmetry are incorrect.

d. Effect of large components such as engines.

e. Experimental modes may be impure, i.e., not orthogonal.

f. Effects of moment of inertia.

g. Nonlinearity.

The work of Ref. 2.26 presents a method for obtaining the flexibility matrix from experimental mode data. The procedure orthogonalizes the experimental modes, using an analytical mass distribution, and then derives the flexibility matrix of the structure. This method can be useful if complete and accurate experimental data are obtained for a system difficult to model. It can also be used to locate possible discrepancies between analytical and experimental results.

2.2.8 DAMPING EFFECTS. Dissipative (damping) forces exist in the vibrating structure as a result of material strain hysteresis and coulomb friction in structural joints. The nature of these damping effects is obscure and does not lend itself to analysis other than an approximate empirical treatment, by which the gross effect of these scattered dissipative mechanisms is represented as equivalent viscous damping, added to each mode as appropriate. The damping is thus assumed to produce no coupling between modes. While this mechanization is not entirely realistic, it is justified by two observations: First, the actual damping is very low and is found by test to produce little coupling. Thus, nearly pure normal modes of a system may be excited and the system observed to decay almost harmonically. The indication given is that velocity-dependent coupling is very small. Secondly, if an attempt is made to show a velocity-dependent coupling, the coefficient would have to be determined experimentally. Since the direct damping coefficient is itself difficult enough to measure it is clear that the accuracy of a study cannot be increased by the introduction of still more suspect data. The structural damping force is a function of the deflection of the generalized coordinate of the mode but in phase with the velocity of the generalized coordinate of that mode. To treat this damping as viscous damping requires that the mode oscillate in a quasi-harmonic manner. This damping force may then be expressed as a damping factor, ζ_n, where $2\zeta_n\omega_n\dot{\xi}_n$ is the internal damping force of the nth mode per unit generalized mass.

Fluid propellant damping forces result from the dissipative nature of a viscous fluid undergoing shear. Although there are some approximate methods for calculating damping forces, these forces are most commonly arrived at by testing the actual tank, in the case of small missiles, and a model tank in the case of large missiles. These forces may be represented as a propellant damping factor, ζ_n, in the expression $2\zeta_n\omega_n\dot{\xi}_n$ which is the damping force per unit sloshing mass and $\dot{\xi}_n$ is the lateral velocity of the nth sloshing mass.

Aerodynamic damping forces result from lateral velocity of the vehicle which causes, for any particular point on the vehicle, a small angle of attack. The aerodynamic force associated with this angle of attack opposes the lateral motion, thereby dissipating energy. The aerodynamic damping forces are easily calculated and are, of course, a function of $\dot{\xi}_n$. Aerodynamic damping on launch vehicles is often not important for dynamic load analyses; however, for some configurations, e.g., hammerhead payloads and winged payloads, it may need to be considered.

2.3 DERIVATION OF NORMAL MODES

2.3.1 SOLUTIONS FOR CHARACTERISTICS. Formulation of the equations of motion of dynamic systems results in a linear differential equation for the continuous exact solution or a series of differential equations for the approximate solutions. For lateral vibration usually only the lower modes are of any significance and therefore the approximate solutions are of practical importance. Two methods are used to describe the system in these approximate solutions: 1) the system is divided into a finite number of segments connected by massless stiffness, and 2) the system is described in terms of assumed functions. Solving for the characteristics of the resulting equations can be categorized into three groups. These are: 1) energy methods, 2) solving the differential equations, and 3) solving the integral equation. The equations may be written in general matrix form as follows,

$$- \omega^2 [M] \{u\} + [K] \{u\} = 0 \qquad \text{(differential equation)} \qquad (2.111)$$

$$\{u\} = \omega^2 [K]^{-1} [M] \{u\} = \omega^2 [D] \{u\} \qquad \text{(integral equation)} \qquad (2.112)$$

The categorizations of the above matrix equations as differential and integral equations, respectively, follow the practice of Bisplinghoff et.al. in Ref. 2.4.

The most general solution of Eq. 2.111 involves expansion of the determinant and solving the polynomial equation. This procedure is adequate for simple systems and up to four degrees of freedom can be solved easily. Methods for higher order systems have been developed in Refs 2.27 and 2.28. However, since often only the lower modes are important some approximate methods have been developed which obtain these modes and frequencies with sufficient accuracy.

2.3.1.1 Matrix Iteration (Stodola and Vianello Method). The matrix iteration technique is essentially the Stodola and Vianello method in matrix form. The integral equation is

$$\{u\} = \omega^2 [K]^{-1} [M] \{u\} \qquad (2.113)$$

It can be seen that $\omega^2 [M] \{u_{n-1}\}$ is the load associated with an assumed mode shape, $\{u_{n-1}\}$, vibrating at a frequency ω. The deflection resulting from this load or the next approximation of the mode shape is obtained by premultiplication by the influence coefficients, or the inverse of the stiffness matrix. Since ω^2 is a constant it can be assumed to be unity and the equation becomes

$$\{u_n\} = [K]^{-1} [M] \{\bar{u}_{n-1}\} \qquad (2.114)$$

where $\{\bar{u}\}$ is a vector normalized on its largest element. Successive iterations of Eq. 2.114 continue until $\{\bar{u}_n\}$ has converged, i.e., every element in $\{\bar{u}_n\}$ satisfies

$$\{\bar{u}_n\} - \{\bar{u}_{n-1}\} \leq \epsilon$$

The frequency of the mode is then

$$\omega^2 = \frac{1}{u_{ni}} \tag{2.115}$$

where u_{ni} is the largest element of the unnormalized vector $\{u_n\}$. Proof of convergence is given in Ref. 2.27.

For most practical problems it is necessary to obtain more than the first normal mode. This is accomplished by applying the condition of orthogonality as a means of purifying the assumed higher modes of lower mode components. The orthogonality condition requires that

$$\{\Phi_1\}' [M] \{\Phi_2\} = 0 \tag{2.116}$$

Therefore, modification of the dynamic matrix to satisfy this condition will allow extraction of the next mode. This is expressed in matrix form as:

$$[D_2] = [D_1] \left[[I] - [\Lambda]\right] \tag{2.117}$$

where [I] is a unity matrix and $[\Lambda]$ is a matrix of zero's except for the row (or rows) imposing the orthogonality. This row is composed of the elements $u_i\ m_i$ normalized on its largest element. This element locates the characteristic row and the row matrix is a good approximation of the characteristic row. As an example,

$$\lfloor u_i' m \rfloor = \lfloor u_{11}\ m_1 \qquad u_{21}\ m_2 \qquad u_{31}\ m_3 \qquad u_{41}\ m_4 \rfloor$$

If $u_{31}\ m_3$ is the largest element, then

$$[\Lambda] = \begin{bmatrix} 0 & 0 & 0 & 0 \\ 0 & 0 & 0 & 0 \\ \dfrac{u_{11}\ m_1}{u_{31}\ m_3} & \dfrac{u_{21}\ m_2}{u_{31}\ m_3} & 1 & \dfrac{u_{41}\ m_4}{u_{31}\ m_3} \\ 0 & 0 & 0 & 0 \end{bmatrix} \tag{2.118}$$

Once $[\Lambda]$ is obtained then D_2 can be formed and iterations proceed to determine the next mode and frequency.

For improved accuracy and subsequent deflation of the D matrix it is recommended that iterations be performed on the row matrix, $\lfloor u_i' M \rfloor$, by post-multiplication by the dynamic matrix. This removes errors in roundoff in the preceding fundamental mode and provides a more accurate characteristic. Thus,

$$\lfloor \overline{u_i' M} \rfloor [D] = \lfloor u_i' M \rfloor$$

where $\overline{[\ ]}$ indicates normalization on its largest element. $\lfloor u_i' M \rfloor$ is then normalized on its largest element and placed in the $[\Lambda]$ matrix. If the characteristic row is found by this method, the deflated dynamic matrix for successive modes can then be obtained by

$$[D_3] = [D_2] \left[[I] - [\Lambda_2] \right]$$

If the deflated matrix is obtained only from the conditions of orthogonality, then

$$[D_n] = [D_1] \left[[I] - [\Lambda_n] \right] \tag{2.119}$$

where $[\Lambda_n]$ satisfies orthogonality between first and n, second and n, ---, and n-1 and n modes.

An alternate method for deflating the matrix is given in Ref. 2.28 and is particularly useful in application with automatic computers. This deflation method gives

$$[D_2] = [D_1] - \frac{1}{\omega_1^2} \{u_1\} \lfloor u_1 \rfloor [M] \tag{2.120}$$

where $\{u_1\}$ is the column of elements of the first mode normalized so that $\lfloor u_1 \rfloor [M] \{u_1\} = 1$. For each succeeding mode the matrix is modified by subtracting the triple matrix product for the preceding mode from the preceding modified dynamic matrix.

$$[D_n] = [D_{n-1}] - \frac{1}{\omega_{n-1}^2} \{u_{n-1}\} \lfloor u_{n-1} \rfloor [M] \tag{2.121}$$

2.3.1.2 Holzer-Myklestad Method. The Holzer-Myklestad method is extremely suitable for obtaining solution of the differential equations of beams represented as concentrated masses connected by massless stiffness elements. A principal advantage of this method is that each mode is obtained independently and therefore all modes are as accurate as represented by the system analyzed.

The technique proposed by Holzer was originally developed for torsional systems. It is equally applicable to any close-coupled system, i.e., represented as a spring-mass system. A frequency is assumed and one element of the mode shape vector is

taken as unity. Through equilibrium equations, the other elements of the vector are calculated. There will be one additional equilibrium equation left after the last element of the mode shape vector is evaluated, which will be satisfied only if the assumed frequency is correct. Successive frequency trials are made until the proper value is obtained. The process is facilitated by plotting net unbalanced force on the final mass against frequency. At the natural frequency of the system, the curve of net force passes through zero.

In reality, the Myklestad method is the Holzer method extended to include far-coupled systems, i.e., beam systems. The slope and deflection at one end of a beam segment are expressible in terms of the slope and deflection at the other end, the loads at the other end and the flexibility of the beam segment. The boundary conditions at one end of the beam give an initial set of values. Two of the four conditions will be unknown. One is set to unity and the interior values are determined in terms of the remaining unknown.

As an illustration, consider the beam segment in Fig. 2.25. The deflections and forces at the right end can be expressed as:

$$\left.\begin{aligned} S_2 &= S_1 - \omega^2 m_2 y_2 \\ M_2 &= M_1 + S_1 L \\ y_2 &= y_1 + C_{11} S_1 + C_{12} M_1 + L\theta_1 \\ \theta_2 &= \theta_1 + C_{21} S_1 + C_{22} M_1 \end{aligned}\right\} \qquad (2.122)$$

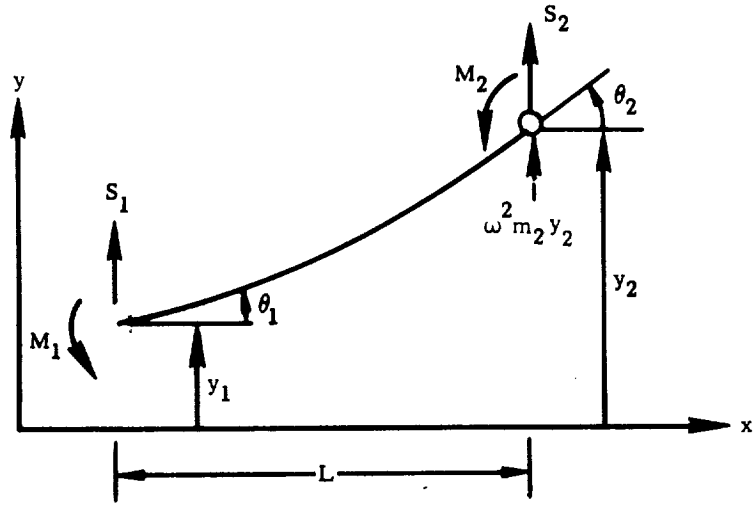

Fig. 2.25. Free-Body Diagram of Vibrating Beam Segment

The quantities C_{11}, C_{12}, C_{21}, and C_{22} are the flexibility influence coefficients of Eq. 2.14. If the left end of the beam segment is the end of the total beam, two of the four variables at that end can be determined from the end conditions for a free end. M_1 is zero and S_1 is equal to the inertia force $m_1 \omega^2 y_1$. Of the two remaining conditions, one is assigned a value of unity and analysis is carried out in terms of the other. For the free end, y_1 is assigned a unity value (making $S_1 = m_1 \omega^2$). The four variables at point two may be evaluated as:

$$y_2 = 1 + m_1 \omega^2 C_{11} + L\theta_1$$

$$\theta_2 = \theta_1 + m_1 \omega^2 C_{21}$$

$$M_2 = m_1 \omega^2 L$$

$$S_2 = m_1 \omega^2 - m_2 \omega^2 \left[1 + m_1 \omega^2 C_{11} + L\theta_1\right]$$

If an arbitrary value for ω is assigned, each of the four variables at point two reduces to an expression involving a constant and a coefficient times θ_1.

The variables at the next point on the beam may be expressed in terms of those just obtained by using Eq. 2.122 and will also be in linear terms of θ_1. The evaluations may thus be propagated across the beam, with the ultimate result that the four variables at the far end of the beam are expressed as linear functions of θ_1.

From the end conditions at this point, the values of two of these variables will be known. One of these known quantities is used to evaluate θ_1, which is then substituted into the expression for the second known variable. For the correct value of ω^2, the expression will produce the known value; otherwise, an error term or residual will be obtained. Several trial values of ω^2 are made, repeating the propagation process each time. If the resultant residuals are plotted against ω^2, the extraction of the proper values of ω^2 is facilitated by extrapolation of the curve. The natural frequencies occur where the curve crosses the axis. Higher frequencies are obtained independently, thus are independent of any inaccuracies which may exist in calculated lower modes.

2.3.1.3 Energy Methods. Lord Rayleigh's method of evaluating the fundamental frequency of a system is based on the principle of conservation of energy. At the maximum deformation of the system vibrating in this fundamental frequency, all the energy of the system is in a potential energy form $\left(PE = \frac{1}{2}\int EI\left(\frac{d^2y}{dx^2}\right)^2 dx\right)$. But at the instant the system passes through the equilibrium position, its energy is entirely in kinetic form ($KE = \frac{1}{2}\int m\dot{y}^2\, dx$). If energy is conserved, the maximums of those two values may be equated. A deflection shape is assumed and for harmonic motion, $y = U \sin \omega t$, and hence,

$$\dot{y} = \omega U \cos \omega t$$

$$\frac{1}{2}\int EI \left(\frac{d^2 U}{d x^2}\right)^2 dx = \frac{1}{2}\int m U^2 \omega^2 d x \tag{2.123}$$

and thus

$$\omega^2 = \frac{\int EI \left(\frac{d^2 U}{d x^2}\right)^2 d x}{\int m U^2 d x} \tag{2.124}$$

It can be shown that close approximations to the fundamental frequency are obtained even if the assumed deflection shape is not very close to the true shape.

The Rayleigh method was generalized by Ritz to give more accurate values for the frequencies as well as to give estimates for several mode frequencies at one time. Basically, Ritz suggested that the assumed deflection curve be expressed as the sum of several functions in the form

$$y = \Sigma f_n (x) \xi_n \tag{2.125}$$

The more functions and constants introduced the more accurate the value of the fundamental frequency. Also, if n functions are introduced then estimates on the first n mode frequencies will be obtained. Having expressed the assumed deflection curve in terms of n functions f (x), the kinetic and potential energies (omitting shear and moments of inertia) are expressed as

$$2\,KE = \int m (x) \dot{y}^2 (x, t) dx \tag{2.126}$$

$$2\,PE = \int EI (x) \left(\frac{d^2 y}{d x^2}\right)^2 dx \tag{2.127}$$

Substituting Eq. 2.125 into Eqs 2.126 and 2.127,

$$2\,KE = \sum_{i=1}^{n} \sum_{j=1}^{n} m_{ij} \dot{\xi}_i \dot{\xi}_j \tag{2.128}$$

$$2\,PE = \sum_{i=1}^{n} \sum_{j=1}^{n} K_{ij} \xi_i \xi_j \tag{2.129}$$

where

$$m_{ij} = \int m \left[f_i(x)\right]\left[f_j(x)\right] dx$$

and

$$K_{ij} = \int EI \frac{d^2}{dx^2}\left[f_i(x)\right] \frac{d^2}{dx^2}\left[f_j(x)\right] dx$$

Substituting Eqs 2.128 and 2.129 into Lagrange's equation gives the differential equation,

$$\sum_{j=1}^{n} m_{ij} \ddot{\xi}_i + \sum_{j=1}^{n} K_{ij} \xi_i = 0 \qquad (2.130)$$

Putting as a solution, $\xi_j = \bar{\xi} \sin \omega t$,

$$\sum_{j=1}^{n} \left(K_{ij} - \omega^2 m_{ij}\right) \bar{\xi}_j = 0 \qquad (2.131)$$

or a set of algebraic equations equal in number to the number of unknown coefficients. The determinental equation for the set will yield frequencies for the first n modes of vibration and eigenvectors which when multiplied by the assumed functions give approximate mode shapes.

The result gives good accuracy in frequency but poor agreement with mode shape. Using the mode shape obtained as a second approximation improves frequency accuracy and greatly improves mode shape.

Also, expressing the strain energy in terms of inertial loading rather than the assumed deflections increases the flexibility of this method in that shear deformation and moments of inertia are then easily included.

2.3.1.4 Jacobi and Givens Method. The Jacobi method solves Eq. 2.112 by diagonalizing the dynamic matrix, [D], by means of orthogonal transformations. The new diagonals contain the eigenvalues, and the orthogonal transformations used in diagonalization contain the eigenvectors. Bodewig (Ref. 2.27) explains the method as follows. First, it is assumed the matrix is symmetric. Eq. 2.112 can be expressed in the form,

$$[D]\{u\} = \{V\}$$

u is subjected to the orthogonal transformation [A] and

$$\{u\} = [A]\{w\}$$

Then, to preserve symmetry, the system is multiplied by $[A]'$.

$$[A]'[D][A]\{w\} = [A]'\{v\}$$

Making the substitutions

$$[B] = [A]'[D][A]$$

$$\{x\} = [A]'\{v\}$$

then

$$[B]\{v\} = \{x\}$$

To eliminate the coefficients d_{12} and d_{21} (the first off-diagonal terms of [D]) put

$$[A] = \left[\begin{array}{c|c} T & \\ \hline & I \end{array}\right]$$

where [T] is a two-rowed orthogonal transformation. By choosing

$$[T] = \begin{bmatrix} \cos\alpha & \sin\alpha \\ \sin\alpha & -\cos\alpha \end{bmatrix}$$

one also gets $[T]' = [T]$ and $[A]' = [A]$.

Then

$$[B] = \left[\begin{array}{c|c} T & \\ \hline & I \end{array}\right] \quad [D] \quad \left[\begin{array}{c|c} T & \\ \hline & I \end{array}\right]$$

or, when in [D] a top left corner matrix $[D_2]$ of order 2 is detached,

$$[D] = \begin{bmatrix} D_2 & E \\ E' & C \end{bmatrix}$$

with $[C] = [C]'$. But then

$$[B] = \begin{bmatrix} TD_2T & TE \\ E'T & C \end{bmatrix} = [B]'$$

Thus [B] differs from [A] only in the first two rows and columns and

$$b_{11} = d_{11}\cos^2\alpha + d_{12}\sin 2\alpha + d_{22}\sin^2\alpha$$

$$b_{12} = (d_{11} - d_{22})\sin\alpha\cos\alpha - d_{12}(\cos^2\alpha - \sin^2\alpha) = b_{21}$$

$$b_{22} = d_{11}\sin^2\alpha - d_{12}\sin^2 2\alpha + d_{22}\cos^2\alpha$$

Now, for α arbitrary,

$$b_{11} + b_{22} = d_{11} + d_{22}$$

and $b_{12} = 0$ if

$$\frac{1}{2}\tan 2\alpha = \frac{d_{12}}{d_{11} - d_{22}}$$

Then

$$b_{11} = \frac{1}{2}(d_{11} + d_{12}) + \sqrt{F}$$

$$b_{22} = \frac{1}{2}(d_{11} + d_{22}) - \sqrt{F}$$

where

$$F = \left(\frac{d_{11} - d_{22}}{2}\right)^2 + d_{12}^2$$

The sign of $\sqrt{F}$ depends on the quadrant of 2α and follows from

$$\sqrt{F} = \frac{d_{11} - d_{22}}{2 \cos 2\alpha} = \frac{d_{12}}{\sin 2\alpha}$$

The above procedure has altered the first two rows and columns. The procedure is repeated on succeeding pairs of rows and columns for the entire matrix. The matrix is operated on in this manner until it is sufficiently diagonalized.

Jacobi worked out his method originally to speed up convergence of iteration problems. It was later that its usefulness in eigenvalue problems was realized. Bodewig expounds in more detail on the application of Jacobi's method to eigenvalue problems and its usefulness.

The Givens method has the general form of Jacobi's method, i.e., making off-diagonal terms small compared to diagonal terms by means of orthogonal transformations. Givens uses a transformation that makes all off-diagonal terms except the upper and lower parallel of the diagonal equal to zero. Solutions for eigenvalues and eigenvectors are then effected. Bodewig (Ref. 2.27, p. 336-340) gives details of the Givens method.

2.3.2 MODAL QUANTITIES. Solutions to the characteristic equations give either the squares or the reciprocals of the squares of the circular frequencies and also the mode shapes of the restrained system. The linear frequencies of vibration are obtained from the circular frequencies. If each mode shape $\{\Phi\}_n$ is considered to be the nth column of a matrix $[\Phi]$ of all the mode shapes, then $[\Phi]' [M] [\Phi]$ is an orthogonality check of the mode shapes. The diagonal element $\left([\Phi]' [M] [\Phi]\right)_{nn}$ is called the generalized mass of the system for mode n. In this discussion the vector $\{\Phi\}$ was stated to be the mode shape of the structural system. For a restrained system, $\{\Phi\}$ is relative to the restrained point(s) and is, therefore, the final mode shape. For a free-free system, $\{\Phi\}$ is relative to the temporarily restrained point (which has translation, y_o, and rotation, θ_o); hence the effect of y_o and θ_o must be included to obtain the final mode shape.

The slope of a node of a beam as computed by the foregoing is the slope due to beam bending, i.e., the slope of the elastic axis. To obtain the total slope, the shearing slope of the beam must be added to the slope due to beam bending. This is done by defining

$$\{\sigma\} = \{\theta\} + \{\gamma\} \tag{2.132}$$

where

$$\{\gamma\} = [C_s] \{F\}$$

Having obtained the modal response, the vehicle response (i.e., displacement, acceleration, force, moment, etc.) can be calculated. The two steps, obtaining modal response and then vehicle response, will be discussed separately.

2.4.1 MODAL RESPONSE. While Eq. 2.135 is easily written the actual numeric solution is often more difficult to obtain. If the forcing function is a simple analytical function the solution is easier; however, the forcing function is often presented to the analyst in graphical form and probably requires an elaborate analytical function which may be unwieldy. Three methods of obtaining a solution will be discussed. While these are not necessarily the only methods, they are the most widely used today.

2.4.1.1 Numeric Integration. The most common method of solving Eq. 2.135 is to simply mechanize it on either a digital or analog computer. Standard numeric integration techniques are employed when using the digital computer. As an example, the Adams four-point formula will be shown. The integration interval is defined as Δt and a subscript n is equal to $t/\Delta t$. The Adams four-point formula is

$$\xi_{n+1} = \xi_n + \frac{\Delta t}{24}\left[55\dot{\xi}_n - 59\dot{\xi}_{n-1} + 37\dot{\xi}_{n-2} - 9\dot{\xi}_{n-3}\right] \tag{2.136}$$

$\dot{\xi}_{n+1}$ is obtained by the same equation. Eq. 2.135 is then used to obtain $\ddot{\xi}_{n+1}$. However, Eq. 2.136 cannot be used until n=4. This necessitates special starting formulas. At n=1, three approximations to ξ_1 and $\dot{\xi}_1$ are made. After each approximation, $\ddot{\xi}_1$ is obtained by Eq. 2.135. The first approximation is

$$\xi_1^{(1)} = \xi_o + \Delta t\,\dot{\xi}_o$$

$$\dot{\xi}_1^{(1)} = \dot{\xi}_o + \Delta t\,\ddot{\xi}_o$$

The second approximation is

$$\xi_1^{(2)} = \xi_o + \frac{\Delta t}{2}\left(\dot{\xi}_1^{(1)} + \dot{\xi}_o\right)$$

$$\dot{\xi}_1^{(2)} = \dot{\xi}_o + \frac{\Delta t}{2}\left(\ddot{\xi}_1^{(1)} + \ddot{\xi}_o\right)$$

The third approximation is

$$\xi_1^{(3)} = \xi_o + \frac{\Delta t}{6}\left[2\dot{\xi}_1^{(2)} + \dot{\xi}_1^{(1)} + 3\dot{\xi}_o\right]$$

$\{\sigma\}$ = total slopes of a beam element

$\{\theta\}$ = bending slopes of a beam element

$\{\gamma\}$ = shearing slopes of a beam element

$\{F\}$ = internal forces on a beam element

$[C_S]$ = shear flexibility matrix

The matrix $[C_S]$ is a diagonal matrix whose elements are 1/KAG at the nodes of a beam element.

The various load quantities (shear, bending moment, torque, force) associated with each mode are often required in dynamic loads analyses. The generalized forces of a restrained system are obtained from either Eq. 2.22 or Eq. 2.26, depending upon whether or not there are any zero generalized force boundary conditions. Another approach for obtaining the generalized forces is to represent these forces in terms of the inertial loading under vibration.

$$\{F\}_n = -\omega_n^2 [M] \{\Phi\}_n \tag{2.133}$$

Either Eq. 2.22, 2.26, or 2.133 is used to define the generalized forces. The load quantities are then obtained by classical summation methods.

Another approach for derivation of load quantities considers each stiffness element (beam or spring) individually. In this approach the load quantities are obtained by multiplying the stiffness matrix of the element by the relative translation and/or rotation between the ends of the element. For example, the shear and bending moment of a beam element are

$$\begin{Bmatrix} S \\ \hline M \end{Bmatrix} = [K] \begin{Bmatrix} \Delta y \\ \Delta\theta \end{Bmatrix} \tag{2.134}$$

where $[K]$ = stiffness matrix

Δy = relative translation between the two ends

$\Delta\theta$ = relative rotation between the two ends

For a free-free system the same approaches are employed; however, the mode shape must be the final mode shape.

2.4 RESPONSE TO TIME-VARYING FORCES

The determination of the response of a launch vehicle to a time-varying force first requires the solving of Eq. 2.7, which, with damping included, becomes

$$\ddot{\xi}_n + 2\zeta_n \omega_n \dot{\xi}_n + \omega_n^2 \xi_n = \mathfrak{M}_n^{-1} Q_n(t) \tag{2.135}$$

$$\dot{\xi}_1^{(3)} = \dot{\xi}_o + \frac{\Delta t}{6}\left[2\,\ddot{\xi}_1^{(2)} + \ddot{\xi}_1^{(1)} + 3\,\ddot{\xi}_o\right]$$

At n=2, two approximations are used. The first approximation is

$$\xi_2^{(1)} = \xi_1^{(3)} + \frac{\Delta t}{2}\left[3\,\dot{\xi}_1^{(3)} - \dot{\xi}_o\right]$$

$$\dot{\xi}_2^{(1)} = \dot{\xi}_1^{(3)} + \frac{\Delta t}{2}\left[3\,\ddot{\xi}_1^{(3)} - \ddot{\xi}_o\right]$$

The second approximation is

$$\xi_2^{(2)} = \xi_1^{(3)} + \frac{\Delta t}{12}\left[5\,\dot{\xi}_2^{(1)} + 8\,\dot{\xi}_1^{(3)} - \dot{\xi}_o\right]$$

$$\dot{\xi}_2^{(2)} = \dot{\xi}_1^{(3)} + \frac{\Delta t}{12}\left[5\,\ddot{\xi}_2^{(1)} + 8\,\ddot{\xi}_1^{(3)} - \ddot{\xi}_o\right]$$

At n=3, two approximations are used. The first approximation is

$$\xi_3^{(1)} = \xi_2^{(2)} + \frac{\Delta t}{12}\left[23\,\dot{\xi}_2^{(2)} - 16\,\dot{\xi}_1^{(3)} + 5\,\dot{\xi}_o\right]$$

$$\dot{\xi}_3^{(1)} = \dot{\xi}_2^{(2)} + \frac{\Delta t}{12}\left[23\,\ddot{\xi}_2^{(2)} - 16\,\ddot{\xi}_1^{(3)} + 5\,\ddot{\xi}_o\right]$$

The second approximation is

$$\xi_3^{(2)} = \xi_2^{(2)} + \frac{\Delta t}{24}\left[9\,\dot{\xi}_2^{(1)} + 19\,\dot{\xi}_2^{(2)} - 5\,\dot{\xi}_1^{(3)} + \dot{\xi}_o\right]$$

$$\dot{\xi}_3^{(2)} = \dot{\xi}_2^{(2)} + \frac{\Delta t}{24}\left[9\,\ddot{\xi}_3^{(1)} + 19\,\ddot{\xi}_2^{(2)} - 5\,\ddot{\xi}_1^{(3)} + \ddot{\xi}_o\right]$$

From n=4 on, Eq. 2.136 is used.

The Adams method is one of many available for numeric solution. The various methods have specific as well as general application. Before incorporating a method, stability and accuracy of that method must be examined for the particular application.

2.4.1.2 Laplace Transforms. The Laplace transformation can be used to obtain a mathematical solution. This assumes that the forcing function can be expressed analytically and that the required transforms exist. Rigorous treatment of the Laplace

transformation is given in many textbooks. Refs 2.29 and 2.30 derive and discuss Laplace transforms at length.

The Laplace transformation associates with a given function F(t) a second function f(s) according to the relation

$$f(s) = L\{F(t)\} = \int_0^\infty e^{-st} F(t)\, dt \tag{2.137}$$

The inverse transformation is

$$F(t) = L^{-1}\{f(s)\} \tag{2.138}$$

and simply means that F(t) is a function whose Laplace transform is f(s). A property of the Laplace transformation which contributes greatly to its success in handling differential equations is that the transform of the derivative can be expressed in terms of the transform of the function itself, i.e.,

$$L\{F'(t)\} = s\, L\{F(t)\} - F(0) \tag{2.139}$$

$$L\{F''(t)\} = s^2\, L\{F(t)\} - s\, F(0) - F'(0)$$

An example will now be worked out using Laplace transforms. The system shown in Fig. 2.26 will be used and F(t) as shown in Fig. 2.27. The differential equation is

$$M\ddot{x}(t) + K x(t) = F(t)$$

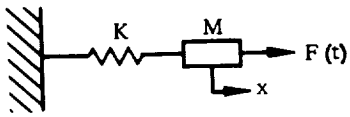

Fig. 2.26. Spring Mass System

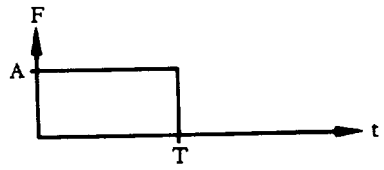

Fig. 2.27. Force Time History

If the initial conditions are $x(0) = 0$ and $\dot{x}(0) = 0$ the equation in the transform x(s) is

$$M s^2 x(s) + Kx(s) = f(s) \tag{2.140}$$

where f(s) is the transform of F(t). The natural frequency is ω and $K = M\omega^2$ so it can be written

$$x(s) = \frac{f(s)}{M(s^2 + \omega^2)} \tag{2.141}$$

Considering the time period $0 \leq t \leq T$ then

$$f(s) = \frac{A}{s}$$

and

$$x(s) = \frac{A}{Ms(s^2 + \omega^2)}$$

Now

$$L^{-1}\left\{\frac{1}{s(s^2 + \omega^2)}\right\} = \frac{1}{\omega^2}(1 - \cos \omega t)$$

and it follows that

$$x(t) = \frac{A}{K}(1 - \cos \omega t) \tag{2.142}$$

If the response for the time period $t > T$ is desired the solution with nonzero initial conditions is needed. With the initial conditions of $x(T)$ and $\dot{x}(T)$ Eq. 2.140 becomes

$$M\left[s^2 x(s) - s\,x(t) - \dot{x}(T)\right] + K\,x(s) = f(s)$$

and Eq. 2.141 becomes

$$x(s) = x(T)\left(\frac{s}{s^2 + \omega^2}\right) + \dot{x}(T)\left(\frac{1}{s^2 + \omega^2}\right) + \frac{f(s)}{M}\left(\frac{1}{s^2 + \omega^2}\right)$$

However, $f(s) = 0$ so the inverse transform is

$$x(t) = x(T)\cos \omega(t - T) + \frac{\dot{x}(T)}{\omega}\sin \omega(t - T)$$

and from Eq. 2.142,

$$x(T) = \frac{2A}{K} \sin^2 \frac{\omega T}{2}$$

$$\dot{x}(T) = \frac{\omega A}{K} \sin \omega T$$

An advantage of this type of solution is that the numeric solution for any time t can be made without first making numeric solutions at other times. The main disadvantage is that, as the forcing function becomes more difficult to express analytically, the mathematics becomes increasingly complicated. Also, more terms appear in the solution which increases the numeric solution time.

2.4.1.3 Duhamel's Integral. It is shown in Ref. 2.31, p. 11, that a solution to Eq. 2.135 is

$$\xi(T) = e^{-\zeta T}\left[\xi(0) \cos \bar{\omega} T + \frac{1}{\bar{\omega}}\left(\dot{\xi}(0) + \zeta \xi(0)\right) \sin \bar{\omega} T\right]$$

$$+ \frac{1}{\bar{\omega}} \int_0^T \frac{1}{m} Q(t)\, e^{-\zeta(T-t)} \sin \bar{\omega}(T-t)\, dt \qquad (2.143)$$

where

$$\bar{\omega}^2 = \omega^2 - \zeta^2$$

The integral in this equation is known in mathematic literature as Duhamel's integral and represents a particular solution of Eq. 2.135. Since terms in brackets in Eq. 2.143 represent the solution for the free vibrations due to initial displacement and/or velocity, it is clear that the Duhamel integral represents that portion of the motion resulting from externally applied force. The problem remains, of course, of performing the integration. For simple forcing functions, closed form solutions may be easily obtained. However, when the forcing function is not easily described analytically, the analyst usually resorts to numeric or graphic techniques.

To illustrate the use of Duhamel's integral the problem previously solved by Laplace transforms in Section 2.4.1.2 will be used. Again referring to Fig. 2.26 and, assuming zero initial conditions and zero damping, the solution is

$$x(T) = \frac{1}{\omega} \int_0^T \frac{A}{M} \sin \omega(T - t)\, dt$$

Expanding the sine function

$$x(T) = \frac{A}{M\omega} \int_0^T (\sin \omega T \cos \omega t - \cos \omega T \sin \omega t)\, dt$$

Evaluating the integral and simplifying,

$$x(T) = \frac{A}{K} (1 - \cos \omega T)$$

This checks with the solution obtained by using Laplace transforms.

2.4.2 VEHICLE RESPONSE. In the design and stress analysis of launch vehicles certain loads are required. In addition, the displacements of certain parts of the structure are needed. The loads usually required (where applicable) are acceleration, bending moment, shear, torque and force. These are calculated using mode displacement or mode acceleration methods, modal quantities, and modal response. Some loads, such as aerodynamic loads, increase due to displacement. This amplification of applied loads is discussed in detail in Section 5 and is not considered here.

2.4.2.1 Mode Displacement Method. The deflection of a structure under load is the summation of the deflection of each of its normal modes. Similarly, the loading or stress in the structure is the summation of the load or stress in each of its normal modes. Thus

$$y_i = \sum_{n=1}^{k} \phi_{in} \xi_n$$

$$M_i = \sum_{n=1}^{k} M_{in} \xi_n \qquad (2.144)$$

$$S_i = \sum_{n=1}^{k} S_{in} \xi_n$$

In this method the rigid body loads and vibratory loads are obtained as a function of the normal mode displacement. The advantages of the mode displacement method are: 1) ability to handle steady-state and elastic response loads for redundant structures, and 2) simplicity of computation. The first advantage is readily apparent after examination of the mode acceleration method for redundant structures. The mode displacement method can handle redundant structures as easily as nonredundant structures. The second advantage is seen by Eq. 2.144. Once the modal moments and shears have been calculated (a one-time operation) the computations are quite simple. The disadvantage of the modal displacement method is a determination

of accuracy. Theoretically, all the modes are required to obtain correct shears and moments. However, the summations of Eq. 2.144 are actually summations of series of which only the lower (frequency) modes significantly affect the total. The problem is, then, to determine the number of terms (modes) needed for accurate results. This is usually determined by trial and error.

2.4.2.2 Mode Acceleration Method. An alternate method of determining loads would be separate calculation of the rigid body and vibratory loads. In this method the vehicle is first treated as a rigid structure and shears and moments are determined from the applied forces, external and inertial, on the vehicle in equilibrium. The vibratory loads are then obtained from the inertial loads due to the acceleration of the modes. The total loads would be

$$M_i = M_{RB_i} - \sum_{n=1}^{k} \frac{M_{in}}{\omega_n^2} \ddot{\xi}_n$$

$$S_i = S_{RB_i} - \sum_{n=1}^{k} \frac{S_{in}}{\omega_n^2} \ddot{\xi}_n \qquad (2.145)$$

The advantage of the mode acceleration method is high accuracy with few modes. In this method the loads due to the rigid body response are calculated separately from elastic response; hence their contribution (which is highly significant) is explicit. However, in the mode displacement method the loads due to rigid body response are implicit in the loads due to elastic mode response. Since the load contribution of each mode is much less for the mode acceleration method, far fewer modes are needed for accurate results. The disadvantage of the mode acceleration method is the additional computation required to obtain the rigid body loads, particularly with redundant structures. However, with present day computer capability this is not a serious problem. The desirable feature of convergence with a small number of modes is often of more importance than the computation time required for the rigid body loads.

2.5 RESPONSE TO TIME-VARYING FORCES WITH A CONTROL SYSTEM INCLUDED

The previous section discussed the response to time-varying forces for the case where no attempt was made to control the vehicle as it responded. The solution will now be expanded to show the inclusion of a control system.

2.5.1 GENERAL SOLUTION. The control system for a launch vehicle (typically referred to as the autopilot) usually controls the vehicle attitude with respect to some frame of reference. While the position in space is all-important, other means (guidance) are used to determine where the vehicle is and the proper maneuver to correct

the position. This results in commands to the autopilot to alter the vehicle attitude and thus (assuming powered flight) to change its position in space. The autopilot must also maintain the desired attitude and correct any errors due to external or internal disturbances. Thus the autopilot has two functions: 1) to maintain vehicle stability and attitude, and 2) perform the steering maneuvers prescribed by guidance.

The autopilot is usually described in block diagram form. The vehicle attitude with respect to some axis is defined as θ, the control system coordinate as δ, and the guidance command as θ_c. The general form of the autopilot is shown in Fig. 2.28. The solution for the forced vibration response as given by Eq. 2.135 is expanded to include the control system. In matrix form this is

$$\begin{Bmatrix} \ddot{\xi} \\ \ddot{\delta} \end{Bmatrix} + \left[\begin{array}{c|c} & \\ \hline & \end{array}\right] \begin{Bmatrix} \dot{\xi} \\ \dot{\delta} \end{Bmatrix} + \left[\begin{array}{c|c} & \\ \hline & \end{array}\right] \begin{Bmatrix} \xi \\ \delta \end{Bmatrix} = \left[\begin{array}{c|c} m & \\ \hline & \end{array}\right]^{-1} \begin{Bmatrix} Q(t) \\ 0 \end{Bmatrix} \tag{2.146}$$

The upper left partitions are the coefficients of the equations for vehicle dynamics. The upper right partitions represent the effect of the control system upon the vehicle and the lower left partitions represent the vehicle input to the control system. The lower right partitions are the coefficients of the control system dynamic equations. While the discussion has been about a fairly specific situation, i.e., launch vehicle with autopilot and in powered flight, Fig. 2.28 and Eq. 2.146 are general forms applicable to any situation of a vehicle with a control system. Once Eq. 2.146 is set up the solution proceeds as discussed in Section 2.4.

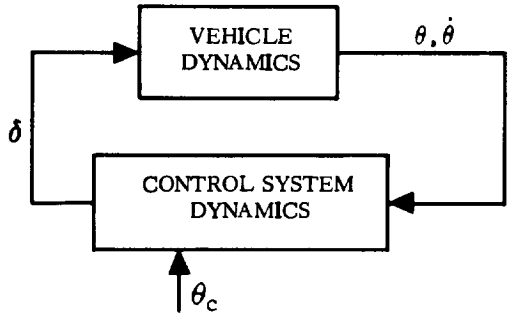

Fig. 2.28. General Autopilot Block Diagram

2.5.2 EXAMPLE SOLUTION. To illustrate the above solution the case of a launch vehicle subjected to a gust will now be solved. A schematic of the vehicle model is shown in Fig. 2.29.

2.5.2.1 Derivation of Equations of Motion. The dynamic response is obtained by the superposition of the rigid body and elastic responses. Use is made of rotating Eulerian axes which coincide with the axes of the vehicle at any instant. Figure 2.30 shows the position of the axes at times t and $t + \Delta t$. A time-slice analysis is used, i.e., mass and trajectory parameters are considered constant.

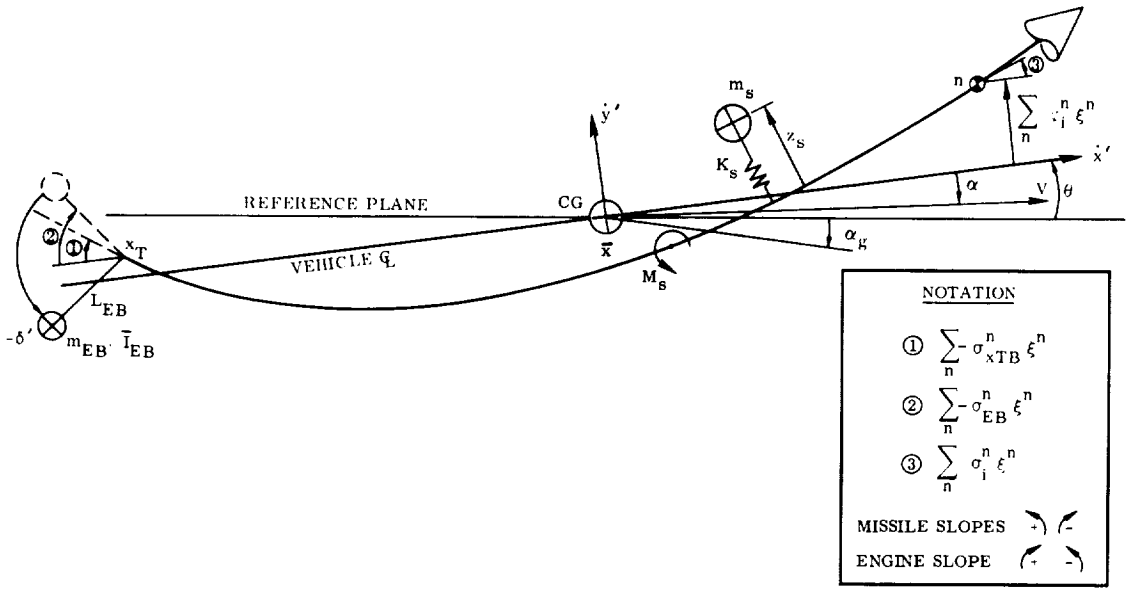

Fig. 2.29. Gust Response Vehicle Model

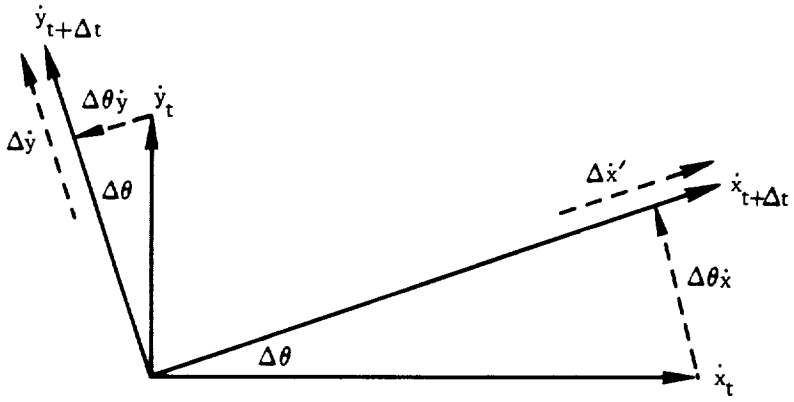

Fig. 2.30. Rotating Eulerian Axes

$$\Sigma F_x = m a_x = m\frac{\Delta \dot{x}}{\Delta t} = \lim_{\Delta t \to 0}\left[\frac{\Delta \dot{x}' - \Delta\theta \dot{y}}{\Delta t}\right] m = [\ddot{x}' + \dot{\theta}\dot{y}]m \approx \ddot{x}' m$$

$$\Sigma F_y = m a_y = m\frac{\Delta \dot{y}}{\Delta t} = \lim_{\Delta t \to 0}\left[\frac{\Delta \dot{y}'}{\Delta t} + \frac{\Delta\theta \dot{x}}{\Delta t}\right] m = [\ddot{y}' + \dot{\theta}\dot{x}]\, m$$

$$\Sigma M = \lim_{\Delta t \to 0} \frac{\Delta \dot{\theta}}{\Delta t} I = \ddot{\theta} I \qquad (2.147)$$

In matrix form, the elastic motion of the vehicle is

$$M\ddot{U} + K U = F(x,t) \tag{2.148}$$

By substituting the transformation $U = \Phi\xi$ into Eq. 2.148 and pre-multiplying by the transpose of Φ, we have

$$\Phi' M \Phi \ddot{\xi} + \Phi' K \Phi \xi = \Phi' F(x,t) \text{ or}$$

$$\ddot{\xi} + [\Phi' M \Phi]^{-1} [\Phi' K \Phi] \xi = [\Phi' M \Phi]^{-1} \Phi F(x,t) \tag{2.149}$$

It can be shown that $[\Phi' M \Phi]^{-1} [\Phi' K \Phi] = \omega^2$, the natural frequencies (diagonal matrix) and $[\Phi' M \Phi] = \mathfrak{M}$, the generalized masses (diagonal matrix) of the system. With these substitutions and the addition of damping, Eq. 2.149 becomes

$$\ddot{\xi} + 2\zeta\omega\dot{\xi} + \omega^2 \xi = \mathfrak{M}^{-1} \Phi' F(x,t) \tag{2.150}$$

2.5.2.2 Derivation of Force Equations. The forces acting on the system are:

a. Aerodynamic forces.

b. Engine thrust forces.

c. Engine inertia due to engine gimballing.

d. Sloshing forces and moments.

e. Engine hydraulic actuator force.

f. Engine gimbal friction.

The following is a derivation of the generalized forces. These generalized forces are derived from work principles. The derivation of these forces is done in indicial notation, rather than matrix notation, because it is easier to show the derivation of the terms from each source of energy. The work done by the aerodynamic forces (see Fig. 2.31) is

$$dW = \sum_i dy_i (A.L.)_i$$

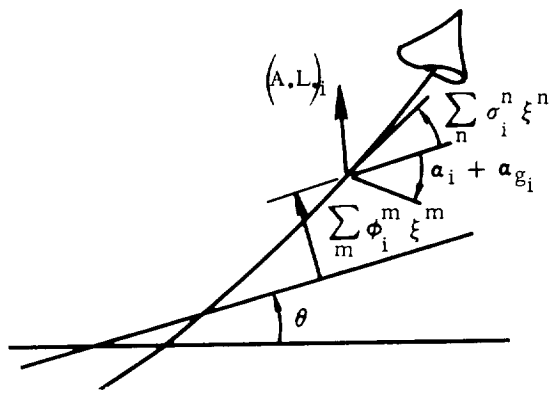

Fig. 2.31. Aerodynamic Forces

$$dW = qS_R \sum_i d\left[y' + (x_i - \bar{x})\,\theta + \sum_m \phi_i^m \xi^m\right] \times \left[\left(C_{N/\alpha}\right)_i \left(\alpha_i + \alpha_{g_i} + \sum_n \sigma_i^n \xi^n\right)\right] \tag{2.151}$$

where $\bar{x}$ is the center of gravity on the x axis. The generalized forces are:

$$\left.\begin{aligned} \frac{dW}{dy'} &= qS_R \sum_i \left[\left(C_{N/\alpha}\right)_i \left(\alpha_i + \alpha_{g_i} + \sum_n \sigma_i^n \xi^n\right)\right] \\ \frac{dW}{d\theta} &= qS_R \sum_i \left\{x_i - \bar{x}\right\} \left[C_{N/\alpha}\left(\alpha_i + \alpha_{g_i} + \sum_n \sigma_i^n \xi^n\right)\right] \\ \frac{dW}{d\xi^m} &= q\,S_R \sum_i \phi_i^m \left[C_{N/\alpha}\left(\alpha_i + \alpha_{g_i} + \sum_n \sigma_i^n \xi^n\right)\right] \end{aligned}\right\} \tag{2.152}$$

where

$$\alpha_i = -\left[\frac{\dot{y}'}{V} + \frac{\left(x_i - \bar{x}\right)}{V}\,\dot{\theta} + \frac{\sum_n \phi_i^n \dot{\xi}^n}{V}\right]$$

The work done by the thrust force of the booster engines (see Fig. 2.32) is

$$dW = F_B\,dy = T_B\left[\sum_n \sigma_{EB}^n \xi^n - \delta_B'\right] d\left[y' + \left(x_T - \bar{x}\right)\theta + \sum_m \phi_{xT}^m \xi^m\right] \tag{2.153}$$

The generalized forces are

$$\left.\begin{aligned} \frac{dW}{dy'} &= T_B\left[\sum_n \sigma_{EB}^n \xi^n - \delta_B'\right] \\ \frac{dW}{d\theta} &= T_B\left[\sum_n \sigma_{EB}^n \xi^n - \delta_B'\right]\left(x_T - \bar{x}\right) \\ \frac{dW}{d\xi^m} &= T_B\left[\sum_n \sigma_{EB}^n \xi^n - \delta_B'\right]\phi_{xT}^m \end{aligned}\right\} \tag{2.154}$$

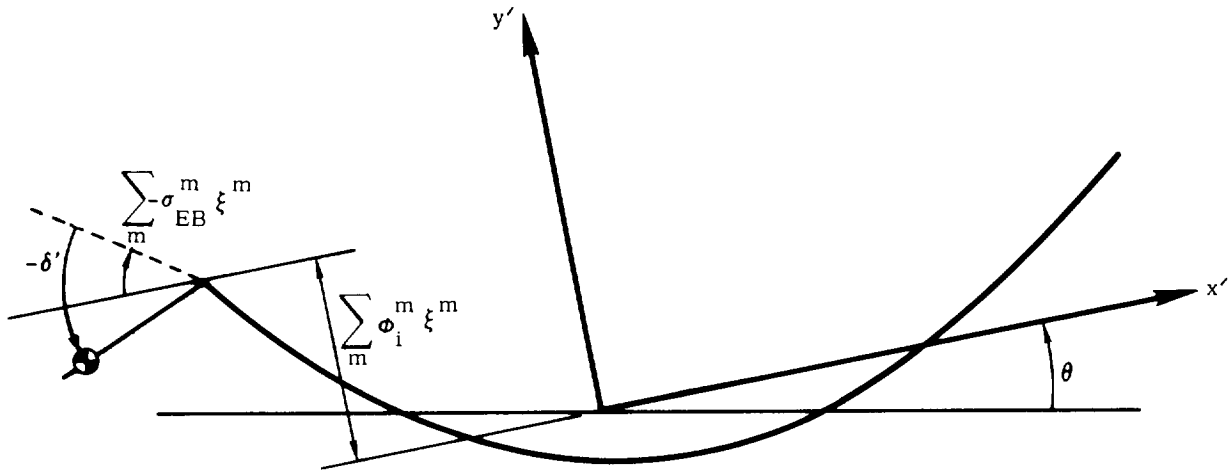

Fig. 2.32. Engine Thrust Forces

For the generalized forces due to the sustainer engine, substitute subscript S for B in the above equations. Since the sustainer engine is not gimballed, $\delta'_S = 0$.

For purposes of autopilot control, the motion of the engine is comprised of two functions. The first, $\sum_n \sigma_{EB}^n \xi^n$, represents the motion of the engine associated with the modes of vibration when the control system is locked. The other, δ', represents the gimballing control with respect to these modes. For analysis, the system is assumed to have a perfect actuator and is later compensated for its structural elasticity, bypass orifice characteristics, etc. The work done by engine inertia is

$$dW = -m_{EB}\left[(\ddot{y}' + V\dot{\theta}) + \left(x_{EB} - \bar{x}\right)\ddot{\theta} + \sum_n \phi_{EB}^n \ddot{\xi}^n + L_{EB}\ddot{\delta}'\right]$$
$$\times d\left[y' + \left(x_{EB} - \bar{x}\right)\theta + \sum_m \phi_{EB}^m \xi^m + L_{EB}\delta'\right]$$
$$- \bar{I}_{EB}\left[\ddot{\theta} + \sum_n \sigma_{EB}^n \ddot{\xi}^n - \ddot{\delta}'\right] d\left[\theta + \sum_m \sigma_{EB}^m \xi^m - \delta'\right]$$

$$\frac{dW}{d\xi^m} = -m_{EB}\left[(\ddot{y}' + V\dot{\theta}) + \left(x_{EB} - \bar{x}\right)\ddot{\theta} + \sum_n \phi_{EB}^n \ddot{\xi}^n + L_{EB}\ddot{\delta}'\right]\phi_{EB}^m$$
$$- \bar{I}_{EB}\left[\ddot{\theta} + \sum_n \sigma_{EB}^n \ddot{\xi}^n - \ddot{\delta}'\right]\sigma_{EB}^m \qquad (2.155)$$

All the terms except $\ddot{\delta}'$ can be placed on the left side of the equations and according to the orthogonality principle, the $n \neq m$ terms will cancel and the $n = m$ terms will become part of the generalized mass. This generalized force then becomes

$$\left.\begin{aligned}
\frac{dW}{d\xi^m} &= \left[\bar{I}_{EB}\,\sigma^m_{EB} - m_{EB}\,L_{EB}\,\phi^m_{EB}\right]\ddot{\delta}' \\
\frac{dW}{d\delta'} &= -m_{EB}\,L_{EB}\left[(\ddot{y}' + V\dot{\theta}) + (x_{EB} - \bar{x})\,\ddot{\theta} + \sum_n \phi^n_{EB}\,\ddot{\xi}^n + L_{EB}\,\ddot{\delta}'\right] \\
&\quad + \bar{I}_{EB}\left[\ddot{\theta} + \sum_n \sigma^n_{EB}\,\ddot{\xi}^n - \ddot{\delta}'\right]
\end{aligned}\right\} \quad (2.156)$$

Moving the $\ddot{\delta}'$ terms to the left side of the equation results in

$$I_R\,\ddot{\delta}' + \cdots = -m_{EB}\,L_{EB}\left[(\ddot{y}' + V\dot{\theta}) + (x_{EB} - \bar{x})\,\ddot{\theta} + \sum_n \phi^n_{EB}\,\ddot{\xi}^n\right] + \bar{I}_{EB}\left[\ddot{\theta} + \sum_n \sigma^n_{EB}\,\ddot{\xi}^n\right] \quad (2.157)$$

where

$$I_R = \left[\bar{I}_{EB} + m_{EB}\,L^2_{EB}\right]$$

Although the actuator is described by a linear equation in this program, the system is nonlinear. Linearization of the $\dot{\delta}'$, δ', and δ_c coefficients is discussed in Section 2.5.2.3.

The sloshing analogy used is the spring-mass analogy. The slosh loads consist of a lateral force applied at the spring attach point, and a moment applied at the equivalent tank bottom (Fig. 2.33).

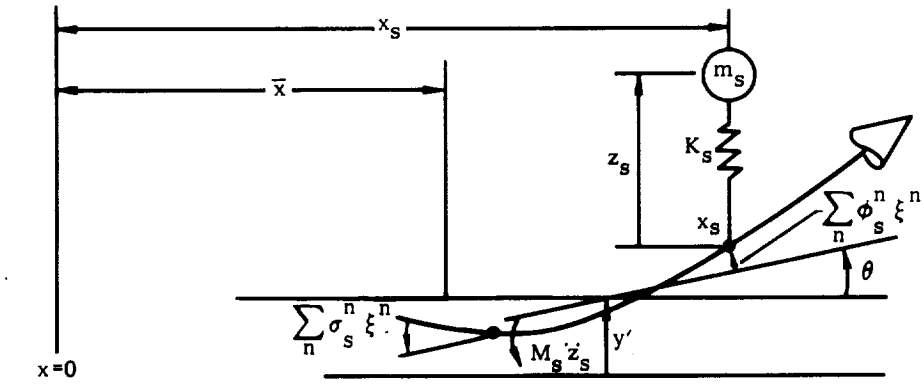

Fig. 2.33. Slosh Loads

The work done by the slosh forces is

$$
\left.
\begin{aligned}
dW &= \sum_s F_s \, dy_s \\
&= \sum_s K_s z_s \, d\left[\sum_m \phi_s^m \xi^m + y' + (x_s - \bar{x})\,\theta\right] \\
\frac{dW}{d\xi^m} &= \sum_s K_s z_s \phi_s^m \\
\frac{dW}{d\theta} &= \sum_s K_s z_s (x_s - \bar{x}) \\
\frac{dW}{dy'} &= \sum_s K_s z_s
\end{aligned}
\right\} \qquad (2.158)
$$

The work done by the slosh moments is

$$
\left.
\begin{aligned}
dW &= \sum_s \left[\ddot{\bar{x}}\, m_s z_s + M_s \ddot{z}_s\right] d\left[\sum_m \sigma_s^m \xi^m + \theta\right] \\
\frac{dW}{d\xi^m} &= \sum_s \left[\ddot{\bar{x}}\, m_s z_s + M_s \ddot{z}_s\right] \sigma_s^m \\
\frac{dW}{d\theta} &= \sum_s \left[\ddot{\bar{x}}\, m_s z_s + M_s \ddot{z}_s\right]
\end{aligned}
\right\} \qquad (2.159)
$$

The pressure P_L developed by the actuator times the actuator piston area supplies the force to gimbal the engine. The work done on the engine (see Fig. 2.34) is

$$
\left.
\begin{aligned}
dW &= (P_L\, AR)\, d\delta' \\
\frac{dW}{d\delta'} &= P_L\, AR \\
\frac{dW}{d\xi^m} &= \frac{dW}{d\theta} = \frac{dW}{dy'} = 0
\end{aligned}
\right\} (2.160)
$$

because δ' is measured relative to the vehicle.

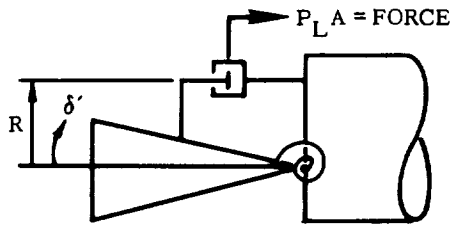

Fig. 2.34. Engine and Actuator Model

Gimbal friction results from the relative velocity between the engine and vehicle. The relative motion (Fig. 2.35) is

$$\left[\sum_n \left(\sigma^n_{EB} - \sigma^n_{xT}\right)\dot{\xi}^n - \dot{\delta}^n\right]$$

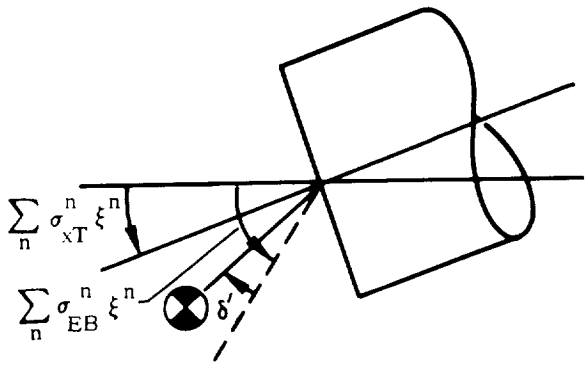

Fig. 2.35. Engine Displacement

The work done is

$$\begin{aligned} dW &= -\bar{C}_F\,\dot{\theta}_{EB}\,d\theta_{EB} \\ &= -\bar{C}_F\left[\sum_n \left(\sigma^n_{EB} - \sigma^n_{xT}\right)\dot{\xi}^n - \dot{\delta}'\right] \\ &\quad \times d\left[\sum_m \left(\sigma^m_{EB} - \sigma^m_{xT}\right)\xi^m - \delta'\right] \end{aligned} \qquad (2.161)$$

The generalized forces are

$$\left.\begin{aligned} \frac{dW}{d\delta'} &= \bar{C}_F\left[\sum_n \left(\sigma^n_{EB} - \sigma^n_{xT}\right)\dot{\xi}^n - \dot{\delta}'\right] \\ \frac{dW}{d\xi^m} &= -\bar{C}_F\left[\sum_n \left(\sigma^n_{EB} - \sigma^n_{xT}\right)\dot{\xi}^n - \dot{\delta}'\right]\left(\sigma^m_{EB} - \sigma^m_{xT}\right) \end{aligned}\right\} \qquad (2.162)$$

2.5.2.3 Derivation of Autopilot Equations. The autopilot system consists of a forward loop, an engine actuator, and a feedback loop. The forward loop contains a simple lead/lag filter, a quadratic lag filter, an integral path, and a proportional path. The engine actuator is represented by a linear second order system. The feedback loop employs a displacement gyro and a second order rate gyro.

The differential equations from the block diagram, Fig. 2.36, are

a. Rate gyro, θ_G

$$\ddot{\theta}_G + 2\zeta_G\,\omega_G\,\dot{\theta}_G + \omega^2_G\,\theta_G = K_R\,\omega^2_G\left[\dot{\theta} + \sum_n \sigma^n_G\,\dot{\xi}^n\right]$$

b. Position gyro, θ_D

$$\theta_D = \theta + \sum_n \sigma^n_D\,\xi^n$$

c. Error signal, θ_ϵ

$$\theta_\epsilon = \theta_G + \theta_D$$

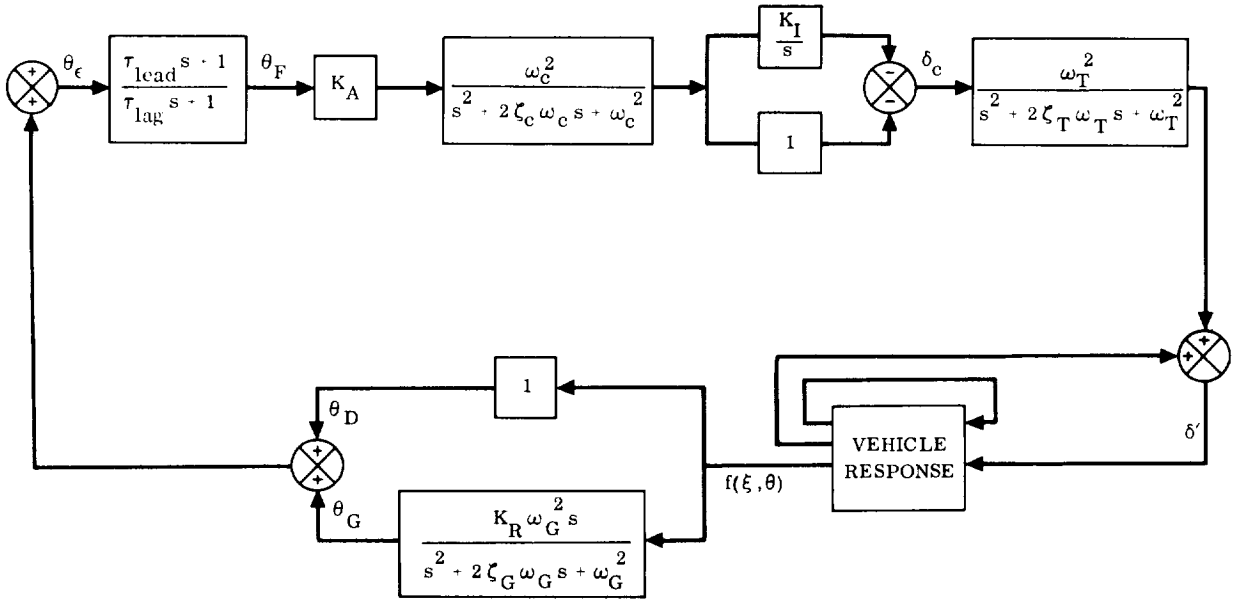

Fig. 2.36. Autopilot Block Diagram

d. Feedback signal, θ_F

$$\tau_{lead}\,\dot{\theta}_\epsilon + \theta_\epsilon = \tau_{lag}\,\dot{\theta}_F + \theta_F$$

e. Engine actuator command signal, δ_c

$$\ddot{\delta}_c + 2\zeta_c\,\omega_c\,\dot{\delta}_c + \omega_c^2\,\delta_c = -K_A\left[\omega_c^2\,\theta_F + K_I\,\omega_c^2 \int \theta_F\,dt\right]$$

f. Engine actuator response, δ'. The engine actuator equation for engines-in-the-modes model is

$$\ddot{\delta}' + 2\,\zeta_T\,\omega_T\,\dot{\delta}' + \omega_T^2\,\delta' = \omega_T^2\,\delta_c - \omega_T^2\,K_E \sum_n \left(\sigma_{xTB}^n - \sigma_{EB}^n\right)\xi^n$$

$$-\frac{\bar{C}_F}{I_R}\sum_n\left(\sigma_{xTB}^n - \sigma_{EB}^n\right)\dot{\xi}^n - \frac{1}{I_R}\sum_n\left(m_{EB}\,L_{EB}\,\phi_{EB}^n - \bar{I}_{EB}\,\sigma_{EB}^n\right)\ddot{\xi}^n$$

$$-\frac{L_{EB}\,m_{EB}}{I_R}\left(\ddot{y}' + V\dot{\theta}\right) - \frac{1}{I_R}\left[m_{EB}\,L_{EB}\left(\bar{x} - \bar{x}_{EB}\right) - \bar{I}_{EB}\right]\ddot{\theta} \qquad (2.163)$$

where

$$K_E = \frac{K_D}{K_D + K_H}$$

$$2\zeta_T \omega_T = \frac{57.3\,\bar{C}_F}{I_R} + \omega_N^2$$

$$\omega_N^2 = \frac{(AR)^2 \sqrt{\bar{P}_L}}{1.11\, I_R\, \bar{C}_L}$$

$$\omega_T = \sqrt{K_C\, \omega_N^2}$$

$$\zeta_T = \frac{2\zeta_T\, \omega_T}{2\omega_T}$$

Since the above terms are frequency and amplitude dependent, they have been linearized to the frequency of the gust, i.e., $\bar{\omega} = 2\pi/\tau_{gust}$, and to a large engine amplitude, say $\bar{\delta} = 1.0$ degree. $\bar{C}_F$ and $\bar{P}_L$ are calculated as follows:

$$\bar{C}_F = C_V + \frac{4\,C_B}{\pi\,\bar{\omega}\,\bar{\delta}} = C_V + \frac{2\,C_B\,\tau_{gust}}{\pi^2\,\bar{\delta}}$$

$$\bar{P}_L = \bar{C}_F\, \frac{2\pi\,\bar{\delta}}{AR\,\tau_{gust}} \qquad (2.164)$$

2.5.2.4 Complete Equations. The complete equations, assembled from Sections 2.5.2.1, 2.5.2.2, and 2.5.2.3, are given by Eq. 2.165. These can be put in the form of Eq. 2.146 and solved. The forcing function in this case is the angle of attack induced by the gust, α_g.

m^{th} Elastic Mode

$$\ddot{\xi}^m + 2\zeta_m \omega_m \dot{\xi}^m + \omega_m^2 \xi^m = \frac{1}{m_m}\Bigg\{ T_{EB}\, \phi^m_{xTB}\left[\sum_n \sigma^n_{EB}\, \xi^n - \delta'\right] + T_{ES}\, \phi^m_{xTS}\left[\sum_n \sigma^n_{ES}\, \xi^n\right] - \left[m_{EB}\, L_{EB}\, \phi^m_{EB} - \bar{I}_{EB}\, \sigma^m_{EB}\right] \ddot{\delta}' + qS_R \sum_i \left[\left(C_{N/\alpha}\right)_i \phi^m_i \left(\alpha_i + \alpha_{g_i} + \sum_n \sigma^n_i \xi^n\right)\right] + \sum_s \left[\left[\ddot{\bar{x}}\, m_s\, z_s + M_s\, \ddot{z}_s\right] \sigma^m_s\right] + \sum_s \phi^m_s \quad K_s\, z_s + \bar{C}_F \left(\sigma^m_{EB} - \sigma^m_{xTB}\right)\left[\dot{\delta}' - \sum_n \sigma^n_{EB} - \sigma^n_{xTB}\, \dot{\xi}^n\right]\Bigg\}$$

Rotation

$$\ddot{\theta} = \frac{1}{I}\Bigg\{ T_B\left[\sum_n \sigma^n_{EB}\, \xi^n - \delta'\right]\left[x_{TB} - \bar{x}\right] + T_S\left[\sum_n \sigma^n_{ES}\, \xi^n\right]\left[x_{TS} - \bar{x}\right] - \left[m_{EB}\, L_{EB}\left(x_{EB} - \bar{x}\right) - I_{EB}\right] \ddot{\delta}' + qS_R \sum_i \left[\left(C_{N/\alpha}\right)_i \left(\alpha_i + \alpha_{g_i} + \sum_n \sigma^n_i \xi^n\right)\left(x_i - \bar{x}\right)\right] + \sum_s \left[\ddot{\bar{x}}\, m_s\, z_s + M_s\, \ddot{z}_s\right] + \sum_s \left[\left(x_s - \bar{x}\right) K_s\, z_s\right]\Bigg\} \qquad (2.165)$$

Translation

$$\left[\ddot{y}' + V\dot{\theta}\right] = \frac{1}{M_T}\Bigg\{ T_B\left[\sum_n \sigma^n_{EB}\, \xi^n - \delta'\right] + T_S\left[\sum_n \sigma^n_{ES}\, \xi^n\right] - m_{EB}\, L_{EB}\, \ddot{\delta}' + qS_R \sum_i \left[\left(C_{N/\alpha}\right)_i \left(\alpha_i + \alpha_{g_i} + \sum_n \sigma^n_i \xi^n\right)\right] + \sum_s K_s\, z_s\Bigg\}$$

Sloshing

$$\ddot{z}_s + 2\zeta_s\, \omega_s\, \dot{z}_s + \omega_s^2\, z_s = -\left[\left(\ddot{y}' + V\dot{\theta}\right) + \left(x_s - \bar{x}\right)\ddot{\theta} + \sum_n \phi^n_s\, \ddot{\xi}^n\right]$$

Engine Output

$$\ddot{\delta}' + 2\zeta_T \omega_T \dot{\delta}' + \omega_T^2 \delta' = \omega_T^2 \delta_c - \omega_T^2 K_E \left[\sum_n \left(\sigma_{xTB}^n - \sigma_{EB}^n \right) \xi^n \right]$$

$$- \frac{\bar{C}_F}{I_R} \left[\sum_n \left(\sigma_{xTB}^n - \sigma_{EB}^n \right) \dot{\xi}^n \right] - \frac{1}{I_R} \left[\sum_n \left(m_{EB} L_{EB} \phi_{EB}^n - \bar{I}_{EB} \sigma_{EB}^n \right) \ddot{\xi}^n \right.$$

$$\left. + m_{EB} L_{EB} (\ddot{y}' + V\dot{\theta}) + \left[m_{EB} L_{EB} \left(x_{EB} - \bar{x} \right) - \bar{I}_{EB} \right] \ddot{\theta} \right]$$

Engine Command

$$\ddot{\delta}_c + 2\zeta_c \omega_c \dot{\delta}_c + \omega_c^2 \delta_c = K_A \left\{ \omega_c^2 \theta_F + K_I \omega_c^2 \int \theta_F \, dt \right\}$$

(2.165 Contd)

Rate Gyro

$$\ddot{\theta}_G + 2\zeta_G \omega_G \dot{\theta}_G + \omega_G^2 \theta_G = K_R \omega_G^2 \left[\dot{\theta} + \sum_n \sigma_G^n \dot{\xi}^n \right]$$

Position Gyro

$$\theta_D = \theta + \sum_n \sigma_D^n \xi^n$$

2.6 RANDOM RESPONSE

The analysis presented here is from the field of endeavor referred to as generalized harmonic analysis. This subject is treated in many texts and articles. Crandall (Ref. 2.32) gives a comprehensive bibliography of the material published prior to 1959. Refs 2.33 through 2.38 are a partial list of the more recent material. Lee (Ref. 2.33) gives a complete discussion of the general theory of harmonic analysis. The monograph by Crandall and Mark (Ref. 2.34) covers the subject as applied to mechanical systems. The subject is also often covered in texts or handbooks on control and/or servomechanisms.

The fundamental difference between deterministic analyses and those involving random variables is that instantaneous values are no longer meaningful. When a system is being excited by randomly varying forces, it follows that its response will also vary in a random manner. Consequently, a statistical description of the excitation is required in which expected values of response replace the usual instantaneous time values. The analysis is quite complicated in its general form. As a result, certain assumptions are made which, although not strictly true, are required to permit analysis.

These assumptions are that the excitation is an ergodic process and that its amplitude has a normal or Gaussian distribution. The first assumption merely states that the time average of the excitation is equal to the statistical average and dependent only upon where it is measured. The second assumption of normal distribution is one often made to aid in interpreting the results and as a requirement for application of some statistical techniques. A brief review of the analysis follows; the reader is directed to various references for proofs and derivations.

Consider a random process described by the time function $u_k(t)$, where the subscript k is used to denote one experiment in a large number of identical experiments of the same random process. The statistical or "ensemble average" is defined as

$$\overline{u(t_1)} = \frac{1}{N} \sum_{k=1}^{N} u_k(t_1) \tag{2.166}$$

which is also called the mean. The $u_k(t_1)$ is the value of the k^{th} ensemble member at an arbitrary time t_1. The amplitude probability density of u may also be determined at time t_1. If the amplitude probability density of the ensemble is independent of time t_1, then the process is said to be stationary.

More often than not, the data available for analysis consist of a few samples, rather than a large number, and the ensemble average is not meaningful. The averaging may be carried out in time in this case, rather than across the small ensemble. The time, or temporal, average of an ensemble member is

$$\overline{u_k(t)} = \lim_{T \to \infty} \frac{1}{2T} \int_{t_o - T}^{t_o + T} u_k(t)\, dt \tag{2.167}$$

If the process is stationary, then $\overline{u_k(t)}$ is independent of t_o. If the amplitude probability density of the ensemble member is the same as that of the ensemble, then the process is also said to be ergodic and $\overline{u_k(t_1)} = \overline{u_k(t)}$. Thus, an ergodic process is, by definition, stationary, but a stationary process is not necessarily ergodic. It can be seen that by making the ergodic assumption the analysis can be performed over the ensemble or over an ensemble member with equal validity. It will be understood that the remainder of the discussion covers only ergodic random processes.

A statistical quantity of considerable importance is known as the autocorrelation function and is defined as

$$\psi_{kk}(\tau) = \lim_{T \to \infty} \frac{1}{2T} \int_{-T}^{T} u_k(t)\, u_k(t+\tau)\, dt \tag{2.168}$$

which represents multiplying the value of the function at a time t by its value at a time τ later, integrating the result, and averaging. It can be seen that the autocorrelation function is independent of t and is a function of the time lag τ only. For zero lag time, Eq. 2.169 reduces to the mean-square value,

$$\psi_{kk}(0) = \overline{u_k^2(t)} = \underset{T \to \infty}{\text{limit}} \frac{1}{2T} \int_{-T}^{T} u_k^2(t)\, dt \tag{2.169}$$

Another useful quantity related to the correlation function by means of the Fourier Transform is the power density spectrum, defined as

$$\Phi_{kk}(\omega) = \frac{1}{2\pi} \int_{-\infty}^{\infty} \psi_{kk}(\tau)\, e^{-i\omega\tau}\, d\tau \tag{2.170}$$

and the inverse relationship,

$$\psi_{kk}(\tau) = \int_{-\infty}^{\infty} \Phi_{kk}(\omega)\, e^{i\omega\tau}\, d\omega \tag{2.171}$$

This relationship is known as the Wiener Theorem of autocorrelation, or Wiener-Khinchin Theorem (see Ref. 2.33, Chapter 2). If we now set $\tau = 0$, Eq. 2.171 becomes

$$\psi_{kk}(0) = \overline{u_k^2(t)} = \int_{-\infty}^{\infty} \Phi_{kk}(\omega)\, d\omega \tag{2.172}$$

or the mean-square value.

A useful relationship, proved in Ref. 2.32 (p. 333), between the response and excitation power spectra for any linear system is

$$\Phi_{kk}^{out}(\omega) = \bar{H}_k(\omega)\, H_k(\omega)\, \Phi_{kk}^{in}(\omega) \tag{2.173}$$

or

$$\Phi_{kk}^{out}(\omega) = |H_{kk}(\omega)|^2 \Phi_{kk}^{in}(\omega)$$

where $H(\omega)$ is the complex frequency response and $\bar{H}(\omega)$ is the conjugate. $H(\omega)$ is a general expression for the relationship between input and output and must be defined in detail for specific cases. For example, the displacement response spectrum of a linear single-degree-of-freedom system to an ergodic random force spectrum is (Ref. 2.34, p. 73 - 75)

$$\Phi^{out}(\omega) = \frac{\Phi^{in}(\omega)}{m^2\left[\left(\omega_n^2 - \omega^2\right)^2 + 4\zeta^2\omega_n^2\omega^2\right]} \tag{2.174}$$

where ω_n is the system's natural frequency, m its mass, and ζ the damping ratio. It is easily seen that the denominator is the absolute value of the square of the complex impedance, $Z(\omega)$, and that

$$|H(\omega)|^2 = \frac{1}{|Z(\omega)|^2} \tag{2.175}$$

The general case for the response of a multidegree-of-freedom system is discussed next.

It is now necessary to consider another property of the excitation, the continuity of its distribution in space. If the random force $f(x, t)$ can be separated such that $F(x, t) = g(x)\, f(t)$, then the field is homogeneous. This means that when there is a change in force at x_i, there is a simultaneous proportional change at x_j. This is analogous to the stationary property in time. If the spatial distribution is not determinable, then the field is inhomogeneous and its is necessary to determine the statistical relation of happenings between all points on the system under consideration.

The required statistical properties for inhomogeneous fields are the crosscorrelations and cross-power density spectra. The crosscorrelation function $\psi_{ij}(\tau)$ between a random process occurring at point i in space and a different random process occurring at point j in space is defined as

$$\psi_{ij}(\tau) = \lim_{T\to\infty} \frac{1}{2T}\int_{-T}^{T} u_i(t)\, u_j(t+\tau)\, dt \tag{2.176}$$

which represents taking the value of the function at point i at time t, multiplying by the value of the function at point j at a time τ later, integrating the result, and averaging. Applying the Wiener-Khinchin Theorem,

$$\Phi_{ij}(\omega) = \frac{1}{2\pi}\int_{-\infty}^{\infty} \psi_{ij}(\tau)\, e^{-i\omega\tau}\, d\tau \tag{2.177}$$

The cross-power density spectrum ($i \neq j$) is, in general, a complex quantity, of which the real part is referred to as the co-spectrum and the imaginary part is called the quadrature spectrum. The inverse transform relations between the crosscorrelation and cross-power spectra are

$$\Phi_{ij}(\omega) = \frac{1}{2\pi}\int_{-\infty}^{\infty} \psi_{ij}(\tau)\, e^{-i\omega\tau}\, d\tau \tag{2.178}$$

$$\psi_{ij}(\tau) = \int_{-\infty}^{\infty} \Phi_{ij}(\omega)\, e^{i\omega\tau}\, d\omega \tag{2.179}$$

Taking all combinations of ij for the system under study, a matrix of cross-power density spectra can be formed. This matrix, $[\Phi_{ij}]$, is of a Hermitian form which contains real terms (power spectra) on the diagonal and complex terms (cross-power spectra) on the off diagonals. It can be shown (Ref. 2.33, p. 74) that

$$\psi_{ij}(\tau) = \psi_{ji}(-\tau) \tag{2.180}$$

so that from Eq. 2.179,

$$\Phi_{ji}(\omega) = \Phi^{*}_{ij}(\omega) \tag{2.181}$$

where the asterisk indicates the conjugate transpose of $\Phi_{ij}(\omega)$. Consequently, the matrix $[\Phi_{ij}]$ is symmetric in the real parts and skew symmetric in the imaginary parts. Eq. 2.173 is now written in the more general form,

$$\Phi^{out}_{ij}(\omega) = H_i(\omega)\Phi^{in}_{ij}(\omega)\,\bar{H}_j(\omega) \tag{2.182}$$

which gives the response spectrum at point i due to an excitation at point j. It is obvious that the cross-power density spectrum of the response must be derived for all points in the system.

Botman (Ref. 2.36) has derived the integral and matrix forms for the response of a mechanical system to an inhomogeneous field. Since the integral form is only applicable to systems for which all $\Phi_{ij}(\omega)$ are known analytically, and this is not the usual case, only the matrix form is presented here.

Assuming that the excitation is homogeneous in the interval $x_i - \epsilon$ to $x_i + \epsilon$, the response power spectra matrix for a lumped parameter system is given by

$$\left[\Phi^{out}_{ij}(\omega)\right] = \left[\frac{1}{Z_n}\right]\left[\gamma_{ni}\right]\left[\Phi^{in}_{ij}(\omega)\right]\left[\gamma_{jm}\right]\left[\frac{1}{Z_m}\right] \tag{2.183}$$

The Z_n and Z_m are the complex impedance and transpose, and the γ_{ni} and γ_{jm} are the mode participation factors, given by

$$\gamma_{ni} = \int_{\frac{x_i - x_{i-1}}{2}}^{\frac{x_{i+1} - x_i}{2}} \phi_n(x)\, dx$$

(2.184)

$$\gamma_{jm} = \int_{\frac{x_j - x_{j-1}}{2}}^{\frac{x_{j+1} - x_j}{2}} \phi_m(x)\, dx$$

where the $\phi(x)$ are the normalized mode shapes.

By equating

$$\left[H_{jm}(\omega)\right] = \left[\gamma_{jm}\right]\left[\frac{1}{Z_m}\right]$$

Eq. 2.183 is rewritten as

$$\left[\Phi_{ij}^{out}(\omega)\right] = \left[\bar{H}_{ni}(\omega)\right]\left[\Phi_{ij}^{in}(\omega)\right]\left[H_{jm}(\omega)\right] \qquad (2.185)$$

This equation is the matrix extension of the simple relation (Eq. 2.173) between the input spectra, the system impedance, and the response spectra.

A representative plot of the response spectrum for point i due to an excitation spectrum at point j is shown in Fig. 2.37.

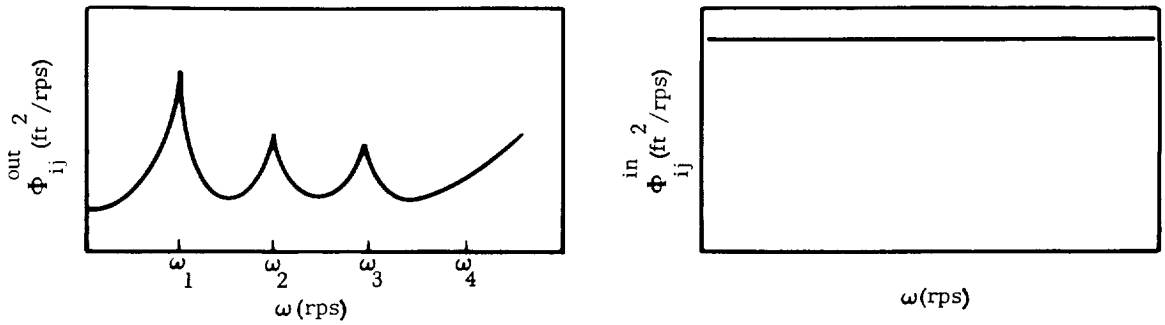

a. Response Spectrum

b. Input Spectrum

Fig. 2.37. Response and Input Spectra

It will be found that the peaks in the response spectrum correspond to system natural frequencies. The quantity

$$\overline{u_{ij}^2(t)} = \int_0^{\omega_n} \Phi_{ij}^{out}(\omega)\, d\omega \tag{2.187}$$

represents the contribution of all frequencies less than ω_n to the mean-square response. By extension, the mean-square response at point i to excitation at all points on the system is

$$\overline{u_i^2(t)} = \sum_j \overline{u_{ij}^2(t)} \tag{2.188}$$

Theoretically the integration would have to be extended to infinity to obtain the mean-square response, but for practical cases the contribution of the power spectrum to the mean-square value becomes negligible at higher frequencies. For lightly damped systems, the energy content of the power spectrum is concentrated mainly about the natural frequencies and falls off sharply to very low magnitudes between them.

The matrix multiplication of Eq. 2.182 is required for a considerable number of frequencies to obtain a smooth curve such as shown in Fig. 2.37 for each point. Consequently, it would probably be best not to use a constant interval for the ω's but rather a small interval near resonant frequencies and a considerably larger one between them.

The above discussion has presented the general form for the solution of mean-square response. In practice, further assumptions are often made which can greatly simplify the solution. Ref. 2.37 contains an excellent example of this. In this case the damping is small so the impedance will undergo a large change near the resonant frequency ω_n; and if the variation in the power density spectrum is of lesser extent in this vicinity, then the mean-square response can be approximated by

$$\overline{u^2(t)} = \frac{\pi}{2\zeta} \sum_n \frac{\Phi^{in}(\omega_n)\, w_n^2\, \phi_n^2}{m_n^2\, \omega_n^3} \tag{2.189}$$

where w_n is the mode participation of the load and is given by

$$w_n = \frac{\int_0^L \Phi^{in}(\omega_n, x_i)\, \phi_n(x_i)\, dx}{\int_0^L \Phi^{in}(\omega_n, x_i)\, dx}$$

It now remains to attach statistical significance to the mean-square response. The assumption of a normal (or Gaussian) probability distribution is quite reasonable for a random function. The normal probability density function is given by

$$f_r(x) = \frac{1}{\sqrt{2\pi}\,\sigma} \exp\left[\frac{-(x-\mu)^2}{2\sigma^2}\right] \quad -\infty < x < \infty \tag{2.190}$$

where r is the random variable, x is the range of the variable, μ is the mean, and σ^2 is the variance. The mean and variance are given by

$$\mu = \overline{x(t)} \tag{2.191}$$

$$\sigma^2 = \overline{x^2(t)} - \overline{x(t)} \tag{2.192}$$

(See Eqs 2.167, 2.168, and 2.188). The cumulative distribution is given by

$$P_r(y) = \int_{-\infty}^{y} \frac{1}{\sqrt{2\pi}\,\sigma} \exp\left[\frac{-(x-\mu)^2}{2\sigma^2}\right] \tag{2.193}$$

which states that the probability of r being equal to or less than y is $P_r(y)$. If the substitution

$$z = \frac{(x-\mu)}{\sigma}$$

is made in Eqs 2.190 and 2.193, the density function and cumulative distributions are normalized, which is the form usually found in tables.

If the excitation has zero mean, then so will the response. In this case, the variance is

$$\sigma_i^2 = \overline{u_i^2(t)}$$

The standard deviation of the response is the square root of the mean-square response, or

$$\sigma_i = \sqrt{\overline{u_i^2(t)}} \tag{2.194}$$

Eqs 2.190 and 2.191 can now be used to establish the response corresponding to the desired probability. For a particular case, data may indicate another probability

distribution to be more applicable. In that event the expressions for the appropriate distribution are used in place of Eqs 2.190 and 2.191. Discussion and information on probability can be found in any handbook or textbook on the subject.

2.7 REFERENCES

2.1 R. H. Scanlan and Robert Rosenbaum, Introduction to the Study of Aircraft Vibration and Flutter, The Macmillian Company, New York, N. Y., 1951.

2.2 N. O. Myklestad, Fundamentals of Vibration Analysis, McGraw-Hill Book Company, New York, N. Y., 1956.

2.3 W. T. Thomson, Mechanical Vibrations, Prentice-Hall, Inc., Englewood Cliffs, N. J., 1953.

2.4 R. A. Bisplinghoff, H. Ashley, and R. L. Halfman, Aeroelasticity, Addison-Wesley Publishing Company, Reading, Mass., 1955.

2.5 F. I. Backus, SLV-3 Bending Stability Analysis of the Atlas/Agena Spring Band Separation Joint, Convair Division Report GD/A-DDE64-054, 17 August 1964.

2.6 D. O. Lomen, Liquid Propellant Sloshing in Mobile Tanks of Arbitrary Shape, NASA CR-222, Marshall Space Flight Center, Huntsville, Alabama, April 1965.

2.7 D. O. Lomen, Digital Analysis of Liquid Propellant Sloshing in Mobile Tanks With Rotational Symmetry, NASA CR-230, Marshall Space Flight Center, Huntsville, Alabama, May 1965.

2.8 J. T. Bergen, Visco-Elasticity Phenomenological Aspects, Academic Press, 1960.

2.9 D. R. Bland, Theory of Linear Viscoelasticity, Pergamon Press, 1960.

2.10 R. K. Gieseke, B. Appleby, and W. Tonelli, General Missile Vibration Program, Convair Division Report GD/A-DDE64-050, 20 August 1964.

2.11 S. Timoshenko and G. L. MacCullough, Elements of Strength of Materials, D. Van Nostrand Company, Inc., Princeton, N. J., 1949.

2.12 R. G. Rose, J. A. Staley, and A. K. Simson, A Study of System-Coupled Longitudinal Instabilities in Liquid Rockets, Part I - Analytic Model, AFRPL-TR-65-163, AFSC, Edwards, California, September 1965.

2.13 L. L. Fontenot and G. Lianis, The Free Vibrations of Thin Elastic Pressurized Cylindrical Shells with a Free and Incompressible Liquid Having a Free Surface, International Symposium on Space Technology and Science, Paper No. 6-6-8, 1963.

2.14 R. G. Rose, Dynamics of the Atlas 5-CPS Longitudinal Oscillation Following Launch as Related to the Tank Pressure Regulation System, Convair Division Report GDA63-0712, Volumes I and II, Contracts AF 04(694)-196 and AF 04 (695)-240.

2.15 S. Timoshenko, Theory of Plates and Shells, McGraw-Hill Book Company, Inc., First Edition, 1940.

2.16 J. D. Wood, Survey on Missile Structural Dynamics, Report 7102-0041-NU-000, Contract No. AF 04(647)-619, 1 June 1961.

2.17 M. J. Turner, R. W. Clough, H. C. Martin, and L. J. Topp, "Stiffness and Deflection Analysis of Complex Structures", Journal of the Aeronautical Sciences, Vol. 23, No. 9, September 1956.

2.18 L. D. Pinson, Longitudinal Spring Constants for Liquid-Propellant Tanks with Ellipsoidal Ends, NASA Technical Note D-2220, November 1964.

2.19 W. H. Gayman and J. A. Garba, Dynamics Loads Analysis of Space Vehicle Systems - Launch and Exit Phase, JPL Technical Memorandum 33-286. (To be published.)

2.20 W. C. Hurty, Dynamic Analysis of Structural Systems by Component Mode Synthesis, TR 32-530, Jet Propulsion Laboratory, Pasadena, California, January 1964.

2.21 R. E. Storey, "Dynamic Analysis of Clustered Boosters with Application to Titan III", AIAA 1963 Summer Meeting, Paper No. 63-208, June 1963.

2.22 Bodley, Ikard, and Schulta, Vibration Analysis Report, Program 624A, Configuration C, Flight Plan VIII, Air Force Report No. SSD-CR-65-1, January 1965.

2.23 I. J. Jaszlics, Program 624A 20%-Scale Dynamic Model Ground Vibration Survey, Final Test Report, Vol. III, SSD-CR-65-47, Martin Company, Denver, Colorado, May 1965.

2.24 J. L. Milner, Three Dimensional Multiple Beam Analysis of a Saturn 1 Vehicle, NASA TM X-53098, July 1964.

2.25 G. Lianis, Matrix Analysis of Vibrations of Clustered Boosters, Convair Division Report AE61-0858, September 1961.

2.26 S. I. Gravitz, "An Analytical Procedure for Orthogonalization of Experimentally Measured Modes", Journal of the Aerospace Sciences, November 1958.

2.27 E. Bodewig, Matrix Calculus, North Holland Publishing Co., Amsterdam, 1959.

2.28 V. N. Faddeeva, Computational Methods of Linear Algebra, Dover Publications, N. Y., 1959.

2.29 R. V. Churchill, Operational Mathematics, McGraw-Hill Book Company, Inc., New York, 1958.

2.30 R. E. Gaskell, Engineering Mathematics, Henry Hold & Co., New York, 1958.

2.31 H. N. Abramson, The Dynamics of Airplanes, The Ronald Press Co., New York, 1958.

2.32 S. H. Crandall, "Random Vibration", Applied Mechanics Reviews, Vol. 12, No. 11, pp. 739 - 742, November 1959.

2.33 Y. W. Lee, Statistical Theory of Communication, John Wiley and Sons, Inc., New York, 1960.

2.34 S. H. Crandall and W. D. Mark, Random Vibration in Mechanical Systems, Academic Press, New York, 1963.

2.35 S. H. Crandall, editor, Random Vibrations, Technology Press of M.I.T., 1958, Vol. II, 1963.

2.36 M. Boteman, "The Response of Linear Systems to Inhomogeneous Random Excitation", AIS Paper No. 61-32, IAS 29th Annual Meeting, New York, January 23 - 25, 1961.

2.37 W. T. Thomson and M. V. Barton, "The Response of Mechanical Systems to Random Excitation", Journal of Applied Mechanics, Vol. 24, pp. 248 - 251, June 1957.

2.38 J. S. Bendat and A. G. Piersol, Measurement and Analysis of Random Data, John Wiley and Sons, Inc., New York, 1965.

2.39 V. L. Alley, Jr. and A. H. Gerringer, A Matrix Method for the Determination of the Natural Vibrations of Free-Free Unsymmetrical Beams With Application to Launch Vehicles, NASA TN D-1247, April 1962.

3/ GROUND WIND INDUCED LOADS

NOMENCLATURE

A	Area	ft^2
C	Damping	$\frac{lb\text{-}sec}{ft}$
C_c	Critical damping	$\frac{lb\text{-}sec}{ft}$
C_{DG}	Aerodynamic drag coefficient for gusts	ND
C_V	Vortex shedding coefficient (see Eq. 3.15)	ND
D	Reference diameter	ft
$D(x)$	Diameter	ft
K	Coefficient, defined in text	adjustable
L	Vehicle length, support to tip	ft
m_n	Generalized mass for the nth natural mode of the vehicle	slugs
m_a	Generalized mass of the fluid media, defined as ρD^3	slugs
$(M'_b)_1$	Modal bending moment of the first natural mode of the model	$\frac{in.\text{-}lb}{ft}$
M_n	Bending moment at model base	$\frac{in.\text{-}lb}{ft}$
$P_r(\ )$	Probability of the statement ( ) being true	N.D.
R_e	Reynolds number, $VD\rho/\mu$	N.D.
S	Strouhal number, fD/V	N.D.
$S_D(f)$	Power density spectrum of the gust velocity in the drag direction	$\frac{(ft/sec)^2}{cps}$
$S_L(f)$	Power density spectrum of the gust velocity in the lift direction	$\frac{(ft/sec)^2}{cps}$
$S_{DL}(f)$	Cross-power density spectrum for the gusts	$\frac{(ft/sec)^2}{cps}$
V	Wind speed	ft/sec

V_e	Uniform wind speed equivalent to a non-uniform profile wind (see Eq. 3.13)	ft/sec
V(h)	Wind profile (see Eq. 3.1)	ft/sec
$\overline{V}$	Mean wind speed	ft/sec
$\overline{V^2}$	Mean-square wind speed (see Eqs 3.9 and 3.11)	$(ft/sec)^2$
V_R	Mean (or average) wind speed at the reference height	ft/sec
W_n	Mode participation of the load for the nth mode $\equiv \dfrac{\int_L \frac{1}{2}\rho V^2(x)\,\phi_n(x)\,D(x)\,dx}{\int_L \frac{1}{2}\rho V^2(x)\,D(x)\,dx}$	N.D.
a	Ratio of the standard deviation of the random drag load to the standard deviation of the random lift load, σ_{DT}/σ_{LT}	N.D.
d	Distance between vortices in the Von Kármán Vortex Street	ft
f	Frequency	cps
h	Height above ground	ft
h_R	Reference height	ft
ℓ	Gust wave length, V_R/f	ft
q	Dynamic pressure	lb/ft^2
u	Displacement	ft
x	Coordinate along neutral axis	ft
$\Phi(f)$	Power density spectra of the square of the gust velocity (see Eqs 3.10 and 3.12)	$(ft/sec)^4/cps$
ϵ_D	Expectation value of the random drag response	ft
ϵ_L	Expectation value of the random lift response	ft

ζ	Damping coefficient	N. D.
λ	Dummy frequency variable	cps
μ	Absolute viscosity	lb-sec/ft^2
ρ	Density	slugs/ft^3
σ_{DG}	Standard deviation of the gust velocity in the drag direction	ft/sec
σ_{LG}	Standard deviation of the gust velocity in the lift direction	ft/sec
σ_{DT}	Standard deviation of the random drag response	ft
σ_{LT}	Standard deviation of the random lift response	ft
$\phi_n(x)$	Normalized displacement of the n^{th} mode	ft/ft
ω	Frequency	rad/sec

SUBSCRIPTS

D	Drag
e	Equivalent
G	Gust
L	Lift
max	Maximum or "3-sigma" value
n	Mode index
R	Reference
S	Steady state
T	Total
V	Vortex shedding
1	First mode

3/ GROUND WIND INDUCED LOADS

3.1 STATEMENT OF THE PROBLEM

Loads imposed on an erected space vehicle in the launch ready condition ordinarily establish the strength requirements for the aft portion of the vehicle and for its supporting structure. Contributors to the total load include such factors was weight, thrust, wind, umbilical line tension, and center-of-gravity offset effects. The determination of most of these loads is straightforward; however, the winds, with their gustiness and vortex shedding effects, require special treatment for response.

The purpose of this section is to discuss the various aspects of the loads induced by ground winds and to present a method of calculating the loads. These loads, when combined into a resultant or total load, may then be employed either for design purposes or for establishing the maximum wind velocity to which the vehicle can be safely exposed.

Fig. 3.1 illustrates the type of vehicle configuration being discussed and the principal factors of the problem. An elastic multistage vehicle is shown on its flexi-

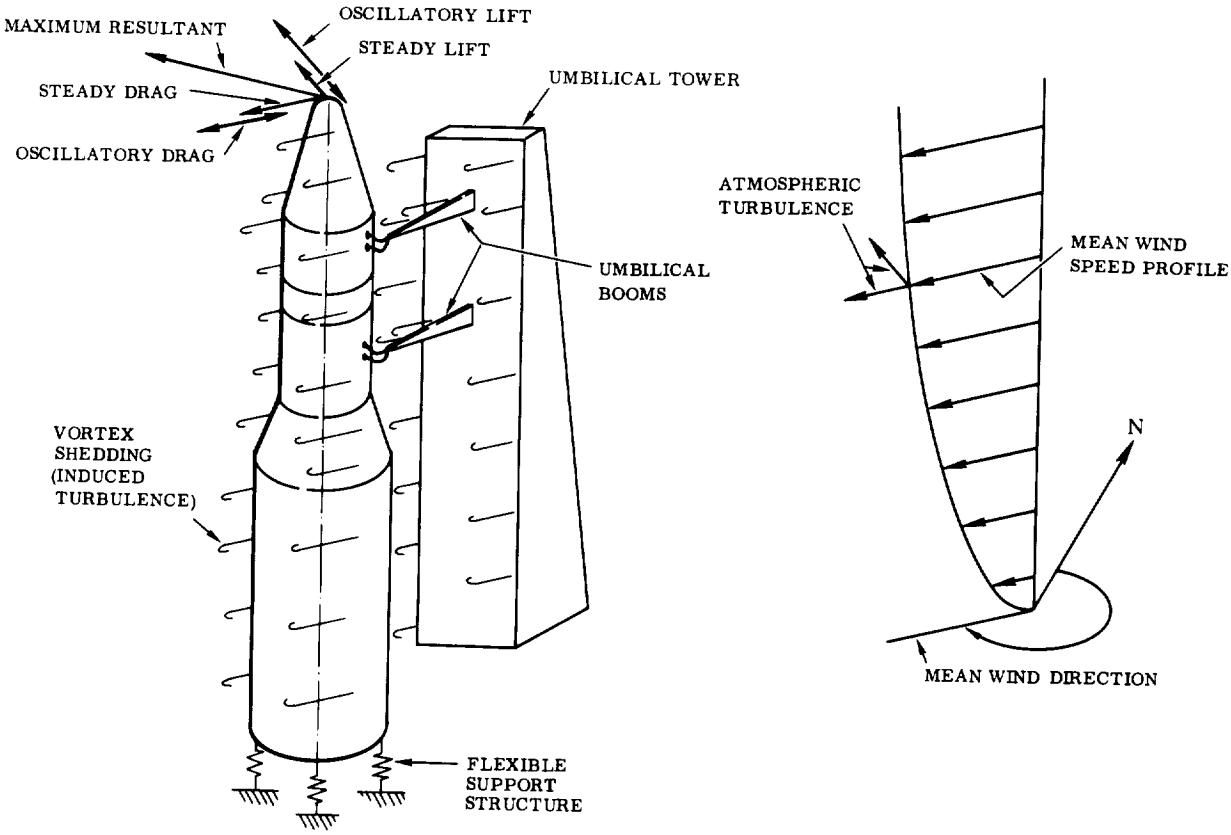

Fig. 3.1. Factors Contributing to Prelaunch Wind Loads

ble support structure, with umbilical lines connected from the umbilical tower. The wind velocity is represented by the profile of the mean wind and its direction azimuth, upon which are superimposed the horizontal components of the random turbulence normal and parallel to the mean wind. Turbulence generated by the flow about the umbilical tower and the vehicle is indicated by vortex shedding. The response of the vehicle to the mean and turbulent components of the wind is composed of a mean (steady) deflection plus oscillatory motion. These deflections can have components parallel and normal to the mean wind direction. The directions parallel and normal to the mean wind are analogous to the drag and lift directions on an aerodynamic surface and hereafter are referred to as such.

It must be pointed out that the discussion and analytical techniques that follow are generally applicable only to those vehicles for which wind tunnel data are available. The effect of nose shape, external piping, and protuberances is such that the vortex shedding may vary by large amounts due to changes which, at first glance, might be considered negligible. For example, it has been shown (Ref. 3.1) that the addition of a single conduit with a diameter of 1/60 of the vehicle diameter can increase the vortex shedding response by a factor of three when the conduit is at the upstream stagnation point on the lower stage. It is apparent that small protuberances cannot be ignored, especially if they are on the forward end. While the current state of the art does not provide for analytical prediction of the effect of changes in nose shape or protuberances, wind tunnel data provide for a qualitative evaluation of relative severity of configurations.

3.2 HISTORICAL BACKGROUND

The method of treating ground wind induced loads has followed a somewhat devious route in its development to its current state. Methods have varied from consideration of only steady drag to treatments using multipoint random pressure input. While civil engineers have been concerned for years with the effect of wind on an elastic body, especially since the collapse of the Tacoma Narrows Bridge, this effect was not fully investigated for missiles until Goldman's investigation for the Vanguard (Ref. 3.2). Since that time, wind tunnel tests have been a part of the development program of nearly all launch vehicles.

Following identification of the vortex shedding problem during the Vanguard tests, several programs were initiated to obtain useful data. These included the literature survey by Midwest Research Institue (Ref. 3.3), which effectively summarized the literature published prior to 1958; the two dimensional cylinder tests of Fung (Ref. 3.4); the work of Roshko (Ref. 3.5); and a rather comprehensive test program at the NASA Ames Research Center 12-Foot Pressure Tunnel.

Publication of Fung's work in 1960 led to several approaches for predicting the vortex shedding loads on existing vehicles. One of the most prevalent approaches was

to use Fung's two-dimensional data (either directly or slightly modified) assuming a correlation coefficient of unity; i.e., it was assumed that the fluctuating pressures were equal in magnitude and phase along the entire length of the vehicle. The root-mean-square (RMS) response of the vehicle to Fung's power spectrum was calculated using the method outlined in Section 2.6. This RMS response, multiplied by an appropriate value to give the desired probability of occurence, was then added vectorially to the steady-state drag.

Later tests of scale and generalized models, such as those of Buell (Refs 3.6 and 3.7), Ezra (Ref. 3.8), Gaffney (Ref. 3.9), et al., have done much to shed light on a complex phenomenon. While these tests have not given too much insight into the mechanism of the phenomenon, they have identified configurations and factors which either require further study or which should be avoided in vehicle design. It has, for example, been repeatedly demonstrated that small changes in configuration (e.g., either addition or deletion of roughness or protuberances) can have drastic effects on the oscillatory load. Further, turbulence shed from nearby towers can cause excessive loads as can either an extremely blunt (e.g., hemispherical) or a narrow conical nose shape. Conduits, cableways, and piping can also cause high loads, particularly when these are at the stagnation point. (Refs 3.1 and 3.25.)

Because of the complexity of the problem, it has been necessary to conduct wind tunnel tests of each configuration to assess the severity of the vortex shedding. The test data must then be scaled to the prototype, for which efforts have been made to find a simplified approach. The approach taken by Buell (Ref. 3.7) and others is similar to the method of handling mechanical systems with random excitation, outlined in Section 2.6. The addition of an aerodynamic damping term to Buell's method, as proposed by Reed (Ref. 3.10), improves the method when mechanical damping is very low.

The method of treating vortex shedding proposed by Bohne (Ref. 3.11) requires power spectra and cross-power spectra of the lift coefficient, or fluctuating pressure, along the entire length of the vehicle. This requires the acquisition of a large amount of data. The data reduction task is many times greater than that required for the method proposed by Buell, although Bohne has shown that his method can be simplified if there are long uniform sections of the vehicle, i.e., so that each section can be treated as though it were in two-dimensional flow. Because of the greater data acquisition and reduction task and the lack of theoretical or empirical techniques for predicting the effect of configurational changes, it is considered that Buell's method is the more optimum at this time. When data become available and the mechanism of vortex shedding becomes better understood, then it should be possible to use Bohne's method without depending on individual wind tunnel tests.

The foregoing discussion has been primarily concerned with vortex shedding, which is only one factor of the overall problem. Other factors are steady-state and gust loads. Steady-state load techniques have not varied significantly over the past 10 years. The effect of atmospheric turbulence, i.e., gustiness, has been discussed in

the literature with various solutions proposed. These discussions have concerned themselves with the direct effect of the turbulence without trying to predict interactions with vortex shedding. The solutions have employed various gust power spectra and correlation techniques.

Early treatment of gust loads consisted simply of calculating steady-state drag based on the peak wind speed and assuming that this load would encompass any dynamic load. Later, discrete gusts were proposed (Refs 3.12 and 3.13) for which dynamic response could be determined. As random response techniques became more prevalent, the use of gust power density spectra became the preferred approach.

Wind gustiness has been studied in a statistical manner only in recent years. The first such investigations were for aircraft gust loading wherein the emphasis was on the vertical component. However, erected space-launch vehicles are loaded by the horizontal components of the turbulence and these data have only recently been made available in a form suitable for loads analysis (see Refs 3.14 through 3.17). The work of Lumley and Panofsky (Ref. 3.16) provides a thorough treatment of atmospheric turbulence. Their bibliography covers the significant literature published prior to 1964. Henry's gust spectrum (Ref. 3.15) has been employed by Fontenot (Ref. 3.18), Bohne (Ref. 3.19), and others in their treatment of gust loads. The method proposed by Reed (Ref. 3.10) is similar to Bohne's vortex shedding response method and is a refinement of earlier treatments in that it accounts for spatial correlation of gusts along the length of the vehicle.

The method of combining the various components of the load has not been discussed to any great extent in the literature. Fontenot's (Ref. 3.18) statistical combination of loads tends to give a combined load that has a lower probability of being exceeded than do the component loads, e.g., the total load may be exceeded only once in 10,000 cycles when the vortex shedding component is set to be exceeded three times in 1000 cycles (3-sigma value). The root-sum-square technique for combining random variables also tends to be conservative when the component loads have the desired "sigma" level. A method employing a bivariant distribution is presented in Section 3.3.3.2 of this report.

3.3 ANALYTICAL APPROACH

Procedures for ground wind loads analysis require a development of mathematical descriptions of the applied wind forces and the structure to be analyzed. With these simulations, a set of equations can be written and solved, using the response solutions of Section 2, to obtain vehicle loads. Because of the random nature of winds and the different types of loads (such as steady, vortex shedding, gusts, and others), there is the added task of combining these loads, obtained from separate response calculations, into a form that can be used for stress analysis. Procedures and analytical techniques to be used for loads analysis are discussed in this section.

3.3.1 REPRESENTATION OF THE WIND VELOCITY AND FORCE. The wind velocity is a random variable in both time and space. The randomness of the time variation is evident from the anemometer recording presented in Fig. 3.2. For loads analysis, the wind velocity may be considered as a mean wind averaged over, say, five minutes, upon which is superimposed the random atmospheric turbulence. The turbulence, or gustiness, may then be represented by the power density spectra of the components that are parallel and normal to the mean wind, i.e., the lift and drag components of the gusts. The problem now involves establishing the appropriate representations for the mean wind and the gust power density spectra.

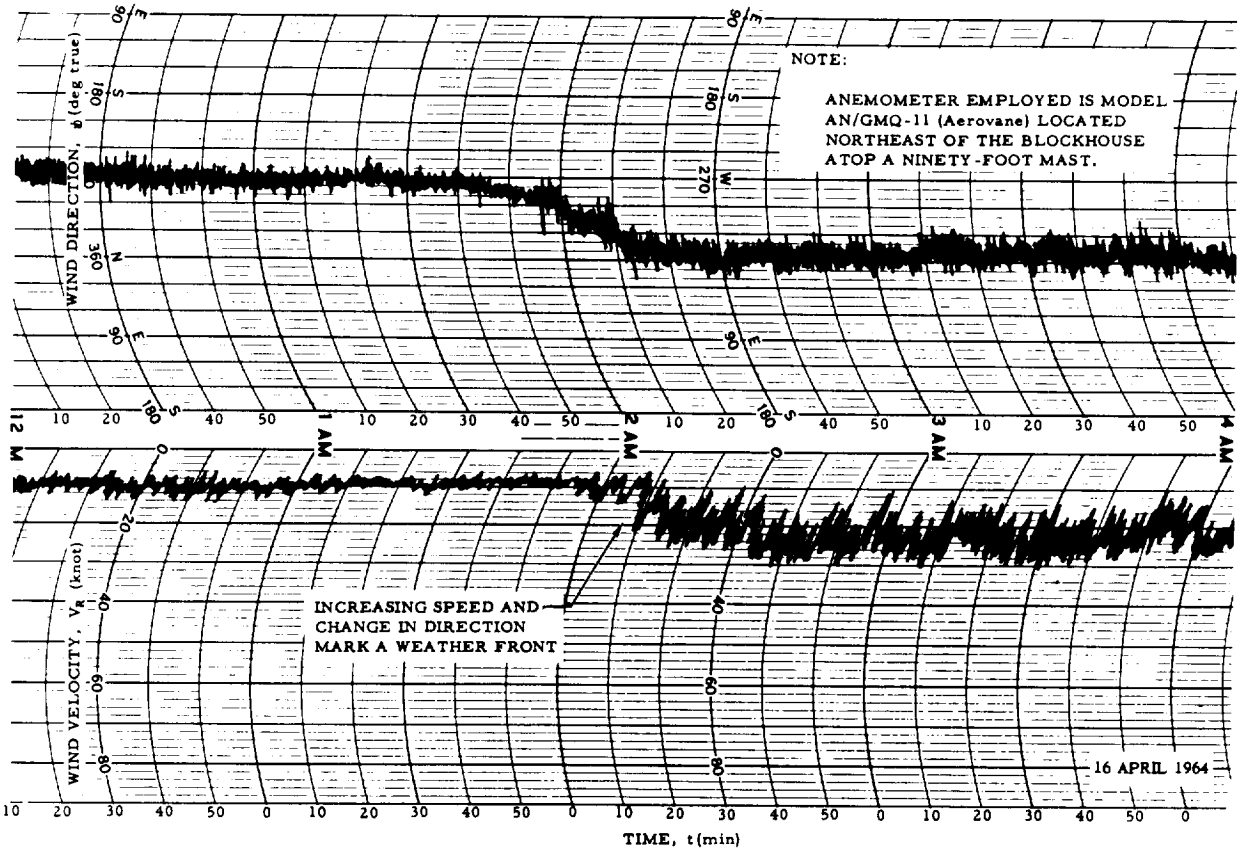

Fig. 3.2. Typical Recording of Ground Wind Velocity and Direction

The mean wind profile varies with height above ground due to frictional effects, temperature gradient, etc. The profile shape recommended uses the power law representation, viz.,

$$V(h) = V_R \left(\frac{h}{h_R}\right)^{1/5} \tag{3.1}$$

where V_R is the average wind speed at reference height h_R. This profile appears to be adequately representative for most analyses. The value of V_R will vary for different launch sites and is dependent upon the desired probability of not exceeding the design wind speed. For example, Table 3.1 lists wind speeds and their associated probabilities of not being exceeded at two launch sites. These data are from Ref. 3.20. The 95-percentile profiles are illustrated in Fig. 3.3.

The gustiness of the wind is represented by the power density spectra of the fluctuating velocity. There are several representations currently in use which are, in the main, curve fit equations based on observed data. The equations given below, describing the power density spectra of the velocity at a point along the vehicle, are taken from the noted references.

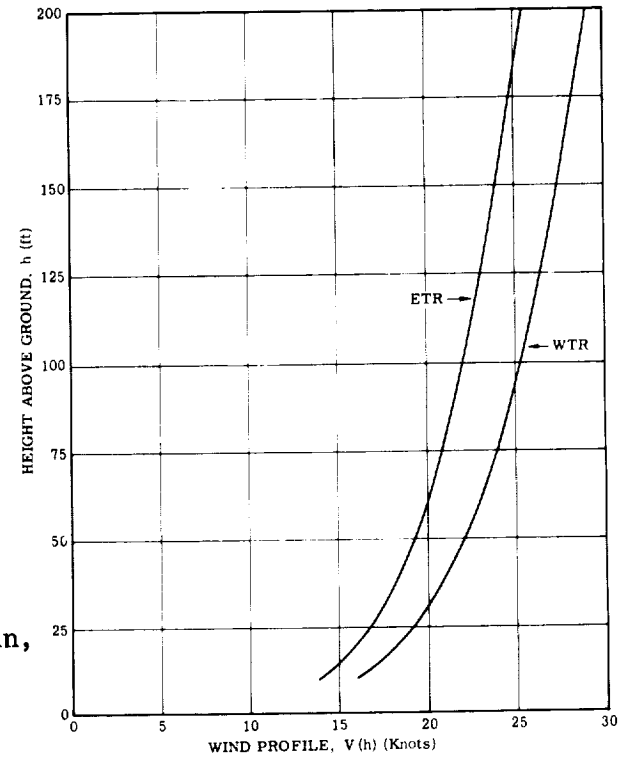

Fig. 3.3. 95-Percentile Ground Wind Profiles

Table 3.1. Average Ground Wind Speeds for Eastern and Western Test Ranges

	ETR	WTR
$P_r(\bar{V} < V_R) = 95\%$	14 knots	16 knots
$P_r(\bar{V} < V_R) = 99\%$	18.4	20
$P_r(\bar{V} < V_R) = 99.9\%$	23.0	--

V_R = steady-state wind.

$\bar{V}$ = average wind speed over a two-minute period.

h_R = 10 ft.

Drag Component

$$S_D(f) = (1.28 \times 10^{-4}) \frac{f V_R^{8/3}}{\left[\left(\frac{V_R}{4000}\right)^2 + f^2\right]^{4/3}} \qquad \text{(Ref. 3.14)} \qquad (3.2)$$

$$S_D(f) = (5.67 \times 10^{-3}) \left(\frac{V_R^7}{h^2 f^5}\right)^{1/3} \tanh\left(\frac{426\, hf}{V_R^2}\right) \qquad \text{(Ref. 3.15)} \qquad (3.3)$$

$$S_D(f) = \frac{(3.036 \times 10^{-4})}{D} \frac{V_R^3}{\left(\frac{V_R}{62.8D}\right)^2 + f^2} \qquad \text{(Ref. 3.10)} \qquad (3.4)$$

$$S_D(f) = (2.15 \times 10^{-2})\ V_R^{5/2} \frac{\left[\frac{1}{3}\left(\frac{V_R}{2\pi h}\right)^2 + f^2\right]}{\left[\left(\frac{V_R}{2\pi h}\right)^2 + f^2\right]^2} \qquad \text{(Ref. 3.17)} \qquad (3.5)$$

Lift Component

$$S_L(f) = (4.56 \times 10^{-4})\ \frac{V_R^3}{D} \frac{\left[\frac{1}{3}\left(\frac{V_R}{62.8D}\right)^2 + f^2\right]^2}{\left[\left(\frac{V_R}{62.8D}\right)^2 + f^2\right]^2} \qquad \text{(Ref. 3.10)} \qquad (3.6)$$

$$S_L(f) = 1.4\, S_D(f) \qquad \text{(Ref. 3.17)} \qquad (3.7)$$

The gust power density spectra for the drag components are illustrated in Fig. 3.4 for the following conditions:

V_R = 10 ft/sec and 40 ft/sec (10-foot reference height)

D = 10 ft

h = 100 ft

f = is in cycles/second

The equation given by Davenport (Eq. 3.2) appears to give the most conservative spectrum. It may be simplified for all reasonable values of V_R, viz.,

$$S_D(f) = (1.28 \times 10^{-4})\left(\frac{V_R^8}{f^5}\right)^{1/3} \tag{3.8}$$

The wind force is proportional to the square of the velocity, so that the power density spectrum of the square of the wind velocity is required, rather than just the power density spectrum of the velocity. Bohne (Ref. 3.19), Fontenot (Ref. 3.18), and Wood (Ref. 3.21) have derived the spectrum of the drag force, ignoring the lateral gusts. In a manner similar to that of the appendix of Ref. 3.21, the square of the total wind velocity at a given height is found to have the form given below.

The mean-square wind velocity, $\overline{V^2}$, is

$$\left[(V_R^2 + \sigma_{DG}^2)^2 + 2\,V_R^2\,\sigma_{LG}^2 + \sigma_{LG}^4 + 2\,\sigma_{DG}^2\sigma_{LG}^2\right]^{1/2} \tag{3.9}$$

The power density spectrum, $\Phi(f)$, is

$$4\,V_R^2\,S_D(f) + \frac{1}{2}\int_{-\infty}^{\infty} S_D(\lambda)S_D(f-\lambda)d\lambda + \int_{-\infty}^{\infty} S_{DL}(\lambda)\,S_{DL}(f-\lambda)d\lambda + \frac{1}{2}\int_{-\infty}^{\infty} S_L(\lambda)\,S_L(f-\lambda)d\lambda \tag{3.10}$$

The first term in the mean-square velocity and the first and third terms in the spectrum will be recognized as the same as those given by Bohne, Fontenot, and Wood for the drag direction. Bohne and Fontenot have indicated that the convolution integral of the drag spectrum is negligible, so it can be expected that the convolution integral of the lift spectrum and of the cross-power spectrum will also be small. The variances will usually be much smaller than V_R^2, so that the above expressions can be well approximated by

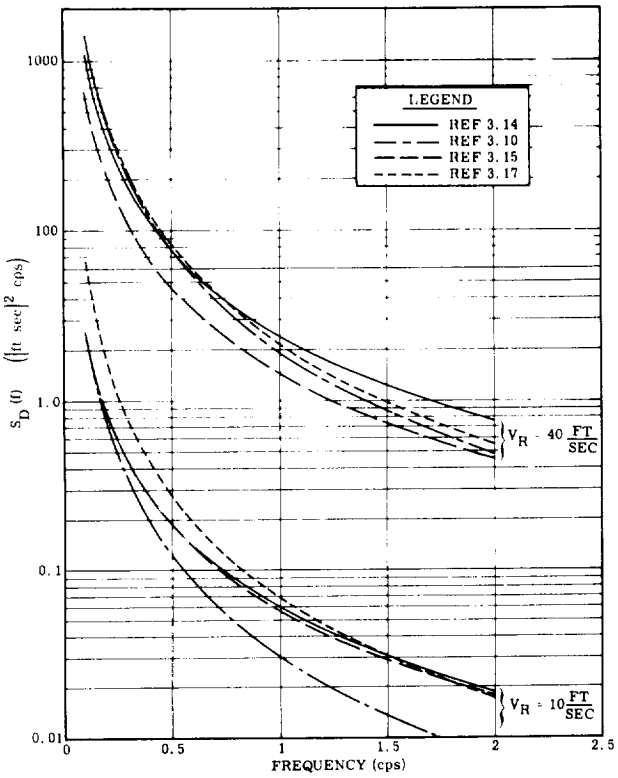

Fig. 3.4. Comparison of Gust Spectra

$$\overline{V^2} \cong V_R \left[V_R^2 + 2\sigma_{DG}^2 + 2\sigma_{LG}^2 \right]^{1/2} \qquad (3.11)$$

$$\Phi(f) \cong 4V_R^2 \; S_D(f) \qquad (3.12)$$

Cross-power density spectra for vertically separated points are not presented since these are not, as yet, well defined. It is known, however, that there is little correlation between gusts at points separated by more than one-quarter wavelength (Refs 3.14 and 3.17), where the wavelength is found by dividing the mean wind speed by the frequency, i.e., $X = V_R/f$. Further, the cross-power density spectra and the covariance between drag and lift components of the gusts have not yet been established, although Reed (Ref. 3.10) has derived a theoretical expression for the drag and lift cross-power density spectra.

The aerodynamic coefficients for a circular cylinder in a fluctuating flow are not well known. Lacking pertinent data, one is left with the choice of using steady-state coefficients or estimating them. The use of steady-state coefficients is recommended until more is known about the problem.

Vortex shedding coefficients will ordinarily have been obtained in a wind tunnel wherein the wind velocity is essentially steady state, i.e., the turbulence is very small (Ref. 3.10 discusses this subject). The analyst must, therefore, establish an "equivalent" steady-state wind for loads analysis purposes. The equivalent wind should represent a uniform profile, i.e., V(h) = constant, and produce the same response to vortex shedding as the real wind. The latter criterion is difficult to establish because little is known about the effect of gusts on vortex shedding. Therefore, it is not unreasonable to use an equivalent mean-square wind based on steady-state loads as given below,

$$V_e^2 = \frac{\int_L V^2(h)\, D(h)\, x(h)\, dh}{\int_L D(h)\, x(h)\, dh} \qquad (3.13)$$

3.3.2 RESPONSE OF THE VEHICLE TO GROUND WINDS

3.3.2.1 Mathematical Model. The mathematical model of the vehicle is given in Figure 3.5. This simplified model will ordinarily be sufficient for ground wind loads calculations. However, for a large multistage vehicle, or a vehicle with thrust augmentation (strap-ons), a more complex model may be in order. Mathematical modeling has been discussed in some detail in Section 2.2.

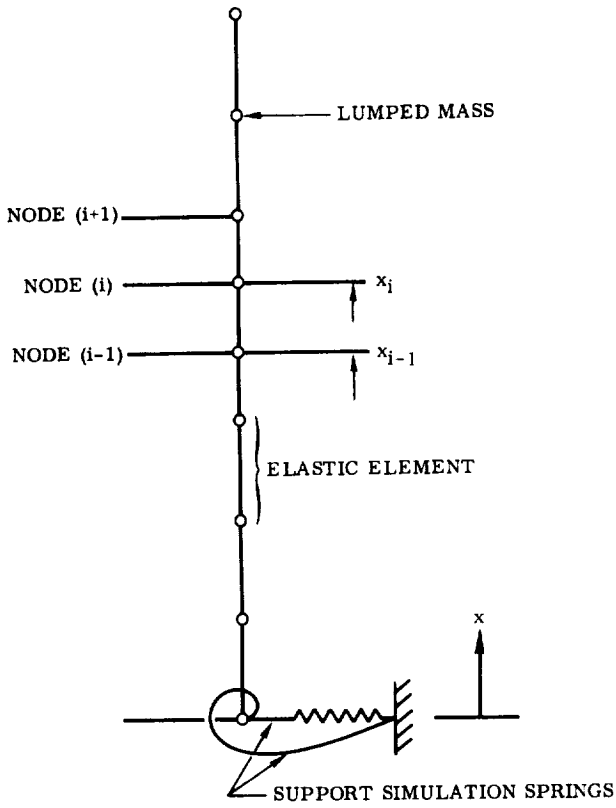

Fig. 3.5 Typical Mathematical Model

3.3.2.2 Steady-State Response. The steady-state wind loads on the erected vehicle are determined from the mean wind and appropriate aerodynamic coefficients. The mean wind profile has been given in Section 3.3.1 (Eq. 3.1 and Table 3.1) and the load equations follow the classical treatment of static loading of a cantilever beam.

With a perfectly symmetrical vehicle, only drag loads need be considered. When there are protuberances, or even differences in surface roughness, some lift load will be developed due to unsymmetric separation of the boundary layer. This lift load will ordinarily be less than 25 percent of the steady-state drag. However, with a lifting body payload or highly unsymmetric vehicle, the lift load may equal the maximum drag load, at certain orientations. Steady-state drag and lift coefficients for typical symmetrical vehicles may be found in Ref. 3.6.

3.3.2.3 Vortex Shedding Response. Vortex shedding is the terminology generally applied to any phenomenon wherein the flow of fluid past an object causes "burbles", or turbulence in the wake. When the object is cylindrical and the Reynolds number, $\frac{VD\rho}{\mu}$ is very low (<5000) the turbulence very often takes the form of the classical Von Kármán Vortex Street, illustrated in Fig. 3.6. Note that the vortices are shed alternately from each side and that they are periodic. The frequency of the vortex shedding in this periodic case is found from the Strouhal number relationship, $S = \frac{fD}{V}$, where S is on the order of 0.2. When the Reynolds number is supercritical (>>5000), the vortex shedding becomes random and the Strouhal number relationship loses its significance.

The shedding of the vortices causes fluctuations in pressure near the separation point. This fluctuating pressure has force components that are parallel and normal to the approach velocity. The lift (normal) component is the more significant effect. If the structure is elastic, the fluctuating pressures will produce oscillatory motion in the lift and drag direction. Further, if an elastic body is in the turbulent wake of another body, it will be excited by that turbulence as well as by its own vortex shedding. The presence of an umbilical tower can have a very pronounced effect on the oscillatory load. The location is usually dictated by considerations other than load, but if it is practical, relocating the tower about two diameters from the vehicle will result in lower loads than at one diameter (Ref. 3.25). The data of Ref. 3.25 also show that the load can be reduced by increasing the effective width of the tower.

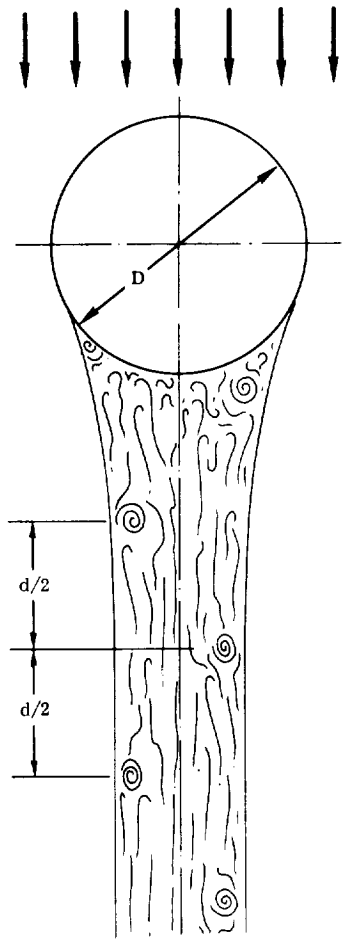

Fig. 3.6. Representation of Von Kármán Vortex Street

Space launch vehicles are seldom clean bodies of revolution. Antennas, equipment pods, and other protuberances have localized effects on vortex shedding that are generally not predictable by analytical means. Each vehicle configuration should therefore be tested to determine the vortex shedding effects. The test program should adopt good modeling techniques, such as discussed in Ref. 3.22. Briefly, the model should be scaled such that the Reynolds number, $\frac{VD\rho}{\mu}$, reduced frequency, $\frac{fD}{V}$, damping ratio, C/C_c, and mass ratio, $\frac{m_n}{m_a}$, are simulated, and such that geometric features, including roughness, are properly scaled.

The most usable form of wind tunnel data is the envelope of the drag and lift bending moments at the model base. This envelope may be obtained by making the two bending moments the X and Y inputs to an oscilloscope and taking a time exposure of the resultant trace. The trace will have the form of a Lissajous figure with an elliptic envelope. The maximum bending moments in the drag and lift directions are then taken from the time-exposed photograph of the oscilloscope traces.

Data from the various wind tunnel tests indicate that the response is predominately in the first structural mode. The response equations are therefore written in terms of only the first mode. The response of the vehicle to the wake turbulence of the umbilical tower may include higher modes, which would require a modification of the

response equations presented below. Further, it is assumed that the motion of the vehicle does not affect the aerodynamics. While there is some evidence to the contrary (Refs 3.10 and 3.25), it is considered that the proposed method adequately accounts for this phenomenon.

The maximum lift and drag loads on the model are scaled to the prototype by use of the following relationships *(Ref. 3.6):

$$u_V(x) = C_V\left[\frac{1}{2}\rho V_e^2 \frac{\phi_1(x) A^2 W_1}{m_1 \omega_1^2 L^2} \sqrt{\frac{\omega_1 D}{2\pi V_e \zeta_1}}\right]_{\text{Full Scale}} \tag{3.14}$$

$$C_V = \left[\frac{(M_b)_{max}}{(M'_b)_1} \frac{m_1 \omega_1^2 L^2}{q A^2 W_1} \sqrt{\frac{2\pi V \zeta_1}{\omega_1 D}}\right]_{\text{Model}} \tag{3.15}$$

Eqs 3.14 and 3.15 are applicable to both the lift and drag directions with the appropriate parameters. If the full-scale damping ratio is very low, say on the order of 0.5 percent of critical, the use of an aerodynamic damping term as discussed in Ref. 3.10 may be advisable.

Bohne (Ref. 3.11) presents a method using multipoint random input in terms of pressures. This method requires cross-power density spectra in addition to the usual power density spectra. A great deal of data must be obtained and reduced; hence the test program is more complicated than that of the method presented above.

3.3.2.4 Gust Reponse. Reed (Ref. 3.10) has presented a method of calculating the response to gusts which includes cross-power density spectra. In this method, the response power density spectra have the form of Eq. 2.181 of Section 2.6, which are then simplified. However, since the cross-power density spectra have not been verified, it is probably best to continue using a homogeneous gust-type solution; that is, assume that the gust envelopes the vehicle. In this case, the mean-square response has the form of Eq. 2.185 of Section 2.6, viz.,

$$\overline{u_G^2(x)} = C_{DG}^2\left(\frac{1}{2}\rho\right)^2 \sum_n \frac{1}{2\pi} \frac{\phi_n^2(x) W_n^2 \Phi(f_n)}{m_n^2 (2\pi f_n)^2} \tag{3.16}$$

This equation is applicable to both the lift and drag gust components.

*The load equations are written in terms of displacement. Any other item of interest may be found by the appropriate substitution for ϕ (x).

The aerodynamic coefficients for a cylinder in a fluctuating flow are not well known. It is therefore recommended that steady drag coefficients be used for the gust response, unless more specific data are available. The square root of Eq. 3.16 is multiplied by three to obtain the "three-sigma" displacement.

3.3.3 RESULTANT RESPONSE. The total resultant load on the vehicle in the launch-ready condition includes the various ground wind components, the axial gravity load, loads due to tank pressurization, and, at ignition, thrust-induced loads. Thrust-induced loads are discussed in Section 4 along with the method for combining all the on-the-pad loads. The axial gravity load and tank pressurization load are determined by classical static analyses. The manner in which the various ground wind load components may be combined is discussed in this section.

The ground wind load is a function of vehicle tanking, as well as a function of the wind. The loads at the supports will ordinarily be most severe for the fully tanked vehicle. However, at some other point the loads may be more severe for some partially tanked condition. To be sure that the worst case has been found for the design, it is advisable to calculate ground wind loads for each possible tanking condition.

3.3.3.1 Equal Probability. One method of combining the individual loads into a resultant is to vectorially add the vortex shedding and gust loads of the desired probability-of-occurrence level to the steady-state loads. This technique, illustrated in Fig. 3.7, tends to be conservative as the probability of the resultant being exceeded is lower than the probability of a component load being exceeded. Secondary loads due to deflection should be accounted for.

3.3.3.2 Combined Probability. Data of Ref. 3.10 indicate that the envelope of the steady-state and vortex shedding loads tends to be an ellipse. The eccentricity of this ellipse is a function of the ratio of the vortex shedding lift and drag loads. Using the above observed distribution of load and assuming that the vortex shedding and gust loads are independent, normally distributed, and have zero correlation it is possible to develop a method wherein the resultant load has the desired probability of occurrence.

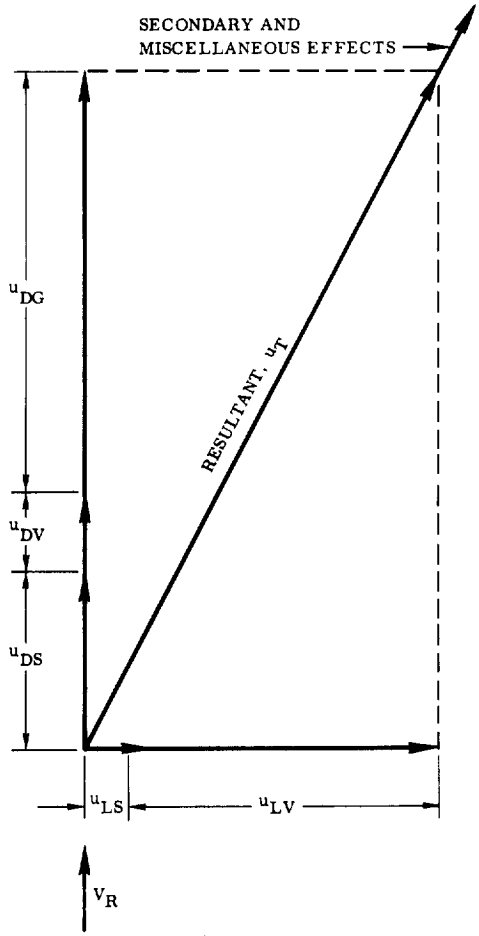

Fig. 3.7. Equal Probability Combination of Loads

The combination of the random loads in the lift and drag direction is assumed to be

bounded by a closed curve R and have the equation:

$$\epsilon_L^2 + \frac{\epsilon_D^2}{a^2} = K_o^2 \sigma_{LT}^2 \tag{3.17}$$

where

$$a = \frac{\sigma_{DT}}{\sigma_{LT}}$$

σ_{DT} = [Sum of the mean-square values of the random drag components]$^{1/2}$

σ_{LT} = [Sum of the mean-square values of the random lift components]$^{1/2}$

The probability of the resultant load (ϵ_L, ϵ_D) falling within the region R is given by the bivariant normal distribution (Refs 3.23 and 3.24).

$$P_r\left[(\epsilon_L, \epsilon_D) \text{is in R}\right] = \iint_R \frac{1}{2\pi\sigma_{DT}\sigma_{LT}} \exp\left[-\frac{1}{2}\left(\frac{\epsilon_L^2}{\sigma_{LT}^2} + a\frac{\epsilon_D^2}{\sigma_{DT}^2}\right)\right] d\epsilon_L d\epsilon_D \tag{3.18}$$

A plot of K_o versus a is shown in Fig. 3.8 for a 99.73-percent probability that ϵ_L, ϵ_D is in R. The region R of Eq. 3.17 has the desired properties as illustrated in Fig. 3.9; i.e., it is circular when $\sigma_{DT} = \sigma_{LT}$ and degenerates to a univariant distribution when $\sigma_{DT} = 0$. The maximum oscillatory lift or drag loads may be found by utilizing

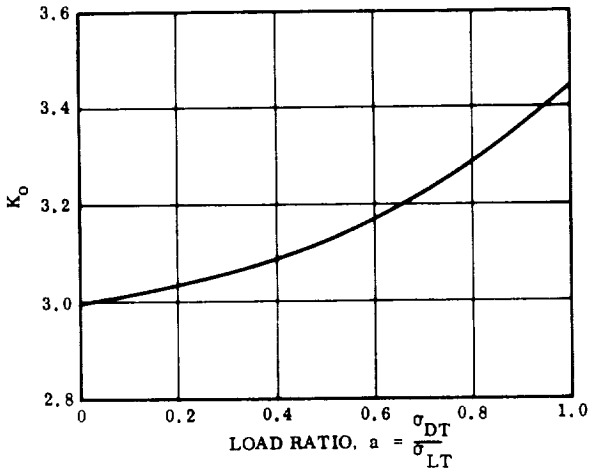

Fig. 3.8. K_o Versus a for $P_r\left[(\epsilon_D, \epsilon_L) \text{ is in R}\right] = 0.9973$

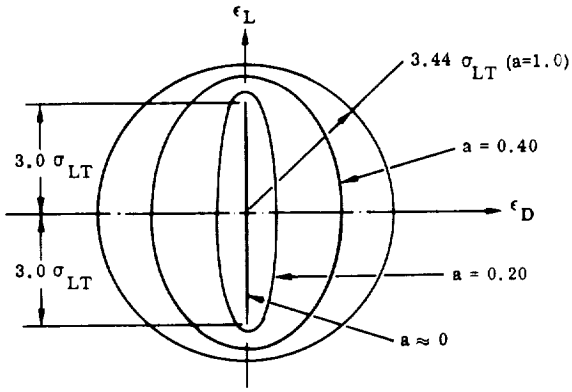

Fig. 3.9. Regions Formed for Various Values of $\sigma_{DT}/\sigma_{LT} = a$, for $P_r\left[(\epsilon_D, \epsilon_L) \text{ is in R}\right] = 0.9973$

Eqs 3.17 and 3.18; that is, $(\epsilon_L)_{max} = K_o \sigma_{LT}$ and $(\epsilon_D)_{max} = \sqrt{a}\, K_o \sigma_{LT}$, respectively. When a > 1, the ratio may be inverted and Fig. 3.9 is still applicable.

The resultant load is found as indicated in Fig. 3.10. The center of the ellipse is biased from the no-load position by the amount of the steady-state load components. The maximum resultant load will be a vector from the origin to a point on the ellipse whose tangent is perpendicular to that vector. This point is found by the following set of equations.

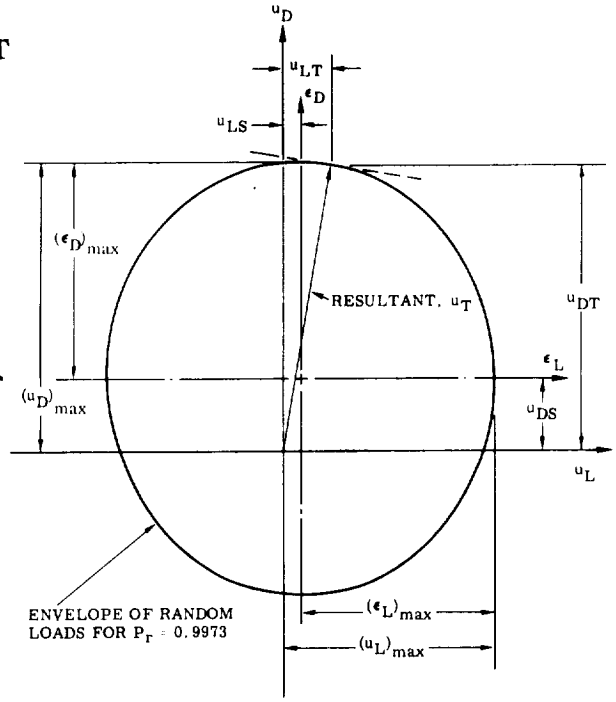

Fig. 3.10. Statistical Combination of Loads

$$K_1 u_{DT}^4 + K_2 u_{DT}^3 + K_3 + u_{DT}^2 + K_4 u_{DT} + K_5 = 0 \qquad (3.19)$$

where

$$K_1 = (r - 1)^2$$

$$K_2 = 2r^2 (u_{DS})(1 - r^2)$$

$$K_3 = r^4 (u_{DS})^2 + r^2 (u_{LS})^2 - r^2 (\epsilon_L)^2_{max} (r^2 - 1)^2$$

$$K_4 = 2r^4 (\epsilon_L)^2_{max} (u_{DS}) (1 - r^2)$$

$$K_5 = -r^6 (\epsilon_L)^2_{max} (u_{DS})$$

$$r = \frac{(\epsilon_L)_{max}}{(\epsilon_D)_{max}}$$

$$u_{LT} = \frac{u_{DT} (u_{LS})}{u_{DT} (r^2 - 1) + r^2 (u_{DS})} \qquad (3.20)$$

Eq. 3.19 is a fourth order equation and will therefore yield four roots. For the case at hand, the four roots are: one maximum, one minimum, and two imaginary. The maximum root is the root of interest. Once the resultant drag, u_{DT} is found, it is substituted into Eq. 3.20 to solve for the resultant lift, u_{LT}. The total resultant is then

$$u_T = \sqrt{\left(u_{DT}\right)^2 + \left(u_{LT}\right)^2} \tag{3.21}$$

3.4 CONCLUSIONS

3.4.1 WIND. The statistical variation of the mean wind and the representation of the profile are adequately defined, and there is reasonable agreement on the power density spectrum of the gusts. The cross-power density spectra for vertically separated drag and lift gusts are required as is the cross-power density spectrum between the drag and lift gusts. Further, since the vehicle may respond in a steady-state manner to low-frequency gusts (half-period on the order of 30 seconds), the probability of occurrence of the gust wave length should also be determined.

3.4.2 RESPONSE. The general form of the response is well known, even for a random force. The real problem here is in defining the forcing function. The total force applied to the vehicle is complicated due to the fact that it is made up of several, possible interacting, random forces, in addition to the steady-state force. The general practice taken in the literature has been to isolate one, or possibly two, aspects of the overall problem and concentrate on obtaining a reasonable solution to that portion alone. What is needed is an integrated treatment of the overall problem, in which an attempt is made to account for all known and suspected force terms and interactions. Such a solution is not immediately obtainable due to lack of data. Additional research is required to obtain a tractable solution that contains the effects of all parameters and their components simultaneously. This solution would then, of course, need to be verified by full-scale tests.

3.4.3 RECOMMENDED PROCEDURE. Within the scope of the present state of the art in ground wind loads analysis, it is recommended that the following procedures be used for design loads.

a. Vehicles that are clean bodies of revolution.

   The first requirement is to establish the desired wind speed for design purposes. This wind speed is determined from the wind data at the launch site and the desired probability of launching on a specific date.

   For the design wind speed, calculate steady-state loads using classical static loads analysis techniques, the mean-square wind speed of Eq. 3.11 and the wind profile of Eq. 3.1. Lift and drag aerodynamic coefficients can be obtained from Ref. 3.6.

Calculate gust loads using Eq. 3.16, the gust spectrum of Eq. 3.12, and steady-state aerodynamic coefficients.

Calculate vortex shedding loads using Eq. 3.14 for a wind speed, V_e, and Eq. 3.13. Applicable coefficients can be obtained from Ref. 3.6.

Combine the stead-state, gust, and vortex shedding loads using the methods of Section 3.3.3.1 or 3.3.3.2. Secondary bending loads, other random loads, and basic vehicle loads such as weight, thrust, etc., must be included.

b. Vehicles that are not clean bodies of revolution.

The procedure is the same as for the clean bodies of revolution except for the vortex shedding loads. It will be necessary to search the literature to determine or estimate vortex shedding coefficients to be used in preliminary design. As soon as possible, wind tunnel tests should be run to determine vortex shedding coefficients for the vehicle.

3.5 REFERENCES

3.1 D. A. Buell, "Some Sources of Ground-Wind Loads in Launch Vehicles," AIAA Fifth Annual Structures and Materials Conference, Palm Springs, California, April 1-3, 1964.

3.2 R. Goldman, The Generation and Suppression of Von Karman Vortex Forces, Martin Co. Report No. 8984, July 1957.

3.3 D. E. Somerville and D. R. Kobett, Research and Development Services Covering Wind-Induced Oscillations of Vertical Cylinders, Midwest Research Institute, Phase Report No. 1, 1958.

3.4 Y. C. Fung, "Fluctuating Lift and Drag Acting on a Cylinder in a Flow at Supercritical Reynolds Numbers," Journal of Aerospace Sciences, Vol. 27, No. 11, pp. 801-804, November 1960.

3.5 A. Roshko, "Experiments on the Flow Past a Circular Cylinder at Very High Reynolds Number," Journal of Fluid Mechanics, Vol. 10, Pt. 3, pp. 345-356, May 1961.

3.6 D. A. Buell, G. B. McCullough, and W. J. Steinmetz, A Wind Tunnel Investigation of Ground-Winds Loads on Axisymmetric Launch Vehicles, NASA TN-D-1893, October 1963.

3.7 D. A. Buell and G. C. Kenyon, The Wind - Induced Loads on a Dynamically Scaled Model of a Large Missile in Launching Position, NASA TM X-109, December 1959.

3.8 A. A. Ezra, Wind Induced Oscillations of the Titan Missile, The Martin Co. Report No. WDD-M-MI-59-7, March 1959.

3.9 E. Gaffney, Ground Wind Loads Wind Tunnel Tests on Several Atlas Vehicles, Convair Division Report No. GD/A63-0999, April 1964.

3.10 W. H. Reed III, "Models for Obtaining Effects of Ground Winds on Space Vehicle Erected on The Launch Pad," Conference on the Role of Simulation in Space Technology, Virgina Polytechnic Institute, August 17-21, 1964.

3.11 Q. R. Bohne, "Ground Wind Induced Loads on Axisymmetric Launch Vehicles," AIAA Fifth Annual Structures and Materials Conference, Palm Spring, California, April 1964.

3.12 Handbook of Geophysics, Rev. Ed., The MacMillian Co., New York, 1960.

3.13 J.R.Scoggins et al., Low Level Wind Profiles Applicable for the Study of Vertically Rising Vehicle Performance Between 3 Meters and 120 Meters, Cape Canaveral (Atlantic Missile Range), Florida, George C. Marshall Space Flight Center, MTP-AERO-60-26, December 1960.

3.14 A. G. Davenport, "The Spectrum of Horizontal Gustiness Near the Ground in High Winds," Quarterly Journal of Met. Soc., Vol. 87, 1961.

3.15 R. M. Henry, A Study of the Effects of Wind Speed, Lapse Rate, and Attitude on the Spectrum of Atmospheric Turbulence at Low Altitude, IAS Preprint No. 59-43, January 1959.

3.16 J. L. Lumley and H. A. Panopky, The Structure of Atmospheric Turbulence, Intensive Publishers Division of John Wiley & Sons, New York, 1964.

3.17 J. K. Zbrozek, The Relationship between The Discrete Gust and Power Spectra Presentations of Atmospheric Turbulence, with a Suggested Model for Low Altitude Turbulence, Technical Note No. AERO 2682, ASTIA Document AD-242944, March 1960, and Addendum, AD-242945, July 1960 (Royal Aircraft Establishment, Bedford).

3.18 L. L. Fontenot, "The Response of a Flexible Missile to Ground Winds," Air Force Surveys in Geophysics No. 140, Proceedings of the National Symposium on Winds for Aerospace Vehicle Design, Vol. I, USAF Geophysics Directorate, AFCRL-62-273(I), March 1962.

3.19 Q. R. Bohne, "Power Spectral Considerations on the Launch Pad," Air Force Surveys in Geophysics No. 140, Proceedings of the National Symposium on Winds for Aerospace Vehicle Design, Vol. I, USAF Geophysic Directorate, AFCRL-62-273 (I), March 1962.

3.20 G. E. Daniels, Terrestrial Environment (Climatic) Criteria Guidelines for Use in Space Vehicle Development, 1964 Revision, NASA TMX053023, March 13, 1964.

3.21 J. D. Wood and J. C. Barry, "Random Excitation of Missiles Due to Winds," Air Force Surveys in Geophysics No. 140, Proceedings of the National Symposium on Winds for Aerospace Vehicle Design, Vol. I, USAF Geophysics Directorate, AFCRL-62-273 (I), March 1962.

3.22 Henry L. Langhaar, Dimensional Analysis & Theory of Models, John Wiley & Sons, Inc., New York, 1951.

3.23 A. M. Mood, Introduction to the Theory of Statistics, McGraw-Hill Book Co., New York, 1950.

3.24 S. O. Rice, "Mathematical Analysis of Random Noise," Selected Papers on Noise and Stochastic Processes, Edited by Nelson Wax, Dover Publications, Inc., New York, 1954.

3.25 G. B. McCullough and W. J. Steinmetz, A Wind Tunnel Study of Ground-Wind Loads on Launch Vehicles Including the Effects of Conduits and Adjacent Structures, NASA TN D-2889, July 1965.

4/ENGINE START AND SHUTDOWN AND VEHICLE LAUNCH

NOMENCLATURE

A	Cross-sectional area of the vehicle structure	$in.^2$
E	Young's modulus	$lb/in.^2$
F	Force	lb
$F(t)$	Force time history	lb
K_i	Stiffness	lb/ft
L	Length	ft
$M(t)$	Moment time history	ft-lb
P	Axial load	lb
$Q_n(t)$	Generalized force as a function of time	lb
T	Thrust	lb
g	Gravity	ft/sec^2
m_i	Mass	$\frac{lb\text{-}sec^2}{ft}$
t	Time	sec
x	Coordinate along neutral axis	ft
ζ	Damping coefficient	N.D.
$\bar{\eta}_r$	Average (mean) of loads	lb or ft-lb
$\bar{\eta}^2$	Square of the mean load	lb^2 or $(ft\text{-}lb)^2$
$\overline{\eta^2}$	Second moment (mean square) of loads	lb^2 or $(ft\text{-}lb)^2$
ξ	Normal mode coordinate	ft
σ	Modal slope	rad/ft
σ_r	Standard deviation of load	lb or ft-lb
ϕ	Mode displacements	ft/ft
ω	Frequency	rad/sec^2
$\mathfrak{M}$	Generalized mass	$\frac{lb\text{-}sec^2}{ft}$

4/ENGINE START AND SHUTDOWN AND VEHICLE LAUNCH

4.1 STATEMENT OF THE PROBLEM

The largest forces acting on space launch vehicles are those produced by thrust of the engines. These thrust loads, and attendant longitudinal inertial loads, design or contribute to the design of almost every part of the vehicle structure. Longitudinal load conditions to be analyzed include rigid body and vibratory loads at engine start and shutdown, liftoff from the launch pad, and steady-state loads between these times. In the case of multiple engines, there exists the possibility of lateral loading induced by unsymmetrical engine start and shutdown. Also, unsymmetrical launcher release can cause lateral loads.

The major problems encountered in the analysis are the adequate description of: 1) a longitudinal mathematical model, and 2) the time history of applied forces. The difficulties in synthesizing the mathematical model are associated with the representation of the propellant in a dynamic model. The procedure of Section 2.2.3 provides a good representation for cylindrical tanks but does not provide good models for tanks approaching spheres or oblate spheriods.

Description of applied forces is difficult because of the random nature of engine starting characteristics. These characteristics vary not only among engines of a given model, but also among firings of the same engine. Two methods of obtaining design loads are: 1) to determine a worst-case buildup (or decay) curve and use this in the analysis for the design condition, or 2) to calculate responses using a large number of engine thrust time histories and obtain design loads from a statistical evaluation of the calculated responses. In multiple engine systems, the time at which different engines receive the start (or shutdown) signal has tolerances that add to the random nature of applied forces. For the liftoff problem, tolerances in engine timing and mechanical, pneumatic, or pyrotechnic operation of the release mechanism must be understood for a complete description of forces acting upon the vehicle.

Vehicle total loads must include those of other sources that can coincide with thrust forces. Typical examples are ground winds and winds aloft, effects of control system response to vehicle motion, and vehicle design and assembly misalignments. Combining these loads can be straightforward based on worst-case combinations or it can be a statistical combination including the random occurrences of all these forces.

4.2 HISTORICAL BACKGROUND

A dynamic analysis of space vehicles for their response to thrust forces usually uses data obtained from engine tests to describe the applied forces and employs

normal-mode theory in the response calculations. Development necessary for the analysis has been mostly in the modeling of the propellant and its containers. The works of Li (Ref. 4.1) and Wood (Ref. 4.2) were among the first attempts to obtain a model representing the first mode of a cylindrical tank. These works either assumed a rigid tank bottom or test data were available to describe the tank bottom effects. Pinson in Ref. 4.3 gives methods for obtaining effective spring rates of the bulkheads at the ends of each tank. Rose (Ref. 4.4) modifies the model by adding the effective spring rate of gases in the propellant tanks. He also proposes a method for representation of more than one propellant mode. The propellant tank model development is given in Section 2.2.3.

4.3 ANALYTICAL APPROACH

Analyses to obtain vehicle response to engine transients follow general normal-mode theory. However, there are several details, not necessary in the general application, that are required for satisfactory solutions of responses to these transients.

4.3.1 ENGINE START AND SHUTDOWN ANALYSES. Consider the simple longitudinal model of Fig. 4.1. Masses 2 through 4 represent major vehicle components, connected by springs K_3 and K_4. Mass 1 is the engine connected to the vehicle through spring K_2. The vehicle is held to the ground by spring K_1. The thrust, T, is applied by the engine. The loads for this condition can easily be analyzed with normal-mode theory by first obtaining the modes with the vehicle fixed to the ground and then writing the equations of motion in terms of normal-mode coordinates. For the n^{th} mode,

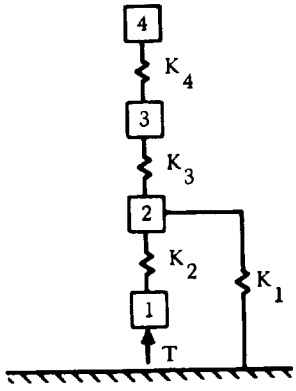

Fig. 4.1. Typical Longitudinal Model

$$\ddot{\xi}_n + 2\zeta_n \omega_n \dot{\xi}_n + \omega_n^2 \xi_n = \frac{Q_n(t)}{m_n} \qquad (4.1)$$

wherein the product of instantaneous thrust and the modal displacement of the engine is the generalized force, $Q_n(t)$. Simultaneous solution of the "n" equations and use of either mode displacement or acceleration methods will give vehicle load and acceleration distributions. The loads due to gravity must be added to obtain total loads.

Such is a typical analysis for engine thrust buildup on a vehicle held to ground by a "launcher." An analysis for engine shutdown in the launcher can be approximated by the same procedure but with the force time history equal to full thrust minus the thrust decay. That is, if the decay is represented by T(t) of Fig. 4.2 then the force time history used in the analysis is T_o - T(t) as shown in Fig. 4.3. This representation would give good results for the transient loads.

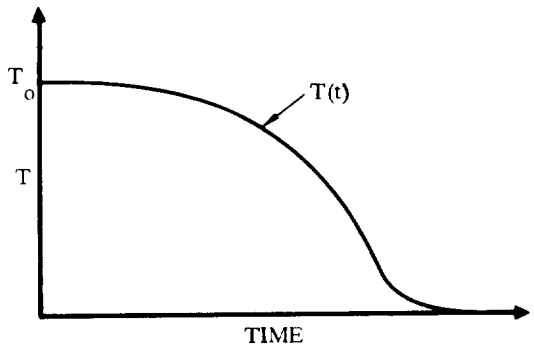

Fig. 4.2. Thrust Decay Time History

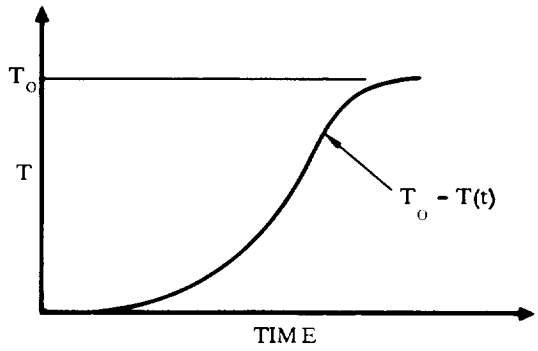

Fig. 4.3. Equivalent Thrust Decay Time History

The exact solution for the shutdown condition should consider the vehicle under its distributed loading at the time of shutdown. For the vehicle of Fig. 4.4, these applied forces are the weight and thrust, as indicated. The time histories of these forces are given in Fig. 4.5, where T_o is the full thrust and T(t) is the thrust decay. The weights remain constant.

The thrust and weight time histories imply step functions at t=0. To eliminate this "step function" it is required to have initial conditions equal to the static deflections under loads $m_i g$ and T. These deflections are obtained from

$$\{x\} = [K]^{-1} \begin{Bmatrix} m_i g \\ T \end{Bmatrix}$$

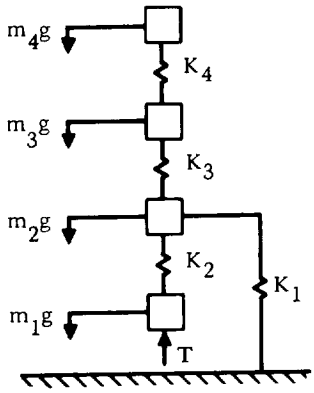

Fig. 4.4. Longitudinal Model and Forces for Engine Thrust Decay

The solution is executed in terms of normal mode coordinates ξ_n. Therefore, it is necessary to represent initial conditions in terms of normal coordinates. Since

$$\{x\} = [\phi]\{\xi\} \qquad (4.3)$$

then

$$\{\xi\} = [\phi]^{-1}\{x\} \qquad (4.4)$$

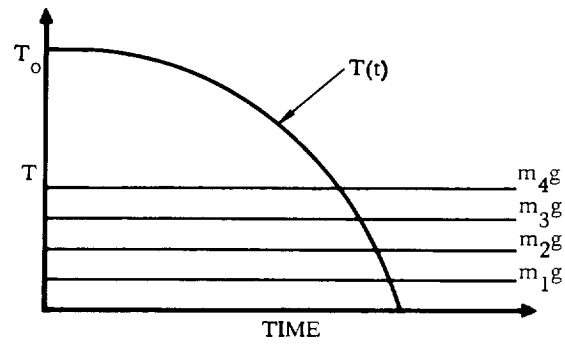

Fig. 4.5. Time Histories of Applied Forces During Engine Thrust Decay

Initial deflections in terms of ξ can also be obtained directly from Eq. 4.5.

$$\{\xi\} = [m]^{-1} [\omega^2]^{-1} [\phi]' \{F\} \tag{4.5}$$

The initial conditions and force time histories are now defined and the solution can be effected. Total loads, including gravity, for engine start could be similarly simulated.

The analyses for inflight engine start and shutdown are similar except that free-free modes replace the fixed modes, the applicable rigid-body modes must be included, and the force due to gravity is replaced by the inertial force of $m_i \ddot{x}$, where $\ddot{x}$ is the steady-state acceleration under thrust.

4.3.2 LIFTOFF ANALYSIS. Liftoff analysis introduces several additional considerations since it involves a model transition from "fixed" to "free" and also entails changes in the model such as elimination of the launcher. The procedure for liftoff analysis is indicated by the case of a free launch, i.e., a vehicle held down only by gravity, which will lift from its launcher when the thrust exceeds the weight. Fig. 4.6 presents a simplified model of vehicle and launcher. The analysis begins with the fixed model in Fig. 4.6a and proceeds as in the buildup and decay analysis above. When the force in K_1 is zero, then the vehicle is free and the analysis switches to the free modes of Fig. 4.6b. Because of oscillations, the vehicle and the launcher can make contact after initial liftoff; to represent this chatter condition the fixed modes of the launcher alone are required. The system is defined by two sets of modes, fixed and free:

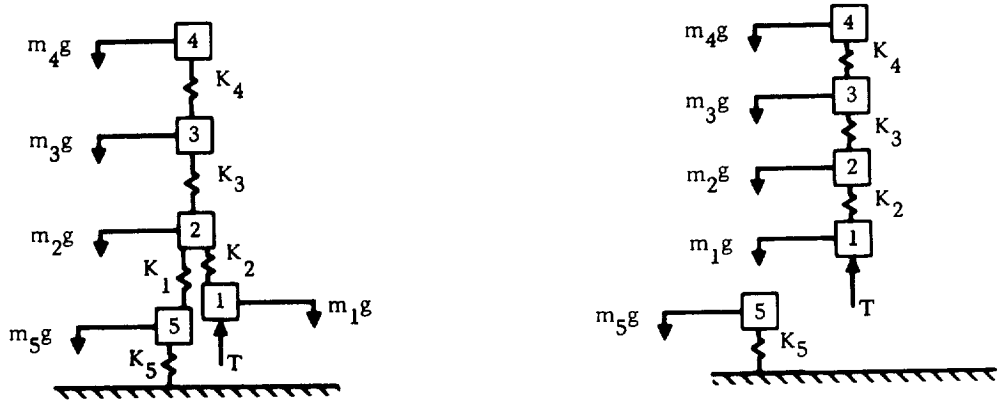

a. Fixed

b. Free

Fig. 4.6. Longitudinal Liftoff Models

$$\{x_{VL}\} = [\phi_{VL}]\{\xi_{VL}\} \qquad \text{(fixed modes)} \qquad (4.6)$$

$$\begin{Bmatrix} x_V \\ x_L \end{Bmatrix} = \left[\begin{array}{c|c} \phi_V & 0 \\ \hline 0 & \phi_L \end{array}\right] \begin{Bmatrix} \xi_V \\ \xi_L \end{Bmatrix} \qquad \text{(free modes)} \qquad (4.7)$$

where x_V, x_L are displacements of the vehicle and launcher, and ϕ_V are free-free (including rigid-body) modes of the vehicle and ϕ_L is the fixed mode of the launcher by itself.

The force in spring K_1 is zero when the relative deflection between masses 2 and 5 is greater than or equal to zero. Computerized monitoring of this quantity determines the time of switching between mode sets. Initial conditions for the second set of mode shapes are obtained by

$$\begin{Bmatrix} \xi_V \\ \xi_L \end{Bmatrix} = \left[\begin{array}{c|c} \phi_V & 0 \\ \hline 0 & \phi_L \end{array}\right]^{-1} \{x_{VL}\} \qquad (4.8)$$

The solution then continues with this set of modes. Forces and accelerations are obtained by either the mode-displacement or mode-acceleration method.

Simulation of an instantaneous release launch is achieved by obtaining initial conditions for the free-free vehicle modes under the thrust, the gravity, and the launcher forces. The forces in the response solution are the thrust and weight time histories. The inclusion of the launcher forces in the initial displacements, but with omission of launcher forces in the response solution, provides the force step-function of instantaneous launcher release. If the launcher force is applied at the same point as the thrust forces, then the solution follows the same procedure, with liftoff being represented by a step change, equal to the launcher force, in effective force at the point of engine-launcher force application.

A controlled-release launch is more complicated since it must include the mechanics of the control. It is often sufficient to follow the procedure of the instantaneous launch with the force time history of launcher load release applied to the free-free modes. This treatment is an approximation because the vehicle is not free until the launcher force is zero. A detailed analysis, with representation of the launcher mechanism modeled, is necessary if loads for this condition are surmised to be critical. The significance of these loads can be investigated by assuming various release time histories for evaluation of important parameters.

4.3.3 LATERAL LOADS. Lateral loads during engine start, shutdown, and vehicle liftoff are caused by misalignment of the thrust vector, unsymmetrical start and shutdown in the case of a multiple engine system, and unsymmetric launcher release. The

analytical approach is identical to that for longitudinal loads with moments and lateral forces replacing the axial forces and, of course, a lateral model replacing the longitudinal model. For thrust misalignment the generalized force in the n^{th} mode is

$$Q_n(t) = \phi_E^n \, F(t)$$

where ϕ_E^n is the modal deflection at the point of thrust application and F(t) is the lateral component of the thrust vector. In the case of unsymmetrical engine start the generalized force is

$$Q_n(t) = \sigma_E^n \, M(t)$$

where σ_E^n is the modal slope at the point of thrust application and M(t) is the product of differential thrust and the distance of the engines from the centerline of the vehicle. At liftoff, M(t) is the moment due to unsymmetrical release. The analysis then follows the mechanics of the longitudinal loads analysis. For most practical systems the lateral deflection due to center-of-gravity offset and gravity can be ignored in the computation of lateral transient loads.

4.4 ILLUSTRATIVE EXAMPLES

Typical analyses and results of engine start and shutdown and vehicle liftoff are presented in this section. The Atlas/Centaur/Surveyor vehicle has multiple engine systems in both the Atlas and Centaur stages. The Atlas stage has three engines, two engines with high thrust called booster engines, and one engine, the sustainer engine, of lower thrust. The booster engines, which are more efficient at sea level, are jettisoned at high altitude and flight is maintained by the more efficient sustainer engine (shutdown and jettison of the booster engines also reduce the maximum axial acceleration as propellant is depleted). The Centaur stage has two engines of nominally identical performance.

4.4.1 MATHEMATICAL MODELS. Models shown in Figs 4.7 and 4.8 are the longitudinal models that will be used for: 1) engine thrust buildup on the launch pad, 2) liftoff, and 3) sustainer shutdown. The model forward of Mass 11 is identical for all three conditions except for a reduction in Masses 5 and 7 to include the effect of jettisoning the nose fairing and insulation panels prior to sustainer engine shutdown. The spring-mass systems attached above Mass 4 represent Surveyor spacecraft modes that are coupled with totaled vehicle modes using the analytical techniques described in Ref. 4.5. The masses include structure and propellant as indicated in the figures. Spring constants for the LH_2 tank are obtained by application of the cylindrical tank model developed in Section 2.2.3. The model for the Centaur oblate spheroid LO_2 tank is obtained from test data interpreted to fit a cylindrical tank model. For purposes of this example the ullage pressure effects are not included and the bulkhead is assumed to be rigid.

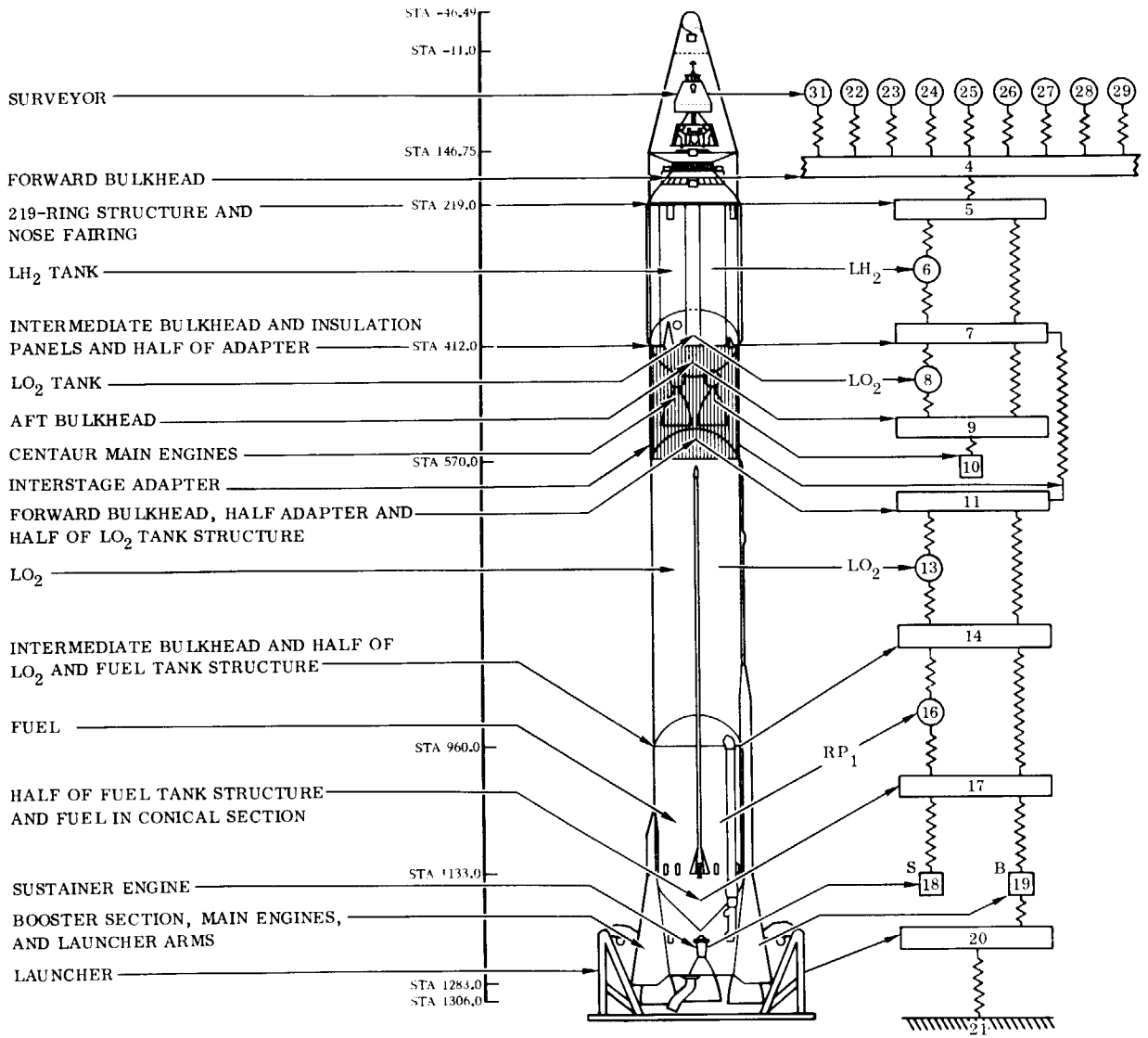

MASS	(lb)	SPRING	(lb/in.)
31	0.138	(31-4)	1.007
22	0.429	(22-4)	12.36
23	2.114	(23-4)	11.86
24	0.789	(24-4)	10.38
25	76.09	(25-4)	1169.2
26	3.785	(26-4)	889.7
27	0.002	(27-4)	0.598
28	19.71	(28-4)	6629.5
29	0.600	(29-4)	2206.2
4	956	(4-5)	0.548×10^6
5	2,567	(5-6)	0.159×10^6
6	5,005	(5-7)	0.639×10^6
7	2,085	(6-7)	0.374×10^6
8	25,082	(7-8)	8.906×10^6
9	1,273	(7-9)	-0.328×10^6
10	754	(8-9)	0.614×10^6
11	2,182	(9-10)	20.0×10^6
		(7-11)	1.44×10^6
13	173,919	(11-13)	0.0885×10^6
14	1,873	(11-14)	0.389×10^6
		(13-14)	0.229×10^6
16	64,422	(14-16)	0.316×10^6
17	14,712	(14-17)	1.38×10^6
18	1,255	(16-17)	0.808×10^6
19	10,600	(17-18)	0.788×10^6
20	44,000	(17-19)	1.50×10^6
		(19-20)	0.625×10^6
		(20-21)	31.083×10^6

LAUNCHER-RELEASE MODEL
IS THE SAME AS ABOVE, EXCEPT THAT

SPRING (19-20) = 0 lb/in.
MASS 13 = 172,159 lb
MASS 16 = 63,580 lb
MASS 19 = 7,010 lb

Fig. 4.7. Atlas/Centaur/Surveyor Longitudinal Model for Atlas Ignition

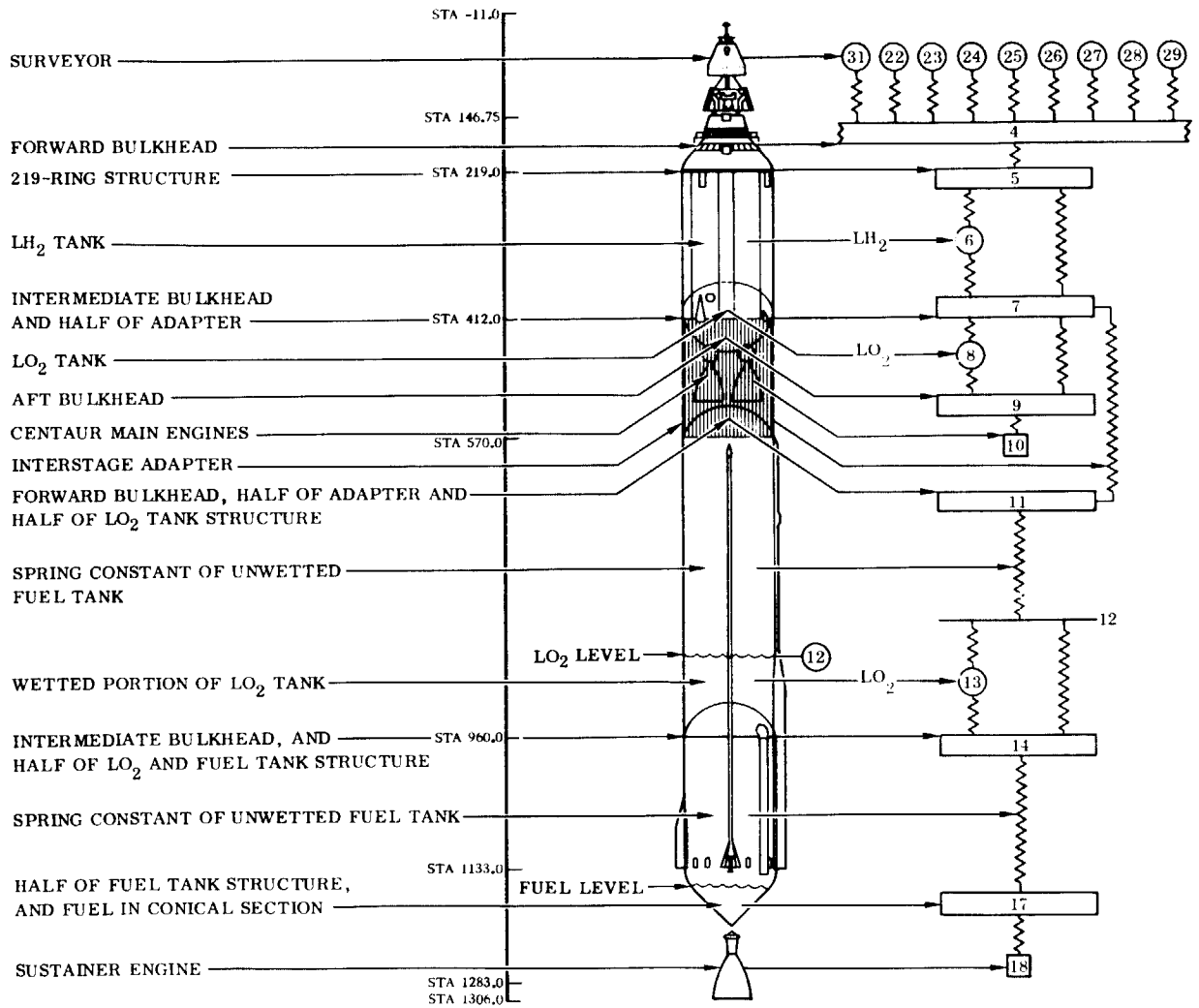

MASS	(lb)	SPRING	(lb/in.)
31	0.138	(31-4)	1.007
22	0.429	(22-4)	12.36
23	2.114	(23-4)	11.86
24	0.789	(24-4)	10.38
25	76.09	(25-4)	1169.2
26	3.785	(26-4)	889.7
27	0.002	(27-4)	0.598
28	19.71	(28-4)	6629.5
29	0.600	(29-4)	2206.2
4	956	(4-5)	$0.548 \cdot 10^6$
5	602	(5-6)	$0.159 \cdot 10^6$
6	5,005	(5-7)	$0.639 \cdot 10^6$
7	819	(6-7)	$0.374 \cdot 10^6$
8	25,082	(7-8)	$8.906 \cdot 10^6$
9	1,273	(7-9)	$-0.328 \cdot 10^6$
10	754	(8-9)	$0.614 \cdot 10^6$
11	2,182	(9-10)	$20.0 \cdot 10^6$
12	0	(7-11)	$1.44 \cdot 10^6$
13	6,648	(11-12)	$0.513 \cdot 10^6$
14	1,873	(12-13)	$0.769 \cdot 10^6$
		(12-14)	$3.35 \cdot 10^6$
17	6,378	(13-14)	$1.98 \cdot 10^6$
18	1,255	(14-17)	$1.60 \cdot 10^6$
		(17-18)	$0.788 \cdot 10^6$

Fig. 4.8. Atlas/Centaur/Surveyor Longitudinal Model Immediately After Nose Fairing Jettison

Below Mass 11 the models for on-the-pad transients and for liftoff are the same except that the launcher has been eliminated for liftoff when the analysis is performed with free modes. In this model the propellant tank representations are as developed in Section 2.2.3. Again ullage pressure effects are omitted and the bulkhead is assumed to be rigid. That part of the fuel in the conical section of the tank is assumed to be a rigid mass lumped with structure at Mass 17. The sustainer engine (Mass 18) is connected to Mass 17 by spring rate AE/L of the conical tank structure. The booster section and its engines (Mass 19) are attached by a spring, the stiffness of which was determined from tests. The launcher-arm mass is included with Mass 19, since it is rigidly attached to the booster and the effective spring rate (19-20) of the launcher is below the arms. The remaining launcher mass is represented at Mass 20, which is connected to ground. The spring rates 20-19 and 20-21 were obtained from static load-deflection tests. For the liftoff condition the masses of LO_2 and fuel are slightly reduced, the mass of the launcher arm is removed from Mass 19, and the vehicle is "freed" (spring 19-20 and the model below are omitted). The modal frequencies and generalized masses are given in Table 4.1.

The sustainer shutdown model has eliminated Mass 19 because it was jettisoned earlier in flight. The fuel is depleted to the extent that all of it is in the conical section. The spring between the conical section and the intermediate bulkhead is the AE/L of the cylindrical fuel tank. The LO_2 level has subsided to Station 918 and the model between Stations 918 and 960 is obtained from Section 2.2.3 by considering the propellant tank extending from Station 918 to 960. The spring from nodes 12 to 11 is the AE/L of the cylindrical tank above Station 918. The modal frequencies and generalized masses corresponding to the representation are given in Table 4.2.

Development of the lateral model of Fig. 4.9 is a straightforward process following the guidelines of Section 2.2. The spring-mass systems attached at Station 173 are derived from modal vibration surveys of the spacecraft. Aft of Station 1133 the model follows two paths, one down the conical portion of the tank to the sustainer engine, the other down the wall of the booster engine section. The wall of the booster section is represented by Masses 46 and 54-59. Masses 60-62 represent the thrust beam, with effective spring rates to the booster wall of K_F (60-54) and K_A (62-56). Mass 63 is the vehicle side of the gimbal point, and Mass 64 is the engine side. The rotational spring between 63-64 is the effective rotational stiffness of the engine actuator system and backup structure, while the lateral spring, 63-64, is the effective stiffness, normal to the thrust axis, of the gimbal block. For convenience, the masses and springs of the two engines are lumped as one. The vehicle is tied to ground by the experimentally determined launcher spring rates between Masses 70 and 71. Tables 4.3 and 4.4 list the stiffness element data and weight data pertaining to the lateral model of Fig. 4.9. The modal frequencies and generalized masses for the lateral model are given in Table 4.5.

Table 4.1. Longitudinal Modal Frequencies and Generalized Masses for Thrust Buildup and Vehicle Liftoff Conditions

THRUST BUILDUP CONDITION, FIXED MODES			VEHICLE LIFTOFF CONDITION, FREE-FREE MODES		
MODE NO.	GEN. MASS ($lb\text{-}sec^2/in.$)	FREQUENCY (cps)	MODE NO.	GEN. MASS ($lb\text{-}sec^2/in.$)	FREQUENCY (cps)
1	553.5	2.75	1	783.9	0
2	20.78	7.12	2	177.5	6.02
3	0.0003580	8.44	3	0.0003580	8.44
4	19.97	9.77	4	7.731	9.43
5	0.001112	16.78	5	0.001112	16.78
6	0.005483	23.42	6	0.005483	23.42
7	69.22	27.74	7	37.05	24.84
8	2.071	29.42	8	2.036	29.40
9	0.6667	33.37	9	0.6667	33.37
10	0.002054	35.87	10	0.002054	35.87
11	1.064	38.90	11	1.066	38.90
12	0.2933	40.02	12	0.2932	40.02
13	0.009846	47.99	13	0.009846	47.99
14	0.000005656	51.75	14	0.000005656	51.75
15	34.85	53.22	15	30.72	56.04
16	0.05178	57.53	16	0.05178	57.53
17	8.470	77.57	17	8.470	77.57
18	4.295	81.91	18	4.374	81.99
19	114.80	84.04	19	33.89	87.35
20	7.686	87.30	20	5.784	115.72
			21	0.001556	189.56

Table 4.2. Longitudinal Modal Frequencies and Generalized Masses for Sustainer Shutdown Condition

MODE NO.	GENERALIZED MASS ($lb\text{-}sec^2/in.$)	FREQUENCY (cps)
1	142.3	0
2	0.0003580	8.44
3	0.4123	16.40
4	0.001115	16.78
5	0.005482	23.42
6	1.737	30.30
7	0.3638	33.64
8	0.002060	35.88
9	1.169	39.16
10	0.3107	40.39
11	0.009863	48.00
12	18.44	51.00
13	0.000005655	51.75
14	0.05187	57.62
15	5.122	87.52
16	33.13	89.26
17	1.642	148.8
18	5.544	163.5
19	0.001556	189.6
20	2.195	368.9
21	3.123	643.3

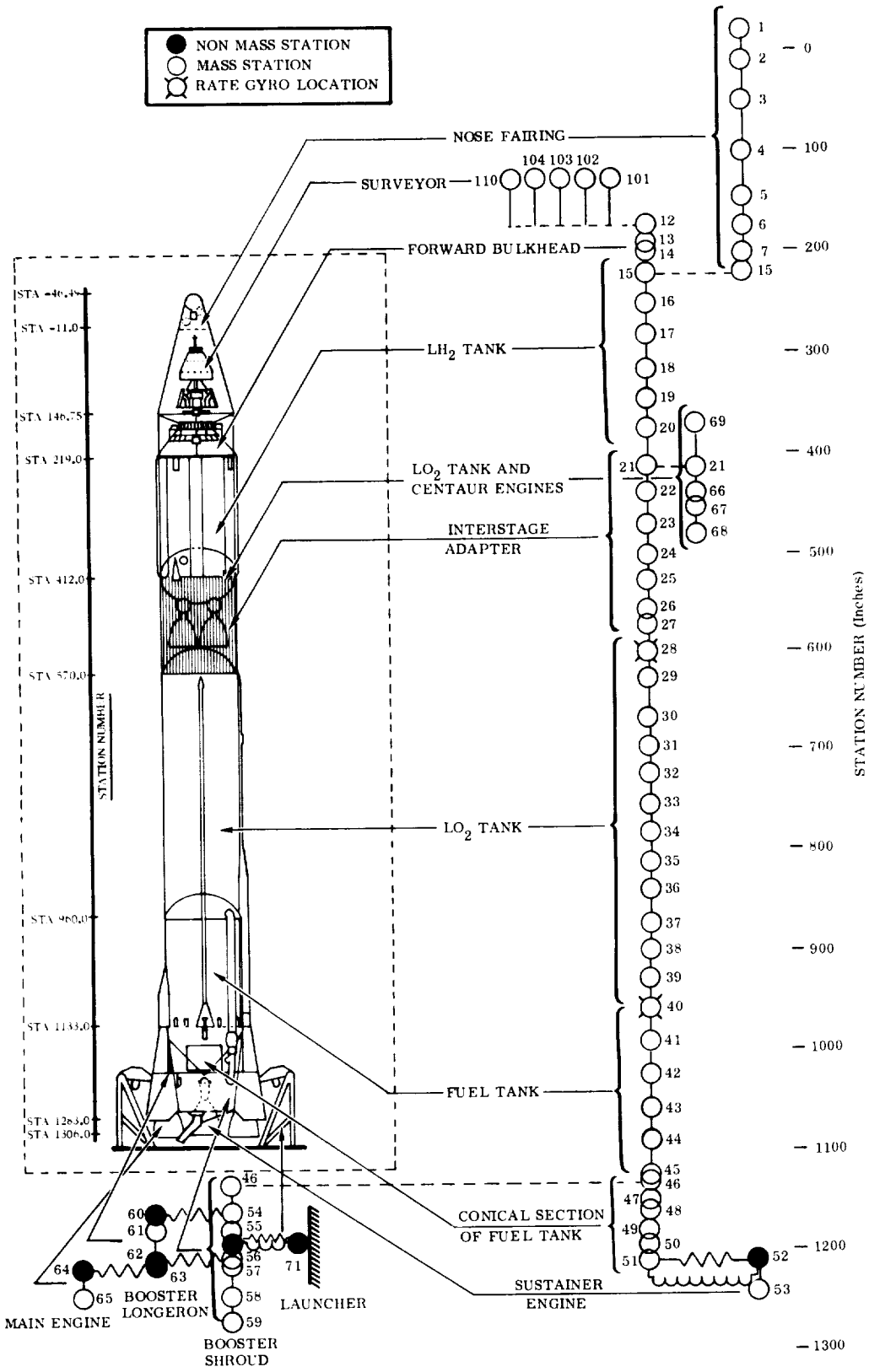

Fig. 4.9. Atlas/Centaur/Surveyor Lateral Model

Table 4.3. Atlas/Centaur/Surveyor Lateral Model Weight Data

NODE NO.	STATION (in.)	WEIGHT (Hundreds of pounds)	MOMENT OF INERTIA (lb-in.^{2})	NODE NO.	STATION (in.)	WEIGHT (Hundreds of pounds)	MOMENT OF INERTIA (lb-in.^{2})
1	-20	1.933833		41	992	104.2039	
2	10	1.489122		42	1025	104.2527	
3	50	1.739427		43	1057	104.1664	
4	100	2.432240		44	1090	103.3811	
5	145	4.121724		45	1122.5	69.42969	
6	173	3.229510		46	1133	46.27086	
7	200	3.028173		47	1150	37.80067	
12	173	7.576172	395,280	48	1160	28.46361	
13	192	2 874967		49	1180	19.06233	
14	200	3.685906		50	1198	6.795801	
15	219	11.310		51	1210	3.585753	
16	250	11.118		52	1210	0.0	
17	280	11.635		53	1240	11.150	884,400
18	315	11.188		54	1160	3.27047	
19	345	10.4267		55	1176	8.8812	
20	375	9.2762		56	1206	13.05785	
21	412	112.686		57	1212	11.47866	
69	388	51.7704		58	1242	7.56912	
66	438	61.54664		59	1267	6.25061	
67	453.5	10.96110		70	1190	0.0	
68	477.7	8.1286		71	1190	0.0	
22	438	2.079684		60	1160	0.0	
23	470	1.912255		61	1176	2.0	28,000
24	500	2.191229		62	1206	0.0	
25	525	3.124462		63	1212	0.0	
26	555	24.17955		64	1212	0.0	
27	570	98.44672		101	70.24	0.74729	
28	600	132.0887		102	78.91	0.26777	
29	630	147.1717		103	-2.22	0.000085	
30	667	144.9370		104	131.87	2.3902	
31	696	127.2731		110	115	17.6685	
32	725	127.1857		76	203.88	3.644	
33	754	129.5109		77	383.7	33.245	
34	784	127.1721	1	78	573.1	101.546	
35	812	122.6780		79	950.6	52.066	
36	840	129.3658	1	80	203.88	0.0	
37	871	131.6285		81	383.7	0.0	
38	900	125.0831		82	573.1	0.0	
39	929	89.67365		83	950.6	0.0	
40	960	99.33865		65	1242	1846.0	1,707,288

Table 4.4. Atlas/Centaur/Surveyor Lateral Model Stiffness Element Data

BEGINNING NODE	ENDING NODE	TYPE	EI AT BEGINNING NODE OR SPRING CONSTANT ($lb\text{-}in.^2$, lb/in., or lb-in./rad)		EI AT ENDING NODE ($lb\text{-}in.^2$)		KAG AT BEGINNING NODE (Millions of pounds)	KAG AT ENDING NODE (Millions of pounds)
101	12	B	1.95251	+08	1.95251	+08		
102	12	B	2.14179	+08	2.14179	+08		
103	12	B	8.72389	+08	8.72389	+05		
104	12	B	7.29353	+08	7.29353	+08		
110	12	B	1.0	+14	1.0	+14		
1	2	B	0.5	+10	1.0	+10	0.3	0.5
2	3	B	1.0	+10	3.0	+10	0.5	0.7
3	4	B	3.0	+10	7.5	+10	0.7	1.5
4	5	B	7.5	+10	14.0	+10	1.5	2.5
5	6	B	14.0	+10	14.0	+10	2.5	2.5
6	7	B	14.0	+10	14.0	+10	2.5	2.5
7	15	B	14.0	+10	14.0	+10	2.5	2.5
12	13	B	4.5	+10	16.7	+10	10.5	19.0
13	14	B	7.00	+10	11.0	+10	19.0	20.5
14	80	B	11.0	+10	16.20	+10	20.5	25.1
80	15	B	16.20	+10	25.0	+10	25.1	22.7
80	76	TS	11.31					
15	16	B	25.5	+10	25.0	+10	28.9	28.9
16	17	B	25.5	+10	25.5	+10	28.9	28.9
17	18	B	25.5	+10	25.5	+10	28.9	28.9
18	19	B	25.5	+10	25.5	+10	28.9	28.9
19	20	B	25.5	+10	25.5	+10	28.9	28.9
20	21	B	25.5	+10	25.5	+10	28.9	28.9
81	69	B	10.0	+10	15.0	+10	21.0	22.5
81	77	TS	178.94					
69	21	B	14.0	+10	25.5	+10	22.58	29.0
21	66	B	32.0	+10	10.5	+10	37.5	30.0
66	67	B	10.5	+10	18.2	+10	30.0	15.0
67	68	B	56.5	+10	6.28	+10	214.0	21.4
21	22	B	43.5	+10	43.5	+10	45.5	45.5
22	23	B	43.5	+10	43.5	+10	45.5	45.5
23	24	B	43.5	+10	43.5	+10	45.5	45.5
24	25	B	43.5	+10	43.5	+10	45.5	45.5
25	26	B	43.5	+10	43.5	+10	45.5	45.5
26	27	B	43.5	+10	43.5	+10	45.5	45.5
27	82	B	25.6	+10	25.6	+10	29.0	29.0
82	28	B	25.6	+10	25.6	+10	29.0	29.0
82	78	TS	441.9					
28	29	B	25.6	+10	25.6	+10	29.0	29.0
29	30	B	25.6	+10	25.6	+10	29.0	29.0
30	31	B	27.6	+10	27.6	+10	31.0	31.0
31	32	B	31.2	+10	31.2	+10	35.0	35.0

Table 4.4. Atlas/Centaur/Surveyor Lateral Model Stiffness Element Data, Contd

BEGINNING NODE	ENDING NODE	TYPE	EI AT BEGINNING NODE OR SPRING CONSTANT ($lb\text{-}in.^2$, lb/in., or lb-in./rad)		EI AT ENDING NODE ($lb\text{-}in.^2$)		KAG AT BEGINNING NODE (Millions of pounds)	KAG AT ENDING NODE (Millions of pounds)
32	33	B	32.9	+10	32.9	+10	37.5	37.5
33	34	B	34.8	+10	34.8	+10	39.5	39.5
34	35	B	34.8	+10	34.8	+10	39.5	39.5
35	36	B	34.8	+10	34.8	+10	39.5	39.5
36	37	B	36.6	+10	36.6	+10	41.5	41.5
37	38	B	38.4	+10	38.4	+10	43.5	43.5
38	39	B	42.0	+10	42.0	+10	47.5	47.5
39	83	B	44.0	+10	44.0	+10	49.8	49.8
83	40	B	44.0	+10	44.0	+10	49.8	49.8
83	79	TS	241.0					
40	41	B	47.6	+10	47.6	+10	54.0	54.0
41	42	B	47.6	+10	47.6	+10	54.0	54.0
42	43	B	49.6	+10	49.6	+10	56.0	56.0
43	44	B	51.3	+10	51.3	+10	58.0	58.0
44	45	B	53.2	+10	53.2	+10	60.0	60.0
45	46	B	62.2	+10	62.2	+10	70.5	70.5
46	47	B	46.0	+10	34.0	+10	47.5	47.5
47	48	B	34.0	+10	27.0	+10	47.5	45.0
48	49	B	39.0	+10	6.5	+10	63.0	25.0
49	50	B	6.5	+10	1.5	+10	25.0	10.0
50	51	B	1.5	+10	1.5	+10	10.0	10.0
51	52	RS	1.2	+07				
51	52	TS	0.92	+09				
52	53	B	2.0	+12	2.0	+12	1000.0	1000.0
46	54	B	88.0	+10	83.0	+10	105.0	107.0
54	55	B	83.0	+10	88.0	+10	107.0	118.0
55	70	B	88.0	+10	89.0	+10	118.0	121.0
70	56	B	89.0	+10	90.0	+10	121.0	125.0
70	71	RS	2.738	+09				
70	71	TS	2.222	+05				
56	57	B	33.8	+10	33.7	+10	18.0	18.0
57	58	B	33.7	+10	33.4	+10	18.0	18.0
58	59	B	33.4	+10	33.0	+10	18.0	18.0
54	60	TS	1.2	+05				
56	62	TS	1.5	+05				
60	61	B	1.0	+12	1.0	+12	500.0	500.0
61	62	B	1.0	+12	1.0	+12	500.0	500.0
62	63	B	1.0	+12	1.0	+12	500.0	500.0
63	64	TS	1.0	+10				
63	64	RS	8.55	+07				
64	65	B	1.0	+12	1.0	+12	500.0	500.0

NOTE: Symbols in third column indicate B = Beam, TS = Translational Spring, RS = Rotational Spring. Values on the right side of the fourth and fifth columns indicate powers of 10, i.e., 1.95251×10^8.

Table 4.5. Lateral Modal Frequencies and Generalized Masses For Thrust Buildup Condition

MODE NO.	GENERALIZED MASS (lb-sec^2/in.)	FREQUENCY (cps)
1	63.12	0.315
2	0.9614	0.553
3	36.05	0.668
4	21.86	0.675
5	10.36	0.750
6	28.26	1.85
7	19.07	4.51
8	8.666	6.93
9	6.572	7.70
10	0.2075	8.44
11	7.264	9.13
12	8.944	10.12
13	2.079	11.88
14	8.995	13.91
15	0.07172	16.83

4.4.2 LONGITUDINAL LOADS

4.4.2.1 Engine Start on the Pad. The analysis for this condition uses the longitudinal model of Fig. 4.7. For longitudinal load analyses the initial deflections due to gravity were calculated and used as initial conditions for the response solution. Gravity forces on each mass were also imposed for the response solution to obtain total loads, including gravity. The engine forces used are shown in Fig. 4.10. These engine thrust buildup curves are envelopes of maximum buildup rates and peak thrusts obtained during manufacturers test runs. (The buildup analysis could be done without gravity forces and initial deflections. The gravity loads would then be added to the transient loads.)

The results of the response calculations using Adam's method of Section 2.4 are given in Figs 4.11 and 4.12. The transient acceleration at the Centaur/Surveyor interface, Station 173, is shown in Fig. 4.11. (The acceleration does not include gravity.) The normal-mode-coordinate displacements in Fig. 4.12 show that the response is primarily in the first four modes. Fifteen modes were used in the analysis but only the first eight are plotted. The initial deflections and gravity loads are seen represented at time zero.

4.4.2.2 Vehicle Liftoff. Liftoff analysis is undertaken using the free-free modes of the model in Fig. 4.7. Initial deflections due to thrust, gravity, and launcher forces are calculated and used as initial conditions. In the response solution the gravity

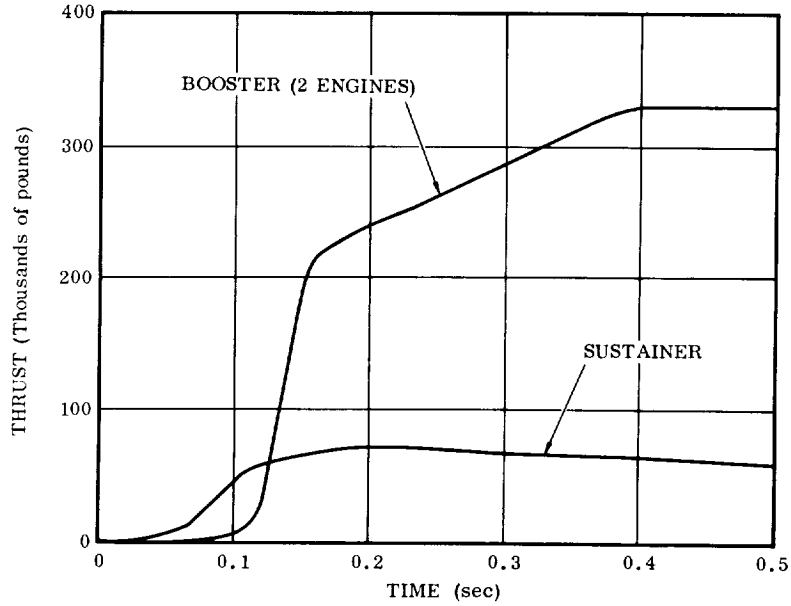

Fig. 4.10. Atlas Engine Thrust Buildup Time Histories

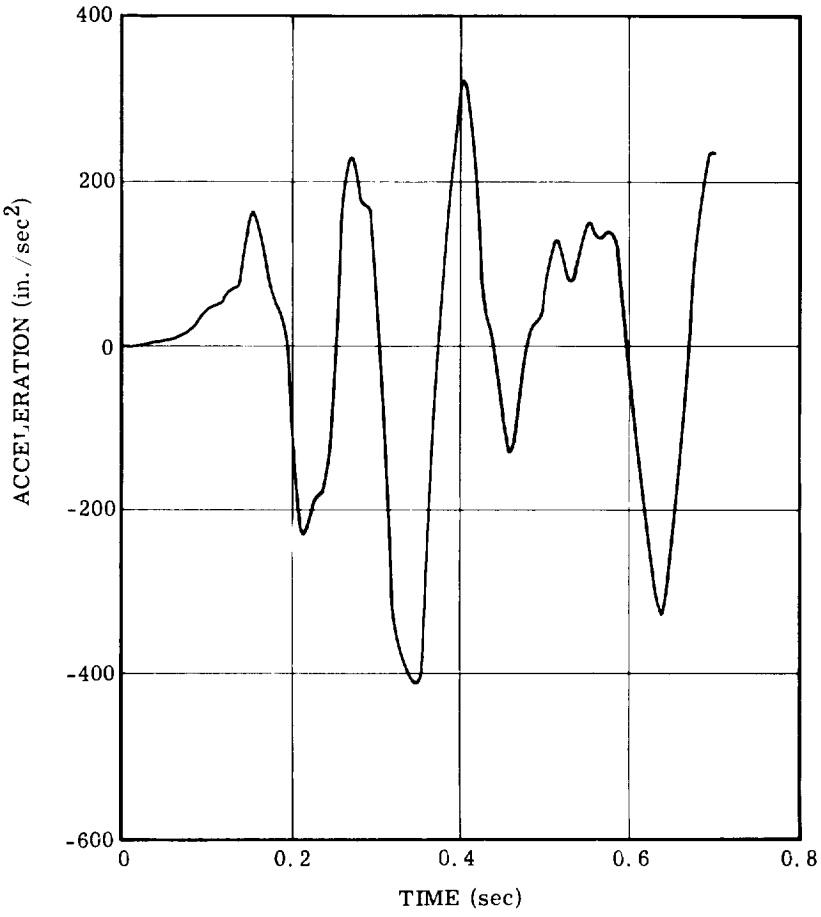

Fig. 4.11. Centaur/Surveyor Interface Longitudinal Accelerations at Atlas Engine Thrust Buildup

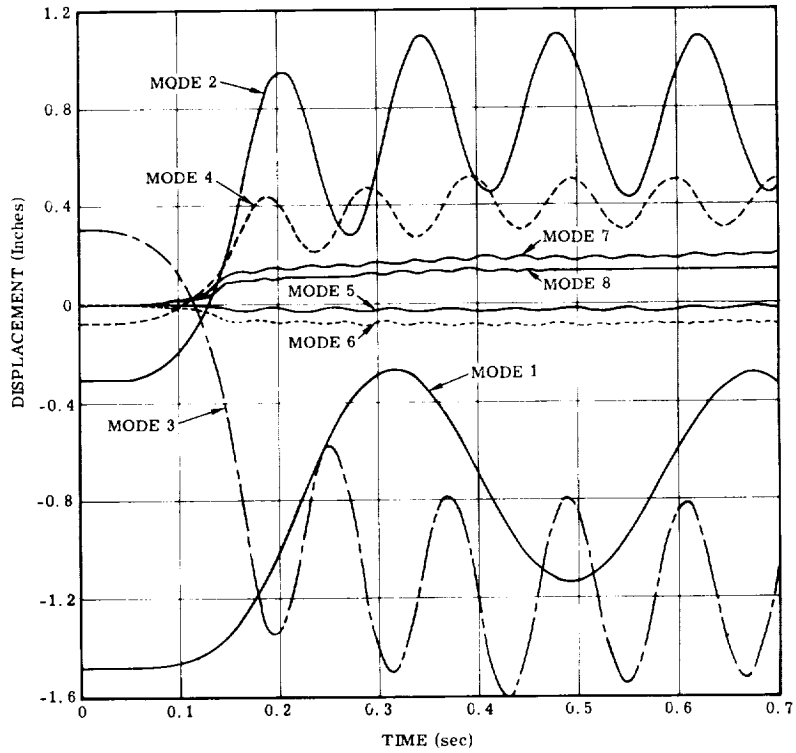

Fig. 4.12. Longitudinal Normal-Mode-Coordinate Displacements at Atlas Engine Thrust Buildup

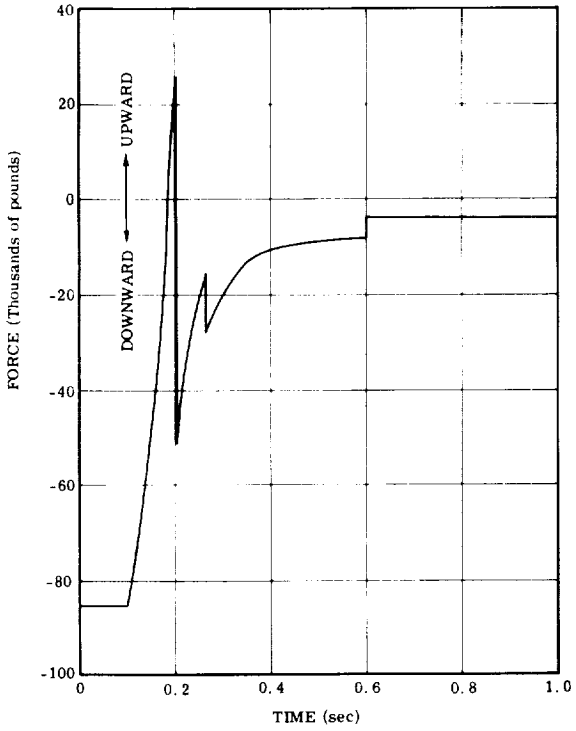

Fig. 4.13. Net Atlas Launcher Force During Launcher Release

forces are applied to each mass, the steady engine thrusts at Masses 18 and 19, and the launcher force at Mass 19. The time history of the net launcher force is given in Fig. 4.13. The net launcher force is the summation of four forces exerted by the launcher on the vehicle. These forces are the holddown launcher arm force, the auxiliary launcher-arm force, the rise-off disconnect force, and the inertial force of the launcher arms. Initially, all these forces are acting; however, as the vehicle moves upward, all are removed. The holddown launcher-arm force is the force exerted by pneumatic cylinders (in the Atlas system) to restrain the vehicle. To accomplish the vehicle release the pressure in the cylinders is released. When the pressure drops below that required to restrain the vehicle the vehicle begins to move upward. When the pressure has dropped sufficiently the arms are

disconnected. In Fig. 4.13, vehicle motion begins at 0.1 second and the arms are disconnected at 0.6 second. The step at 0.6 second represents a small residual pressure at arm disconnect. The auxiliary arm force is a constant upward force for the first 0.102 second of motion and is then removed. This removal is seen at 0.202 second in Fig. 4.13. The rise-off disconnect force is a constant upward force for the first 0.164 second of motion. Its removal is seen at 0.264 second in Fig. 4.13. The weight of the launcher arms is a downward force; it is assumed constant from 0 to 1.0 second.

With the model and applied forces described, the response is calculated using Adam's numeric integration. The acceleration at Station 173 is shown in Fig. 4.14 and the normal-mode-coordinate displacements are given in Fig. 4.15. In contrast to the thrust buildup condition, there is significant response in higher modes caused by the abrupt changes in the applied force.

4.4.2.3 Inflight Engine Shutdown. Engine shutdown in flight is illustrated with the model of Fig. 4.8. The initial conditions for this analysis are the quasi-steady inertial loads on the masses, the sustainer thrust at altitude, and the associated deflections. The sustainer engine shutdown characteristics are given in Fig. 4.16,

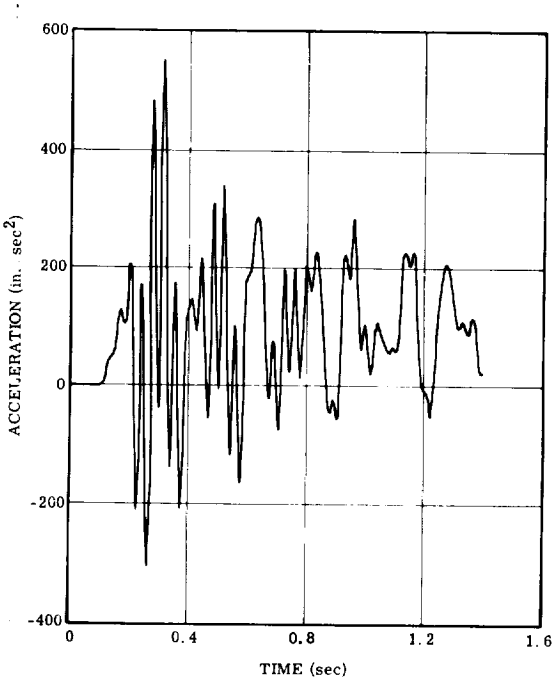

Fig. 4.14. Centaur/Surveyor Interface Longitudinal Accelerations at Liftoff

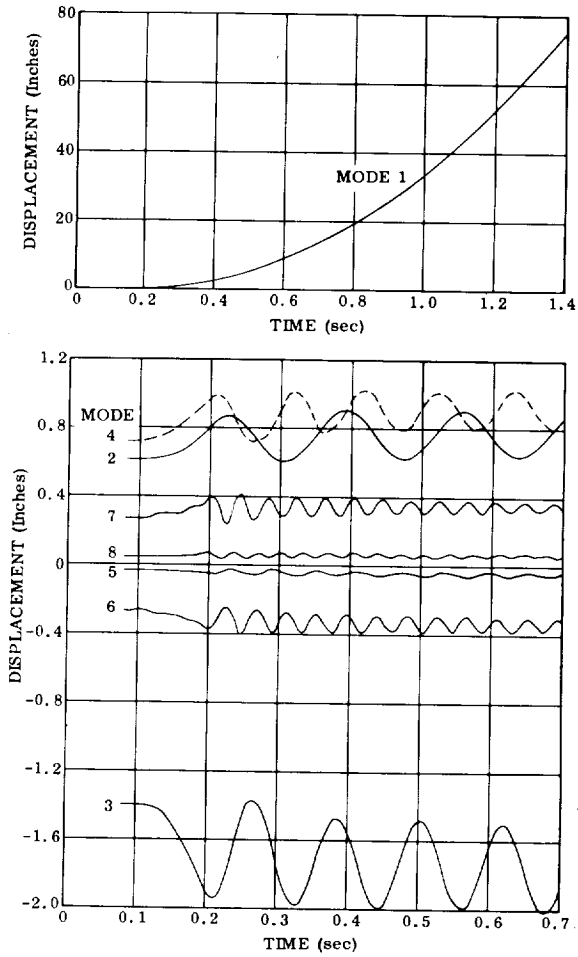

Fig. 4.15. Longitudinal Normal-Mode-Coordinate Displacements at Vehicle Liftoff

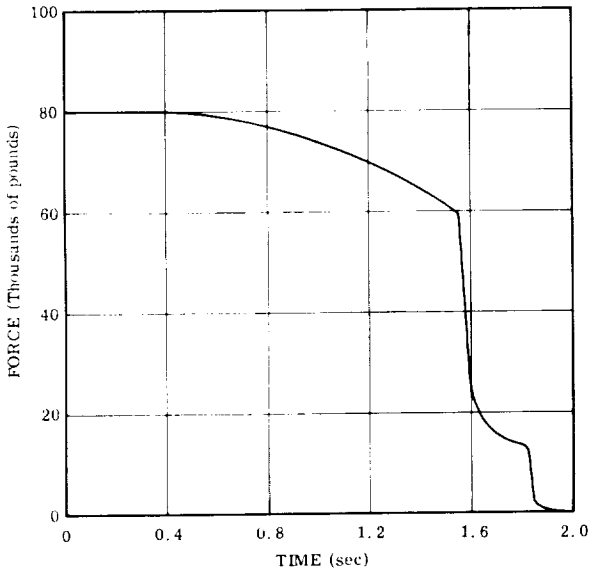

Fig. 4.16. Thrust Decay Time History at Sustainer Engine Shutdown

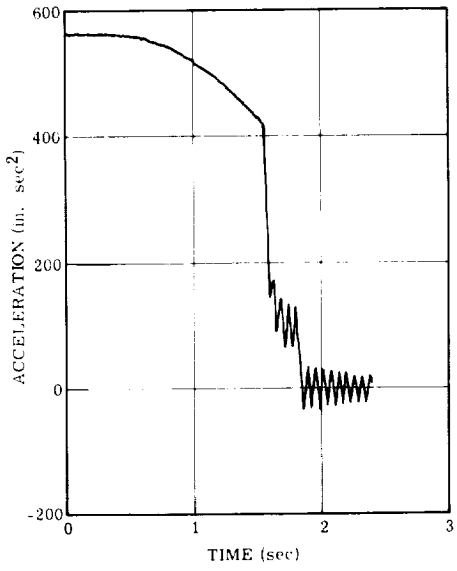

Fig. 4.17. Centaur/Surveyor Interface Longitudinal Accelerations at Sustainer Engine Shutdown

which is taken from test data. The acceleration at Station 173 is given in Fig. 4.17 and the normal-mode-coordinate displacements are shown in Fig. 4.18. It should be noted that the results apply only while vehicle is under some thrust. As the thrust drops, the energy in the structure supporting the propellant will give the liquid a velocity relative to the tank. At some time, the propellant is moving inside the tank without physical contact longitudinally. When this "free fuel" situation occurs a new mathematical model is required. Generally, the items of significance are the peak transients, which are valid. (The propellant velocity at the time the acceleration of the liquid becomes zero will give initial conditions for the liquid under zero g conditions.)

4.4.3 LATERAL LOADS. Lateral loads have been calculated for the condition of differential buildup of engine thrust. The applied loads are the result of lateral components of the thrust vector and differential thrust of the two engines. For this example it is assumed that there is no thrust-vector misalignment. The moment due to unsymmetric engine start has been obtained by taking the differential thrust of the two engines in an actual firing and multiplying by the lateral distance from the vehicle centerline of the engine support point. The associated moment time history is shown in Fig. 4.19. Applying this moment at Mass 57 of the lateral model in Fig. 4.9 provides the necessary description of excitation to proceed with response calculations. Results are shown in the graphs of Figs 4.20 and 4.21. The normal-mode-coordinate displacements are shown in Fig. 4.22.

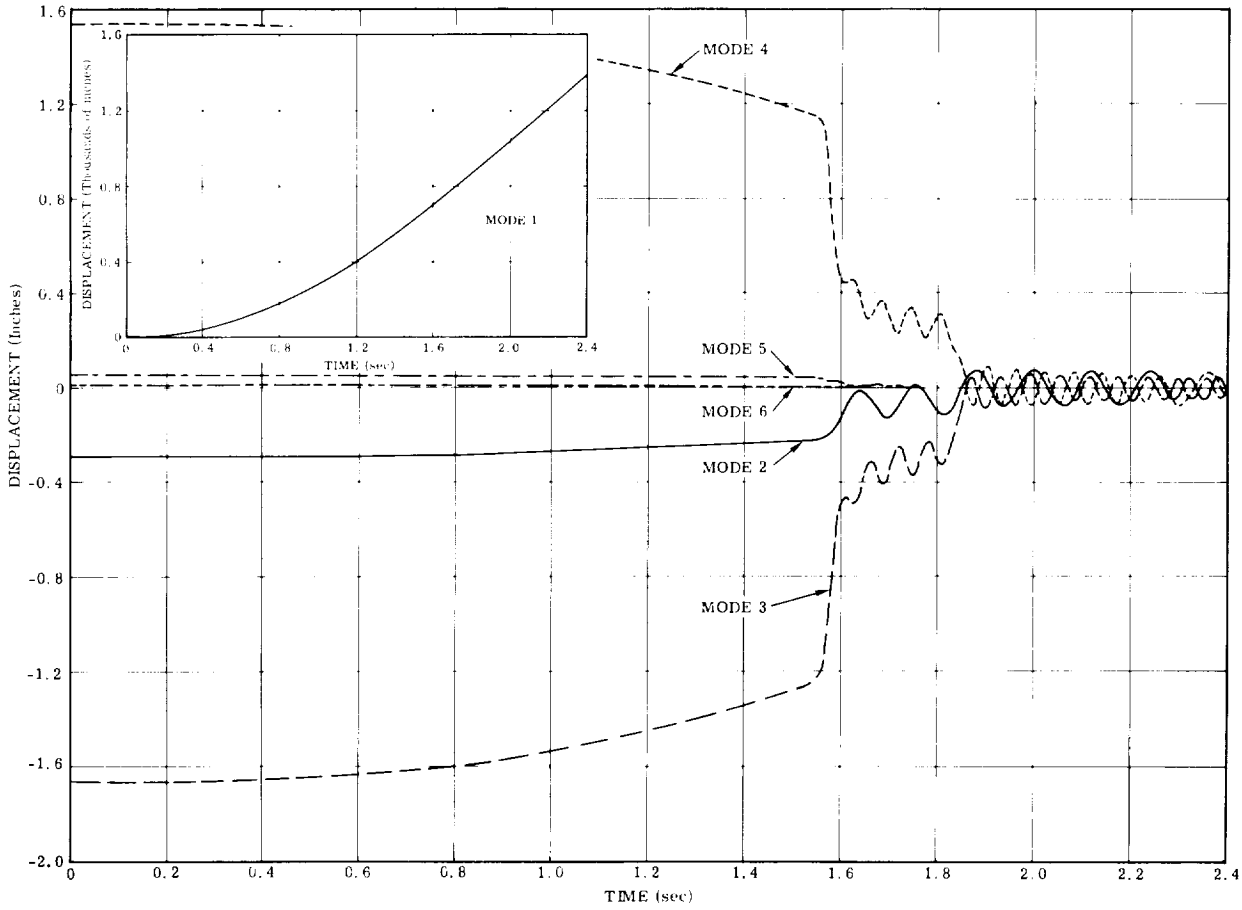

Fig. 4.18. Longitudinal Normal-Mode-Coordinate Displacements at Sustainer Engine Shutdown

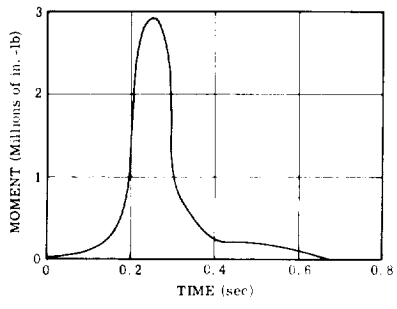

Fig. 4.19. Applied Moment Time History at Atlas Engine Thrust Buildup

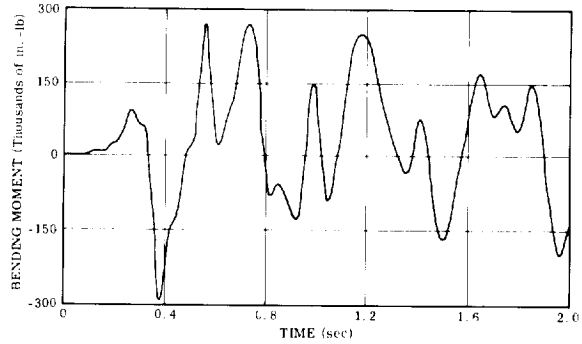

Fig. 4.20. Atlas/Centaur Interface Bending Moments at Atlas Thrust Buildup

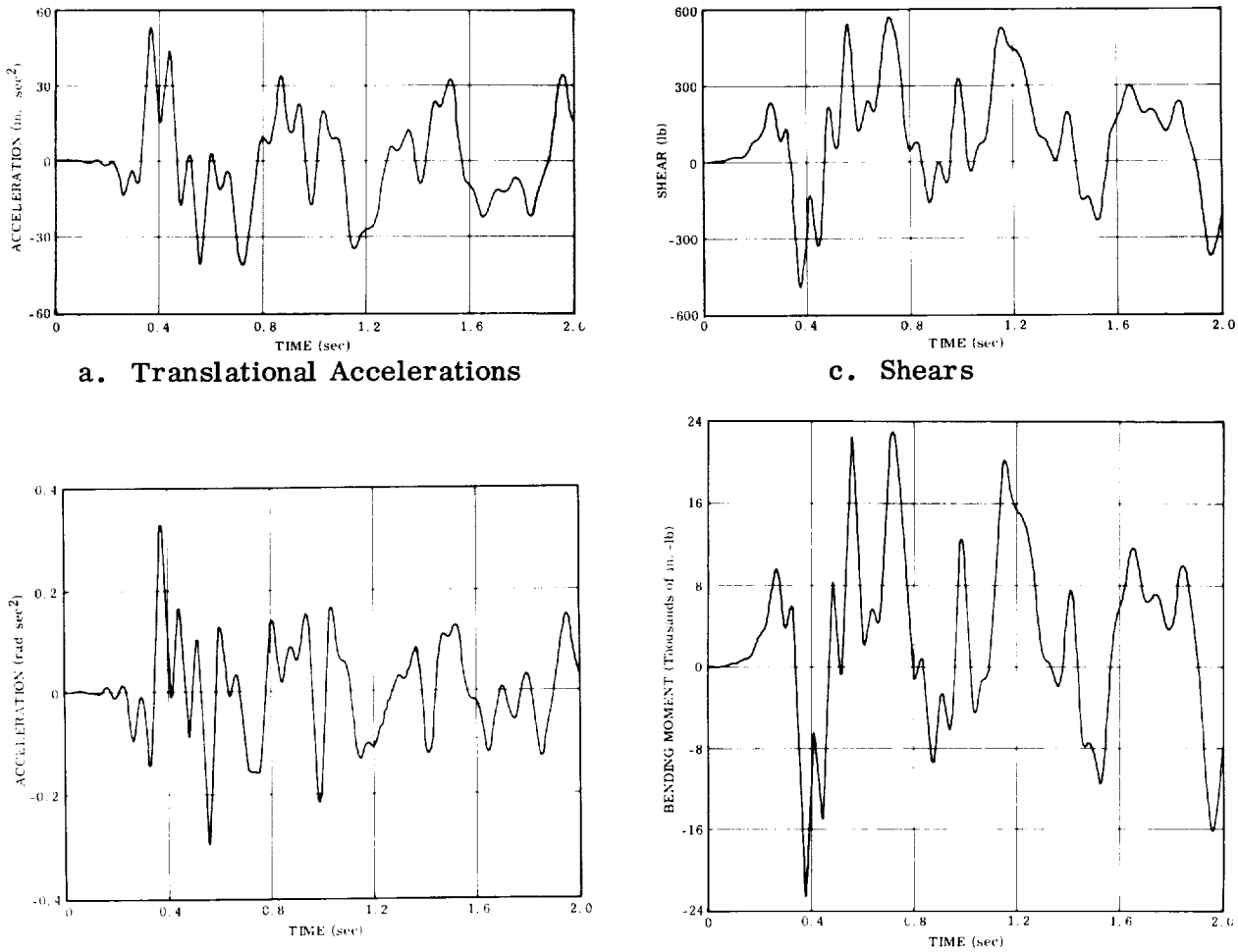

Fig. 4.21. Centaur/Surveyor Interface Lateral Loadings at Atlas Engine Thrust Buildup

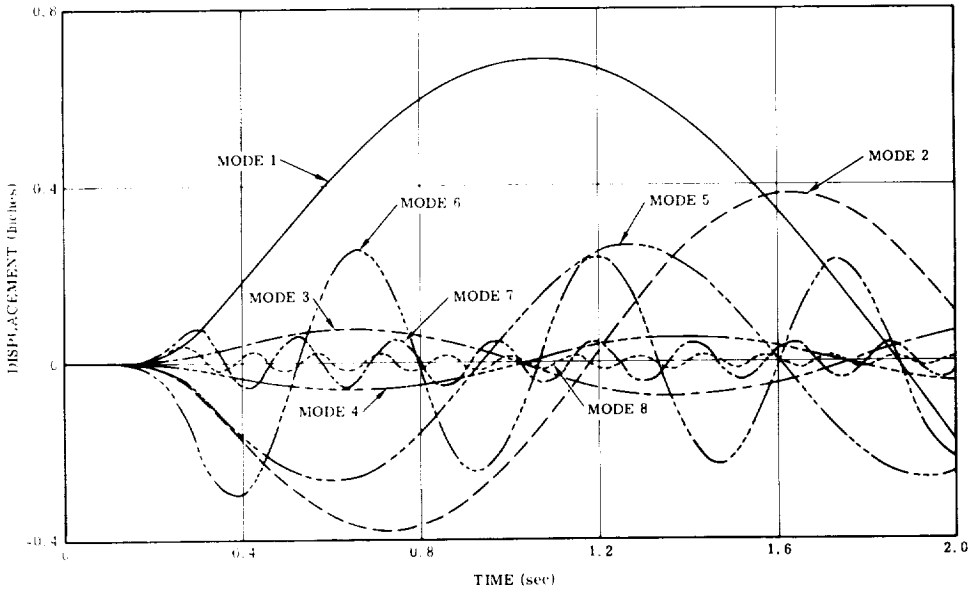

Fig. 4.22. Lateral Normal-Mode-Coordinate Displacements at Atlas Engine Thrust Buildup

4.5 DISCUSSION

From the preceding examples it is evident that the thrust-transient loads analyses are relatively straightforward after the mathematical model and applied forces are defined. Comments on the model development are given in Sections 2.2.3 and 4.4.1. In this discussion comments will be related to applied forces, resulting loads, and combinations of loads. Special considerations to be examined for vehicles include engine-vehicle stability and high-frequency transients. It must be remembered that these comments are general and that often in practice what could be done and what is done are dependent on schedule, available information, and relative importance of various aspects of the total vehicle program. As an example, design loads can be determined from worst-case combinations or from a statistical evaluation of all the loads. From a schedule standpoint, it may not be possible to gather all the data necessary for a statistical study (or the data are just not available) to provide design loads; therefore, the expedient and conservative worst-case combination approach is indicated.

Other problems, such as Pogo (discussed in Section 4.5.5), have occurred on some vehicles but not on others. Possible behavior of this nature should be examined in enough detail such that the probability of surprise is small.

4.5.1 ENGINE FORCES. Liquid-propellant rocket-engine characteristics during starting and shutdown are dependent on propellant temperatures, head pressure, manufacturing tolerances, and other parameters. As a result, the engine thrust buildup and decay curves have significant variations from run to run on one engine and also among different engines. These variations are compounded with launch vehicle configurations using multiple-engine systems because timing delays, variations in plumbing, thrust-vector alignment, and variations in engine performance all have tolerances. No single thrust time history accurately describes the propulsive excitation applied to the vehicle. For longitudinal loads analyses, either of two basic approaches is used to derive the design loads. In the first approach, a few response analyses are made with typical thrust time histories to determine significant parameters. From this preliminary analysis with available thrust time histories, a synthetic force time history is developed to represent a worst-case envelope. The significant parameters are usually rise rate, peak transient thrust, and frequency content. The envelope so derived is then used for loads analysis.

The second approach is a statistical study of response to a large number of thrust time histories. A response analysis is performed for every available (or a very large sample) thrust time history, or in the case of multiple-engine systems, combinations selected at random. A statistical study of the response will then give the mean and the variance of loads from which design loads are specified. This approach involves the expenditure of considerable execution time which must be repeated whenever there is a significant design change in the vehicle.

Inputs for lateral responses are obtained by similar procedures. Thrust misalignment can be the maximum allowed by the manufacturer or it can be a statistical distribution of the tolerance. With multiple engines, there is the added consideration of combining the direction of misalignment of individual engines. Also, with multiple-engine systems, the engines undoubtedly will have different thrust time histories which will produce a time-varying application of moment to the vehicle. Establishment of the thrust differential constituting the applied moment may, again, be developed from worst-case combinations. A Monte-Carlo technique, using engine test curves selected at random, can provide a method for describing the response statistically. The variation in the time at which the different engines receive the start signal must also be considered in establishing meaningful bounds on the differential thrust. In general, secondary loads, such as produced by lateral response to thrust-vector misalignment and differential engine thrust are small compared with total loads on the vehicle. A worst-case simulation is often adequate for establishing a "design" load associated with the mode of "loads addition." For some vehicles, the start time is deliberately staggered to reduce transient effects. The staggered start time must be examined in great detail, including performance tolerances in the separate engine systems, to obtain the system-peculiar loads criteria defining input forces and response. It is, indeed, possible to select a staggered start which will reduce vehicle elastic response, but is it also possible to select a start sequence which will result in more critical loads than a simultaneous start with random engine characteristics.

The reduction in transient longitudinal load by staggered start or by statistical study of response can be significant in designing certain parts of the vehicle and launcher system. It is necessary to examine all the relevant loading conditions during vehicle life and then to establish a compatible structural design. An evaluation of this type often determines the detail of the analysis. Also, other phenomena may be a controlling variable. As an example, a simultaneous start of all engines can produce pressure waves in the exhaust ducts which could be harmful to the vehicle. The design significance of the pressure wave is subject to reduction by a staggered start. This consideration could be the predominant factor in deciding between staggered and simultaneous starts and could be important in establishing the stagger time. Deciding what has to be done and what can be done is often more difficult than performing the analysis.

4.5.2 METHOD OF LAUNCH. Two methods are employed for launch of space vehicles. Most commonly, a vehicle is held down until its engines are at full thrust. It is released at some specified time interval after full thrust. The release is commonly "instantaneous" or "controlled." One other method is the "free launch," wherein the vehicle is not held down and will lift off when the thrust is equal to the weight. The holddown is used for almost all space launches, while the free launch is used in weapon systems. Free launch eliminates complicated launcher and control mechanism and thus is better from maintenance and operations standpoints. Holddown permits abort if initial engine and vehicle operation is not satisfactory. Thereby, it adds a safety factor in the success of a specific payload mission.

Advantages and disadvantages between the two methods related to vehicle loads are dependent on vehicle and engine characteristics. With a holddown, minimum transient loads are incurred during engine thrust buildup if the launcher tiepoints are close to points of engine load application and the stiffness of the launcher is great so that most of the thrust forces are reacted by the launcher with small deflection. The same effect is obtained in a free launch system if the vehicle structure from the engine to the ground support point is very stiff. This permits a transition from gravity loads being supported by ground to support by engine thrust without significant change in deflections and, in turn, no large transient loads to upper parts of the vehicle.

The liftoff loads are determined by the rate that thrust minus launcher forces exceeds the weight of the vehicle. An instantaneous release would give a step change and the most severe liftoff transients. The free launch would give a liftoff transient determined by the engine thrust time history. One disadvantage of free launch is that the engine buildup and liftoff transients are in fact one condition. With a holddown these transients are separated slightly and some relief, due to damping and phasing, can be expected because of the time interval.

In general, a holddown and controlled release will result in minimum vehicle loads. The amount of load reduction will depend on the vehicle and launcher characteristics. Indeed, launcher characteristics can be specified as a function of vehicle loads. These characteristics may be effective spring rate, tie-down point, and rate and stroke of release.

4.5.3 COMBINATION OF LOADS. A complete description of loads at engine ignition and vehicle liftoff would include longitudinal and lateral steady-state and transient loads discussed in the preceding sections, wind loads, vehicle misalignment or center-of-gravity offset, vehicle loads incurred due to controlling the vehicle, or any other load that is imposed at this time. Adding the worst-case conditions of all the above loads is often used to obtain the total load. Certainly for ground equipment this is the only reasonable approach. For parts of the vehicle designed by this total load some weight saving could be gained by statistical combination of loads but, generally, the weight saving is small in terms of pounds of payload and the applied forces are not too well described so that a good statistical analysis cannot be made. Therefore, it is recommended that worst-case combinations be used to specify design loads for vehicles.

There are occasions when a designed vehicle is to be used with a new stage or payload. In order to minimize modification costs it may be necessary to determine whether the vehicle is able to sustain the loads. In this case the reduction in load by a statistical combination of loads is justified.

For purposes of statistical analyses the loads to be combined are assumed to be independent and normally distributed. The quantities required for analyses are (from Ref. 4.6)

$\bar{\eta}_r$ = average of load r (mean)

σ_r ≡ variance or standard deviation of load r

$\bar{\eta}_r^2$ ≡ square of the mean

$\overline{\eta_r^2}$ ≡ second moment (mean square)

$$\overline{\eta_r^2} = \bar{\eta}_r^2 + \sigma_r^2$$

Probability theory shows that for any number of random variables η_r, the combined values η are obtained by

$$\bar{\eta} = \sum_r \bar{\eta}_r$$

$$\overline{\eta^2} = \sum_r \overline{\eta_r^2} + \sum_r \sum_s \bar{\eta}_r \bar{\eta}_s \Big|_{r \neq s}$$

$$\sigma^2 = \overline{\eta^2} - \bar{\eta}^2$$

$$= \sum_r \bar{\eta}_r^2 + \sum_r \sigma_r^2 + \sum_r \sum_s \bar{\eta}_r \bar{\eta}_s \Big|_{r \neq s} - \sum_r \bar{\eta}_r^2 - \sum_r \sum_s \bar{\eta}_r \bar{\eta}_s \Big|_{r \neq s}$$

$$= \sum_r \sigma_r^2$$

$$\sigma = \sqrt{\sum_r \sigma_r^2}$$

The three-sigma combined load is then $\bar{\eta} + 3\sigma$.

As an example, consider combining vertical and lateral loads due to thrust rise with ground wind loads. The probability distributions of these loads are illustrated in Fig. 4.23. The lateral loads are to be considered as expressed in terms of equivalent axial loads. Also, the three loading conditions are assumed to be independent.

The sum of the mean loads is

$$P_{AVE} = A + C + E \tag{4.9}$$

and the combined variance is

$$\sigma_P = \left(\sigma_{P_Z}^2 + \sigma_{P_L}^2 + \sigma_{P_W}^2 \right)^{1/2} \tag{4.10}$$

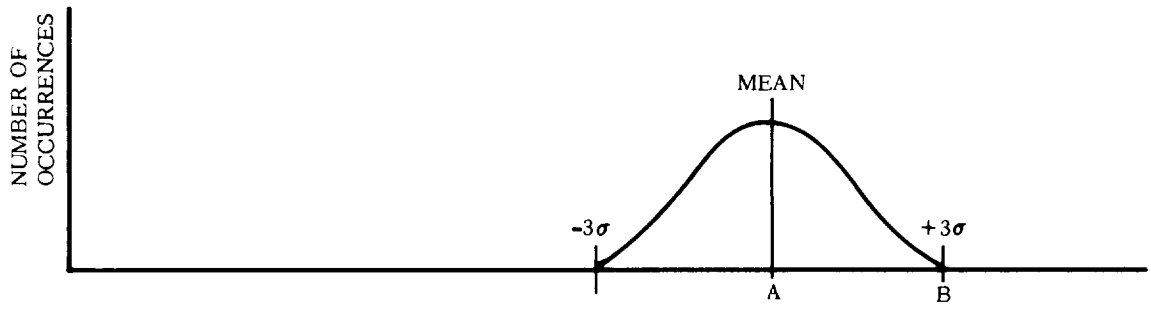

a. P_Z, Axial Loads Due to Thrust Buildup and Gravity

b. P_L, Lateral Loads Due to Thrust Buildup

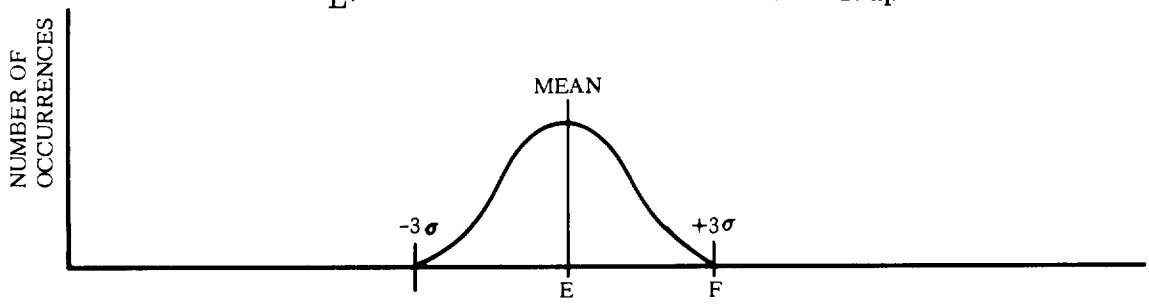

c. P_W, Lateral Loads Due to Ground Winds

Fig. 4.23. Load Distribution Probability

where

$$\sigma_{P_Z} = \frac{B - A}{3}$$

$$\sigma_{P_L} = \frac{D - C}{3}$$

$$\sigma_{P_W} = \frac{F - E}{3}$$

The three-sigma combined load is then

$$P = P_{AVE} + 3\sigma_P \tag{4.11}$$

Although the statistical combination appears straightforward it is necessary to gather much information to describe the properties of each variable. Indeed, this information is not always readily available.

4.5.4 CONTROL SYSTEM ACTIVATION. The disturbances of engine thrust buildup or decay and vehicle liftoff can cause an error in vehicle orientation with respect to the desired trajectory and can also excite the bending modes. Upon activation of the control system it will command the engines to correct vehicle attitude. Also, the control system may respond to the sensed vehicle bending. Loads corresponding to the attitude correction can be obtained from control studies which would give an envelope of commanded engine gimbal angle required for the correction. Applying this amplitude (as a force), with a time history compatible with maximum possible engine gimbal rate, to the vehicle will give the vehicle loads. The control system should be designed so that it does not aggravate these initial bending moments. However, if a limit-cycle* instability should occur because of bending mode feedback from the sensor, the magnitude of load during this limit cycle can be determined by the frequency response solution presented in Section 6.

4.5.5 LONGITUDINAL INSTABILITIES. The combined vehicle system of structure, mass, pneumatic system, propellant ducting, and propulsion system can couple to produce instabilities and limit cycles. An example is the 5-cps limit cycle shortly after liftoff on the Atlas vehicle. This phenomenon is due to coupling between the vehicle modes and the pneumatic sensing and feed systems. Another example is the Pogo problem of the Titan and Thor vehicles where limit cycles later in flight were caused by coupling of the vehicle, propellant ducting, and engine systems. Problems of this nature are very dependent on characteristics of each system. These characteristics can vary considerably from one vehicle to another. The work of Ref. 4.4 discusses these problems and gives methods for analyses which can be used for predesign evaluation on the existence of the problem and for identification of significant parameters.

4.5.6 HIGH-FREQUENCY EXCITATION. The discussion in the previous sections pertains to excitation of the low-frequency modes of the vehicle. Perturbations in some of the vehicle systems can also excite the higher frequency modes of the vehicle or its systems. Sources of the excitation can be high-frequency pressure oscillations in the thrust chambers, pump speeds, and operation of other mechanical equipment. These phenomena are not amenable to analysis because of unsatisfactory mathematical models for representation of the higher modes. In these higher modes there generally is coupling between lateral, longitudinal, torsion, shell, and individual component modes. The problem can be attacked by two methods. One, the vibration tests for components should include provision for adequate levels in the suspect frequency regions. Two, using test data describing input, response, or vehicle modes an approximate analysis can be made that will give some information on loads. As an example, a 70-cps transient of a few cycles in duration exists in booster engine chamber pressure during the shutdown of the Atlas engines. From flight data it was found that

*Limit cycle is a term describing an "instability" which reaches a peak amplitude but does not diverge beyond this peak, usually because of system nonlinearities.

a torsional mode was excited by this transient. Physical coupling between longitudinal excitation and torsion response of a magnitude indicated by the flight data could not be established. Therefore, using theoretical torsion modes and flight response data, a fictitious forcing function was derived which gave the recorded response. To evaluate the accuracy of this analysis a physical change in the vehicle was made on a succeeding flight and the change in response was found to agree with predicted change. This established some validity in the analysis.

The solution of these problems is not straightforward and does require test data to identify the problem and controlling variables. Wherever possible, the conditions should be treated analytically so that subsequent vehicle changes do not require expensive test programs to verify the effect of the change.

4.6 CONCLUSIONS AND RECOMMENDATIONS

Methods of analysis for response to engine transients are well developed for cylindrical-tank liquid-propellant launch vehicles. For propellant tank shapes other than cylindrical, development work is necessary to obtain a satisfactory mathematical model representing the vehicle.

The recommended procedure is as follows.

1. Develop a mathematical model as given in Sections 2.2.4.3 and 4.3.
2. Obtain a description of applied force time history from engine test data.
3. Use a worst-case condition for design loads. If the worst-case condition is detrimental to vehicle performance then a statistical analysis of engine characteristics and vehicle response should be attempted.
4. Perform analyses for lateral loads due to engine misalignment and, in the case of multi-engine systems, unsymmetrical start. A worst-case analysis is usually sufficient.
5. Obtain liftoff response by the methods of Section 4.3.2. A more detailed simulation may be necessary for some controlled-release launches.
6. Combine thrust-transient loads with other loads imposed on the vehicle using the methods of Section 4.5.3.

4.7 REFERENCES

4.1 T. Li, Spring Constants, C.G. Location, and Volume Increment of a Missile, General Dynamics/Convair Report ZU-7-056-TN, April 1956.

4.2 J. D. Wood, Survey on Missile Structural Dynamics, Report 7102-0041-NU-000, Contract No. AF 04(647)-619, 1 June 1961.

4.3 L. D. Pinson, Longitudinal Spring Constants for Liquid Propellant Tanks with Ellipsoidal Ends, NASA Technical Note D-2220, November 1964.

4.4 R. G. Rose, A Study of System-Coupled Longitudinal Instabilities in Liquid Rockets, AFRPL-TR-65-163, September 1965.

4.5 W. H. Gayman and J. A. Garba, Dynamics Loads Analyses of Space Vehicle Systems-Launch and Exit Phase, JPL Technical Memorandum 33-286 (To Be Published).

4.6 Y. W. Lee, Statistical Theory of Communication, John Wiley & Sons, Inc., New York, pp 155-176, 1960.

5/ATMOSPHERIC DISTURBANCES

NOMENCLATURE

A	Actuator piston area; cross-sectional area of the vehicle structure	ft^2
C	Flexibility matrix	ft/lb
C_D	Drag coefficient	N.D.
$C_{N/\alpha}$	Normal force coefficient per pitch plane angle of attack	1/rad
C_{NO}	Normal force coefficient at zero pitch plane angle of attack	N.D.
$C_{Y/\beta}$	Yaw force coefficient per yaw plane angle of attack	1/rad
C_{YO}	Yaw force coefficient at zero yaw plane angle of attack	N.D.
$C_{S\alpha}$	Shear coefficient per pitch plane angle of attack	1/rad
C_{SO}	Shear coefficient at zero pitch plane angle of attack	N.D.
$C_{S\ddot{z}}$	Shear coefficient per unit normal acceleration	$lb/ft/sec^2$
$C_{S\ddot{\theta}}$	Shear coefficient per unit pitch plane rotational acceleration	$lb/rad/sec^2$
$C_{M\alpha}$	Moment coefficient per pitch plane angle of attack	ft/rad
C_{MO}	Moment coefficient at zero pitch plane angle of attack	ft
$C_{M\ddot{z}}$	Moment coefficient per unit normal acceleration	$ft\text{-}lb/ft/sec^2$
$C_{M\ddot{\theta}}$	Moment coefficient per unit pitch plane rotational acceleration	$ft\text{-}lb/rad/sec^2$
C_{SA}	Static aeroelastic coefficient	N.D.
F	Force	lb
G	Shear Modulus	lb/ft^2
I	Moment of inertia	$lb\text{-}sec^2\text{-}ft$
K	Stiffness; shear effectiveness factor	lb/ft or $\frac{ft\text{-}lb}{rad}$; N.D.

K_A	Autopilot transfer functions described in text	rad/rad
K_R		rad/rad or rad/rad/sec
K_C		rad/rad
K_{LR}		rad/ft/sec^2 or rad/rad or rad/lb/ft^2
L	Length; vector of lengths	ft
M	Moment	ft-lb
M_i	Mass supported by structure at i^{th} station	lb-sec^2/ft
M_N	Mach number	N.D.
M_T	Total mass of vehicle	lb-sec^2/ft
P	Axial load	lb
Q	Generalized force	lb
S	Shear	lb
S_R	Reference area	ft^2
T	Thrust	lb
V	Velocity	ft/sec
W	Weight	lb
X	Sensed parameter for load-relief autopilot	variable
d	Penetration distance into gust	ft
f	Function, e.g., f(x)	variable
h	Altitude	ft
i	Station index	N.D.
m	Mass, vector of lumped masses	lb-sec^2/ft
m_i	Lumped mass at i^{th} station	lb-sec^2/ft
p	Pressure	lb/ft^2
q	Dynamic pressure	lb/ft^2
t	Time	sec
x	Coordinate along neutral axis	ft
y	Coordinate normal to neutral axis, yaw plane	ft
z	Coordinate normal to neutral axis, pitch plane	ft
Δ	Increment	N.D.

α	Angle of attack, pitch plane	rad
α_g	Angle of attack, gust	rad
β	Angle of attack, yaw plane	rad
γ	Flight path angle (angle between local horizontal and velocity vector)	rad
δ	Engine gimbal angle	rad
ϵ	Iteration convergence tolerance	N.D.
ζ	Damping coefficient	N.D.
$\bar{\eta}$	Average of load	lb or ft-lb
θ	Angle between local horizontal and vehicle centerline; angle between undeformed axis and deformed axis	rad
λ	Gust length	ft
ξ	Normal mode coordinate	ft
π	3.1416	N.D.
ρ	Density	$\frac{\text{lb-sec}^2}{\text{ft}}/\text{ft}^3$
σ	Standard deviation of load; modal slopes	lb or ft-lb; rad/ft
ϕ	Modal displacements	ft/ft
ψ	Angle between launch azimuth and vehicle centerline	rad
ω	Frequency	rad/sec^2
$\mathfrak{m}$	Generalized mass	$\text{lb-sec}^2/\text{ft}$
$\lfloor \rfloor$	Row matrix	
$\{ \}$	Column matrix	
$[ ]$	Square matrix	
$\dot{}$	First derivative with respect to time	
$\ddot{}$	Second derivative with respect to time	

5/ATMOSPHERIC DISTURBANCES

5.1 STATEMENT OF THE PROBLEM

The powered phase of flight through the atmosphere is a condition that often dictates design of a significant portion of the vehicle structure. Axial and lateral loads imposed during this period are functions of axial acceleration, atmospheric disturbances (winds and gusts), vehicle shape, Mach number, trajectory, and atmospheric density. Axial loads are primarily drag loads and inertial loads of the quasi-steady acceleration. Lateral loads are the result of vehicle (or structure) orientation with respect to the relative air velocity, which is called the angle of attack. The magnitudes of lateral loads are functions of angle of attack and dynamic pressure. The angle-of-attack magnitude is primarily a result of vehicle trajectory and atmospheric disturbances. Vehicle shape, Mach number, and atmospheric density determine the distribution of drag and lateral loads. Also, vehicle shape and Mach number determine the type of air flow and can lead to phenomena such as buffeting.

Axial load values are relatively straightforward computations of trajectory parameters such as acceleration, Mach number, altitude, dynamic pressure, and weight. Lateral load calculations are also straightforward computations of these parameters with the addition of angle of attack; however, the angle of attack is a function of atmospheric disturbances which are random in nature. Thus, the major problem in lateral loads is the determination of wind criteria. Once these are established, analytical techniques are used to obtain the loads.

Winds are large-scale movements of air persisting for a period of time considerably longer than the vehicle flight and extending over a significant altitude range. Fig. 5.1a presents a detailed wind profile taken by the smoke-trail method. Fig. 5.1b shows the same wind as measured by a balloon system and also the averaged (smoothed) smoke-trail data.

Wind speeds at launch are small (compared to wind speeds at altitude) and increase with altitude in an uneven manner, reaching a peak in the 25,000- to 40,000-foot-altitude range. The wind speed then decreases up to approximately 100,000 feet where it starts to increase. Little data are available on wind speeds above 60,000 feet; however, loading due to wind above this altitude is quite small becuase of low dynamic pressure and is rarely considered. Gusts are defined as short-period disturbances in the air and are usually considered to account for the profile detail not measured by the balloon system (seeFig. 5.1). For highly accurate wind profiles only the elastic response to gust is generally considered. For most launch vehicles the time span of exposure to a discrete gust is on the order of less than one second. While data on gusts are meager they are usually considered to exist in the same altitudes in which high wind speed is prevalent.

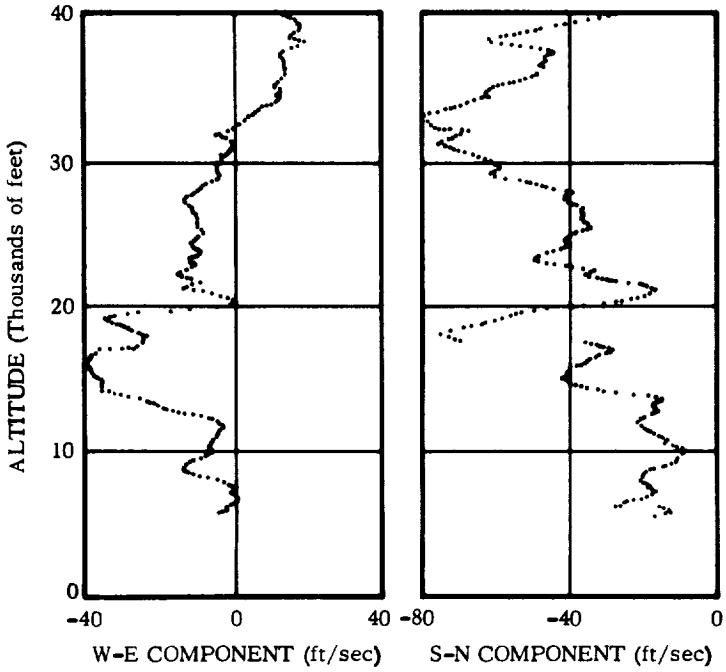

a. Measured Smoke-Trail Winds

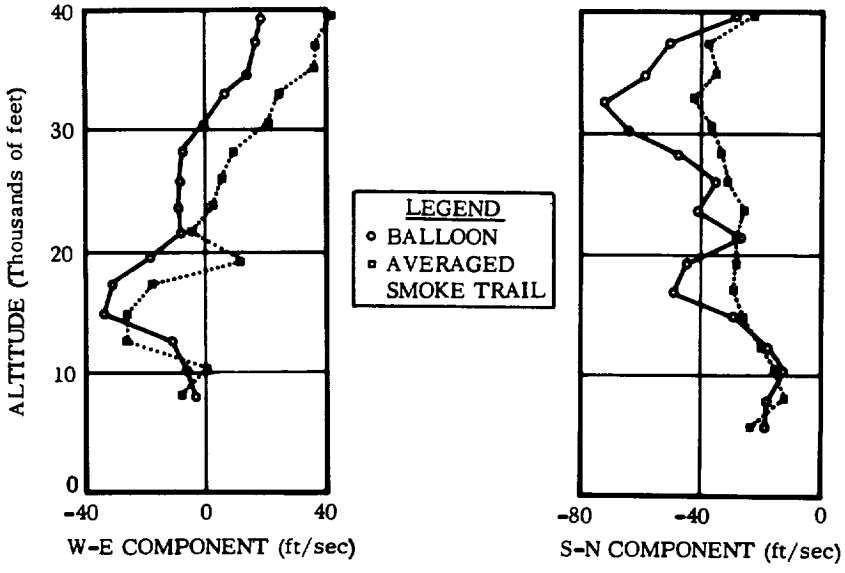

b. Balloon and Averaged Smoke-Trail Winds

Fig. 5.1. Typical Wind Profile

The general procedure for calculation of lateral loads consists of a trajectory simulation through a specified wind and gust profile (or profiles) to obtain the required parameters for loads. Generally rigid-body plus aeroelastic loads due to wind are obtained and added to the loads due to elastic response to a gust.

In the transonic region ($0.8 \leq M_N \leq 1.2$) shock waves begin to build up and areas of random turbulence form aft of points where the geometry changes. This random turbulence is referred to as buffet. Buffet is first discernible as the transonic region is entered, builds up sharply in the region $0.8 \leq M_N \leq 1.0$, and then somewhat slowly decreases with increasing Mach number. Hence buffet is strongly dependent on Mach number. Buffet loads analysis is accomplished by random response analysis of experimental pressure distribution data or by scaling of experimental response data.

In summary, the loads due to atmosphere come from two principal sources: 1) wind and gusts, and 2) buffet. The angle of attack due to wind and gust reaches a maximum value during the period of flight when dynamic pressure is near its peak, i.e., at a 25,000- to 40,000-foot altitude. This produces a critical condition for this type of loading. The buffet loads are mostly local loads although some response of the complete vehicle may occur. The maximum buffet condition occurs in the transonic region which for most space vehicles is earlier than the maximum wind and gust loads; however, the combination of maximum buffet loads and all other loads at that time may be critical. Other minor loads may occur while in the atmosphere; these will be discussed in detail later. Guidance steering is not usually used while in the atmosphere; however, if used it may produce another critical condition.

5.2 HISTORICAL BACKGROUND

The historical background of analysis of loads due to atmospheric disturbances centers around efforts first to obtain accurate wind and gust data and then to derive useful, accurate criteria from the data. It became apparent early in the history of launch vehicles that the wind profile (wind speed vs altitude) that would be encountered was important. It was also recognized that the available wind data, especially the wind shear (the rate of change of speed with altitude), were inaccurate. The need for methods to reduce the data to criteria that were accurate, yet economical and simple in application, was also recognized.

The bulk of wind data obtained in the 1950's was taken with the AN/GMD-1 balloon system. This system used data radioed from the balloon to compute altitude and then used the cotangent of the elevation angle to obtain horizontal distance. At low elevation angles the errors could be large, errors in wind shear sometimes approaching the value of the wind shear. The AN/GMD-2 balloon system was developed in the late 1950's to provide better data. In this system the slant range is obtained by a radio-ranging attachment and sine and cosine are used to compute altitude and horizontal distance. This system is approximately six times more accurate then the AN/GMD-1 system. Comparisons of the two systems are made in Refs 5.1 and 5.2. However,

both systems yield accurate data at 1000-foot-altitude increments. To provide accurate data at shorter altitude increments the FPS-16 Radar/Spherical Balloon system was developed. This system yields data at 25-meter-altitude increments and is several times more accurate than the AN/GMD-2 system. An evaluation of the system is given in Ref. 5.3. Two other methods of obtaining wind data have been tried on an experimental basis. One of these is the smoke-trail method. In this method a rocket leaves a continuous trail of smoke as it ascends, photographs are taken at given times, and the dispersions of the trail are analyzed to provide wind data. Ref. 5.4 discusses the application of the method and some experimental results. The other method uses a doppler radar system to track a column of chaff. The dispersions of the chaff column are used to obtain wind velocity profiles. Ref. 5.5 describes the method and some experimental results obtained from it. Neither system is, nor is planned to be, operational.

The development of wind criteria has taken two approaches. One approach is to do a statistical analysis of the wind data and then develop synthetic wind profiles. Loads are then obtained by application of these profiles. Synthetic profiles have been generated by many persons involved in wind criteria. The first widely used profile was the Sissenwine profile developed in the early 1950's. It is given in Ref. 5.6 and has since been modified by Ref. 5.7. Currently, the most widely used synthetic profile criteria are the Marshall Space Flight Center (MSFC) criteria. MSFC has developed a computer analysis of wind data that yields, for a given launch site and azimuth, wind speed and shear data from which synthetic profiles are constructed. Refs 5.8 and 5.9 are examples of the criteria generated by MSFC.

The second approach is to obtain loads for each wind sounding in a set of soundings and then do a statistical analysis of the loads. This approach is referred to as a statistical load survey. The original development of this approach was done by Avidyne Research, Inc., and reported in Refs 5.10, 5.11, and 5.12. The approach requires a trajectory simulation for each sounding; this approach entails a considerable amount of computer time. To decrease the computer time involved, several approximate metohds have been developed. The influence coefficient method uses an influence coefficient matrix derived from "basic" profiles, i.e., triangular spike, ramp, etc. The vector of wind speeds from a particular wind sounding is multiplied by an appropriate influence coefficient matrix to obtain loads for that sounding. The method was studied by Avidyne and the results are given in Ref. 5.13. Clingan (Ref. 5.14) uses a closed-form trajectory solution to reduce computer time for the statistical load survey. The trajectory solution is obtained by using perturbation equations and neglecting rotational rate and acceleration. Van der Maas (Ref. 5.15) developed a method that uses two basic parameters of a wind sounding to obtain loads on a vehicle. The parameters are maximum wind velocity and the integral of the wind velocity from ground to the altitude of the maximum wind velocity.

The statistical load survey, as developed by Avidyne, is the most accurate method since no assumptions are made concerning either the trajectory simulation or the

correlation between wind data and resulting loads (as is done for synthetic profiles). Avidyne investigated the several methods and compared them, using the statistical load survey as the standard of comparison. The results are given in Ref. 5.13. In order of decreasing accuracy, Avidyne ranked the methods as follows: influence coefficient method, Clingan's method, discrete profiles, and Van der Maas method.

The data available on which to base gust criteria are sparse. Refs 5.16 and 5.17 give some of the available data. These data were gathered by aircraft flying horizontally and then measuring the aircraft vertical accelerations. Randomness of the data is not necessarily established and correlation with wind speed is lacking. Also, most of the data were taken below a 20,000-foot altitude; however, peak launch vehicle loads generally occur in the 25,000- to 40,000-foot-altitude range. Thus, assumptions have to be made when applying these data to launch vehicles. Currently, the gust criteria cover any short-period disturbance not adequately measured during the wind sounding. As wind soundings become more accurate, and especially as the incremental altitude for measurement becomes smaller, the wind sounding will include more and more of what is now included as gust. Thus the question of improving gust criteria will probably be resolved not by gust measurements but by highly accurate wind soundings.

Analysis for loads due to atmospheric disturbances consists of a five or six degree-of-freedom rigid-body trajectory simulation through the design wind profile. The parameters from the simulation are used to calculate vehicle loads. With large boosters the trajectory simulation should include the low-frequency bending modes (less than 2 cps) since these modes can be excited by the wind profile. As wind profile representation improves, it will be necessary to include elastic modes for most vehicles in the trajectory simulation. Ref. 5.18 presents work examining the inclusion of elastic modes in the simulation with detailed wind profiles. Here the problem is not one of methodology but one of determining a sufficiently accurate procedure with economical execution.

The gust effects are added by either of two methods: 1) adding the gust profile to the wind profile to obtain rigid-body gust loads, and performing an elastic analysis with the gust only to obtain those loads due to elastic response, and 2) calculating rigid and elastic body gust loads independently of the wind profile and adding these to the loads resulting from the wind profile. The end result is essentially the same and use of either method is usually at the discretion of the analyst.

The buffeting during the transonic regime of flight is not an atmospheric disturbance, but a phenomenon caused by the shape of the vehicle. It is mentioned here because loads caused by buffeting must be considered in combination with wind loads for total vehicle loads. Ref. 5.19 gives a complete discussion on buffeting historical background and state of the art. Ref. 5.20 contains criteria for determining whether or not a particular configuration is buffet prone. Both references have their own extensive lists of references on the subject.

5.3 QUASI-STEADY FLIGHT LOADS

The term, "quasi-steady flight loads," is used to describe loads and/or response produced by long-period maneuvers and disturbances. The primary sources are winds and steering to accomplish a desired trajectory, either by a predetermined pitch program or by a guidance system. The period is sufficiently long that the vehicle is characterized elastically as deflecting statically and possibly responding in its lower frequency normal modes. The gross wind speed changes take place during altitude spans of several thousand feet; however, recent wind data are providing wind detail for altitude spans of less than a hundred feet.

5.3.1 ANALYTICAL APPROACH. The initial step in obtaining quasi-steady flight loads is to simulate, analytically, the trajectory so that the required trajectory parameters can be obtained. While all trajectory simulations have the same basic analytical features, they usually differ in the detail of these features. Factors influencing the detail composition of a trajectory simulation include optional ways of calculating some parameters, the intended use of the simulation (loads analysis, performance analysis, etc.), the degree of complexity deemed necessary to provide accurate results, and the coordinate system(s) used. With this in mind, the basic form and equations will now be outlined. The vehicle coordinate system is shown in Fig. 5.2. The vehicle forces are illustrated in Fig. 5.3.

The equations of motion for the trajectory of a launch vehicle are derived in Ref. 5.21. An inertial reference frame, usually having its origin at and fixed to the center of the earth, is used. However, forces on the vehicle are expressed in body axes. It is also desirable to fix the vehicle position relative to the launch site. Thus several coordinate systems and the accompanying coordinate transformations are needed. The range of launch vehicles while in the atmosphere is usually on the order of 20-30 miles; hence a flat nonrotating earth will suffice for determining quasi-steady flight loads. The acceleration of the vehicle is obtained by consideration of the thrust, aerodynamic, gravitational, and centrifugal forces. The resultant acceleration produces, over its time integral, a vehicle velocity, V, which is relative to still air and a fixed launch point. The flight path angle, γ, is defined as the angle between the horizontal datum at a fixed launch point and the vehicle velocity vector. The altitude is given by

$$h = \int V \sin\gamma \, dt \tag{5.1}$$

In vehicle coordinates, the axial, lateral, and vertical velocities with respect to the atmosphere are (assuming a flat nonrotating earth and α and β to be small)

$$\left.\begin{aligned} \dot{x} &= V - V_H \cos\theta \\ \dot{y} &= V \sin\beta - V_L \cos\Psi \\ \dot{z} &= V \sin\alpha - V_H \sin\theta \end{aligned}\right\} \tag{5.2}$$

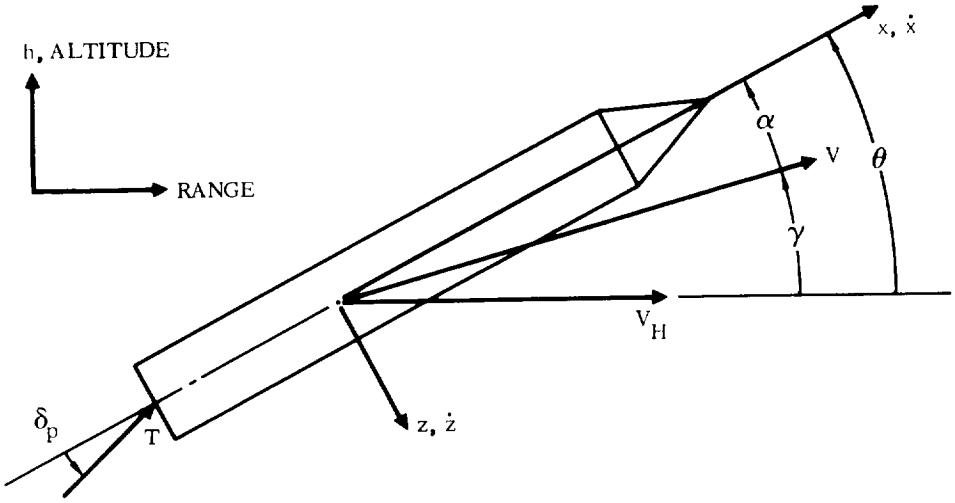

a. Pitch Plane

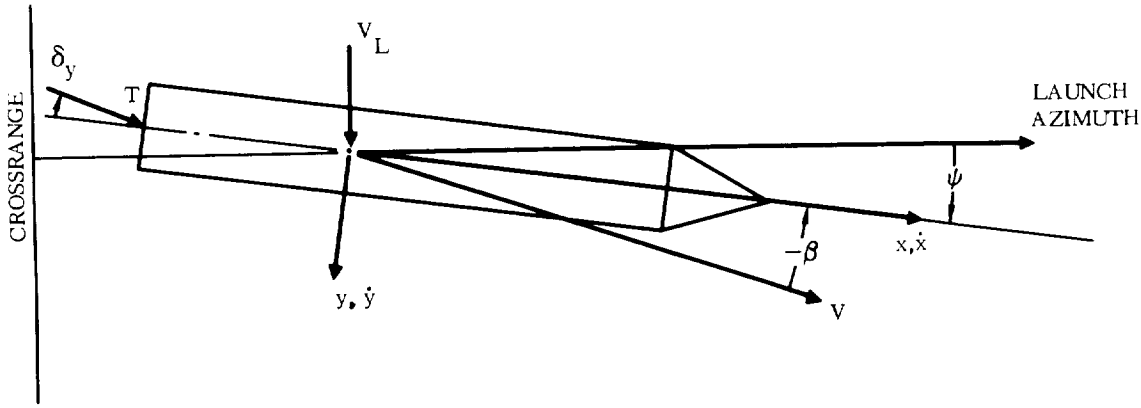

b. Yaw Plane

Fig. 5.2. Coordinate Systems

where

V_H = horizontal wind velocity parallel to launch azimuth

V_L = horizontal wind velocity normal to launch azimuth

θ = angle between vehicle centerline and launch horizontal

The Mach number is

$$M_N = \frac{\sqrt{\dot{x}^2 + \dot{y}^2 + \dot{z}^2}}{V_S} \tag{5.3}$$

where V_S is the speed of sound at the particular altitude. The dynamic pressure is

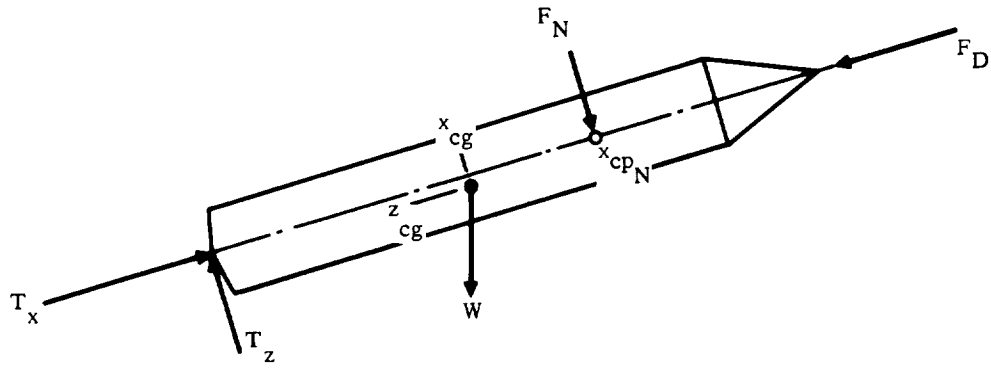

a. Pitch Plane

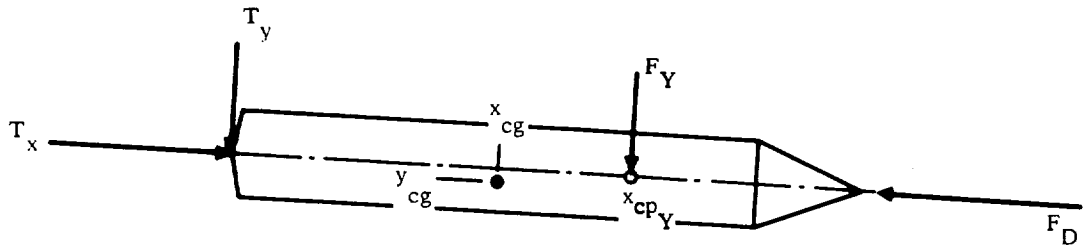

b. Yaw Plane

Fig. 5.3. Vehicle Force Diagrams

$$q = \frac{1}{2}\rho\left(\dot{x}^2 + \dot{y}^2 + \dot{z}^2\right) \tag{5.4}$$

The angles of attack in the pitch and yaw planes are

$$\left.\begin{aligned} \alpha &= \frac{\dot{z}}{\dot{x}} \quad \text{(pitch plane)} \\ \beta &= \frac{\dot{y}}{\dot{x}} \quad \text{(yaw plane)} \end{aligned}\right\} \tag{5.5}$$

The total aerodynamic drag, normal, and yaw forces are

$$F_D = q\, S_R\, C_D \tag{5.6}$$

$$\left.\begin{aligned} F_N &= q\,S_R\left(\alpha\,C_{N/\alpha} + C_{NO}\right) \\ F_Y &= q\,S_R\left(\beta\,C_{Y/\beta} + C_{YO}\right) \end{aligned}\right\} \qquad \text{(5.6 Contd)}$$

where

S_R = aerodynamic reference area

C_D = drag coefficient (function of M_N)

$C_{N/\alpha}$ = normal force coefficient per pitch plane angle of attack (function of M_N and α)

C_{NO} = normal force coefficient at zero pitch plane angle of attack (function of M_N)

$C_{Y/\beta}$ = yaw force coefficient per yaw plane angle of attack (function of M_N and β)

C_{YO} = yaw force coefficient at zero yaw plane angle of attack (function of M_N)

The reference area, S_R, is an arbitrary area used in the derivation of aerodynamic coefficients. For Space Vehicle Systems the reference area usually is taken as the cross-sectional area of the stage with the largest diameter.

The normal and yaw centers of pressure are defined as x_{cp_N} and x_{cp_Y}. They are functions of M_N and α or β as appropriate. The weight is the weight at launch minus all propellant weight expended and jettisoned weight as appropriate. The centers of gravity x_{cg}, y_{cg}, and z_{cg} and the moments of inertia I_{yy} (pitch) and I_{zz} (yaw) are easily computed. The information required for the autopilot simulation is now available. There are three types of autopilots to discuss and since the discussion is fairly lengthy, it is simply stated here that the autopilot will provide engine angles in pitch, δ_P, and in yaw, δ_Y, and the angular attitude of the vehicle in pitch, θ, and in yaw, ψ. The axial, lateral, and normal thrust forces are

$$\left.\begin{aligned} T_x &= T\cos\delta_P\cos\delta_Y \\ T_z &= -T\,\delta_P \\ T_y &= T\,\delta_Y \end{aligned}\right\} \qquad (5.7)$$

The thrust, aerodynamic, and inertial forces can now be combined to obtain the total acceleration vector. The computational loop is now complete. The problem is one of numeric integration, and standard techniques are employed.

The function of the autopilot is twofold: 1) to maintain vehicle attitude when errors arise from disturbances, and 2) to execute the steering commands. The simulation of the autopilot can be simple or complicated depending on the analysis requirements. There are three general types of autopilot simulations used in trajectory simulations, the instantaneous, the standard, and the load-relief autopilots.

The instantaneous autopilot is based on an assumed zero rotational acceleration condition. The engine is, at every instant, assigned the proper angle to balance all moments about the center of gravity. The rotational rates are simply those supplied by the pitch programmer or by guidance, and there is no feedback from the vehicle to the autopilot since the vehicle always has the prescribed attitude. The engine angles are

$$\left.\begin{aligned} \delta_P &= \frac{F_N\left(x_{cp_N} - x_{cg}\right)}{T\left(x_{cg} - x_T\right)} \qquad \text{(pitch plane)} \\ \delta_Y &= \frac{F_Y\left(x_{cp_Y} - x_{cg}\right)}{T\left(x_{cg} - x_T\right)} \qquad \text{(yaw plane)} \end{aligned}\right\} \tag{5.8}$$

where x_T is the engine gimbal point location.

The standard autopilot attempts to closely simulate the actual autopilot. The autopilots used on launch vehicles are usually of the form shown in Fig. 5.4. The following definitions are made:

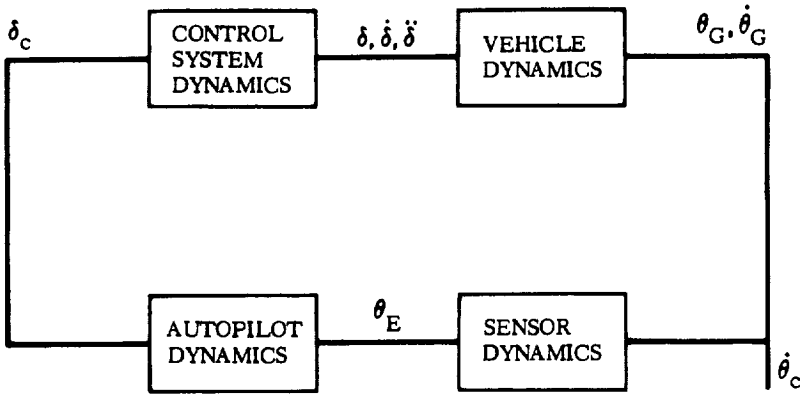

Fig. 5.4. Standard Autopilot Block Diagram

K_R = transfer function between rate ($\dot{\theta}_G$) and/or displacement (θ_G) sensed by gyros plus pitch programmer and/or guidance command ($\dot{\theta}_c$) and the attitude error (θ_E).

K_A = transfer function between attitude error (θ_E) and commanded engine angle (δ_c)

K_C = transfer function between commanded engine angle (δ_c) and the actual engine angle, angular velocity or angular acceleration (δ, $\dot{\delta}$, $\ddot{\delta}$)

Considering only the pitch plane, the vehicle pitch acceleration, velocity and displacement are, respectively,

$$\left.\begin{aligned} \ddot{\theta} &= \frac{\left[T_Y\left(x_{cg} - x_T\right) + F_N\left(x_{cg} - x_{cp_N}\right) - z_{cg}\, M_T\, \ddot{x}\right]}{I_{yy}} \\ \dot{\theta} &= \int \ddot{\theta}\, dt \\ \theta &= \int \dot{\theta}\, dt \end{aligned}\right\} \qquad (5.9)$$

where M_T is the total mass of the vehicle. Assuming the actual engine angular acceleration is the output parameter of the control system, the engine gimbal quantities are

$$\left.\begin{aligned} \ddot{\delta}_P &= f\left(K_C, K_A, K_R, \theta_G, \dot{\theta}_G, \dot{\theta}_c\right) \\ \dot{\delta}_P &= \int \ddot{\delta}_P\, dt \\ \delta_P &= \int \dot{\delta}\, dt \end{aligned}\right\} \qquad (5.10)$$

Similar expressions are obtained for the yaw plane. Normally there is an autopilot for each plane and the two autopilots are uncoupled. The details of the expression for $\ddot{\delta}_P$ (and $\ddot{\delta}_Y$) depend on the specific autopilot hardware being used.

The load-relief autopilot is basically the standard autopilot with an additional feedback loop designed to reduce the angle of attack; hence the name "load-relief autopilot." The form is shown in Fig. 5.5. Sensors are used to measure one of three parameters. These parameters are normal (or lateral) acceleration, angle of attack, and differential pressure. Any of these will indicate when airloads are increasing. When an increase occurs the load-relief loop generates an error signal for the autopilot that causes the vehicle attitude to be changed so that the angle of attack is reduced. The autopilot analysis is the same as for the standard autopilot except that the engine angular acceleration becomes

$$\ddot{\delta}_P = f\left(K_C, K_A, K_R, \theta_G, \dot{\theta}_G, \dot{\theta}_c, K_{LR}, X\right) \qquad (5.11)$$

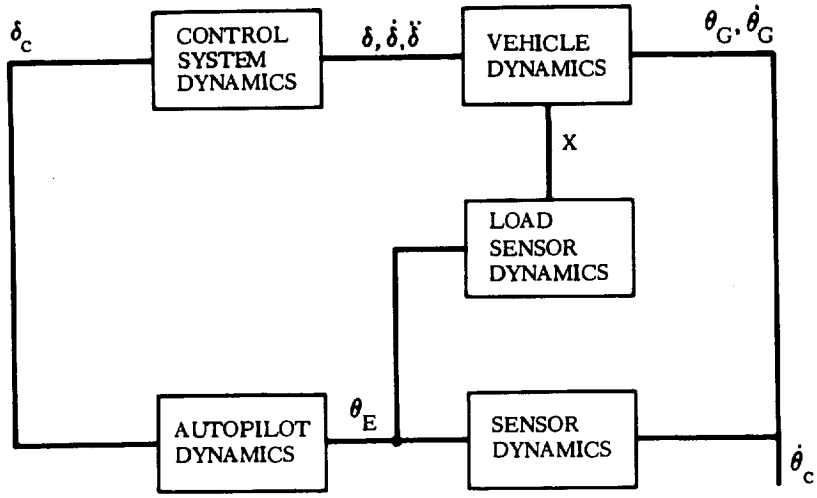

Fig. 5.5. Load-Relief Autopilot Block Diagram

where

K_{LR} = transfer function between the sensed parameter (X) and the error signal to the autopilot (θ_E)

$X = \ddot{z}$ or α or Δp

With the trajectory parameters available the shear and bending moment distributions for the vehicle can now be calculated. Two approaches can be taken in calculating rigid-body shear and bending moment due to airloads. One approach is to apply the airloads due to αq (or βq) from the trajectory and to balance moments with the engine, so that the rotational acceleration and rate are zero. This approach, referred to as the "trimmed vehicle condition," is a good approximation and is widely used. Here, the aerodynamic normal force distribution along the vehicle is lumped at panel points in the same manner as the weight is lumped (see Section 2). The required engine angle is

$$\delta = \frac{F_N\left(x_{cp_N} - x_{cg}\right)}{T\left(x_T - x_{cg}\right)} \tag{5.12}$$

The normal acceleration is

$$\ddot{z} = \frac{T\,\delta + F_N}{M_T} \tag{5.13}$$

The net force at each panel point is

$$F_i = q S_R \left[\alpha C_{N/\alpha_i} + C_{NO_i} \right] - m_i \ddot{z} \tag{5.14}$$

When $x_i = x_T$ the thrust force $T\delta$ is added. The shear and bending moment distribution can now be obtained in the classical manner of summation and integration of forces. When the mathematical model contains branch beams, the analyst must be careful to sum and integrate correctly.

The second approach is to calculate shear and bending moment coefficients for aerodynamic forces, translational accelerations, and rotational accelerations and to use these in conjunction with trajectory parameters to obtain shear and bending moment. The equations for shear and bending moment are

$$\left.\begin{aligned} S_i &= q S_R \left(\alpha C_{S\alpha_i} + C_{SO_i} \right) + \ddot{z} C_{S\ddot{z}_i} + \ddot{\theta} C_{S\ddot{\theta}_i} \\ M_i &= q S_R \left(\alpha C_{M\alpha_i} + C_{MO_i} \right) + \ddot{z} C_{M\ddot{z}_i} + \ddot{\theta} C_{M\ddot{\theta}_i} \end{aligned}\right\} \tag{5.15}$$

where the C's are the following coefficients.

$$C_{S\alpha_i} = \int_{x_N}^{x_i} \frac{d C_{N/\alpha}}{dx} \, dx$$

$$C_{SO_i} = \int_{x_N}^{x_i} \frac{d C_{NO}}{dx} \, dx$$

$$C_{S\ddot{z}_i} = \int_{x_N}^{x_i} \frac{dm}{dx} \, dx$$

$$C_{S\ddot{\theta}_i} = \int_{x_N}^{x_i} \frac{dm}{dx} (x - x_{cg}) \, dx$$

$$C_{M\alpha_i} = \int_{x_N}^{x_i} \frac{d C_{NO}}{dx} (x - x_i) \, dx$$

$$C_{MO_i} = \int_{x_N}^{x_i} \frac{d\, C_{N/\alpha}}{dx} (x - x_i)\, dx$$

$$C_{M\ddot{z}_i} = \int_{x_N}^{x_i} \frac{dm}{dx} (x - x_i)\, dx$$

$$C_{M\ddot{\theta}_i} = \int_{x_N}^{x_i} \frac{dm}{dx} (x - x_{cg})\, (x - x_i)\, dx$$

and where x_N is the vehicle nose station.

The quasi-steady axial loads come from the vehicle axial acceleration and aerodynamic drag. The axial load at the i^{th} station is

$$P_i = M_i \ddot{x} + q\, S_R\, C_{D_i} \tag{5.16}$$

where

M_i = the mass supported by the structure of the i^{th} station

C_{D_i} = cumulative drag coefficient to the i^{th} station

The foregoing discussion on loads has been for a rigid vehicle. Aerospace vehicles are usually sufficiently flexible to have considerable deflection under limit (design) load. In the case of air loads, this deflection causes changes in local angle of attack and, in turn, the load distribution on the vehicle. The change in load distribution again changes the local angle of attack. Thus an iterative process is begun which rapidly converges on a suitable airload distribution. Experience to date indicates that inclusion of quasi-static aeroelastic effects in analysis can give loads for aerospace vehicles of 5 to 20 percent over rigid vehicle loads.

Two methods employed for obtaining static aeroelastic effects are: 1) finding deflections and changes in load using the flexibility matrix and 2) obtaining deflections and changes in load by using normal mode theory. In the first method, the restrained stiffness matrix of Eq. 2.34 is inverted to obtain the flexibility matrix, C. Since the configuration under study is a free-free vehicle, the displacements of the fixed point must be added to obtain the total displacements. Also, vehicle slope due to shear should be added if these slopes are significant terms for the vehicle under consideration. The total displacement is

$$\begin{Bmatrix} y \\ \theta \end{Bmatrix}_T = \begin{Bmatrix} y \\ \theta \end{Bmatrix}_E + \begin{Bmatrix} 1 \\ \hline 0 \end{Bmatrix} y_0 + \begin{Bmatrix} L \\ \hline 1 \end{Bmatrix} \theta_0 + \begin{Bmatrix} 0 \\ \hline \theta \end{Bmatrix}_S \tag{5.17}$$

where $\{L\}$ is a vector of $(x_i - x_0)$ and

$$\begin{Bmatrix} y \\ \theta \end{Bmatrix}_E = \begin{bmatrix} C \end{bmatrix} \begin{Bmatrix} F \\ \hline 0 \end{Bmatrix}$$

$$\begin{Bmatrix} 0 \\ \theta \end{Bmatrix}_S = \begin{bmatrix} 0 & \vdots & 0 \\ \hline 0 & \vdots & \dfrac{1}{KAG} \end{bmatrix} \begin{Bmatrix} 0 \\ \hline S \end{Bmatrix}$$

The shear, $\{S\}$, is obtained from

$$\begin{Bmatrix} S \\ M \end{Bmatrix} = \begin{bmatrix} K \end{bmatrix} \begin{Bmatrix} y \\ \theta \end{Bmatrix}_E \tag{5.18}$$

The displacements of the constraints, y_0 and θ_0, are obtained from a development similar to that in Section 2.2.4.1 by satisfying the equations of linear and angular momentum in conjuction with the compatible elastic deflections. Satisfying both linear and angular momenta

$$\begin{aligned} m_0 y_0 + \lfloor \mu \rfloor \begin{bmatrix} m \\ \searrow \end{bmatrix} \begin{Bmatrix} y \\ \theta \end{Bmatrix}_E &= 0 \\ I_0 \theta_0 + \lfloor \tau \rfloor \begin{bmatrix} m \\ \searrow \end{bmatrix} \begin{Bmatrix} y \\ \theta \end{Bmatrix}_E &= 0 \end{aligned} \tag{5.19}$$

where μ and τ are as defined in Section 2.2.4.1. The deflection equation is

$$\begin{Bmatrix} y \\ \theta \end{Bmatrix}_R - \begin{Bmatrix} \mu \end{Bmatrix} y_0 - \begin{Bmatrix} \tau \end{Bmatrix} \theta_0 = \begin{bmatrix} C \end{bmatrix} \begin{Bmatrix} F \\ M \end{Bmatrix} \tag{5.20}$$

Following the development of Section 2.2.4.1 we obtain

$$\left.\begin{aligned} y_0 &= \frac{1}{W} \left[\bar{S} \lfloor B \rfloor - I_T \lfloor A \rfloor \right] \begin{Bmatrix} y \\ \theta \end{Bmatrix}_E \\ \theta_0 &= \frac{1}{W} \left[\bar{S} \lfloor A \rfloor - M_T \lfloor B \rfloor \right] \begin{Bmatrix} y \\ \theta \end{Bmatrix}_E \end{aligned}\right\} \tag{5.21}$$

where W, $\bar{S}$, A, B, M_T, and I_T are as defined in Section 2.2.4.1. The applied forces are

$$\{F\} = q S_R \left(\left[C_{N/\alpha_i} \right] \{\alpha + \theta_i\} + \{C_{NO_i}\} \right) - \ddot{z}_{cg} \{m\} + T \begin{Bmatrix} 0 \\ \delta \end{Bmatrix} \tag{5.22}$$

where

$$\ddot{z}_{cg} = \frac{q S_R}{M_T} \left(\lfloor 1 \rfloor \left[C_{N/\alpha_i} \right] \{\alpha + \theta_i\} + \lfloor 1 \rfloor \{C_{NO_i}\} \right) + \frac{T\delta}{M_T}$$

and

$$\delta = \frac{q S_R}{T \left(x_{cg} - x_T \right)} \lfloor x_i - x_{cg} \rfloor \left(\left[C_{N/\alpha_i} \right] \{\alpha + \theta_i\} + \{C_{NO_i}\} \right) \tag{5.23}$$

For the first iteration, θ_i is assumed to be zero and values are found for θ_E, θ_o, and θ_S. The second iteration uses $\{\alpha + \theta_i\}$ in computing airloads, and another set of values for θ_E, θ_o, and θ_S are found. This process continues until

$$\{\theta\}^n - \{\theta\}^{n-1} \leq \epsilon$$

The shears and moments are then obtained from

$$\begin{Bmatrix} S \\ M \end{Bmatrix} = [K] \begin{Bmatrix} y \\ \theta \end{Bmatrix}_E \tag{5.24}$$

If the trimmed-vehicle-condition approach is being used, the static aeroelastic solution just derived will yield both rigid-body and static aeroelastic loads. If the coefficient approach is being used, the static aeroelastic effects must be handled in another form. One convenient method is to calculate static aeroelastic coefficients and to apply these to the rigid-body loads obtained by Eq. 5.15. The static aeroelastic coefficients are obtained by calculating both the rigid-body loads (S_{RB}, M_{RB}) and static aeroelastic loads (S_{SA}, M_{SA}) by Eqs 5.13 through 5.28. The coefficient is, then, for the moment at a particular station

$$C_{SA_i} = \frac{M_{SA_i}}{M_{RB_i}} \tag{5.25}$$

Shear coefficients are obtained similarly. The shear and moment in Eq. 5.15 are multiplied by the appropriate coefficient to obtain rigid-body plus static aeroelastic loads.

If the normal modes are available an alternate method of solution exists. Eq. 2.163 states that

$$\{\ddot{\xi}\} + 2[\zeta][\omega]\{\dot{\xi}\} + [\omega^2]\{\xi\} = [m]^{-1}\{Q\} \tag{5.26}$$

For static loads the derivatives are set equal to zero

$$[\omega^2]\{\xi\} = [m]^{-1}\{Q\} \tag{5.27}$$

where

$$\{Q\} = qS_R[\phi]'\left\{\left\{\alpha\, C_{N/\alpha_i}\right\} + \left\{C_{NO_i}\right\}\right\} + \left\{\phi_{xT}\right\} T\delta$$

$$+ q\, S_R[\phi]'\left[C_{N/\alpha_i}\right][\sigma]\{\xi\} \tag{5.28}$$

The engine angle is

$$\delta = \frac{q\, S_R}{T\left(x_{cg} - x_T\right)}\left\{\left\{\alpha\, C_{N/\alpha_i}\right\} + \left\{C_{NO_i}\right\}\right\} \lfloor L \rfloor$$

$$+ \frac{q\, S_R}{T\left(x_{cg} - x_T\right)} \lfloor L \rfloor \left[C_{N/\alpha_i}\right][\sigma]\{\xi\} \tag{5.29}$$

where $\lfloor L \rfloor$ is a vector of $(x_i - x_{cg})$. Substituting Eq. 5.29 for δ in $\{Q\}$ and rearranging terms and solving for $\{\xi\}$ in Eq. 5.27, we have

$$\{\xi\} = \left[[m][\omega^2] - \frac{q\, S_R}{x_{cg} - x_T} \lfloor L \rfloor \left[C_{N/\alpha_i}\right][\sigma] - q\, S_R\, [\phi]' \left[C_{N/\alpha_i}\right][\sigma]\right]^{-1}$$

$$\times \left[q\, S_R\, [\phi]'\left\{\left\{\alpha\, C_{N/\alpha_i}\right\} + \left\{C_{NO_i}\right\}\right\} + \frac{q\, S_R}{x_{cg} - x_T}\left\{\phi_{x_T}\right\}\left\{\left\{\alpha\, C_{N/\alpha_i}\right\}\right.\right.$$

$$\left.\left. + \left\{C_{NO_i}\right\}\right\} \lfloor L \rfloor\right] \tag{5.30}$$

The deflection, slope, shear, and bending moment are then obtained by mode displacement (Eq. 2.179).

5.3.2 ILLUSTRATIVE EXAMPLE. A trajectory simulation, with a wind included, of the Atlas/Centaur/Surveyor vehicle is used to illustrate the determination of vehicle response and loads due to winds. The wind used was picked at random simply for illustration, hence no significance is to be attached to the results for design purposes or for launch probability considerations. Simulations were made with "instantaneous autopilot," "standard autopilot," and "load-relief autopilot" to show the effects of control options.

The trajectory simulation used is, in its basic form, that described in Section 5.3.1. Propellant sloshing is not included. A linear control system is employed, even though the actual Atlas control system is nonlinear. The coefficient method is used to compute loads. Static aeroelastic effects are included by the use of coefficients computed by Eq. 5.25. The vehicle and aerodynamic data used are those employed in the wind monitoring procedure for the Atlas/Centaur/Surveyor vehicle. The wind speed and direction are shown in Fig. 5.6.

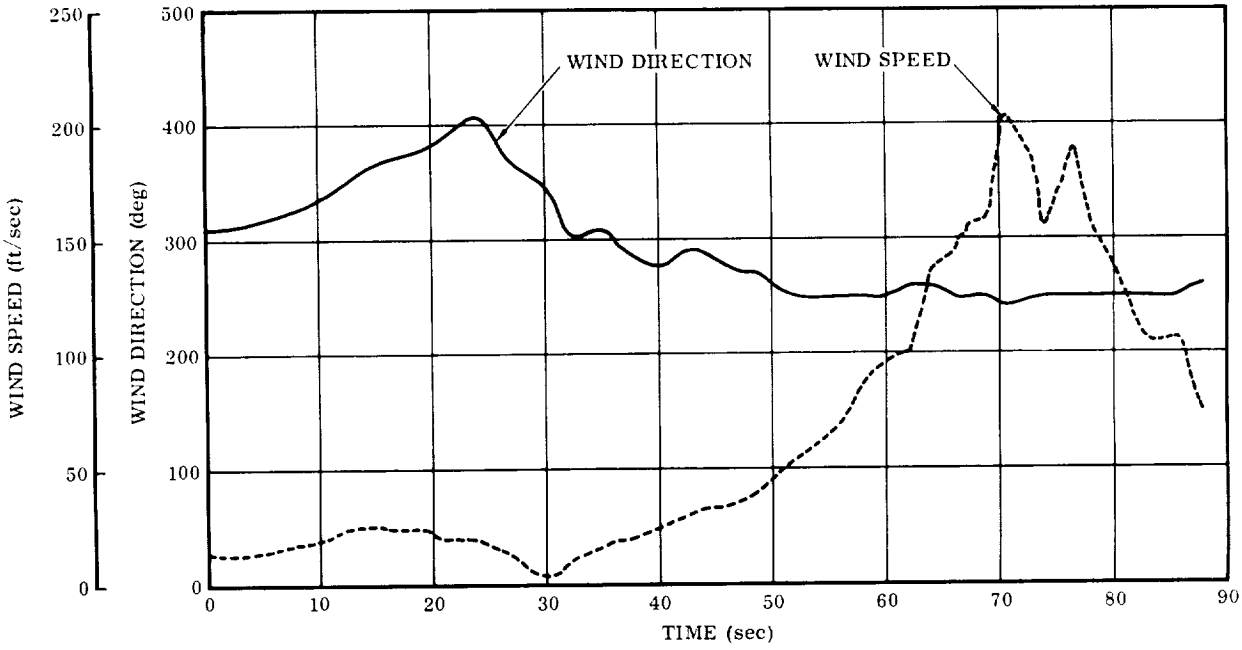

Fig. 5.6. Wind Speed and Direction Time History

The wind loads, which included the static aeroelastic effects, have been calculated for the pitch and yaw planes and then summed vectorially. The translational accelerations, shears and bending moments at the Centaur/Surveyor interface are shown in Fig. 5.7. The bending moments at the Atlas/Centaur interface are shown in Fig. 5.8. The standard autopilot and instantaneous autopilot simulations yield loads that are quite similar. The similarity is expected since the standard autopilot is an attitude control system and is closely approximated by the instantaneous autopilot. The loads using the standard autopilot simulation are, in general, slightly higher at the peak. The loads using the load-relief autopilot simulation are, of course, significantly lower at the peaks since the autopilot is designed to achieve the reduction in loads. The

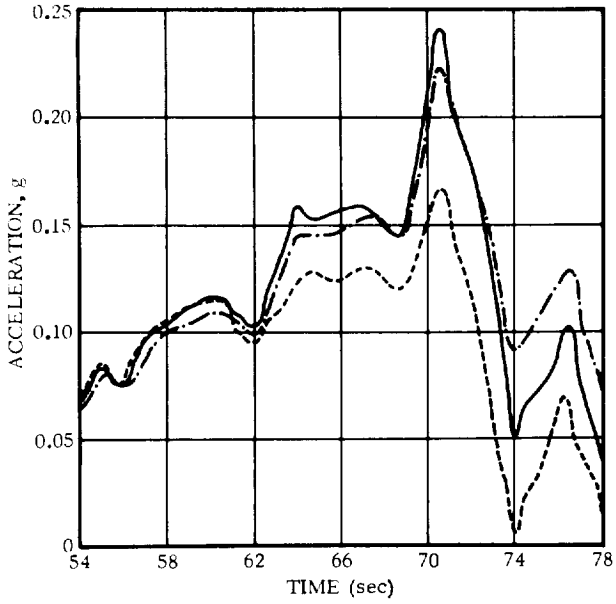

a. Translational Acceleration

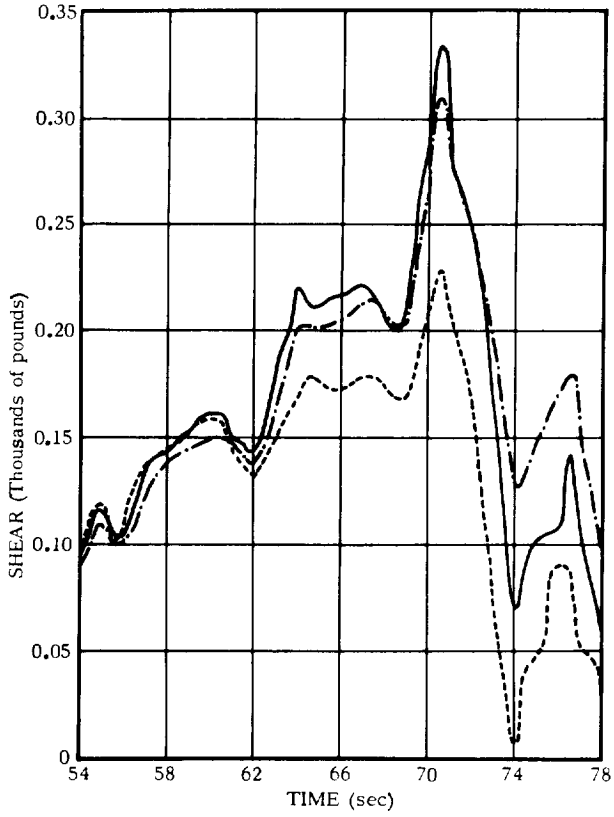

b. Shear

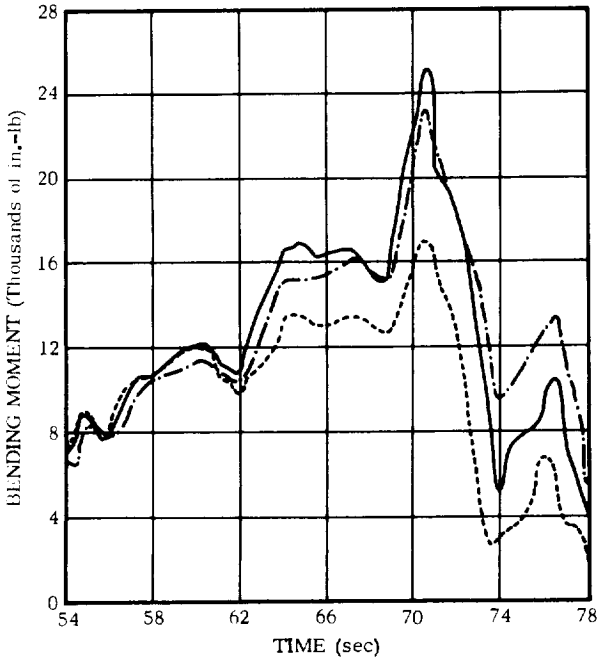

c. Bending Moment

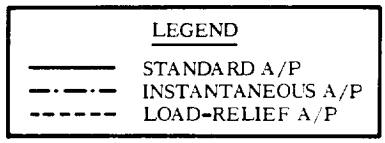

Fig. 5.7. Centaur/Surveyor Interface Loads Due to Wind

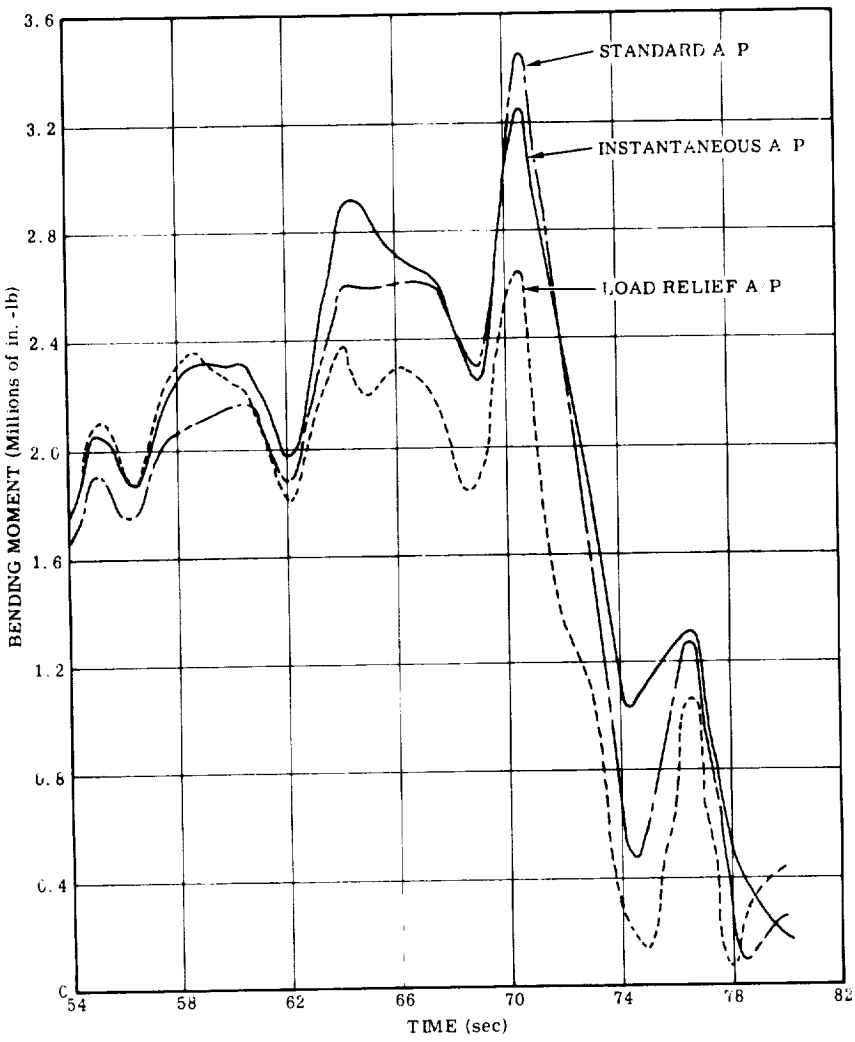

Fig. 5.8. Atlas/Centaur Interface Bending Moments Due to Wind

rotational acceleration is the same (at any instant) at every point on the vehicle since the vehicle is nonvibrating. The rotational acceleration time history is shown in Fig. 5.9. Its form is quite different from the other loads due to the character of the rotational motion. The rotational motion oscillates about zero whereas angles of attack and translational motion have large aperiodic excursions. However, the vector summation of loads has resulted in the absolute values of the loads. Thus the accelerations and bending moments in Figs 5.7 through 5.9 are plotted as positive.

5.4 GUST RESPONSE

5.4.1 ANALYTICAL APPROACH. The equations for gust response have already been given in Section 2.4. The basic equations are applicable to any vehicle; however, the autopilot equations are for a particular form of autopilot and may need modification for the particular vehicle under analysis. The general approach is well illustrated and little additional work should be required to accommodate various autopilot representations.

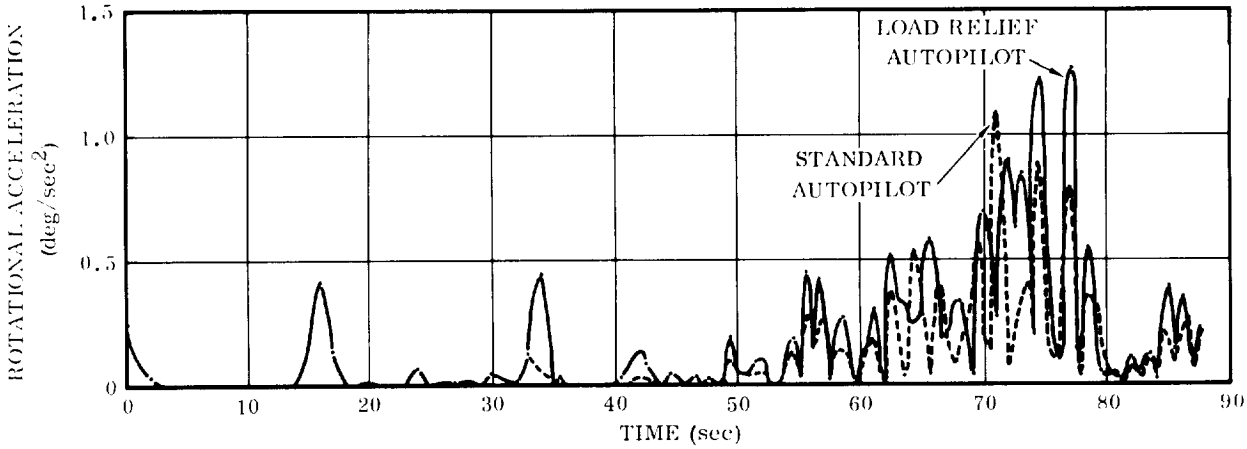

Fig. 5.9. Rotational Accelerations Due to Wind

The aerodynamic forces used in Section 2.4 are for a gust angle of attack, α_{g_i}, the form of which has not been specified. For an "immersion" gust the vehicle is subjected to the same gust velocity over its entire length. In this case, α_g is constant with respect to vehicle station and it varies in time according to the gust shape. Another representation for aerodynamic forces is a "penetration" gust, for which the forces are applied along the vehicle as it penetrates the gust or shear layer. For a penetration gust the α_g is a function of vehicle station as well as time. In this case, the α_g in Eqs 2.151, 2.152, and 2.165 is defined as follows. First, it is assumed that the beginning of the gust is at the most forward station at t = 0. The distance the most forward station (x_1) has traveled into the gust at time t is

$$d_1 = Vt + \frac{1}{2}\ddot{x}\, t^2 \tag{5.31}$$

where

V = vehicle velocity

$\ddot{x}$ = vehicle axial acceleration

The distance that the i^{th} station (x_i) has traveled into the gust at time t is

$$d_i = d_1 - (x_i - x_1) \tag{5.32}$$

The position of the i^{th} station within the gust can be expressed as the ratio d_i/λ where λ is the length of the gust. The general form for α_{g_i} is now

$$\alpha_{g_i} = \alpha_{g_{max}} f(d_i/\lambda) \tag{5.33}$$

where $\alpha_{g_{max}}$ is the maximum gust angle of attack and f (d_i/λ) is a function describing the shape of the gust. To illustrate, the particular description of a "1-cosine" gust is

$$\left.\begin{aligned} \alpha_{g_i} &= \alpha_{g_{max}} \frac{[1 - \cos 2\pi (d_i/\lambda)]}{2} && \text{for } 0 \le d_i/\lambda \le 1 \\ \alpha_{g_i} &= 0 && \text{for } d_i/\lambda < 0 \end{aligned}\right\} \qquad (5.35)$$

5.4.2 ILLUSTRATIVE EXAMPLE. The gust response of the Atlas/Centaur/Surveyor vehicle in the yaw plane at 60 seconds flight time has been obtained as an illustration of gust response analyses. The gust wavelength has been "tuned" in the sense that the vehicle transit time through the gust has produced (on the computer) the maximum response in a particular mode; here, the third bending mode. The transit time for maximum excitation of a particular mode is nearly equal to the period of that mode. In this example, with a third mode period of 0.088 second and a vehicle velocity of 1128 feet per second, the "tuned" wavelength is 100 feet. Both "immersion" and "penetration" gusts have been used with "1-cosine" gust profiles. The gust, in this example, is applied normal to the vehicle longitudinal axis.

The spacecraft response is greater at short gust wavelengths due to higher response of the second, third, and fourth bending modes at these wavelengths. These modes produce high translational and rotational accelerations at the ends of a vehicle; however, the first bending mode and the rigid-body modes produce the highest bending moments in the central portion of a vehicle. The lower frequency modes have peak gust response at longer wavelengths. A 30-foot-per-second gust velocity, which is rather unrealistic for such a short wavelength, has been used in this illustration.

The mathematical model is shown in Fig. 4.9. The model derivation is discussed in Section 4.4.1. The modal frequencies and generalized masses are given in Table 5.1. The lumped aerodynamic coefficients are listed in Table 5.2. The normal modes are presented in Ref. 5.22. The model damping coefficients are given in Table 5.3. The trajectory, autopilot, and control system parameters are listed in Table 5.4.

The translational accelerations, rotational accelerations, shears, and bending moments at the Centaur/Surveyor interface are shown in Fig. 5.10. The dominant response is in the tenth mode (third bending mode at 11.33 cps) with some structurally significant response in the lower modes. Since the gust wavelength was set equal to the period of the tenth mode this behavior is to be expected. The bending moments at the Atlas/Centaur interface are presented in Fig.5.11. Here the dominant response is in the sixth mode (second bending mode at 6.24 cps). The difference in the characteristics of the bending moments at the two interfaces (see Figs 5.10d and 5.11) is attributable to the type of loading encountered. At the Centaur/Surveyor interface the loads

Table 5.1. Modal Frequencies and Generalized Masses for Flight Time of 60 Sec

MODE NO.	GENERALIZED MASS (lb-sec^2/in.)	FREQUENCY (cps)
1	0.9555	0.553
2	16.28	0.729
3	28.66	0.763
4	64.72	0.783
5	28.69	2.47
6	5.012	6.26
7	5.746	7.78
8	0.2048	8.45
9	8.624	9.75
10	1.761	11.33
11	7.729	12.58
12	0.07099	16.82
13	24.13	21.02
14	0.3779	22.07
15	0.00002202	23.66

Table 5.2. Lumped Aerodynamic Coefficients for Gust Response Analysis

MODE NO.	STATION (in.)	AERODYNAMIC COEFFICIENT, C_{N/α_i} (1/deg)
1	-20	0.0035045
2	10	0.0038855
3	50	0.0071037
4	100	0.0092550
5	145	0.0057220
6	173	0.0058178
7	200	0.0058139
15	219	0.0043591
16	250	0.0034393
17	280	0.0007659
18	315	-0.0016652
19	345	-0.0020418
20	375	0.0014364
21	412	0.0009813
22	438	-0.0025994
23	470	-0.0018201
24	500	0.0001090
25	525	0.0006557
26	555	0.0010347

Table 5.2. Lumped Aerodynamic Coefficients for Gust Response Analysis (Contd)

MODE NO.	STATION (in.)	AERODYNAMIC COEFFICIENT, C_{N/α_i} (1/deg)
27	570	0.0011025
28	600	0.0001349
29	630	-0.0000769
30	667	0.0001674
31	696	0.0002750
32	725	0.0002886
33	754	0.0002550
34	784	0.0002483
35	812	0.0000707
36	840	0.0007345
37	871	0.0031814
38	900	0.0024361
39	929	0.0018514
40	960	0.0000527
41	992	-0.0015103
42	1025	0.0000362
43	1057	0.0028011
44	1090	0.0064948
45	1122	0.0046974
46	1133	-0.0013529
54	1160	-0.0010350
55	1176	0.0020909
56	1206	0.0039168
57	1212	0.0055976
58	1242	0.0089609
59	1267	0.0055240
Total		0.0927500

Table 5.3. Damping Coefficients for Gust Response Analysis

MODE NO.	DAMPING COEFFICIENT (% Critical)	MODE NO.	DAMPING COEFFICIENT (% Critical)
1	0.02	9	1.00
2	0.02	10	1.50
3	0.02	11	1.00
4	0.02	12	3.00
5	1.25	13	1.00
6	1.50	14	4.00
7	1.00	15	4.00
8	2.00		

Table 5.4. Trajectory, Control System, and Autopilot Parameters for Gust Response Analysis (Atlas/Centaur/Surveyor)

SYMBOL	PARAMETER (see Section 2.5 for further definition)	VALUE	UNITS
V	Velocity	1128	ft/sec
q	Dynamic pressure	674	lb/ft^2
S_R	Reference area	78.5	ft^2
$\ddot{x}$	Longitudinal acceleration	58.7	ft/sec^2
T_B	Thrust of booster engines	352,900	lb
T_S	Thrust of sustainer engine	72,176	lb
$\bar{\delta}$	Engine gimbal angle used in linearization of control system	1.0	deg
C_V	Viscous friction coefficient	63	ft-lb-sec/deg
C_B	Coulomb friction coefficient	565	ft-lb
C_L	Discharge coefficient of leakage bypass orifice	0.00000478	$ft^3/sec\sqrt{lb/ft^2}$
A	Actuator piston area	0.0247	ft^2
R	Engine moment arm	1.769	ft
K_C	No-load open-velocity gain	36.18	1/sec
K_E	Ratio of hydraulic compliance to hydraulic plus structural compliance	0.104	N.D.
K_A	Autopilot rate gain	1.8	deg/deg
K_I	Integrator loop gain	0.178	1/sec
K_R	Rate gyro loop gain	0.45	sec
τ_{lag}	Time constant, lag filter	0.0116	sec
ω_c	Natural frequency of second order lag filter in autopilot	15.5	rad/sec
ζ_c	Damping ratio of second order lag filter in autopilot	0.5	N.D.
ω_G	Natural frequency of rate gyro	157	rad/sec
ζ_G	Damping ratio of rate gyro	0.6	N.D.
x_G	Station at which rate gyro is located	600	in.
x_D	Station at which displacement gyro is located	991	in.

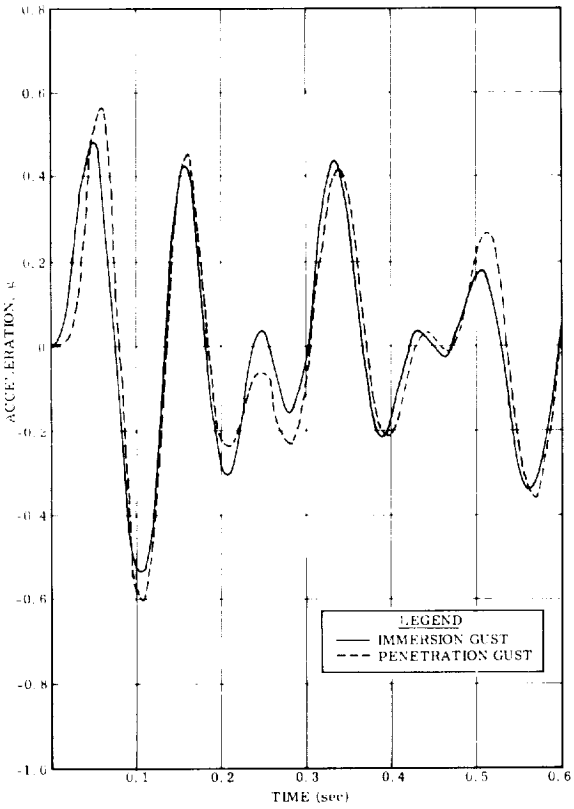

a. Translational Accelerations

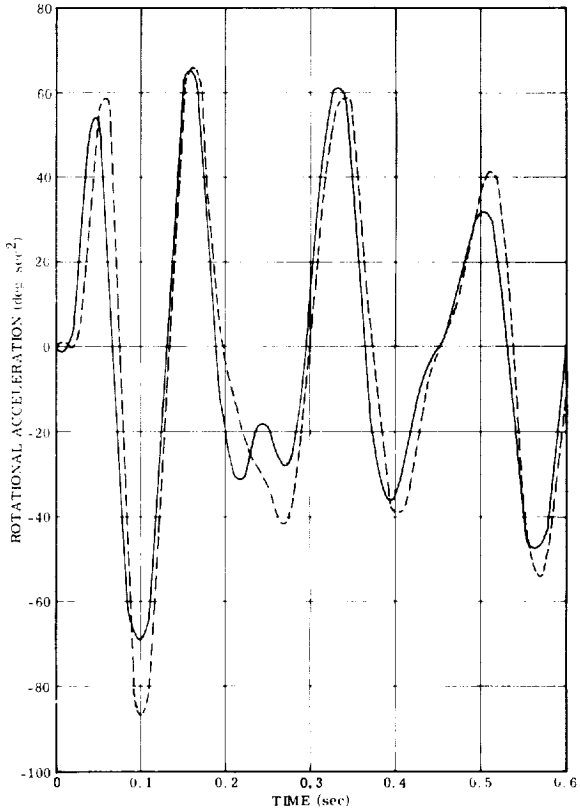

b. Rotational Accelerations

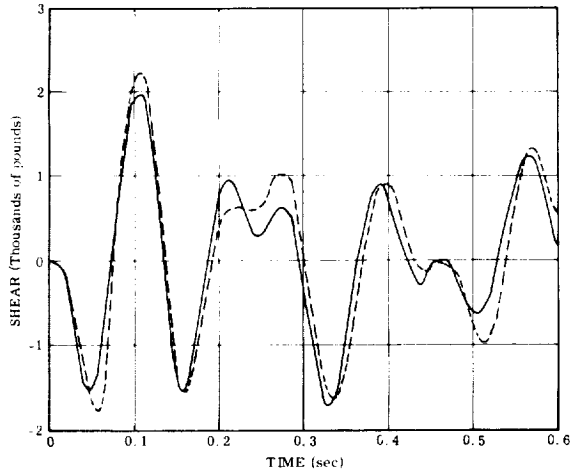

c. Shears

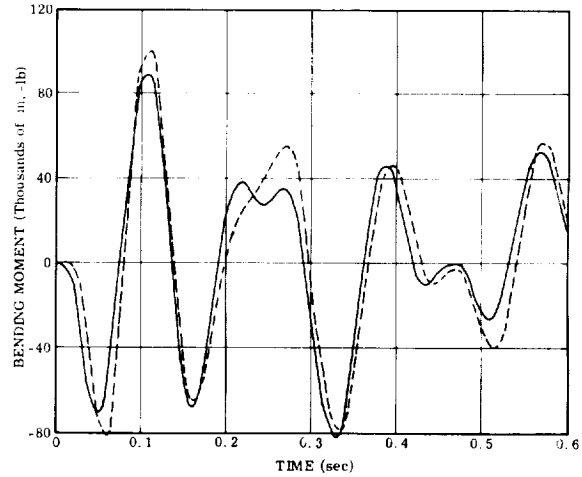

d. Bending Moments

Fig. 5.10. Centaur/Surveyor Interface Loads Due to Gust

are inertial loads due to spacecraft response whereas at the Atlas/Centaur interface the dominant load is aerodynamic loading on the nose fairing. This illustrates the variation in response characteristics that can occur for various points on the vehicle. The loads from both the "immersion" and "penetration" gusts shown for the Atlas/Centaur/Surveyor vehicle are quite similar; however, there is no reason to expect this similarity for other atmospheric descriptions or space vehicle configurations.

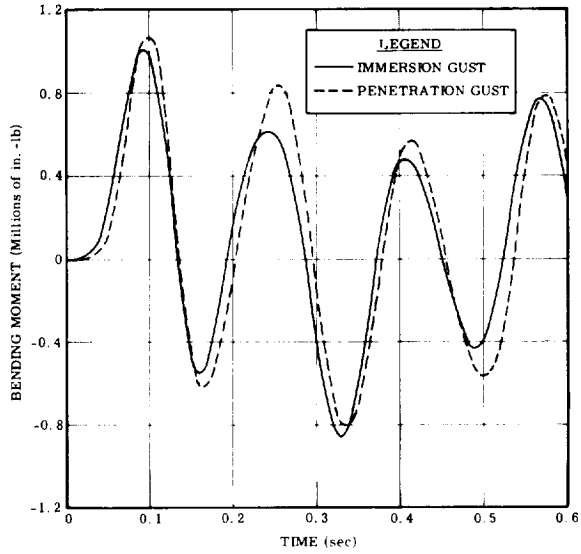

Fig. 5.11. Atlas/Centaur Interface Bending Moments Due to Gust

The relative deflection between the payload and fairing (at a critical point) is shown in Fig. 5.12. Here the peak response is at approximately 8.45 cps, the frequency of the eighth mode (payload "first mode"). Of note here is that the maximum loads occur on the first or second peak but the maximum relative deflection occurs on the fourth peak. The reason is the phasing of the response of the fifth, sixth, and eighth modes. These three modes contribute most of the relative deflection. Initially, the fifth and sixth modes subtract from the eighth mode response, then cancel each other, and, at the peak, add to the eighth mode response. The process is then reversed.

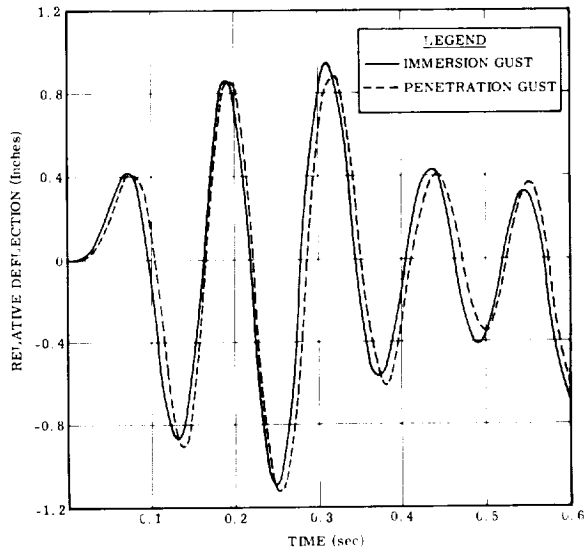

Fig. 5.12. Relative Deflections Between Surveyor and Fairing Due to Gust

The normal-mode displacements for the immersion gust are presented in Fig. 5.13. Where the displacements are not shown, the response was negligible. The displacements for the penetration gust are not presented due to the similarity of results for the particular configuration subjected to exemplary analysis.

5.5 DISCUSSION

The importance of loads due to atmospheric disturbances on the design of space launch vehicles will depend upon the particular vehicle systems. The lower portion of the first stage is generally designed by thrust buildup conditions. Structural design of the upper portions of second and third stages is usually governed by the maximum

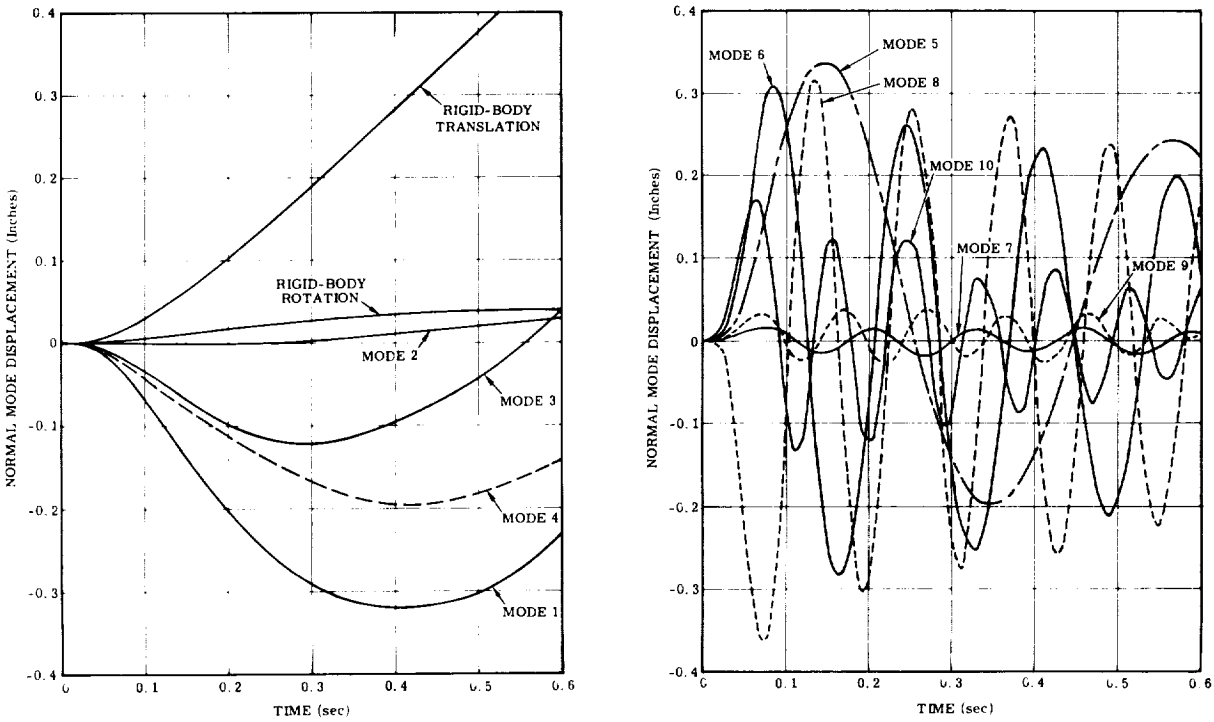

Fig. 5.13. Normal-Mode-Coordinate Displacements Due to Immersion Gust

accelerations at first stage burnout. The design of the structure between these two areas may be dictated by the predicted loads due to atmospheric disturbances. These considerations suggest only general trends which may apply to a particular system. Such considerations are mentioned here to place the proper perspective on the problem areas discussed below.

5.5.1 QUASI-STEADY FLIGHT LOADS. Loads imposed during flight in the atmosphere are axial loads due to drag and vehicle acceleration and lateral loads due to winds and vehicle trajectory. The axial loads are essentially static loads determined from thrust, weight, and vehicle drag. Disturbances affecting longitudinal loads at this time are very small and can be neglected.

The lateral loads are predominantly those due to winds but the pitch program (trajectory) contributions can be a significant parameter. The nominal performance trajectory (without winds) for most missions demands only a small angle of attack through the period of maximum dynamic pressure. This required angle of attack is approximately one-fifth or less of the total angle of attack. The remainder is due to winds.

5.5.1.1 Wind Criteria. Development of wind criteria to be used for design of a vehicle has been discussed in Section 5.2. For an operational system to be launched at many sites and at many azimuths, it is generally practical only to apply synthetic wind profiles as headwinds, tailwinds, and crosswinds to the vehicle. The synthetic

profiles should be an envelope of the wind speeds and shears which can be expected within a required probability of successful launch for that operational system.

Vehicles to be launched from one site with small deviation in azimuth can make use of more detailed wind criteria. Examples are the directional criteria for Eastern Test Range developed by MSFC. These criteria result in significantly lower loads compared to loads obtained by applying the maximum profile in any direction. Another wind criterion is a set of actual wind profiles for that launch site, statistically sampled as in Refs 5.10 to 5.12. A statistical load survey can be accomplished by simulation of the vehicle flight through these profiles.

In the wind profiles, the wind shear (the change in velocity with altitude) is as important as the wind speed. As the vehicle rises, the wind causes the vehicle to drift and build up a lateral velocity. The lateral velocity reduces the angle of attack induced by the wind. For low wind shear, e.g., a profile increasing linearly with altitude, the vehicle has considerable time to build up the lateral velocity. However, for high wind shear the vehicle has much less time to build up a lateral velocity. It is apparent, then, that the wind shear has an important effect on the angle of attack.

5.5.1.2 Pitch Program. For vehicles launched from a single site at constant azimuth it is possible to fly a trajectory that will give an angle of attack, without wind, opposite in direction to the angle of attack induced by the critical wind. Thus, a properly preselected pitch-program can provide some reduction in load. The reduction is usually in the area of 5 to 15 percent. Selection of this pitch program is mostly by trial and error to produce the best compromise of payload capability, thermodynamic effects, and aerodynamic loads.

5.5.1.3 Trajectory Simulation. The degree of physical representation in the trajectory simulation is open to question with the shortcomings in wind criteria. Generally a flat, nonrotating earth is sufficient for the earth model. The vehicle can be represented as a rigid body for determination of significant trajectory parameters with the present available wind criteria. The vehicle autopilot can be simplified to its rigid-body terms. Actually, a trimmed vehicle condition would be sufficient for loads analysis; however, it is advisable to include a simplified version of the autopilot to insure against a significant increase in loads because of the autopilot. Loads can be calculated by either the coefficient method or trimmed condition of Section 5.3.1. Usually the trimmed method will be used with synthetic profiles and the coefficient method with actual wind profiles.

5.5.1.4 Elastic Modes. A good comparison of wind loads with and without inclusion of elastic modes in the simulation has not been made at this time. The wind criteria, either synthetic profiles or actual wind soundings, are not sufficiently detailed to include the transients that would produce modal excitation. With more detailed wind data available, inclusion of elastic modes may be necessary. However, flight data to date do not show significant response in any elastic modes.

5.5.2 GUST LOADS. Gust loads are the lateral loads due to short-period wind speed variations. For wind data taken at large altitude intervals, the gust treatment accounts for the loads due to that wind profile detail not measured by the wind-measuring system. With more detailed wind data, the gust loads may reflect only the elastic response to the measured wind profile detail. Gusts are random in nature. Therefore they have a probability of occurrence (though ill-defined) for a given gust velocity. There are insufficient data to establish a correlation between gust velocity and wind velocity; hence peak gusts and winds are generally considered to act simultaneously. An immersion gust is generally used although insufficient investigations have been made to indicate a preference between analytical usage of "immersion" and "penetration" gusts. As with trajectory simulations, the degree of physcial representation is open to question. Generally rigid-body, slosh, and elastic modes will be considered. The complete autopilot representation will be needed, but the engine control system nonlinearities can usually be ignored.

5.5.3 BUFFET LOADS. Buffet is loading of a structure by an unsteady aerodynamic flow. The flow is usually measured as a fluctuating pressure and exists at all frequencies. Buffet is usually significant only in those areas where a change of vehicle radius occurs or a protruberance exists. It is especially severe in, and downstream from, the transition region from a larger diameter to a smaller diameter. Ref. 5.20 contains criteria for determining whether or not a vehicle shape is a clean body of revolution or is buffet prone. The response analysis is done using the techniques discussed in Section 2.6. The input spectra to use can be difficult to obtain. Either wind tunnel tests must be made, or estimates must be derived from tests of similar configurations. The analysis is usually conservative because of the unknown validity of the chosen assumptions. Buffet can be important for the design of local structure and of components mounted on structure affected by buffet. Theoretically, some overall vehicle response can occur, but flight data do not indicate any significant response of the gross vehicle to buffet.

5.5.4 OTHER LOADS. The previous discussions have covered the major loads applied to the vehicle. There are minor loads applied which, depending on the particular case, may need to be considered. One of these is the center-of-gravity offset load due to the center of gravity not being on the vehicle centerline. A similar load is the load due to angular misalignment of various stages of the vehicle. These loads are quite small compared to axial loads, wind loads, and gust loads and therefore need not be considered unless a large amount of unsymmetry exists. Dispersions in trajectory parameters, principally in angle of attack, dynamic pressure, and axial acceleration, cause additional axial and lateral loading. Again these loads are small compared to the major loads and are also random. When they are combined statistically with the gust loads, the loads virtually disappear.

5.5.5 COMBINED LOADS. The loads discussed previously need to be combined for design purposes and for comparison with allowable loads. It is to be noted that loads other than dynamic loads may be important for the complete load analysis of the space vehicle. Examples are assembly pre-loads, internal tank pressures and differential

pressures associated with nose fairing venting systems. Such loads are outside the scope of this report. The combination of loads is discussed in Section 4.5.3. Eqs 4.9 and 4.10 become, in this case,

$$\bar{\eta} = \bar{\eta}_{XI} + \bar{\eta}_{XD} + \bar{\eta}_{Ycg} + \bar{\eta}_{YW} + \bar{\eta}_{YB} + \bar{\eta}_{YG}$$

$$\sigma^2 = \sigma^2_{XI} + \sigma^2_{XD} + \sigma^2_{Ycg} + \sigma^2_{YW} + \sigma^2_{YB} + \sigma^2_{YG}$$

where the subscripts are defined as follows:

X = axial loading

Y = lateral loading

I = inertial load due to axial acceleration

D = drag load

cg = center-of-gravity offset and misalignment load

W = wind and pitch program loads

B = buffet load

G = gust load

Since some loads are axial loads and some are lateral loads, it is necessary either to convert axial loads to equivalent bending moment, or vice versa. This conversion is usually easily accomplished.

5.5.6 WIND MONITORING. The usual procedure for space launches is to take wind soundings on launch day and determine if the launch is acceptable from the standpoint of loads. The entire process is referred to as the wind-monitoring procedure or simply wind monitoring. The basic steps of the procedure are

1. Calculate, in advance, all loads except those due to wind.
2. Obtain the wind sounding at the launch site and transmit it to the engineering facility.
3. Obtain the loads due to the wind.
4. Compare applied loads with the allowable load either by: 1) comparing the total load with the allowable, or 2) subtracting the loads obtained in step 1 from the allowable load and comparing this with the wind load.
5. Transmit the results of this comparison to the person(s) authorized to decide whether to continue with the launch.

The procedure (except step 1) is repeated several times, beginning 1-3 days prior to launch and becoming more frequent as launch time approaches. A small allowance is usually made for the wind changing during the time between the wind sounding and

the launch. The change in wind velocity over a period of 2-8 hours is approximately 5-10% and to some degree, can be predicted. This persistence also exists, to a lesser extent, over a period of days. A strong wind condition will generally persist for a period of 2-8 days.

In connection with space launches the term "launch probability" is frequently used. Launch probability is the probability of not having a delayed launch due to winds aloft. If the vehicle is being designed, this corresponds to the probability of winds not exceeding the wind criteria used. If the vehicle is already designed, the launch probability corresponds to the probability of winds not exceeding the maximum winds that the vehicle is capable of withstanding.

Launch probability is usually stated with reference to launch on a given day. However, the launch opportunity (window) for space launches usually extends over several consecutive days. The probability of a launch sometime during the launch window is higher than the probability of launch on a given day and, for some launch vehicles, this increase may be significant. An example of this applying to the Atlas/Centaur vehicle is Ref. 5.23; for one case the launch probability for one day was approximately 50% but the launch probability for a five-day window was 95%.

5.6 CONCLUSIONS AND RECOMMENDATIONS

5.6.1 WIND CRITERIA. Wind soundings have, in the past, been taken at relatively large altitude intervals. As a result, the actual wind profile has been effectively smoothed and filtered to the extent that the profile detail for short altitude intervals (especially less than 1000 feet) has been lost. To correct this, the FPS-16 Radar/Spherical Balloon system is being used to obtain more accurate wind soundings and is providing data for an altitude interval of 25 meters. These data are becoming available in quantity and the wind and gust criteria should be changed to reflect the new data.

5.6.2 ANALYSIS. The "state of the art" of the analysis of vehicle response to winds and gusts is regarded to be sufficiently advanced at this time. With the advent of more detailed wind soundings, the elastic mode(s) will probably be required in the trajectory simulation. This does not require any new analytical techniques, being merely another application of existing techniques.

5.6.3 PROCEDURE. With present available wind criteria the following procedure should be followed for calculating loads caused by atmospheric disturbance.

1. Wind and gust criteria for design must be specified.
2. Proceed with rigid trajectory simulation using a nonrotating flat earth model and a simplified rigid-body autopilot.
3. Calculate wind loads using a trimmed vehicle condition or the coefficient method of Section 5.3.

4. Calculate gust loads using the methods of Section 2.4 and 5.4.1 with immersion or penetration gust.

5. Calculate axial inertial and drag loads.

6. Calculate other loads such as center-of-gravity offset and misalignment effects and trajectory dispersions (if necessary).

7. Combine loads using the methods of Section 4.5.3.

8. Set up launch wind-monitoring procedures as discussed in Section 5.5.6.

5.7 REFERENCES

5.1 Dvoskin and Sissenwine, Evaluation of AN/GMD-2 Wind Shear Data for Development of Missile Design Criteria, AFCRC-TN-58-259, April 1958.

5.2 Salmela and Sissenwine, A Note Comparing 1-km Vertical Wind Shears Derived from Simultaneous AN/GMD-1A and AN/GMD-2 Winds Aloft Observations, AFCRC TN-59-496, November 1959.

5.3 Scoggins, An Evaluation of Detail Wind Data as Measured by the FPS-16 Radar/Spherical Balloon Technique, NASA TN D-1572, May 1963.

5.4 Tolefson and Henry, "A Method of Obtaining Detailed Wind Shear Measurements for Application to Dynamic Response Problems of Missile Systems," Journal of Geophysical Research, Volume 66, No. 9, September 1961, pages 2849-2862.

5.5 Jiusto, High Resolution Wind and Wind Shear Measurement With Doppler Radar, CAL Report No. 1H-1525-p-1, June 1962.

5.6 Sissenwine, Windspeed Profile, Windshear, and Gusts for Design of Guidance Systems for Vertical Rising Air Vehicles, AFCRC TN-54-22, November 1954.

5.7 Sissenwine, Revised 1% Sythetic Wind Profile, AFCRC, June 1959.

5.8 Scoggins and Vaughan, Description of Wind Shears Relative to a Missile/Space-Vehicle Axis and a Presentation of the Cape Canaveral, Florida, 95 and 99 Percent Probability Level Standardized Wind Profile Envelopes (1-80 km) and Associated Wind Shears for use in Design and Performance Studies, MSFC MTP-Aero-61-48, June 8, 1961.

5.9 Daniels, Revision of Natural Environmental Design Criteria, In-Flight Wind Conditions, Saturn C-1, Block II Vehicle, MSFC M-Aero-G-35-62, October 19, 1962.

5.10 L. L. Mazzola, N. P. Hobbs, and E. S. Criscione, Wind, Wind Shear, and Gust Design Criteria for Vertically-Rising Vehicles as Recommended on the Basis of Montgomery, Ala., Wind Data (U), WADD TR 61-99 (AD 333174), Avidyne Research, Inc., August 1962 (Secret).

5.11 L. L. Mazzola, J. Putukian, E. S. Criscione, and N. P. Hobbs, Wind, Wind Shear, and Gust Design Criteria for Vertically-Rising Vehicles as Recommended on the Basis of Wind Data from Eleven United States and Foreign Locations (U), ADS-TDR-62-908 (AD 338892), Avidyne Research, Inc., June 1963 (Secret).

5.12 N. P. Hobbs, E. S. Criscione, L. L. Mazzola, and G. J. Frassinelli, Development of Interim Wind, Wind Shear, and Gust Design Criteria for Vertically-Rising Vehicles (U), WADC TR 59-504 (AD 316913), Avidyne Research, Inc., July 1959 (Secret).

5.13 Hobbs, Criscione, and Ayvazian, Simplified Analytical Methods For Use in Preliminary Design of Vertically-Rising Vehicles Subjected to Wind Shear Loads, FDL-TDR-64-8 Part 1, Avidyne Research, Inc., May 1964.

5.14 B. E. Clingan, "A Rapid Method for Determining Wind Shear Design Loads Based on a Set of Measured Profiles," Proceedings of the National Symposium on Winds for Aerospace Vehicle Design, Vol II, pp 49-69, Air Force Surveys in Geophysics No. 140 (AD 275846), AFCRL-62-273 (II), March 1962.

5.15 C. J. Van Der Maas, High Altitude Wind Response of Missile Systems, Lockheed Aircraft Corporation, Missile Systems Division, Report No. LMSC-A062400 (AD 408258), 30 October 1962.

5.16 Press, Meadows, and Hadlock, Estimates of Probability Distribution of RMS Gust Velocity of Atmospheric Turbulence from Operational Gust-Load Data by Random Process Theory, NASA TN 3362, March 1955.

5.17 Walker and Copp, Summary of VGH and V-G Data Obtained from Piston-Engine Transport Airplanes from 1947 to 1958, NASA TN D-29, September 1959.

5.18 B. E. Clingan, R. M. Gates, and J. S. Andrews, Dynamic Loads During Boosted Flight, The Boeing Company, ADD-TDR-63-302, May 1963.

5.19 A. G. Rainey, "Progress on the Launch-Vehicle Buffeting Problem," Fifth Annual AIAA Structures and Materials Conference, April 1964.

5.20 NASA Space Vehicle Design Criteria - Buffeting During Launch and Exit, NASA SP-8001, May 1964.

5.21 A. L. Greensite, Design Criteria for Control of Space Vehicles, Vol. I, Part 3, Trajectory Equations, GDC-DDE65-058, November 1965.

5.22 W. H. Gayman and J. A. Garba, Dynamics Loads Analyses of Space Vehicle Systems - Launch and Exit Phase, JPL Technical Memorandum 33-286 (To Be Published).

5.23 Surveyor Mission Launch Wind Constraints Study for Month of March, Space Technology Laboratories, Inc., 8414-6131-RU-000, October 1963.

6/ FREQUENCY RESPONSE

PRECEDING PAGE BLANK NOT FILMED.

NOMENCLATURE

F	Force	lb
I_E	Moment of inertia of engine about engine center of gravity	$lb\text{-}sec^2\text{-}ft$
L_E	Distance from gimbal point to engine center of gravity	ft
M_E	Mass of engine	$\frac{lb\text{-}sec^2}{ft}$
T	Thrust	lb
i	Station index	N.D.
n	Mode index	N.D.
t	Time	sec
δ	Engine gimbal angle	rad
ζ	Damping coefficient	N.D.
θ	Phase angle	rad
ξ	Normal mode coordinate	ft
σ	Modal slope at engine center of gravity	rad/ft
ϕ_{Fi}	Modal displacement at point i	ft/ft
ϕ_{xT}	Modal displacement at gimbal point	ft/ft
ϕ_{xE}	Modal displacement at engine center of gravity	ft/ft
ω	Frequency	rad/sec^2
$\mathfrak{m}$	Generalized mass	$\frac{lb\text{-}sec^2}{ft}$

6/ FREQUENCY RESPONSE

6.1 STATEMENT OF THE PROBLEM

The forces applied to Space Vehicle Systems or components of Space Vehicle Systems are often sinusoidal in nature. If the systems respond in a set of normal modes, vibrating at fundamental frequencies, then the dynamic response at discrete frequencies can be determined from the summation of the response of each normal mode. The problem then reduces to finding the response of single-degree-of-freedom systems to a harmonic force.

The applied harmonic forces are most frequently encountered in the various vibration tests of the system or its components. Modal vibration surveys require excitation of the system at its natural frequencies. Checkout of vehicle control and engine actuator systems requires sinusoidal gimballing of the engine. Also, limit cycles of some magnitude can occur during flight. Typical examples are vehicle bending mode and propellant sloshing limit cycles caused by feedback to the control system.

The vibration tests and control systems are designed such that these limit cycles are not excessive; however, response analysis must be performed to establish maximum limits.

6.2 HISTORICAL BACKGROUND

The analysis of a single-degree-of-freedom system's response to harmonic excitation is developed in many text books on vibration. Adequate background for control system analysis related to limit cycles and frequency response can be obtained in Refs 6.1 to 6.5.

6.3 ANALYTICAL APPROACH

The equation of motion describing a vehicle natural mode subjected to a sinusoidal force can be written as

$$\ddot{\xi}_n + 2\zeta_n \omega_n \dot{\xi}_n + \omega_n^2 \xi = \frac{1}{m_n} \sum_i \phi_i^n F_i \sin \omega t \qquad (6.1)$$

where ξ_n is the normal mode coordinate and ζ_n, ω_n, and m_n are damping, frequency, and generalized mass of the n^{th} mode. The quantity ϕ_i^n is the normalized mode

deflection at point i and F_i is the applied force at point i with frequency ω. The solution of Eq. 6.1 is

$$\xi_n = Ae^{-\zeta_n\omega_n t}\sin\omega_n t + Be^{-\zeta_n\omega_n t}\cos\omega_n t + \frac{\sin(\omega t - \theta)\sum_i \phi_i^n F_i}{m_n\omega_n^2\sqrt{\left[1-\left(\frac{\omega}{\omega_n}\right)^2\right]^2 + \left[2\zeta_n\frac{\omega}{\omega_n}\right]^2}} \tag{6.2}$$

The terms associated with coefficients A and B represent the starting transients of the system. The steady-state vibration is given by the third term in the right-hand side of Eq. 6.2. Phase angle θ is defined by

$$\tan\theta = \frac{2\xi_n\omega_n\omega}{\omega_n^2 - \omega^2} \tag{6.3}$$

In frequency response problems the quantity of interest is the maximum steady-state vibration after the starting transients have decayed. For maximum response as a function of forcing frequency, Eq. 6.2 reduces to

$$\xi_n = \frac{\sum_i \phi_i^n F_i}{m_n\omega_n^2\sqrt{\left[1-\left(\frac{\omega}{\omega_n}\right)^2\right]^2 + \left[2\zeta_n\frac{\omega}{\omega_n}\right]^2}} \tag{6.4}$$

The acceleration of the normal mode coordinate is

$$\ddot{\xi}_n = \frac{-\omega^2\sum_i \phi_i^n F_i}{m_n\omega_n^2\sqrt{\left[1-\left(\frac{\omega}{\omega_n}\right)^2\right]^2 + \left[2\zeta_n\frac{\omega}{\omega_n}\right]^2}} \tag{6.5}$$

The maximum deflections, accelerations, moments, and shears in a natural mode of the system can now be obtained by either the mode acceleration or mode displacement methods of Section 2. Examination of Eqs 6.2 and 6.3 shows that maximum response occurs when the forcing frequency is nearly equal to a natural frequency.

For the case of zero damping, the maximum response occurs when the forcing frequency is equal to a natural frequency. However, the addition of damping shifts the frequency at which maximum response occurs away from the natural frequency. Further, the amount of shift depends upon the amount of damping. For Space Vehicle Systems, the damping is quite small; therefore the shift in frequency at which maximum response occurs is small. The phase angle between input and response is about 90 degrees. Therefore, at the time of maximum response at resonance, the applied force is almost zero. This means that for the case of ω almost equal to ω_n, either method (mode acceleration or mode displacement) will give the same accurate result.

At a given forcing frequency the complete load description requires time history responses of all the modes or the phasing between the maximum responses of all the modes. If the mode acceleration method is used, the time history of phasing of rigid-body loads due to the applied force along with the time histories or phasing of modal accelerations are required. However, in most cases, the peak response at the resonance of a mode is much larger than contributions from other modes. Usually, therefore, it is sufficient to be concerned with the summation of modal response at forcing frequencies equal to natural frequencies.

6.4 ILLUSTRATIVE EXAMPLE

The Atlas/Centaur/Surveyor vehicle response to booster engine gimballing is used to illustrate the solution to the problem and to show typical results. The mathematical model is that of Section 5, i.e., t=60 seconds. The aerodynamic forces are omitted in the example.

The forces acting on the vehicle are the lateral thrust component, $T\delta$, and the inertial loads, $M_E L_E \ddot{\delta}$ and $I_E \ddot{\delta}$, as shown in Fig. 6.1. The generalized force of Eq. 6.1 is

$$\sum_i \phi_i^n F_i = \left[\phi_{xT}^n T - \left(M_E L_E \phi_{xE}^n + I_E \sigma_{xE}^n \right) \omega^2 \right] \delta \qquad (6.6)$$

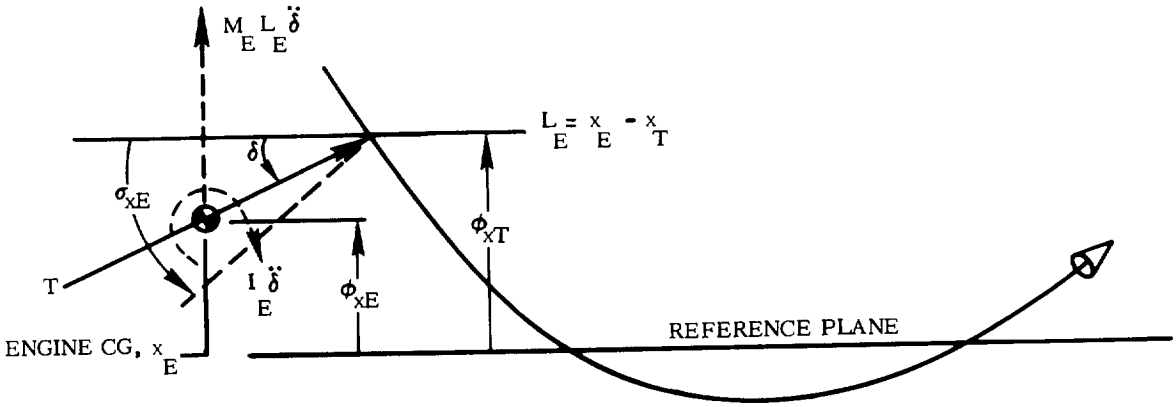

Fig. 6.1. Engine Gimballing Forces

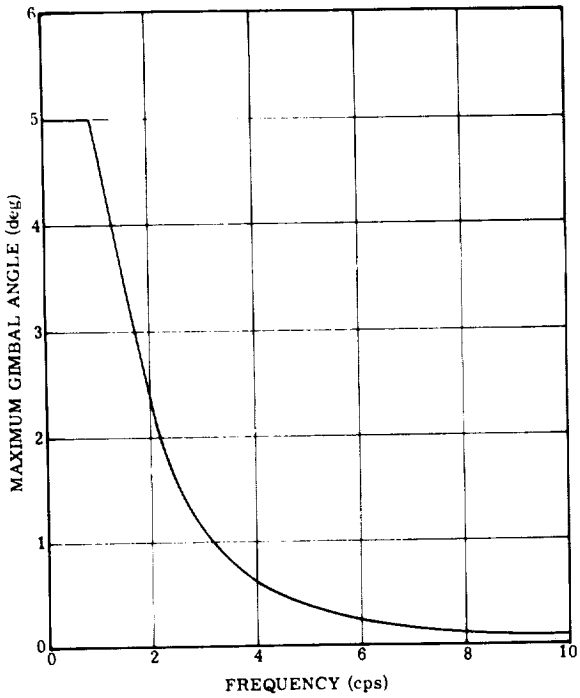

Fig. 6.2. Maximum Gimbal Angle for Atlas Booster

The available engine gimbal angle, as a function of frequency, is established by displacement, velocity, and acceleration characteristics of the engine-actuator system. The maximum gimbal displacement is set by mechanical stops in the actuator. Engine velocity is limited by the flow rate of the hydraulic fluid to and from the actuator piston. The maximum displacement, as limited by velocity, is a function of frequency since the time available to gimbal depends on the gimballing frequency. Engine acceleration is limited by the torque available from the actuator system. The maximum displacement, as limited by acceleration, is also a function of frequency. Plotting the three limits and selecting the lowest limit at each frequency yields the maximum gimbal angle as a function of frequency, shown in Fig. 6.2.

Table 6.1. Modal Damping Values

MODE NUMBER	DAMPING COEFFICIENT, ζ
1	0
2	0
3	0
4	0
5	0.025
6	0.015
7	0.010
8	0.010
9	0.010
10	0.015
11	0.010
12	0.010
13	0.010
14	0.010
15	0.010

The thrust of the two booster engines at t = 60 seconds is 352, 900 pounds. The mass of the booster engines, the distance from the gimbal point to the engine center of gravity, and the moment of inertia of the engines about their centers of gravity are 57.5 slugs, 2.5 feet, and 368 slug-ft^2, respectively. The damping values used are given in Table 6.1.

Calculations were made at frequencies corresponding to those of the fifth, sixth, and the eighth through eleventh modes. These modes are vehicle bending and booster engine rotation modes. (Modes one through four are propellant sloshing modes. Mode seven is the sustainer engine rotation mode. For this example, excitation at their frequencies was not performed although significant loads can result from limit cycles at the sloshing frequencies.) At each forcing frequency the peak responses of the first 17

vehicle modes (including two rigid-body modes) were summed to obtain total vehicle response. The responses, in terms of translational acceleration, rotational acceleration, moment, and shear at the Centaur/Surveyor interface (Station 173) and the Atlas/Centaur interface (Station 412) are listed in Table 6.2. Nearly all the response at a particular frequency came from the mode with a natural frequency equal to the exciting frequency. The much larger response at 2.47 cps is mainly due to the larger engine capability at that frequency. Above 8 cps, where engine capability is nearly constant, the variation in response is due to modal quantities such as generalized force, generalized mass, and mode shape.

It must be remembered that this example does not represent a flight condition. However, it does point out that engine gimballing up to the full capability of the engine

Table 6.2. Summary of Loads Due to Engine Gimballing

LOCATION	FREQUENCY (cps)	TRANSLATIONAL ACCELERATION (g's)	ROTATIONAL ACCELERATION (rad/sec^2)	SHEAR (lb)	BENDING MOMENT (in.-lb)
Station 173	2.47	3.76	12.50	13,300	579,000
	6.26	0.09	0.24	340	16,000
	8.45	0.02	0.03	60	5,200
	9.75	0.10	0.31	170	5,500
	11.33	0.18	0.27	550	22,600
	12.58	0.12	0.19	370	15,800
Station 412	2.47	0.73	9.75	38,950	8,450,000
	6.26	0.06	0.08	760	223,000
	8.45	0.01	0.02	50	17,000
	9.75	0.12	0.40	2,670	271,000
	11.33	0.04	0.22	120	100,000
	12.58	0.05	0.04	450	81,000

system at frequencies greater than 6 cps does not produce excessive vehicle loads. Below 5 cps, large response can occur and this illustrates the reason control design is concerned primarily with rigid-body, sloshing, and first and second vehicle bending modes in a system with hydraulic engine actuators.

6.5 DISCUSSION

The analyst is interested in the vehicle response as a function of the forcing frequency. From this response the acceptability of forces at certain frequencies and amplitudes can be determined. It is seen from Eq. 6.4 that the response will peak sharply at the modal frequencies, i.e., $\omega = \omega_n$. The response will decrease rapidly when ω is unequal to ω_n, even if by a small amount. Since only the peak values are of interest in most cases, it is often necessary to make numeric solutions only at the modal frequencies.

The response is a function of modal quantities (generalized mass, frequency, shape), forcing frequency, force amplitude, and damping. All but damping are usually available with sufficient accuracy for analysis. Damping can be obtained only by test; since response is inversely proportional to damping, care must be exercised to obtain and use correct damping values.

6.6 CONCLUSIONS AND RECOMMENDATIONS

The analysis for frequency response is straightforward if vehicle modes are available. Damping of the system is very important in the response solution and therefore importance of this quantity cannot be overemphasized. In the analysis it is usually sufficient to determine the response of the n^{th} mode with an excitation frequency equal to the mode frequency. These results will indicate areas needing further investigation.

6.7 REFERENCES

6.1 J. G. Truxal, Control System Synthesis, McGraw-Hill Book Company, Inc., 1955.

6.2 J. G. Truxal, Control Engineers' Handbook, McGraw-Hill Book Company, Inc., 1958.

6.3 J. C. Gille, et al., Feedback Control Systems, McGraw-Hill Book Company, Inc., 1959.

6.4 R. L. Gosgriff, Nonlinear Control Systems, McGraw-Hill Book Company, Inc., 1958.

6.5 D. R. Lukens, et al., Approximate Transfer Functions for Flexible-Booster- and Autopilot Analyses, WADD TR-61-93, 1961.

7/ STAGING AND JETTISON

PRECEDING PAGE BLANK NOT FILMED.

NOMENCLATURE

a	Vehicle acceleration	ft/sec^2
D_1	Base diameter of fairing	ft
D_2	Diameter at the base of the forward cone of the fairing	ft
$F = F(t, \theta)$	Thruster force	lb
F_{HY}	Hinge reaction load, radial	lb
F_{HX}	Hinge reaction load, axial	lb
K_Y	Radial hinge spring	lb/ft
K_X	Axial hinge spring	lb/ft
L_1	Length of aft section of fairing	ft
L_2	Length of forward cone of fairing	ft
M	Mass of the fairing	slugs
$M_F = M_F(t, \theta)$	Moment due to eccentricity of the thruster force	ft-lb
X, Y	Reference frame centered at hinge point	
$\bar{X}, \bar{Y}$	Rotating axes centered at hinge point	
$\bar{X}_{cg}$	Location of center of gravity	ft
$\bar{X}_F, \bar{Y}_F$	Point of application of thruster force	ft
X_H, Y_H	Displacement of hinge point	ft
t	Time	sec
$\alpha = \alpha(t, \theta)$	Angle of thruster force from $\bar{X}$ axis	rad
β	Initial angle of $\bar{X}$ and X axes	rad
θ	Rotation angle of $\bar{X}$ axis	rad
$\dot{}$	First derivative with respect to time	
$\ddot{}$	Second derivative with respect to time	

PRECEDING PAGE BLANK NOT FILMED.

7/STAGING AND JETTISON

7.1 STATEMENT OF THE PROBLEM

The problems associated with separation are as varied as the number of possible systems or techniques used to accomplish it. Separation can be classed according to two objectives: 1) staging to separate a spent stage, and 2) jettison to separate a part of a stage, such as a fairing, after it has accomplished its mission. Each of these can be divided into several operational phases for dynamics analysis. First is the actual disconnect of the two parts. This disconnection can be accomplished by explosive bolts or clamps, pneumatic latches, or an explosive shaped charge which actually cuts a separation plane. Problems at this time generally are related to shocks of high frequency and amplitude content.

The second operational phase is the force which actually causes relative motion. This may be in the form of retrorockets, pneumatic thruster bottles, energy stored in springs or structure, rocket thrust of the next stage, plus others. The loads of primary concern at this time would be the local loads at the points of application and reaction. These loads generally are low and do not excite the overall vehicle significantly. If devices such as guide rails or hinges are employed to assure proper clearance, then loads on these structures are also a consideration.

A third operational phase involves clearance and vehicle control during separation. Adequate clearance is often maintained by the use of guide rails or hinges, although adequate clearance may be obtained without them. Control during this phase is generally of two types, inactive and active. With inactive control separation, the vehicle is trimmed prior to disconnect and then the control system is re-activated after separation is complete. Re-activation of control should be accomplished in such a manner that it does not cause significant disturbing forces to the overall vehicle. An active control separation would maintain the vehicle in proper trim condition throughout the maneuver. During staging it is possible that either control method could be employed on either, or both, of the stages.

This section will present a typical rigid-body analysis for jettisoning of a fairing and will discuss elastic effects as well as the typical problems involved with separation in general.

7.2 HISTORICAL BACKGROUND

The early ballistic missiles were single stage vehicles with only one separation problem, that of separating the warhead from the vehicle, and sometimes even this was not a requirement. Attempts were made to minimize errors in rates and attitude due to separation but generally this was not critical since total errors of guidance,

control, and propulsion were large compared to the errors encountered with separation. With the advent of the ICBM, additional problems were caused by the separation of various stages. Also, the attitude and rate errors due to separation became more critical because of increased accuracy of guidance, control, and propulsion. Sophisticated scientific payloads require protective fairings that are usually jettisoned after the period of maximum heating to optimize performance.

The analysis for clearance and control is quite often satisfied by solution of the rigid-body equations of motion. A parametric study is usually necessary for consideration of possible combinations of the variables such as thrust, weight and center of gravity, aerodynamics, installation tolerances, and timing tolerances. Where possible, the worst-case combination of the above is used for design. If this imposes a severe restriction on design, then a more complete statistical study may be required, although this is an exception rather than a general procedure. Examples of the various conditions and combinations to be analyzed are given in Refs 7.1 and 7.2, which provide clearance studies for the Titan IIIC and Atlas/FIRE vehicles, respectively.

Loads and deflections for rails and hinges which may be used for the separation sequence are usually obtained by normal mode theory. Again, the worst-case analysis is usually sufficient although many parameters require evaluation to determine the worst case. The analysis for ejection of flexible fairings requires use of modes for half or quarter shells to determine loads at hinge points (if used) and also to obtain separation velocity if the separation force is a short-duration impulse. Methods for calculating modes for these partial shells are still in the development stage. Refs 7.3 and 7.4 are examples of efforts to develop these methods. As a result, this type of problem is solved by tests to determine modes and tests to determine separation velocities.

The shocks resulting from the activation of the disconnect systems are not amenable to analytical solutions; however, data have been obtained from ground tests and from flight data to adequately describe shocks and shock tests. The data of Ref. 7.5 give results from several types of systems. Refs 7.6 and 7.7 present results for shaped charge systems.

7.3 ANALYTICAL APPROACH

The detail of analysis is often determined by the properties and parameters of importance for the specific event. In staging and jettison this detail can vary from a planar rigid-body analysis to a multidirectional rigid and elastic body representation. The analytical technique employs the equations of motion describing the event to the required degree of detail. A solution for nose fairing jettison is presented in the next section to illustrate the approach taken on this type of problem. The general case of a rigid fairing on an elastic hinge is discussed and then a specific fairing is analyzed to illustrate the type of results that may be obtained.

7.3.1 NOSE FAIRING JETTISON. Nose fairing jettison has three problem areas that require investigation:

a. Loads due to activation of the separation system.

b. Loads due to action of thrusters and/or motion of the fairing.

c. Clearance.

Loads due to activation of the separation system are not generally amenable to analytical techniques and are usually evaluated by tests. Effects of thruster gas impingement on components are also handled by tests. Loads due to thruster force and the clearance evaluation can be handled analytically. The remainder of this section is devoted to development of the fairing trajectory equations. For this development, the fairing will be considered rigid, but mounted on an elastic hinge.

The type of nose fairing configuration under discussion is illustrated in Fig. 7.1. The fairing is composed of two halves which are separated by explosive bolts, latch pins, a shaped charge, or a combination of these. Each half rotates about a single hinge point during initial rotation and is released from the hinge at an angle such that its center of gravity is outboard of the hinge. A typical hinge is detailed in Fig. 7.2. The impulse to rotate the fairing may be provided by springs or other thruster systems. The vehicle is assumed to be trimmed during jettison and the dynamic pressure is assumed to be negligible.

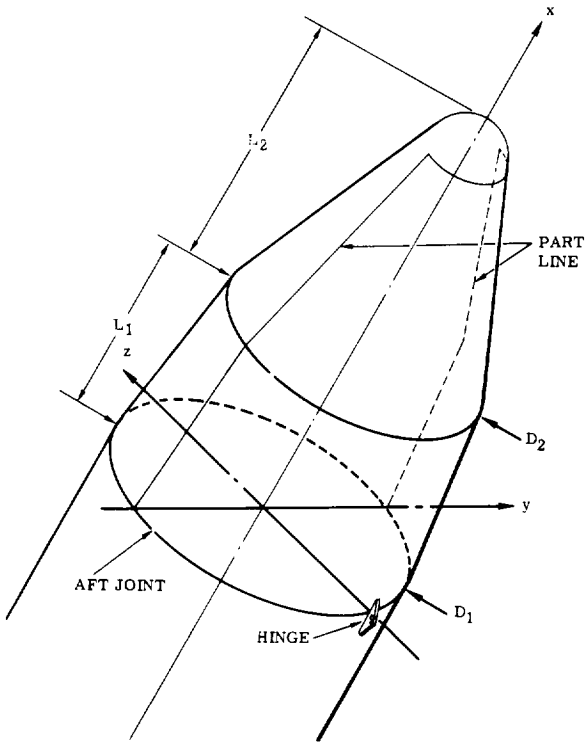

Fig. 7.1. Typical Nose Fairing Configuration

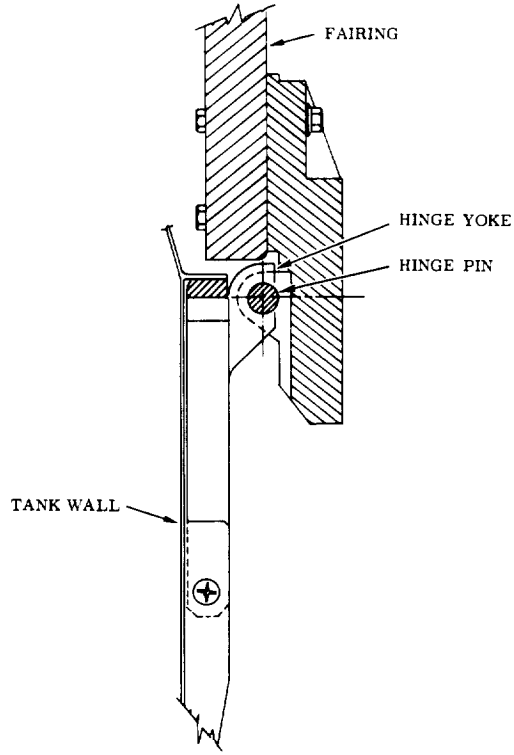

Fig. 7.2. Hinge Detail

The mathematical model is illustrated in Fig. 7.3. The basic coordinate system and those values which will usually be known are given in Fig. 7.3a. The Y, X coordinate system is the reference frame and moves with the vehicle, which has a constant linear acceleration of a ft/sec^2. This system was chosen since the items of interest are relative to the vehicle. The center of gravity of the fairing mass (M slugs) is located at Y_{cg}, X_{cg} in the fixed coordinates, and at 0, $\bar{X}_{cg}$ on the rotating axes. The rotating $\bar{X}$ axis passes through the center of gravity and the hinge, and rotates with the fairing. The fairing is supported through the hinge by springs K_Y and K_X and is rotated by thruster force $F(t, \theta)$ which acts at $\bar{Y}_F$, $\bar{X}_F$ at an angle $\alpha(t, \theta)$ from the $\bar{X}$ axis. The force and the angle at which it acts may be a function of only time t or rotation angle θ, but they can be a complicated function of both.

Fig. 7.3b shows the model and free-body diagram at t=0. The fairing is represented by the rigid beam 0, 0 to 0, $\bar{X}_F$. To simplify the representation, the thruster force has been moved to the $\bar{X}$ axis and the moment

$$M_F(t, \theta) = \bar{Y}_F F(t, \theta) \cos\alpha(t, \theta) \tag{7.1}$$

added to compensate for moving the force from its line of action. The hinge reaction loads are given by

$$\left.\begin{aligned} F_{HY} &= -K_Y Y_H \\ F_{HX} &= -K_X X_H \end{aligned}\right\} \tag{7.2}$$

where Y_H, X_H are the displacements of the hinge, as indicated in Fig. 7.3c. This figure also indicates the rotation angle θ, which is taken from the rest position of the $\bar{X}$ axis, at a time after actuation of the thruster force. The angular velocity $\dot{\theta}$ and acceleration $\ddot{\theta}$ are also indicated. The items of interest are the forces at the hinge, F_{HY} and F_{HX}, and rotation angle θ (t).

The solution is now obtained by classical rigid-body analysis, e.g., application of Newton's second law or LaGrange's equation. The Newtonian approach is taken here. It is assumed that all forces lie in the same plane so that only planar motion need be considered. Thus, the motion of the fairing is completely described by three coordinates. The translation in the reference plane of a point on the body and the angle the $\bar{X}$ axis makes with some reference position will provide the three coordinates, viz., X_H, Y_H, and θ. The notation of t and θ will be dropped from $F(t, \theta)$, $M_F(t, \theta)$, and $\alpha(t, \theta)$ for simplicity but it will be understood that these are explicit functions of time and/or angle of rotation.

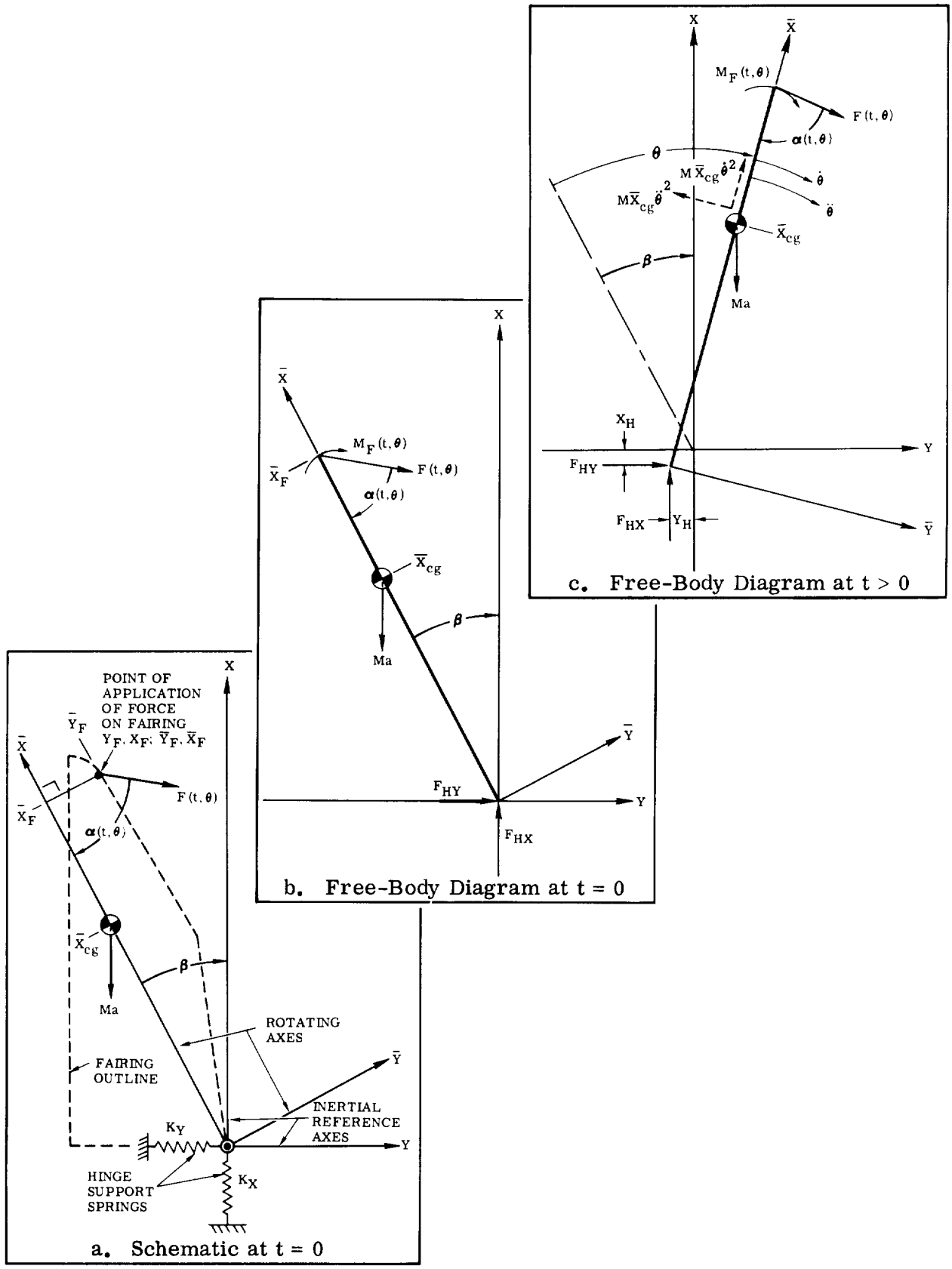

Fig. 7.3. Nose Fairing Mathematical Model

The sum of the moments about the hinge (Fig. 7.3c) is given by

$$\Sigma M_H; \qquad I_H \ddot{\theta} = M_F + F \bar{X}_F \sin\alpha + Ma \bar{X}_{cg} \sin(\theta - \beta)$$

$$+ M \ddot{X}_H \bar{X}_{cg} \sin(\theta - \beta) - M \ddot{Y}_H \bar{X}_{cg} \cos(\theta - \beta) \tag{7.3}$$

The sums of the forces along the X and Y directions are

$$\Sigma F_X; \qquad M \ddot{X}_H - M \bar{X}_{cg} \dot{\theta}^2 \cos(\theta - \beta) - M \bar{X}_{cg} \ddot{\theta} \sin(\theta - \beta) + Ma$$

$$= F_{HX} - F \cos[\alpha - (\theta - \beta)] \tag{7.4}$$

$$\Sigma F_Y; \qquad M \ddot{Y}_H - M \bar{X}_{cg} \dot{\theta}^2 \sin(\theta - \beta) + M \bar{X}_{cg} \ddot{\theta} \cos(\theta - \beta)$$

$$= F_{HY} + F \sin[\alpha - (\theta - \beta)] \tag{7.5}$$

Substituting for M_F, F_{HX}, and F_{HY}, and collecting terms with one second order derivative on the left, Eqs 7.3 through 7.5 become:

$$\ddot{\theta} = \frac{F}{I_H}\left(\bar{Y}_F \cos\alpha + \bar{X}_F \sin\alpha\right) + \frac{M \bar{X}_{cg}}{I_H}\left[\left(a + \ddot{X}_H\right)\sin(\theta - \beta)\right.$$

$$\left. - \ddot{Y}_H \cos(\theta - \beta)\right] \tag{7.6}$$

$$\ddot{X}_H = \bar{X}_{cg}\left[\dot{\theta}^2 \cos(\theta - \beta) + \ddot{\theta} \sin(\theta - \beta)\right] - \frac{F}{M}\cos(\alpha + \beta - \theta)$$

$$- \frac{K_X X_H}{M} - a \tag{7.7}$$

$$\ddot{Y}_H = \bar{X}_{cg}\left[\dot{\theta}^2 \sin(\theta - \beta) + \ddot{\theta} \cos(\theta - \beta)\right] + \frac{F}{M}\sin(\alpha + \beta - \theta)$$

$$- \frac{K_Y Y_H}{M} \tag{7.8}$$

It can be seen that these equations are coupled at the hinge, that is, either X_H or Y_H appear in all three equations. It will also be noted that a Coriolis acceleration term does not appear due to the conditions of a nonrotating reference frame. Damping in the hinge has been assumed to be negligible.

Eqs 7.6 through 7.8 can be solved by standard numeric techniques. Several methods are avilable (Section 2.4) and the choice will be dependent on the desired accuracy. The velocities and displacements are found by integration of the accelerations.

Referring to Eq. 7.6, it will be noted that when F=0, the fairing weight, Ma, will tend to rotate the fairing. This rotation is restrained by the opposite fairing half and the base of the fairing in the real case. For the simplified model being used, however, equilibrium must be obtained by addition of a ficticious thruster force or moment at the hinge. The ficticious hinge moment will yield more realistic initial conditions. This reaction moment (M_R) is found by solving Eq. 7.3 for $\ddot{X}_H = \ddot{Y}_H = \ddot{\theta} = F = 0$, viz.,

$$M_R = Ma\, \bar{X}_{cg} \sin \beta \tag{7.9}$$

This moment goes to zero when the thruster moment equals M_R.

Eqs 7.6 through 7.8 apply to the fairing prior to hinge release. After hinge release, a similar set of equations is required for motion of and about the center of gravity. The initial conditions for these equations are those existing at the instant of hinge release. The item of interest here is the motion of the fairing relative to the vehicle. Thus, the same reference frame may be employed as above.

7.3.2 ILLUSTRATIVE EXAMPLE. An example of fairing jettison is given in this section to illustrate the type of information obtained from a typical analysis. The fairing used in this example is that used on the Atlas/Centaur/Surveyor. The dimensions are (see Fig. 7.1) $D_1 = D_2 = 10$ ft, $L_1 = 6$ ft, $L_2 = 16.1$ ft. The hinge design is that illustrated in Fig. 7.2, which forces the pin from the yoke at about 35 degrees of rotation. The inertial and dimensional quantities necessary for the analysis are given in Table 7.1. The nominal thruster force, supplied by a cold-gas jet, is shown in Fig. 7.4. The variations in thrust angle are caused initially by pressure buildup within the fairing and then, as the fairing halves separate, by gas impingement upon the fairing. The vehicle acceleration at the time of thruster activation was 46 ft/sec^2 (1.43g).

The results of the analysis are presented in Figs 7.5 and 7.6. The hinge loads of Fig. 7.5 indicate that the maximum radial and axial loads occur at about 0.01 and 0.02 second, respectively. From Fig. 7.6, it can be seen that the fairing clears the vehicle during all phases of the trajectory. A close examination of the displacement of the hinge point near the time of hinge release may be necessary to establish that the hinge assembly does not strike the vehicle.

Table 7.1. Properties of Example Fairing

Mass	$M = 29$ slugs
Moment of inertia about hinge	$I_H = 3293.6$ slug-ft^2
C.G. location	$\bar{X}_{cg} = 10.47$ ft
Force location	$\bar{X}_F = 19.47$ ft
	$\bar{Y}_F = 5.42$ ft
Radial spring	$K_Y = 1.8 \times 10^6$ lb/ft
Longitudinal spring	$K_X = 6 \times 10^6$ lb/ft

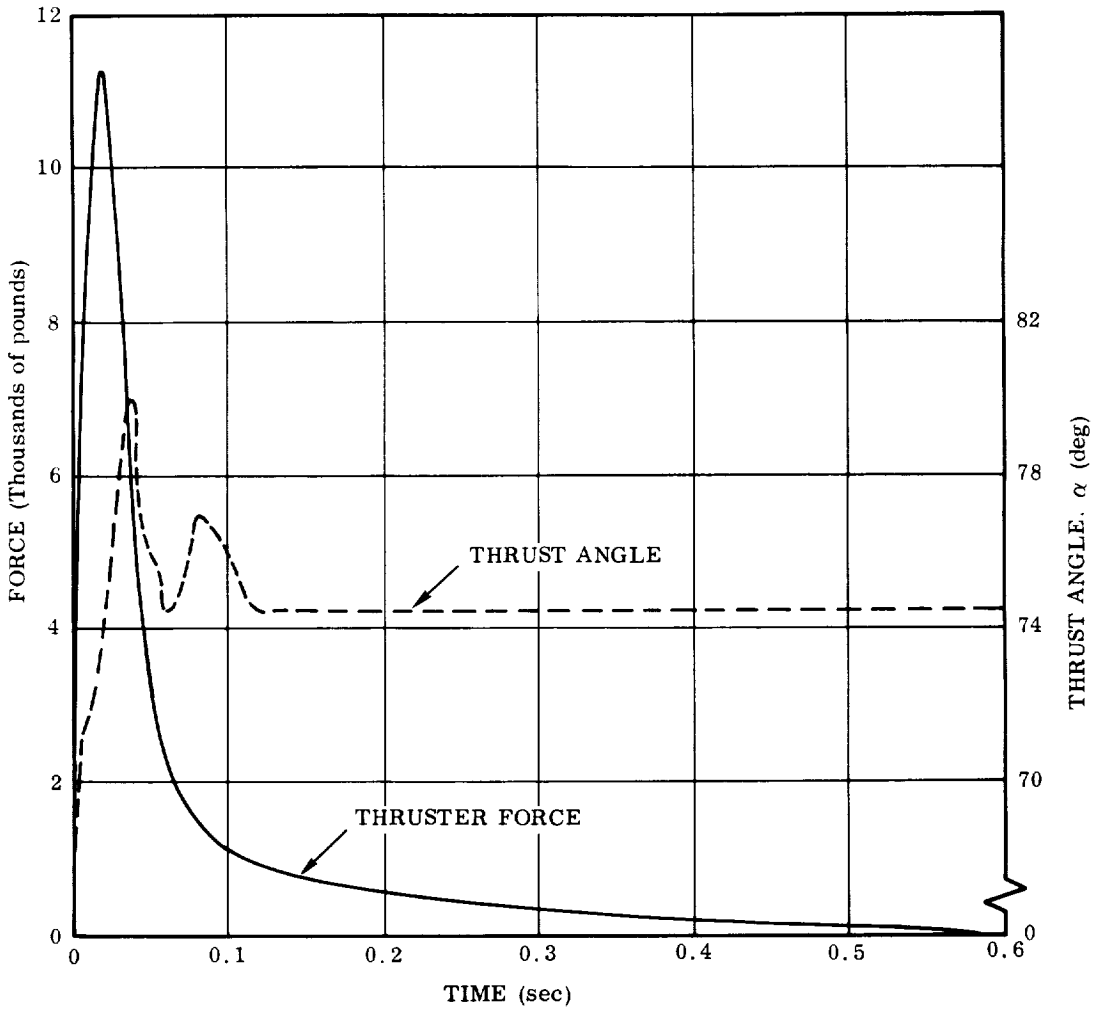

Fig. 7.4. Thruster Force Time History

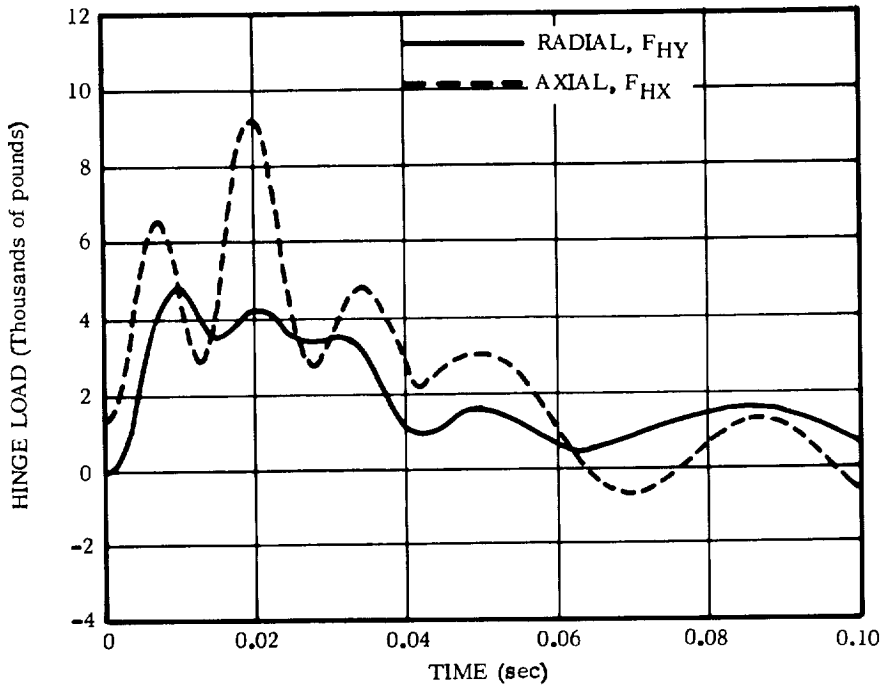

Fig. 7.5. Hinge Load Time History

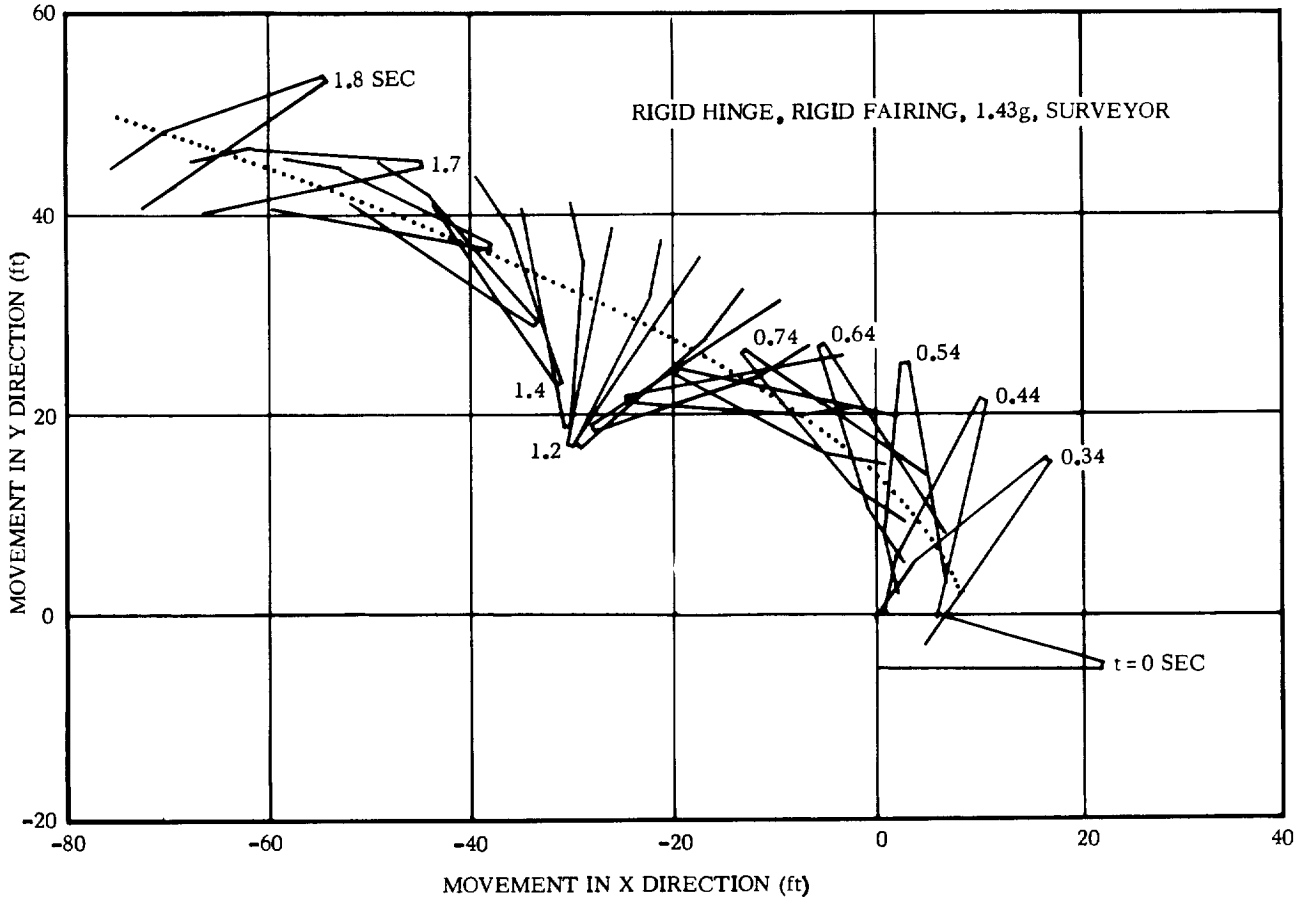

Fig. 7.6. Fairing Trajectory

The radial hinge loads of the two fairing halves will nearly balance each other so that there will be little, if any, excitation of lateral vehicle modes. However, the vertical loads act together and can excite longitudinal vehicle modes. To investigate these longitudinal loads, the free longitudinal model of Section 4.3 was employed with the force time history equal to twice the axial load of Fig. 7.5. This load was applied to mass number 5 of the model shown in Fig. 4.5, when the vehicle was under 1.43g acceleration.

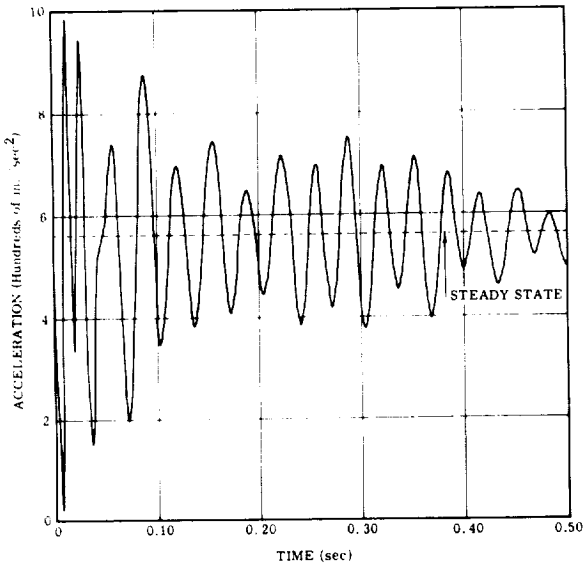

Fig. 7.7. Longitudinal Acceleration at the Centaur/Surveyor Interface Due to Nose Fairing Jettison

The results of this analysis are presented in Figs 7.7 through 7.9. The oscillatory motion due to the nose fairing jettison load is superimposed on that due to steady-state vehicle acceleration. The accelerations at the Centaur/Surveyor interface (Fig. 7.7) are important in that the oscillations may excite the payload significantly. The axial load at the Centaur/Surveyor interface is shown (Fig. 7.8) to illustrate that, due to the flexible spacecraft, the acceleration at the interface times the spacecraft weight does not necessarily yield the load at the interface. The normal coordinate displacements presented in Fig. 7.9 indicate the contribution of each mode to the total response. Nearly all modes are excited because of the high-frequency pulse loading.

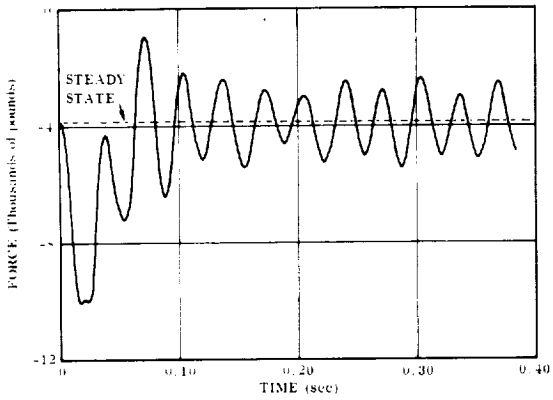

Fig. 7.8. Axial Load at the Centaur/Surveyor Interface Due to Nose Fairing Jettison

7.4 DISCUSSION

7.4.1 JETTISON. The effective force of a gas thruster is more than just the thrust of the nozzle. Prior to actual opening of the fairing, there will be a pressure buildup in the cavity. There is also the gas impingement force from the jet of the opposite fairing half. Both these forces are effective only during the first few degrees of rotation, but they can increase the impulse significantly. These factors make prediction of the thrust time history a difficult task. Other types of thrusters, such as springs, may be more predictable.

7.4.2 ELASTIC EFFECTS. When a fairing and/or its hinge support are relatively flexible, a rigid-body analysis may not suffice for hinge loads and initial angular

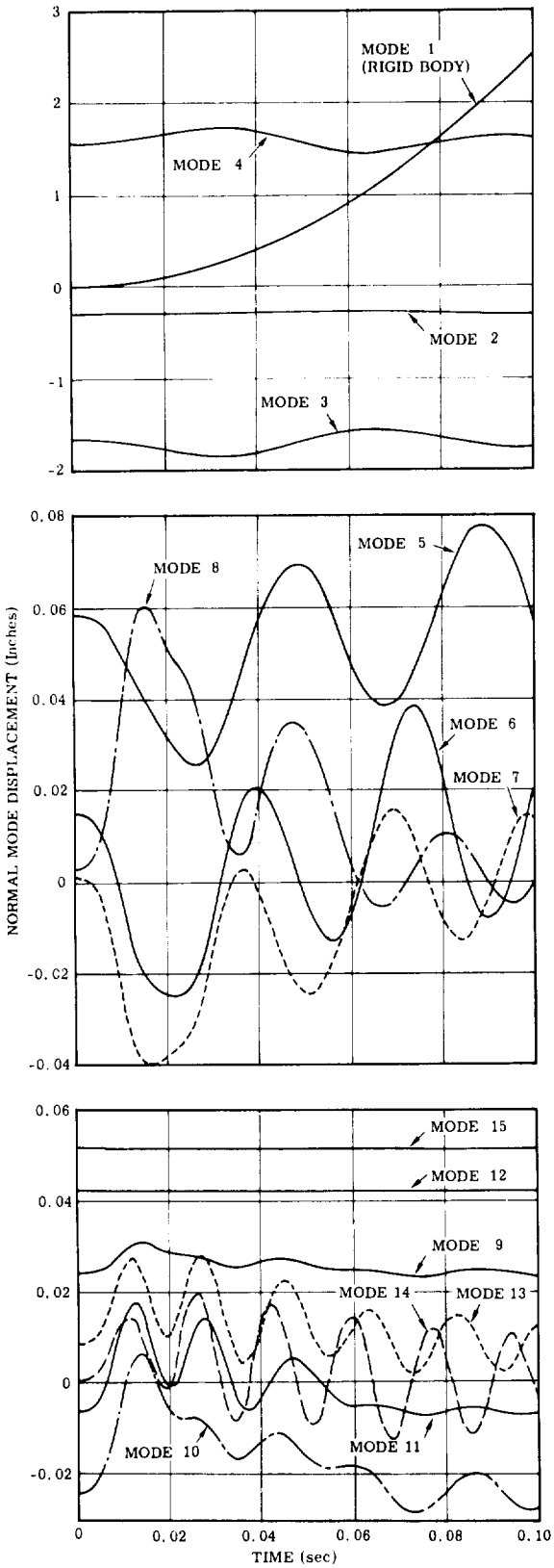

Fig. 7.9. Normal Coordinate Displacements Due to Nose Fairing Jettison Longitudinal Loads

motion. The fairing modes may be excited which can increase the hinge loads over those of a rigid-body analysis. Further, under certain circumstances, modal response of the fairing can affect the time history of the ejection mechanism itself and thereby reduce the total applied impulse. In such a case the total momentum imparted to the fairing may be less than nominal and difficulty may be encountered in clearing the missile.

Analytical techniques for calculating modes of partial shells are in the development stage; e.g., Refs 7.3 and 7.4. As a result, tests must be performed to determine these modes. These modal surveys should give the following information:

a. Frequencies.

b. Displacements in the radial, tangential and axial directions (mode shapes).

c. Damping.

d. Generalized mass.

The axial and tangential displacements have often been ignored in the analysis of small fairings, but they cannot be ignored for larger, more flexible fairings.

7.4.3 STAGING. The full spectrum of concern during staging encompasses the period from prior to engine shutdown to after ignition of the next stage. The operations involved must be optimized for minimum payload loss, while at the same time minimizing potentially critical design loads. For example, disconnection of stages cannot be performed until the transients of engine shutdown have reduced sufficiently to preclude bumping*, ignition

*The exception to these is staging by firing in the hole, as with Titan II. This case will be discussed later in this section.

of the next stage cannot occur until separation is complete, and control reactivation should not produce excessive engine gimbal angles and resultant vehicle loads. The effects of engine shutdown and thrust buildup have been discussed in Section 4. The optimization of sequencing of operations is beyond the scope of this report.

The majority of the current space launch vehicles are multistage and it is possible that more than one type of system will be encountered on a single vehicle. The staging system consists of two parts:

a. That required to sever the structural and mechanical connection, i.e., a disconnect system.

b. That required to produce relative displacement, i.e., a thruster system.

Types of disconnect systems include latches, explosive bolts, linear shaped charge, and Marman-type clamp arrangements. Latches may be activated by high-pressure gas or by pyrotechnic devices such as pin pullers. Explosive bolts, shaped charge, and clamp arrangements require investigation of possible damage from loose fragments ranging in weight from milligrams to possibly several pounds. Structure and equipment must be protected from the high-velocity particles that can result from the detonation of pyrotechnic devices. Nearly all the above systems have some shock associated with their activation.

Once the spent stage has been separated, the problem then becomes one of assuring that there is no collision and to minimize turning rates to the rejected stage and the following stage. Guide rails are often employed to eliminate any possibility of collision during staging. The problem here is to define the loads on the rails so that deflections and weight are optimized. The selection of a thrust system to provide relative displacement may be straightforward or may require statistical analysis, depending on the variables involved. Thrust systems that may be encountered include springs, gas thrusters, monopropellant or hypergolic engines, solid-propellant rockets, or firing of the upper stage engines. These devices may be on the upper or lower stage or in combination.

Loads that must be considered during staging include shock due to disconnect and those associated with the thruster system. Shocks range from as high as 3000g in the immediate vicinity of shaped charges to less than 50g for latches. The shock amplitude, frequency content, and propagation through the structure will depend upon the device used and the type of structure. Analysis of loads due to thruster activation is usually straightforward. The impulse resulting from release of restrained elastic energy (pretensioning, for example) should not be overlooked.

The case of staging by "firing in the hole" presents some rather special problems, although it does represent the most efficient method. For example, there is a greater

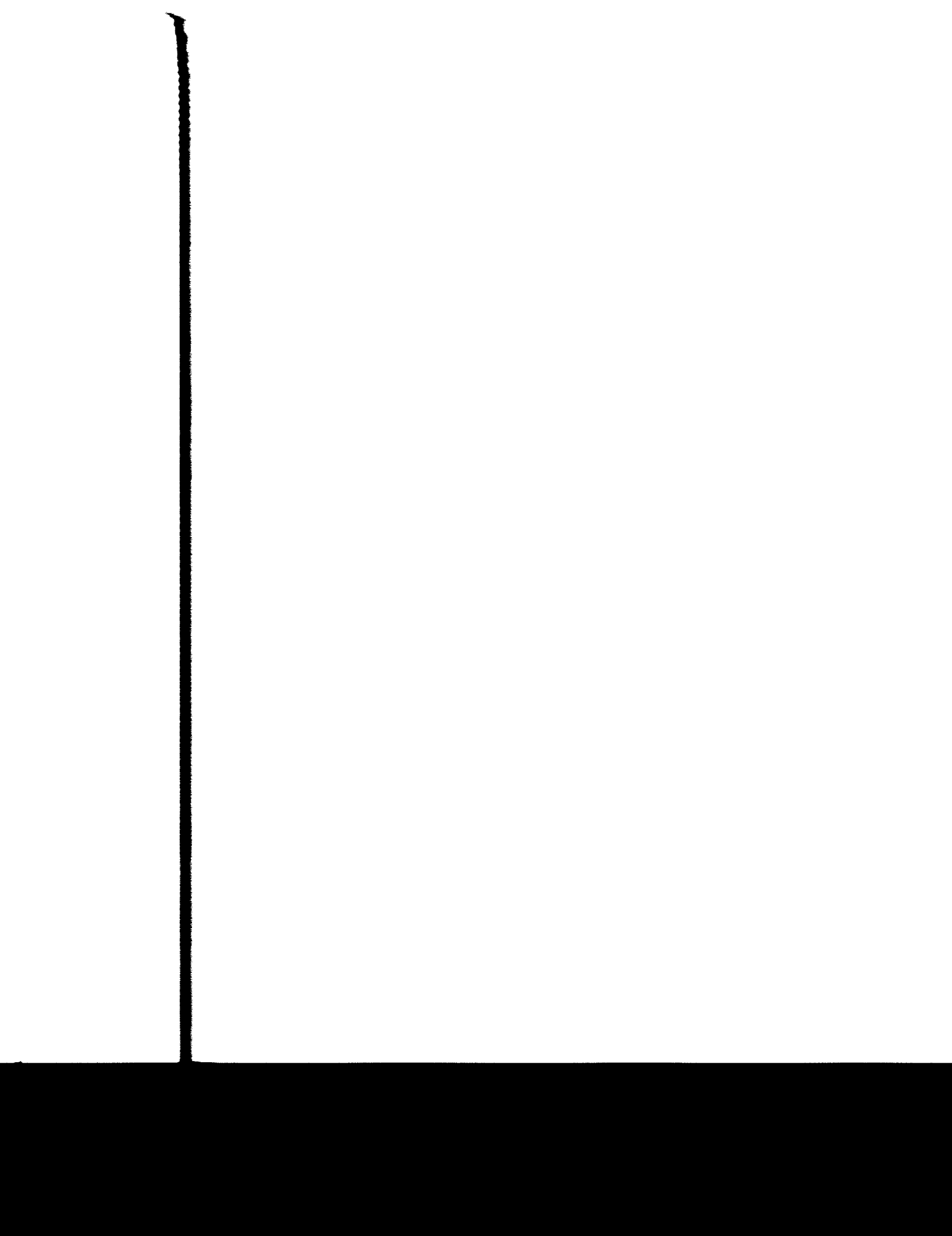

possibility of explosion at engine ignition due to trapped gases in the interstage adapter. Moreover, the thermal environment in the engine compartment may be more severe than with other methods, and the vibration and acoustic environment may be more severe.

7.5 CONCLUSIONS AND RECOMMENDATIONS

The analytical techniques required to determine staging and jettison loads are, for the most part, well developed. While the Newtonian approach was used to develop the analysis of Section 7.3.1, the Lagrangian approach is more suitable for more complicated systems. When the elastic effects are considered in the analysis, Lagrange's equation has a decided advantage. It may also be desirable to derive the equations initially with respect to the center of gravity and then, if necessary, transform them into another set having the desired variables.

Shock and gas impingement loads must ordinarily be determined from tests.

Methods for calculating modes of partial shells require further development for direct project support applications. In order to reliably predict hinge loads and fairing deflections the flexibility of the fairing and hinge must be taken into account.

7.6 REFERENCES

7.1 Program 624A Standard Space Launch Vehicle Staging Dynamics Analysis Report, Flight Test Plan VIII, Martin Company Report SSD-CR-65-35, February 1965.

7.2 R. L. Goble, Analytical Investigation of the Motion of a Clamshell-Type Heat Shield on Deployment From a Parent Vehicle in the Atmosphere, NASA TN D-3280, March 1966.

7.3 T. E. Lang, Summary of the Functions and Capabilities of the Structural Analysis System Computer Program, Jet Propulsion Laboratory, TM 33-220, June 1965.

7.4 L. E. Penzes, Frequency, Dynamic Response and Jettison Analysis for Jettisonable Payload Shrouds, with Application to the Orbital Astronomical Observatory (OAO) Fairing, Institute of Environmental Sciences, 1966.

7.5 Separation Joint Test Program, Lockheed Missiles and Space Company Report LMSC/A639047, April 15, 1964.

7.6 R. L. Batten, and E. C. Noble, Jr., "Shaped Charge Shock Environment for Centaur Vehicle Components", 35th Symposium on Shock and Vibration, New Orleans, La., October 1965.

7.7 Centaur Insulation Panel Unlatch Shock Measurements, General Dynamics Convair Division Report RAC ZZA-65-303, 22 September 1965.

7.8 "G" Series Centaur Forward Bulkhead Vibration Response Test, General Dynamics Convair Division Report RAC ZZA-65-130, 19 March 1965.